



N 7 3 3 0 2 4 0

NASA CR 121248

PSU AERSP 73-9

# CASE FILE COPY

## **INVESTIGATION OF BOUNDARY LAYER AND TURBULENCE CHARACTERISTICS INSIDE THE PASSAGES OF AN AXIAL FLOW INDUCER**

by

A. ANAND, C. GORTON, B. LAKSHMINARAYANA, H. YAMAOKA

Prepared from work done under

NASA Grant NGL 39-009-007

Technical Management  
NASA Lewis Research Center  
Cleveland, Ohio  
Liquid, Rocket Technology  
Werner R. Britsch

Department of Aerospace Engineering  
The Pennsylvania State University  
University Park, Pa.  
July, 1973

NASA CR 121248

PSU AERSP 73-9

INVESTIGATION OF BOUNDARY LAYER AND  
TURBULENCE CHARACTERISTICS  
INSIDE THE PASSAGES  
OF AN AXIAL FLOW INDUCER

By

A. Anand, C. Gorton, B. Lakshminarayana & H. Yamaoka

NASA GRANT NGL 39-009-007

Department of Aerospace Engineering  
The Pennsylvania State University  
University Park, Pa. 16802

1. Report No. NASA CR 121248		2. Government Accession No.		3. Recipient's Catalog No.	
4. Title and Subtitle  Investigation of Boundary Layer and Turbulence Characteristics Inside the Passages of an Axial Flow Inducer.				5. Report Date July 1973	
				6. Performing Organization Code	
7. Author(s) A. Anand, C. Gorton, B. Lakshminarayana and H. Yamaoka				8. Performing Organization Report No. PSU AERSP. 73-9	
9. Performing Organization Name and Address  The Pennsylvania State University 233 Hammond Building University Park, Pennsylvania 16802				10. Work Unit No. YON 0559	
				11. Contract or Grant No. NGL 39-009-007	
12. Sponsoring Agency Name and Address  National Aeronautics and Space Administration Washington, D.C. 20546				13. Type of Report and Period Covered Contractor Report	
				14. Sponsoring Agency Code	
15. Supplementary Notes					
16. Abstract <p>A study of the boundary layer and turbulence characteristics inside the passages of an axial flow inducer is reported in this report. The first part deals with the analytical and experimental investigation of the boundary layer characteristics in a four bladed flat plate inducer passage operated with no throttle. An approximate analysis for the prediction of radial and chordwise velocity profiles across the passage is carried out. The momentum integral technique is used to predict the gross properties of the boundary layer. Equations are given for the exact analysis of the turbulent boundary layer characteristics using the turbulent field method. Detailed measurement of boundary layer profiles, limiting streamline angle and skin friction stress on the rotating blade is also reported.</p> <p>Part two of this report deals with the prediction of the flow as well as blade static pressure measurements in a three bladed inducer with cambered blades operated at a flow coefficient of 0.065. In addition, the mean velocity and turbulence measurements carried out inside the passage using a rotating triaxial probe is reported.</p>					
17. Key Words (Suggested by Author(s))  Rocket Pump Inducer Turbomachinery Three-Dimensional Boundary Layer				18. Distribution Statement  Unclassified - Unlimited	
19. Security Classif. (of this report) Unclassified		20. Security Classif. (of this page)		21. No. of Pages 220	
				22. Price*	

\* For sale by the National Technical Information Service, Springfield, Virginia 22151

## PREFACE

This report is written in two parts. The first part deals with the investigation of boundary layer development inside the passages of a four bladed flat plate inducer. The second part is concerned with the flow prediction, blade pressure and turbulence measurements inside the passages of a three bladed inducer with cambered blades.

The research contained in this report was performed under the sponsorship of National Aeronautics and Space Administration, and was conducted at the Department of Aerospace Engineering, of the Pennsylvania State University under the NASA Grant NGL 39-009-007. The author's wish to thank W. R. Britsch of NASA Lewis Research Center for his continued encouragement of fundamental research relevant to Turbomachinery Fluid Mechanics. Grateful acknowledgement is made to George Gurney for his help in the development of the rotating probe traversing device, and to Edward Jordan for his assistance in electronic instrumentation.

We should like to note that all the authors, listed alphabetically on the cover page, shared the work equally and no significance should be attached to the order in which the names appear.

B. Lakshminarayana

Principal Investigator



Part I

THREE DIMENSIONAL TURBULENT BOUNDARY  
LAYER CHARACTERISTICS INSIDE THE  
PASSAGES OF A FLAT PLATE HELICAL  
INDUCER

## CONTENTS

	page
1. Introduction . . . . .	1
2. Theoretical Considerations . . . . .	3
2.1 Equations of Motion . . . . .	6
2.2 Velocity Profile Analysis in the Outer Region . .	7
2.3 Flow Near the Blade Surface . . . . .	8
2.4 Momentum Integral Solution . . . . .	12
2.5 Asymptotic Solution . . . . .	21
2.6 Turbulent Field Method . . . . .	25
3. Experimental Program . . . . .	32
3.1 Facility Description . . . . .	32
3.2 Experimental Method and Instrumentation . . . . .	33
3.3 Effect of Throttle . . . . .	35
3.4 Blade Static Pressures . . . . .	37
3.5 Limiting Streamline Angle Measurement . . . . .	38
3.6 Determination of the Wall Shear Stress . . . . .	40
3.7 Velocity Profiles Inside the Blade Passages . . .	47
4. Future Measurements . . . . .	59
4.1 Hot Wire Measurements . . . . .	59
4.2 Wall Shear Measurements . . . . .	64

## NOMENCLATURE

$a^* \frac{\overline{-uv}}{q^2}$	Universal boundary layer parameter in Bradshaw's turbulent field method
A, B, C	Constants
c	Curvature of external streamlines
$C_f$	Skin friction coefficient
d	Outside diameter of the Preston tube
$d_h$	Hydraulic diameter
e	Instantaneous voltage
E	Mean voltage
$E(H_{\delta-\delta^*})$	Head's entrainment function
f	Function representing relation between cross flow and main flow velocity components
F	Function representing relation between normalized main stream velocity component and distance from the wall
g	Gravitational acceleration/cross flow profile function
G	Main flow profile function/diffusion parameter
h	Static head
H	Shape factor (ratio of local displacement thickness to momentum thickness)
i	Repetitive index (1,2,3)
k	Height of surface roughness/ $U_e/\Omega r$ , the ratio of main flow velocity to peripheral velocity/von karman constant
$l$	Mixing length
L	Dissipation length
n	Constant/index in a power law
p	Static pressure
$\Delta p$	Dynamic pressure
q	Magnitude of velocity/r.m.s. value of turbulent kinetic energy

## NOMENCLATURE (CON'T.)

$r$	Radial distance
$R$	Nondimensional radial distance $r/r_t$
$R_R$	Reynolds Number based on passage averaged main flow velocity and local radius
$R_x$	Reynolds Number based on peripheral velocity and distance from leading edge
$RG$	Normalized radial pressure gradient imposed on the boundary layer $= (R/U_e) (\partial U_e / \partial R)$
$S$	Semi-width of the channel
$TG$	Normalized tangential pressure gradient imposed on the boundary layer $= (1/U_e) (\partial U_e / \partial \theta)$
$u, v, w$	Velocity components in the reference coordinate system in $x, z, r$ directions respectively
$U, V, W$	Velocity components in region external to the boundary layer
$U_e$	Main flow velocity component at the edge of the boundary layer
$U_\tau$	Friction velocity $\sqrt{\tau_o / \rho}$
$v$	Fluctuating component of effective cooling velocity on a hot wire
$V_e$	Total instantaneous effective cooling velocity on a hot wire
$V_z$	Averaged axial velocity
$W$	Wake function/total velocity in relative frame of reference
$X$	Distance measured in the tangential direction
$x, z, Y$	Orthogonal nonlinear coordinate system in rotating frame of reference.
$Z$	Distance normal to the wall
$Z^+$	Nondimensional distance $U_\tau Z^+ / \nu$

NOMENCLATURE (CON'T)Greek Symbols

$\alpha$	Limiting streamline angle/angle between radial and mainstream velocity components
$\alpha_o$	Flow angle measured from the tangential direction at distanced away from the wall
$\beta$	Main flow turning angle
$\gamma$	Angle characteristic of an individual pitot tube
$\delta$	Boundary layer thickness
$\delta^*, \delta_2^*$	Boundary layer displacement thickness parameters
$\Delta = \delta R_e^{1/5}$	Boundary layer thickness variable
$\epsilon_o/\epsilon_w$	Limiting streamline parameter = $\tan \alpha$
$\epsilon$	Dissipation term of turbulent kinetic energy
$\theta$	Angular variable
$\theta_{11}$	Main stream momentum thickness
$\theta_{12}, \theta_{21}, \theta_{22}$	Momentum thickness parameters
$\nu$	Kinematic viscosity
$\eta = z/\delta$	Nondimensional distance from the wall
$\rho$	Density of the fluid
$\tau_o$	Wall shear stress
$\tau_x, \tau_r$	Shear stress components inside the boundary layer
$\Omega$	Angular velocity of rotation
$\psi$	Blade loading coefficient
$\psi_s$	Blade static pressure coefficient
$\pi$	Cole's parameter for imposed pressure gradients on the boundary layer
$\phi$	Flow coefficient

NOMENCLATURE (CON'T)Superscripts

-	Time averaged value
'	Fluctuating value

Subscripts

c	Critical value/transition
e	Value in the flow external to the boundary layer
h	Hub
s	Static conditions
t	tip
x,z,r	Values in the coordinate directions
o	Value at the Wall/at zero numerical value
1	Main flow direction
2	Cross flow direction

## LIST OF FIGURES

1. The Triangular Model
2. The Hodograph Plot
3. Four Bladed Inducer Configuration (Flat Plate Type)
4. Existing Traverse Facility for Rotating Probe Measurements
5. Static Pressure Distribution for 3 Bladed Inducer (Ref. 15)
6. Radial Variation of Blade Static Pressure on 3 Bladed Inducer
7. Radial Variation of  $K = U_e / \Omega R$
8. Chordwise Variation of RG
9. Chordwise Variation of TG
10. Chordwise Variation of Momentum Thickness for a Single Helical Blade
11. Chordwise Distribution of Limiting Streamline Angle for a Single Helical Blade
12. Tangential Variation of Momentum Thickness ( $\theta_{11}$ ) in 3 Bladed Inducer
13. Tangential Variation of Limiting Streamline Angle for 3 Bladed Inducer
14. Qualitative Nature of Velocity Profiles in an Inducer Channel
15. Nature of Velocity Profiles in the Asymptotic Region
16. Coordinate System for Turbulent Field Method
17. Schematic Diagram of Experimental Setup
18. Annulus Wall Static Pressure Distribution
19. Distribution of Stagnation Pressure Coefficient  $\psi_T$  at the Inducer Exit at Different Throttle Positions
20. Radial Distribution of Outlet Angle  $\alpha$  at the Exit of 4 Bladed Flat Plate Inducer
21. Performance Characteristics of 4 Bladed Flat Plate Inducer
22. (a), (b) Radial Distribution of Blade Static Pressure Coefficient

## LIST OF FIGURES

23. Chordwise Distribution of Blade Static Pressure Coefficient
24. (a)(b)Radial Distribution of Limiting Streamline Angle
25. (a),(b),(c) Chordwise Variation of Limiting Streamline Angle
26. Variation of Total Pressure with Probe Angle
27. Variation of Skin Friction Coefficient with Reynolds Number
28. Calibration Curve for the Disk Probe
29. Developed View of the Hub
30. (a),(b),(c),(d),(e) Blade to Blade Distribution of Tangential Velocity at Stations #1, 2, 3, 4 and 5 respectively
31. (a),(b),(c) Comparison of Experimental Velocity Profile to the Power Law
32. (a),(b),(c) Cole's Plot of Experimental Velocity Profiles
33. Comparison of Passage Averaged Tangential Velocity Component
- 34 (a),(b),(c),(d),(e) Blade to Blade Distribution of Radial Velocity Component at Stations #1, 2, 3, 4 and 5 respectively
35. Radial Velocity in Midchannel at Station #1
36. (a),(b),(c) Mager's Plot of Radial Velocity Component
37. (a),(b),(c),(d),(e),(f),(g) Hodograph Plots
38. (a) Hodograph Representation on Trailing Side Boundary Layer  
(b) Hodograph Representation on Leading Side Boundary Layer
39. Hodograph Plot for Inward Radial Flow Region
40. (a),(b),(c) Defect Representation of the Interference Region
41. Radial Distribution of Passage Averaged Mean Radial Velocity
42. (a) Tangential Variation of Momentum Thickness on Leading Side of 4 Bladed Flat Plate Inducer  
(b) Tangential Variation of Momentum Thickness on Trailing Side  
(c) Tangential Variation of Limiting Streamline Angle on Leading Side  
(d) Tangential Variation of Limiting Streamline Angle on Trailing Side
43. Shape Factor Distribution Inside the Rotor Channel
44. Shape Factor Distribution Obtained from Power Law Fit
45. (a),(b) Skin Friction Variation with Reynolds Number on Trailing and Leading Sides



## LIST OF FIGURES

46. (a),(b) Clauser Plots to Obtain Skin Friction from Velocity Profiles
47. Orientation of 3 Sensor Probe
48. 3 Channel Signal Handling System

## 1. INTRODUCTION

Since 1963, an extensive investigation of the inducer flows has been carried out at the Department of Aerospace Engineering at The Pennsylvania State University under NASA sponsorship. A model of an inducer was constructed and characteristics of two, three and four bladed inducers were investigated. The inducer blade had radially variable thickness, camber, and tangential extent of average 290 degrees. The flow through a long and narrow passage is subjected both to the potential flow effect determined by the rotor blade geometry and to the effect of the viscosity of fluid. Attempts to predict the flow in these passages is dealt with in Refs. 10 and 15.

It is seen that, due to the effect of viscosity, the fluid in the immediate vicinity of the blade surfaces is set in rotating motion, and is subjected to centrifugal and Coriolis forces. As a result, direction of the flow outside the boundary layer becomes different from the direction of the flow inside the boundary layer, i.e., the skewed, or three-dimensional, boundary layer is formed. Thus, it becomes essential to investigate the behavior of three-dimensional boundary layer flow in order to understand behavior of the flow in the inducer passage.

Since the blade passages are long and narrow, the boundary layers on the inducer surfaces experience channel effects. They interact strongly with the comparatively inviscid external flow, and with the annulus wall boundary layer, producing the observed radial inward flows. (23,24). These radial flows are found to increase as the blade boundary

layers grow and merge with stress-reversal, and reduction in mainstream velocity, etc. (23, 39). Since these phenomena have not been observed in a stationary channel, these are anticipated to have been caused by the rotation of the blade passages.

General treatment of the three-dimensional boundary layer flow is extremely difficult because of the mathematical difficulties involved in solving the governing equations. The method used most often to solve this problem is to assume the mean velocity distribution in the boundary layer based on various laws that are obtained mainly for two-dimensional boundary layer flows. Though this approach has been successful for the treatment of the three-dimensional boundary layer flows that do not deviate much from the two-dimensional ones, it is expected that such approach cannot be applied satisfactorily to the highly skewed boundary layer flows which are created by the effect of rotation, i.e., the rotating type three-dimensional boundary layer flows. With an intention to obtain general information on the rotating type of boundary layer flow, a helical blade was constructed and some characteristics of turbulent boundary layer flow on the rotating helical blade were investigated (5,9). The previous analysis of the flow carried out at Penn State are based on assumptions for velocity profiles, which is largely derived from the existing information on two-dimensional and three-dimensional boundary layers. The prediction so obtained are only qualitative. The main reason for this being the lack of information on the velocity profiles and shear stress in a narrow rotating channel of type used in an inducer. The objective of this investigation is to provide this important scientific information in the eventual viscous solution of the flow field in an inducer.

An attempt is made in this report to predict the three-dimensional boundary layer characteristics in a rotating channel. Sections 2.2 and 2.3 deal with the velocity profile analysis and the momentum integral solution is described in section 2.4. An approximate solution of the flow in the radial flow reversal region (mid passage) is dealt with in section 2.4 and a future method of approach is outlined in section 2.5

In order to investigate the effect of the fluid viscosity, a rotor assembly was constructed with a simple geometry. The fabrication details of this new rotor assembly, machined accurately to avoid vibration, is described in section 3.1. Instruments used are described in section 3.2. Measurements of the blade static pressure, limiting streamline angle and skin friction were carried out on the blade surfaces of open throttle conditions (Sec. 3.5, 3.6, 3.7). Total pressure and flow angle measurements were carried out inside the rotor channel (Section 3.8). A throttle was installed to study the flow in the inducer at different flow coefficient (Section 3.3) and the flow measurements at the rotor exit are reported in Section 3.4. All measurements were carried out at 450 RPM and at Reynolds Number (based on tip radius)  $6.6 \times 10^5$ . Unless otherwise indicated, the measurements refer to no throttle conditions.

## 2. THEORETICAL CONSIDERATIONS

Flow in the rotating helical channel can be divided into two parts. One is the boundary layer flow near the blade surfaces where the effect of viscosity of the fluid is large, and the other is the flow outside the boundary layer where the effect of viscosity of the

fluid is negligible. Since the boundary layer flow has a rotational motion, it is subjected to two additional forces, centrifugal and Coriolis forces. As a result, a radial flow, or cross flow, is produced. The direction of the boundary layer flow becomes different from the direction of the flow outside the boundary layer, i.e., three-dimensional boundary layer is formed on the blade surfaces.

The first general model of the three-dimensional boundary layer flow was proposed by Prandtl in 1946 (16). He considered that the flow in the free stream direction  $u$  and the cross flow  $w$  can be represented by

$$\begin{aligned}\frac{u}{U} &= G(\eta) \\ \frac{w}{U} &= \epsilon_0 g \cdot G\end{aligned}\tag{1}$$

where  $g$ ,  $G$  are universal functions of  $\eta = z/\delta$ .  $U$  is a free stream velocity,  $\epsilon_0$  is the limiting streamline parameter,  $z$  the distance normal to the surface, and  $\delta$  the boundary layer thickness. This model has been used by many. Perhaps the most well known model was given by Mager (11). This model can be considered as an extension of two-dimensional power law approximation to three-dimensional boundary layer flow.

Coles (1) suggested that his model for the two-dimensional boundary layer flow could be extended to the three-dimensional boundary layer flow. He considered that the mean velocity profile could be represented by,

$$\bar{u} = \bar{U}_T f(z^+) + \bar{U}_T \Pi W(\eta), \text{ where } \eta = z/\delta .\tag{2}$$

where  $f$ ,  $W$  are universal functions representing the "law of the wall" and the "law of the wake" respectively.  $\bar{U}_\tau$  is a friction velocity vector; its magnitude is given by  $\sqrt{\tau_0/\rho}$  and its direction is the same as the wall shear stress direction.  $\pi$  is a tensor such that  $\bar{u}$  is in the direction of the free stream velocity at  $z = \delta$ . Validity of the Coles model was experimentally investigated by Hornung and Joubert (4). Pierce (13) also demonstrated that the Coles model was appropriate for the skewed flow.

In 1960, Johnston (7) presented a new approach to the three-dimensional boundary layer flow analysis. He considered that the cross flow component was related to the main flow component by

$$\frac{w}{U} = f(\epsilon_0, A, \frac{u}{U}) \quad (3)$$

where  $\epsilon_0$ ,  $A$  are parameters. In the outer part of the boundary layer he obtained a linear relationship given by

$$\frac{w}{U} = A(1 - \frac{u}{U}) \quad (4)$$

By considering that in the region very close to the wall the direction of the flow must be the same as the wall shear stress direction, i.e.,

$$\frac{w}{U} = \epsilon_0 \frac{u}{U} \quad (5)$$

he noticed that the velocity profile can be represented by the two straightlines in the hodograph plane. This is known as the Johnston triangular model (Figure 1). Variations of this model have been used by many. Eichelbrenner and Peube (2) considered that the cross flow component can be represented by a higher degree polynomial of the main flow component, and Shanebrook (19) used the fifth degree polynomial expression.

Klinksiek and Pierce (8) produced a simultaneously laterally skewed boundary layer flow and showed validity of the polynomial expressions. Lakshminarayana, Jabbari and Yamaoka (9) used 1/7th profile for the mainstream velocity and Mager's profile for radial velocity and predicted the momentum thickness and limiting streamline angle on a rotating single blade. The agreement between theory and experiment was found to be reasonably good. They also derived an expression for radial velocity profile in the nearly inviscid region. This is briefly mentioned in section 2.2

### 2.1 Equations of Motion:

For the purpose of this analysis the helical channel (Figure 3), whose pitch is very small, is approximated by a flat circular channel with a leading and trailing edge. The calculation makes use of this approximation, but the asymmetry of the flow that would prevail in the case of a helical channel is taken into account (i.e., it is assumed that the trailing edge does not influence the leading edge flow). This model is similar to those of reference 9.

The equations of motion in cylindrical coordinates  $(r, \theta, z)$  rotating with an angular velocity  $\Omega$  about the  $z$  axis is given by,

$$\frac{1}{r} \frac{\partial u}{\partial \theta} + \frac{\partial v}{\partial z} + \frac{\partial w}{\partial r} + \frac{w}{r} = 0 \quad (6)$$

$$\frac{u}{r} \frac{\partial u}{\partial \theta} + v \frac{\partial u}{\partial z} + w \frac{\partial u}{\partial r} - \frac{w}{r} (2\Omega r - u) = -\frac{1}{\rho} \frac{\partial p}{r \partial \theta} + \frac{1}{\rho} \frac{\partial \tau_{\theta u}}{\partial z} \quad (7)$$

$$\frac{u}{r} \frac{\partial w}{\partial \theta} + v \frac{\partial w}{\partial z} + w \frac{\partial w}{\partial r} - \frac{(\Omega r - u)^2}{r} = - \frac{1}{\rho} \frac{\partial p}{\partial r} + \frac{1}{\rho} \frac{\partial \tau_w}{\partial z} \quad (8)$$

Equations (7) and (8) are  $\theta$  momentum and  $r$  momentum equations respectively.  $u$ ,  $v$ , and  $w$  are components of velocity along  $r$ ,  $\theta$ , and  $z$  directions.  $\tau_u$  and  $\tau_w$  are shear stresses in the direction of  $u$  and  $w$ . The flow is assumed to be incompressible and steady relative to the blade.

## 2.2 Velocity Profile Analysis in the Outer Region:

In the outer part of the boundary layer, the shear forces are considered to be negligibly small. For a fully developed flow ( $\frac{\partial}{\partial \theta} = 0$ ) equations 7 and 8 reduce to (assuming that the velocity in the external flow is  $\Omega r$ ),

$$v \frac{\partial u}{\partial z} + w \frac{\partial u}{\partial r} - \frac{w}{r} (2\Omega r - u) = 0 \quad (9)$$

$$v \frac{\partial w}{\partial z} + w \frac{\partial w}{\partial r} - \frac{u^2}{r} + 2\Omega u = \frac{U^2}{r} \quad (10)$$

If  $w$  is assumed to be a function of  $u$ , the following expression can be derived (9, 21) for radial velocity

$$\frac{w}{U} = c_1 \sqrt{(1 - \frac{u}{U}) (c + \frac{u}{U})} \quad (11)$$

The experimental data obtained for the boundary layer flow on a rotating helical blade are well represented by the relation

$$\frac{w}{U} = 0.3 \sqrt{\frac{u}{U} (1 - \frac{u}{U})} \quad (12)$$

as shown in Fig. 2. It is interesting to note that, while the velocity profile at the outer part of the stationary type boundary



layer flow is represented by the linear relation given by Johnston, the velocity profile at the outer part of the rotating type boundary layer flow is represented by the circular arc.

### 2.3 Flow Near the Blade Surface:

In a region very close to the blade surface, flow must be mainly a viscous one, since all velocities, including turbulent fluctuations, become zero at the surface. In this region, velocity components are so small that the inertia terms become negligibly small compared to Coriolis terms. In this region equations 7 and 8 become

$$- 2\Omega w = \nu \frac{\partial^2 u}{\partial z^2} \quad (13)$$

$$+ 2\Omega u = \frac{U^2}{r} + \nu \frac{\partial^2 w}{\partial z^2} \quad (14)$$

where  $\nu$  is the kinematic viscosity,  $U$  is the free stream velocity ( $\Omega r$ ). By eliminating the Coriolis forces from the above equations, following equation is obtained

$$\frac{U^2}{r} w + \nu \left( w \frac{\partial^2 w}{\partial z^2} + u \frac{\partial^2 u}{\partial z^2} \right) = 0 \quad (15)$$

It is considered that the cross flow component can be represented by a function of the velocity component in the direction of the streamline

$$\frac{w}{U} = f\left(\frac{u}{U}\right) \quad (16)$$

Substituting this relation, equation (15) becomes

$$\frac{U^2}{r} f + \nu \left\{ \frac{u}{U} \frac{\partial^2 u}{\partial z^2} + \frac{1}{U} f' f'' \left( \frac{\partial u}{\partial z} \right)^2 + f f' \frac{\partial^2 u}{\partial z^2} \right\} = 0 \quad (17)$$

Here,  $f'$ ,  $f''$  represent the derivatives of  $f$  with respect to  $u/U$ .

It is generally accepted that the law of the wall does exist for three-dimensional boundary layer flows. Experimental verifications of the existence of the law were given by Pierce and Krommenhoek (14) for the stationary type boundary layer flow and by Lakshminarayana et al (9) for the rotating type boundary layer flow. It is considered that the velocity component in the direction of the streamline is represented as a function of  $z^+ = U_\tau z/\nu$ .

$$\frac{u}{U_\tau} = F(z^+) \quad (18)$$

In the region very close to the blade surface, it is considered that the flow is very little affected by the presence of the pressure gradient outside the boundary layer. Then, by the use of equation 18, after some calculation, equation 17 becomes

$$-\frac{\frac{u}{U} + ff'}{f} F'' - \frac{U_\tau}{U} f'' F'^2 = \frac{1}{r^+} \left(\frac{U}{U_\tau}\right)^2 = \text{constant} \quad (19)$$

The second term on the left-hand side is very small and hence let us assume it is zero for the moment. Later we will prove that this term is identically zero.

The first term gives

$$\frac{\frac{u}{U} + ff'}{f} = \text{constant } C_1 \quad (20)$$

$$F'' = \text{constant } C_2 \quad (21)$$

where  $C_1$  and  $C_2$  are constants, such that  $C_1 C_2 \neq 0$ .

Equation (20) has a solution  $w/U = f = \varepsilon_0 (u/U)$ , where  $\varepsilon_0$  is a constant. (22)

This also gives  $f'' = 0$  which shows second term on the left hand side is equal to zero.

Therefore, substituting expression for (f) in Equation (19),

$$F'' = - \frac{\epsilon_0}{1+\epsilon_0^2} \cdot \frac{1}{r^+} \cdot \left(\frac{U}{U_\tau}\right)^2 = C_2 \quad (23)$$

Upon integration twice, the expression for F is obtained.

$$F = \frac{1}{2} C_2 (z^+/2)^2 + C_3 z^+ + C_4 \quad (24)$$

Boundary conditions at the wall are

$$F = 0, \quad \frac{dF}{dz^+} = 1 \quad \text{at } z^+ = 0$$

and

$$F = z^+ \left\{ 1 - \frac{\epsilon_0}{2(1+\epsilon_0^2)} \frac{1}{r^+} \left(\frac{U}{U_\tau}\right)^2 z^+ \right\} = z^+ (1 - Bz^+) \quad (25)$$

where B is a constant with a value of order  $10^{-2} - 10^{-3}$  for turbulent boundary layers depending upon the extent of cross flow. For small values of  $z^+$ , equation (25) approximates to

$$F \approx z^+ \quad (26)$$

This is identical to the expression given for the laminar sublayer of two dimensional boundary layer flows.

The analysis developed above shows that the collateral region does exist in the rotating type three-dimensional boundary layer flows. The collateral region is defined as a region where the inertia terms are negligible and the viscous forces are balanced by the Coriolis forces. As the distance approaches zero, it becomes identical to the expression given for the laminar sublayer of two-dimensional boundary layer flows.

In the present analysis, equation 11 is obtained in the outer region of the boundary layer where the shear stresses are considered negligible;

it is valid only in the region near the outer edge of the boundary layer. It is considered that majority of the boundary layer flow is represented by a region in which neither the Reynolds stresses nor the inertia terms may be neglected. Solution of this region can only be obtained by numerical integration of the entire equations of motion.

## 2.4 Momentum Integral Solution:\*

The method is an extension of Lakshminarayana et al's (9) method for predicting the boundary layer growth on a single rotating helical blade. The method described below includes the effect of the pressure gradients imposed by the external flow. The two momentum integral equations (one in the main stream and the other in cross flow direction) are reduced to two first order partial differential equations using a power law profile for the main stream velocity, Mager's profile for the cross flow and the skin friction relation is based on the boundary layer flow on a flat, stationary plate with modification to include the effect of rotation (9). The imposed pressure gradients are obtained from the three-dimensional inviscid numerical solution of the flow field (15). The resulting two first order partial differential equations are solved numerically by a finite-difference scheme. Details of the assumptions involved, equations and the method of solution has been described in an earlier report (3D). The two momentum equations in cylindrical coordinate systems are:

$$\frac{\partial \theta_{11}}{\partial \theta} + \frac{r}{U_e} \frac{\partial U_e}{\partial r} (2\theta_{12} - \delta_2^*) + (2\theta_{11} + \delta_1) \frac{1}{U_e} \frac{\partial U_e}{\partial \theta} \quad (27)$$

$$+ r \frac{\partial \theta_{12}}{\partial r} + 2\theta_{12} + \delta_2^* \left(\frac{2}{k} - 1\right) = \frac{c_{f\theta} \eta}{2}$$

$$\frac{\partial (r\theta_{22})}{\partial r} + 2 \frac{r}{U_e} \frac{\partial U_e}{\partial r} \theta_{22} + 2 \theta_{21} \frac{1}{U_e} \frac{\partial U_e}{\partial \theta} + \frac{\partial \theta_{21}}{\partial \theta} \quad (28)$$

$$+ \theta_{11} - \delta_1 \left(\frac{2}{k} - 1\right) + \epsilon_w \frac{c_{f\theta} \eta}{2} = 0$$

\*The equations developed and the solutions given in this as well as the next two sections have general validity; applicable equally to flow investigated here as well as the inducer flow investigated in Part 2 of this report.

where  $\theta_{11}$ ,  $\theta_{12}$  etc. are momentum thickness,  $\delta_1$ ,  $\delta_2^*$  are displacement thicknesses in main stream and cross flow directions defined as follows,

$$\theta_{11} = \int_0^{\delta} \frac{u}{U_e} \left(1 - \frac{u}{U_e}\right) dz$$

$$\delta_1 = \int_0^{\delta} \left(1 - \frac{u}{U_e}\right) dz$$

$$\theta_{12} = \int_0^{\delta} \left(1 - \frac{u}{U_e}\right) \frac{w}{U_e} dz$$

$$\theta_{22} = \int_0^{\delta} \left(\frac{w}{U_e}\right)^2 dz \quad (29)$$

$$\delta_2^* = \int_0^{\delta} \left(\frac{w}{U_e}\right) dz$$

$$\theta_{21} = \int_0^{\delta} \frac{uw}{U_e^2} dz$$

and  $k = \frac{U_e}{\Omega r}$ ,  $U_e$  is the velocity in the main stream direction at the edge of the boundary layer.

The assumed main stream velocity profile is

$$\frac{u}{U_e} = \left(\frac{z}{\delta}\right)^{\frac{1}{n}} = \left(\frac{z}{\delta}\right)^{\frac{H-1}{2}} = \eta^{\frac{H-1}{2}} \quad (30)$$

where  $H$  is the local shape factor and  $\eta$  is nondimensional  $z$  coordinate.

The assumed cross flow velocity profile is

$$\frac{w}{u} = \epsilon_w (1 - \eta)^2 \quad (31)$$

The skin friction relation used is given by,

$$C_{f\theta} = 0.0582 R_\theta^{-1/5} (1 + 0.85 \sqrt{\epsilon_w \theta}) \quad (32)$$

where  $R_\theta$  is the Reynolds Number based on relative tangential velocity and distance from the leading edge. It is proposed to use the following Ludweig's and Tillmann's skin friction relation

$$C_{f\theta} = 0.246 10^{-0.678H} R_{\theta_{11}}^{-0.268} (1 + 0.85 \sqrt{\epsilon_w \theta}) \quad (33)$$

Use of the above assumed relations (equations 30-33) simplifies equations (27) and (28) in terms of three parameters  $\theta_{11}$ ,  $\epsilon_w$  and  $H$ . The resulting equations are,

$$\frac{\partial \theta_{11}}{\partial \theta} + (2 + H) \frac{\theta_{11}}{U_e} \frac{\partial U_e}{\partial \theta} + 2J\epsilon_w \theta_{11} \left(1 + \frac{\gamma}{U_e} \frac{\partial U_e}{\partial r}\right) + J\gamma \frac{\partial}{\partial r} (\theta_{11} \epsilon_w) \quad (34)$$

$$+ L \left( \frac{2}{k} - 1 - \frac{\gamma}{U_e} \frac{\partial U_e}{\partial r} \right) \epsilon_w \theta_{11} = \frac{C_{f\theta}}{2}$$

and

$$N \frac{\partial (\epsilon_w \theta_{11})}{\partial \theta} + 2N\epsilon_w \frac{\theta_{11}}{U_e} \frac{\partial U_e}{\partial \theta} + \theta_{11} + \frac{2\gamma}{U_e} \frac{\partial U_e}{\partial r} M\epsilon_w^2 \theta_{11} + M \frac{\partial}{\partial r} (r\epsilon_w^2 \theta_{11}) - H\theta_{11} \left( \frac{2}{k} - 1 \right) + \epsilon_w \frac{C_{f\theta}}{2} = 0 \quad (35)$$

where

$$\begin{aligned}
 J &= \frac{\theta_{12}}{\epsilon_w \theta_{11}} = \frac{n^2 (11n+7)}{(2n+1) (3n+1) (3n+2)} = \frac{(30+14H)}{(H+2) (H+3) (H+5)} \\
 L &= \frac{\delta_2^*}{\epsilon_w \theta_{11}} = \frac{2n^2 (n+2)}{(2n+1) (3n+1)} = \frac{16H}{(H-1) (H+3) (H+5)} \\
 M &= \frac{\theta_{22}}{\epsilon_w^2 \theta_{11}} = \frac{6n^4}{(2n+1) (3n+2) (5n+2)} = \frac{24H}{(H-1) (H+2) (H+3) (H+4)} \\
 N &= \frac{\theta_{11}}{\epsilon_w \theta_{11}} = \frac{n^2}{(3n+2)} = \frac{2}{(H-1) (H+2)}
 \end{aligned} \tag{36}$$

We now have two equations and three unknowns ( $\theta_{11}$ ,  $\epsilon_w$ , and  $H$ ), since  $U_e$  is assumed to be known and values of  $C_f$  will be based on empirical relationships. Anyone of the following relationships for  $H$  can be used for the additional equation needed for the solution of the boundary layer integral momentum equations.

- (1) From the data of an isolated airfoil (VonDoenhoff and Tetrevin (26)),

$$\frac{\theta_{11}}{r} \frac{\partial H}{\partial \theta} + e^{4.68(H-2.975)} \left\{ \frac{4}{r} \frac{\theta_{11}}{U_e C_{f\theta}} \frac{\partial U_e}{\partial \theta} + 2.035 (H-1.286) \right\} = 0 \tag{37}$$

- (2) Head's Entrainment Equation (27)

$$\frac{\partial}{r \partial \theta} [U_e \theta_{11} H_{\delta-\delta^*}] + \frac{U_e}{r} \theta_{11} H_{\delta-\delta^*} - L \frac{\partial}{\partial r} (U_e \epsilon_w \theta_{11}) = E(H_{\delta-\delta^*}) \tag{38}$$

where  $E(H_{\delta-\delta^*})$  is an empirical function obtained from two-dimensional experiments.



$$E(H_{\delta-\delta}^*) = 0.0306 (H_{\delta-\delta}^* - 3.0)^{-0.653}$$

(39)

where  $H_{\delta-\delta}^* = 2H/(H-1)$

(3) Integral form of Continuity Equation with external flow assumed to be two dimensional, inviscid and in radial equilibrium:

$$\frac{\partial}{\partial \theta} (\theta_{11} H) + \frac{1}{U_e} \frac{\partial U_e}{\partial \theta} \theta_{11} H - L \frac{\partial}{\partial r} (r \epsilon_w \theta_{11}) - L \frac{r}{U_e} \frac{\partial U_e}{\partial r} \epsilon_w \theta_{11} \quad (40)$$

$$= \frac{\partial S}{\partial \theta} \left(1 + \frac{2\alpha}{\pi} \left(\frac{1-k}{k}\right)\right) + S \left(1 - \frac{2\alpha}{\pi}\right) \frac{1}{U_e} \frac{\partial U_e}{\partial \theta} + \frac{2\alpha}{\pi U_e} \frac{\partial}{\partial \theta} (U_e' \delta)$$

where  $U_e' = \Omega r - U_e$  and  $\delta = \frac{H(H+1)}{(H-1)} \theta_{11}$ ,  $S$  is the semiwidth of channel and

$\alpha$  is a parameter to account for the velocity defect in the midchannel.

$\alpha \approx 0\left(\frac{\delta}{S}\right)$  if the two boundary layers from the adjacent blade surfaces have

not merged. If the external flow has radial velocity component, as has

been observed inside the blade passage near the tip when the two blade

boundary layers and the annulus wall boundary layer have merged to form

an "Interference region,"  $\alpha \approx 1$ .

For small pressure gradient in the streamwise direction,  $H = 1.286$  and

equations 27 and 28 reduce to (for  $r_t = 1.5$  feet),

$$\begin{aligned} \frac{\partial \Delta}{\partial \theta} + 0.543 \epsilon_w R \frac{\partial \Delta}{\partial R} + \Delta \{ 3.285TG + 0.543R \frac{\partial \epsilon_w}{\partial R} + \epsilon_w \left( \frac{5.348}{K} - 1.588RG - 1.805 \right) \\ - \frac{0.2}{\theta} \} - 0.0442 AR = 0 \end{aligned} \quad (41)$$

and

$$\begin{aligned} \epsilon_w \frac{\partial \Delta}{\partial \theta} + 0.53 \epsilon_w^2 R \frac{\partial \Delta}{\partial R} + \Delta \{ (0.3175 + 1.058RG) \epsilon_w^2 + \epsilon_w (2.4TG - \frac{0.2}{\theta} + 1.06R \frac{\partial \epsilon_w}{\partial R}) \\ + \frac{\partial \epsilon_w}{\partial \theta} + (1.073 - \frac{1.208}{K}) \} + 0.0207 \epsilon_w AR = 0 \end{aligned} \quad (42)$$

where  $\Delta = \theta_{11} R_e^{1/5}$ ,  $\theta_{11}$  is the momentum thickness in the mainstream direction and  $R_e$  is the Reynold's number based on peripheral velocity and distance from the leading edge.

$\epsilon_w$  is the limiting streamline angle representing crossflow effect.

$TG = \frac{1}{U_e} \frac{\partial U_e}{\partial \theta}$  represents a term due to pressure gradient in  $\theta$  direction.

$RG = \frac{R}{U_e} \frac{\partial U_e}{\partial R}$  represents a term due to radial pressure gradient.

$k = \frac{U_e}{\Omega r}$ ,  $U_e$  is the velocity at the edge of the boundary layer and

$\Omega$  is the angular velocity of the rotor.

$A = 1 + 0.85 \sqrt{\epsilon_w \theta}$  is a rotation parameter

$R = \frac{r}{r_{tip}}$  is the normalized local radius.

The boundary conditions are

(1) At the leading edge  $\Delta(0, R) = \epsilon_w(0, R) = 0.0$

(2) At  $\Delta(\theta, 0.5)$  and  $\epsilon_w(\theta, 0.5)$  are assumed to be known and are given by the values for a single blade (9)

### Effect of Laminar Region near the Leading Edge ;

The flow near the leading edge is found to be laminar and its extent ( $\theta_c$ ) has been approximately predicted by a critical Reynolds number defined as  $\Omega R^2 \theta_c / \nu = 3 \times 10^5$ , where  $\nu$  is the kinematic viscosity of air. Banks and Gadd's (25) analysis is used to predict  $\theta_{11}$  and  $\epsilon_w$  in the laminar region up to the point of transition. It is to be noted that this analysis is valid for the laminar boundary layer over a single rotating blade, and so does not take into account the effect of imposed pressure gradients on the boundary layer. Since the actual pressure gradients (Fig. 4) are very small, the neglect of this effect may be justified. For  $\theta > \theta_c$ , the flow is assumed to be turbulent and the turbulent flow equations (41) and (42) are used to predict  $\theta_{11}$  and  $\epsilon_w$ .

#### 2.4.1 Theoretical Results and Discussion

The momentum integral technique described in the previous section has been used to predict the momentum thickness ( $\theta_{11}$ ) and limiting streamline angle at various  $r$  and  $\theta$  locations for (a) a single blade (b) four bladed flat plate inducer (c) three bladed inducer with cambered blade. The first test case is used as a check on the previous analysis of reference 9. For the last case, the three-dimensional inviscid solution of Poncet and Lakshminarayana(15) is used to obtain the chordwise and radial variation of RG, TG, and K. The inviscid prediction of  $\psi_s$  (static pressure rise coefficient) obtained at mid passage of the three bladed inducer are plotted in Figure 5 and 6. The variation of K, RG, and TG are shown in Figures 7, 8 and 9 respectively.

The predicted variation of  $\theta_{11}$  and  $\epsilon_w$  for a single blade are shown in Figures 10 and 11 respectively. The momentum thickness predicted by this theory is in close agreement with those of reference 9. Use of new skin friction correlation seems to predict larger growth in momentum thickness towards the trailing edge (Fig. 10). The analysis developed here seems to predict the larger values of  $\epsilon_w$  towards the hub and the variation  $\epsilon_w$  with radius is not allowed for in the theory developed by Lakshminarayana et al (9).

Figure 12 shows the chordwise ( $\theta$ ) variation of the mainstream momentum thickness ( $\theta_{11}$ ) for the three bladed inducer. It is seen that for  $\theta < 1.5$  radians, the pressure gradients are small and the values are closer to those for a single blade. ( $\sim 1\%$  of maximum value of  $\theta = 5$  rad.).

Further downstream ( $1.5 < \theta < 4$  radians)  $\theta_{11}$  is nearly constant and infact decreases at higher radii. This is unlike the single blade case where in  $\theta_{11}$  continually increases with  $\theta$  reaching an asymptotic value at large values of  $\theta$ . A study of equation (41) for  $\theta_{11}$  shows that the effect of positive chordwise pressure gradients is to increase the boundary layer thickness, while the effect of positive radial pressure gradients is to decrease it compared to the single blade case. It can therefore be concluded that in the present case, the effect of radial pressure gradient is much larger than the chordwise pressure gradient. This is confirmed by large decrease in  $\theta_{11}$  near tip radius where the radial pressure gradients are found to be much larger than the chordwise pressure gradients.

The experimental results of a four bladed flat plate inducer operated at 450 rpm and open throttle are also shown in Fig. 12. They confirm the trend of the numerical solution for three bladed inducer but the  $\theta_{11}$

values are larger and fall in between the single blade case and the three-bladed case. This is due to the fact that the four bladed inducer has been operated at open throttle and therefore smaller pressure gradients compared to those of the three-bladed inducer.

Figure 13 shows the chordwise ( $\theta$ ) variation of the limiting streamline angle  $\epsilon_w$  at various radial locations. In the turbulent part of the boundary layer i.e.,  $\theta > \theta_c$ ,  $\epsilon_w$  first decreases very rapidly with  $\theta$  up to  $\theta$  of the order of two radians then increases with increase in  $\theta$ . At given chordwise ( $\theta$ ) location,  $\epsilon_w$  decreases with radius (for values of  $\theta$  up to about two radians) and increases with radius at larger values of  $\theta$ . A comparison of  $\epsilon_w$  for three bladed inducer and single blade (Fig. 13) shows that the trend is similar in both cases except that there is no jump in  $\epsilon_w$  at  $\theta \sim 2$  radians for the single blade case. An examination of equation (42) indicates that  $\epsilon_w$  is very sensitive to pressure gradients and its value increases in the presence of positive radial and chordwise pressure gradients. As noted earlier both of these pressure gradients are positive for a three bladed inducer and hence confirm the earlier conclusion.

The experimental results of  $\epsilon_w$  for the four bladed flat plate inducer lie in between the numerical results for the three-bladed inducer and the single blade values. The experimental results of  $\epsilon_w$  at the trailing edge for the three-bladed inducer are also shown in Figure 13. They fall in the same range as the numerical solution but the variation with radius is opposite. The numerical results show an increase in  $\epsilon_w$  with the radius, while the experimental results show an opposite trend. This clearly points out to the fact that the flow model (velocity profiles, shear stress etc) need to be improved to get accurate prediction of

$\epsilon_w$  and  $\theta_{11}$ . However, it is quite evident from the study of the behavior of the two boundary layer parameters  $\theta_{11}$  and  $\epsilon_w$  that the presence of imposed pressure gradients substantially change the boundary layer characteristics in a rotating channel.

### 2.5 Asymptotic Solution:

It is anticipated that far downstream in the blade channel, in the interference region (Figure 14), where the two blade boundary layers have merged an asymptotic solution should exist. Since the flow is assumed to be fully developed, all the velocity and shear stress components don't vary with  $\theta$ . Assuming the fluid to be incompressible and perfect gas, the flow as steady and applying boundary layer approximations, the equations of motion become,

$$\theta \text{ direction} \quad W_e \left( \frac{\partial U_e}{\partial r} + \frac{U_e}{r} - 2\Omega \right) + V_e \frac{\partial U_e}{\partial z} = \frac{1}{\rho} \frac{\partial \tau_{\theta z}}{\partial z} - \frac{1}{\rho} \frac{\partial p}{r \partial \theta} \quad (43)$$

$$r \text{ direction} \quad W_e \frac{\partial W_e}{\partial r} + V_e \frac{\partial W_e}{\partial z} - \frac{1}{r} (\Omega r - U_e)^2 = - \frac{1}{\rho} \frac{\partial p}{\partial r} + \frac{1}{\rho} \frac{\partial \tau_{rz}}{\partial z} \quad (44)$$

$$z \text{ direction} \quad W_e \frac{\partial V_e}{\partial r} + V_e \frac{\partial V_e}{\partial z} = 0 \quad (45)$$

$$\text{Continuity} \quad \frac{1}{r} \frac{\partial}{\partial r} (W_e r) + \frac{\partial V_e}{\partial z} = 0 \quad (46)$$

$$\text{Energy} \quad \frac{1}{\gamma-1} \cdot \frac{1}{r} \frac{\partial p}{\partial \theta} \approx \frac{\tau}{(\Omega r - U_e)} \cdot \frac{\partial U_e}{\partial z} \quad (\text{Adiabatic flow}) \quad (47)$$

where  $U_e$ ,  $W_e$  and  $V_e$  are the velocity components in chordwise, radial and blade normal directions respectively,  $\bar{\rho}$  is density,  $\gamma$  is the ratio of specific heats. From the energy equation, it is clear that pressure drop in  $\theta$  direction is due to shear gradients in the boundary layer and since for fully developed flow the latter don't vary with  $\theta$ , the pressure drop is also constant in  $\theta$  direction. From the boundary layer approximation, the pressure variation in  $Z$  direction can be neglected. Assuming  $\tau = \nu_T \partial U_e / \partial Z$ , the energy equation gives  $\partial \tau / \partial z$  also independent of  $z$ . In other words, in the equation 43, the right hand side can be assumed to be a function of radius only. Differentiating equation 43 with respect to  $z$  and using continuity equation, we obtain,

$$W_e \left\{ \frac{\partial^2 (Fr)}{\partial r \partial z} - \frac{1}{r} \frac{\partial (Fr)}{\partial z} \right\} + \frac{\partial W_e}{\partial z} \frac{\partial (Fr)}{\partial r} - \frac{\partial W_e}{\partial r} \frac{\partial (Fr)}{\partial z} = 0 \quad (48)$$

where  $F = \Omega r - U_e$ .

Equations 46 and 48 can be solved by the method of separation of variables by writing,

$$\begin{aligned} W_e &= A_1(r) B_1(z) \\ Fr &= (\Omega r - U_e)r = C_1(r) D_1(z) \\ V_e &= E_1(r) F_1(z) \end{aligned} \quad (49)$$

The resulting equations are:

$$\frac{A_1 \left[ \frac{dC_1}{dr} - \frac{C_1}{r} \right] - \frac{dA_1}{dr} \cdot C_1}{-A_1 \frac{dC_1}{dr}} = \frac{\frac{dB_1}{dz} D_1}{B_1 \frac{dB_1}{dz}} = \text{Constant } C_3 \quad (50)$$

$$\frac{1}{B_1} \frac{dF_1}{dz} = \frac{1}{E_1 r} \cdot \frac{d}{dr} (A_1 r) = \text{Constant } C_4 \quad (51)$$

The solution of these equations are: 23

$$C_1 = C_4 (A_1 r)^{\frac{1}{1+C_3}}$$

$$B_1 = C_6 D_1 C_3$$

$$F_1 = -C_4 C_6 \int D_1 C_3 dz + C_8$$

where  $C_3$ ,  $C_4$ , and  $C_8$  are constants to be evaluated from the following boundary conditions:

$$W_e = 0 \text{ at } R = R_t \text{ \& } R = R_c$$

$$\frac{\partial W_e}{\partial z} = \frac{\partial U_e}{\partial z} = 0 \text{ at } z = S$$

(54)

$$\Omega r - U_e = 0 \text{ at } R = R_c, V_e = 0 \text{ at } Z = S$$

(55)

The boundary conditions require the solution to be periodic. Equation (51) requires

$$A_1 = C_5 \sin \phi / r \text{ and } E_1 = C_7 \cos \phi$$

(56)

where

$$\phi = \frac{\pi(R^2 - R_c^2)}{R_t^2 - R_c^2}$$

The solution of velocity components is

$$W_e = \frac{C_{11}}{r} \cdot \sin \phi D_1$$

(57)

$$U_e = \Omega r - \frac{C_{12}}{r \sqrt{\sin \phi}} D_1$$

(58)

$$V_e = C_{13} \cos \phi$$

$$\int D_1 dz + C_{10}$$



Since  $\partial\tau/\partial z$  varies in the radial direction only,  $\partial^2 U_e / \partial z^2$  varies radially only. This gives  $d^2 D_1 / dz^2 = \text{constant } a_1$  (60)

On integration,  $D_1 = a_1(2S - z)z + a_3$ . The velocity defect is maximum at the center of the channel and is given by

$$U_c(r) = \Omega r - \frac{(S^2 + a_4)}{r} a_5 \sqrt{\sin \phi} \quad (61)$$

This gives

$$U_e = U_c + \frac{(S^2 - (2S - z)z)}{r} a_5 \sqrt{\sin \phi} \quad (62)$$

$$(63)$$

The other velocity components can be written in a convenient form as

$$W_e = \frac{C_{14}}{r} \cdot \sin \phi \{(2S - z)z + a_4\} \quad (64)$$

and 
$$V_e = C_{15} \cos \phi \{a_4(z - S) + S(z^2 - S^2) - \frac{(z^3 - S^3)}{3}\} \quad (65)$$

From equations 58, 64 and 65 it is seen that

$$W_e / \Omega r - U_e = \epsilon_e \sqrt{\sin \phi} \text{ where } \epsilon_e \text{ is a constant} \quad (66)$$

and 
$$V_e / W_e r = (z - S) \{1 + 2/3 (z - S)^2 / (a_4 + (2S - z)z)\} \cot \phi \quad (67)$$

Equations (66) and (67) show that (i) radial inward flow is directly proportional to the velocity defect in the mainstream direction.

(ii) Blade to blade flow velocity  $V_e$  varies directly as the product of radial velocity  $W_e$ , radius  $r$  and distance from the center of the channel ( $z - S$ ). The predicted variation of  $U_e$  and  $W_e$  across the passage is in conformity with experimental observations in a three and four bladed inducer (Reference 22).

## 2.6 Turbulent Field Method

In turbulent field method, the turbulence quantities are suitably modelled using either the turbulence stress equation or the turbulent energy equation. This model equation along with the three momentum equations and continuity equations are solved simultaneously by finite difference technique. This method was proposed by Bradshaw (28) for two dimensional boundary layer. He later extended this to three dimensional (non-rotating) boundary layers (29). Referring to Figure 16, the momentum and continuity equations referred to blade coordinates ( $x, z, r$ ) are,

$$u \frac{\partial u}{\partial x} + v \frac{\partial u}{\partial z} + w \frac{\partial u}{\partial r} + cwu + \frac{1}{\rho} \frac{\partial p^*}{\partial x} - 2\Omega_z w = \frac{1}{\rho} \frac{\partial \tau_x}{\partial z} \quad (68)$$

$$u \frac{\partial w}{\partial x} + v \frac{\partial w}{\partial z} + w \frac{\partial w}{\partial r} - c u^2 + \frac{1}{\rho} \frac{\partial p^*}{\partial r} + 2\Omega_z u \quad (69)$$

$$- 2\Omega_x v = \frac{1}{\rho} \frac{\partial \tau_r}{\partial z}$$

$$v \frac{\partial v}{\partial x} + w \frac{\partial v}{\partial r} + v \frac{\partial v}{\partial z} + \frac{1}{\rho} \frac{\partial p^*}{\partial z} + 2\Omega_x w = \frac{1}{\rho} \frac{\partial \tau_z}{\partial z} \quad (70)$$

$$\frac{\partial u}{\partial x} + \frac{\partial v}{\partial z} + \frac{\partial w}{\partial r} + wc = 0 \quad (71)$$

where  $C$  = curvature of the external streamlines.

$$p^* = \text{reduced pressure} = p - \frac{1}{2}(\underline{\Omega} \times \underline{r}) \cdot (\underline{\Omega} \times \underline{r}).$$

$u, v, w$  = velocity components along the coordinate directions  $x, z$  and  $r$

(Fig. 16).

$$\tau_x = \nu \frac{\partial u}{\partial z} - \overline{u'v'}$$

$$\tau_r = \nu \frac{\partial w}{\partial z} - \overline{w'v'} \quad (72)$$

$$\tau_z = \nu \frac{\partial v}{\partial z} - \overline{v'^2}$$

$\Omega_x, \Omega_z$  = components of  $\underline{\Omega}$  in  $x$  and  $z$  directions respectively.

Equations for the Reynolds stress in the streamwise ( $x$ ) and radial ( $r$ ) directions are (Ref. 27), respectively,

$$\begin{aligned} \frac{D}{Dt} (-\overline{u'v'}) &= \left( \frac{\partial}{\partial t} + w \frac{\partial}{\partial r} + \frac{w}{r} + u \frac{\partial}{\partial x} + v \frac{\partial}{\partial z} \right) (-\overline{u'v'}) \\ &= \overline{v'^2} \frac{\partial u}{\partial z} + \overline{u'v'} \frac{\partial v}{\partial z} - \frac{\overline{p'}}{\rho} \left( \frac{\partial u'}{\partial z} + \frac{\partial v'}{\partial x} \right) \\ &\quad \text{generation of shear stress by mean velocity gradients} \quad \text{pressure strain terms} \\ &+ \frac{\partial}{\partial z} \left( \frac{\overline{p'u'}}{\rho} + \overline{u'v'^2} \right) + c \overline{(w'v' u)} + \frac{\partial u}{\partial r} \overline{wv} \\ &\quad \text{diffusion term} \quad \text{curvature term} \\ &+ 2\Omega_z \overline{w'v'} - \nu (\overline{u'\nabla^2 v'} + \overline{v'\nabla^2 u'}) \\ &\quad \text{rotation term} \quad \text{dissipation term} \end{aligned} \quad (73)$$

$$\begin{aligned}
\frac{D}{Dt} (\overline{-w'v'}) &= \left\{ \frac{\partial}{\partial t} + w \frac{\partial}{\partial r} + \frac{w}{r} + v \frac{\partial}{\partial z} + u \frac{\partial}{\partial x} \right\} (\overline{-w'v'}) \\
&= \overline{v'^2} \frac{\partial w}{\partial z} + \overline{v'w'} \frac{\partial v}{\partial z} - \frac{p'}{\rho} \left( \frac{\partial v'}{\partial r} + \frac{\partial w'}{\partial z} \right) \\
&+ \frac{\partial}{\partial z} \left( \frac{p'w'}{\rho} + \overline{v'^2 w'} \right) - 2 \Omega_z \overline{u'v'} - cw \overline{w'v'} \\
&- 2c (\overline{u'v'} u) - v (\overline{v' \nabla^2 w'} + \overline{w' \nabla^2 v'})
\end{aligned} \tag{74}^*$$

In the transport equations for Reynolds stress (equations 73 and 74), the effects of curvature and rotation are to introduce additional production terms  $(cu + \frac{\partial u}{\partial r} + 2\Omega_z) \overline{w'v'}$  in the mainstream (x) direction and  $(2Cu + 2\Omega_z) \overline{(-u'v')}$  in the radial (r) direction.

In addition curvature terms are introduced in the transport of stresses due to turbulence and viscous diffusion. Since the diffusion terms are of second order and curvature is assumed to be much larger compared to boundary layer thickness, its effect in these terms is neglected. Using Bradshaw's (28, 29) modelling, equations 73, and 74 can be expressed as:

$$\frac{D\tau_x}{Dt} + (2\Omega + cu + \frac{\partial u}{\partial r}) \tau_r = 2a_1 \left\{ \tau_x \frac{\partial u}{\partial z} - \frac{\tau_x}{L_x} \int \frac{\tau}{\rho} - \frac{\partial}{\partial z} (G_x \sqrt{\frac{\tau_{\max}}{\rho}} \tau_x) \right\} \tag{75}$$

and

$$\frac{D\tau_r}{Dt} - (2\Omega + 2Cu) \tau_x = 2a_1 \left\{ \tau_x \frac{\partial w}{\partial z} - \frac{\tau_r}{L_x} \int \frac{\tau}{\rho} - \frac{\partial}{\partial z} (G_x \sqrt{\frac{\tau_{\max}}{\rho}} \tau_r) \right\} \tag{76}$$

where  $\tau_{\max}$  = maximum value of shear stress vector.

\*The term  $cw (-v'w')$  on the right hand side of the equation is negligible compared to  $cu(-u'v')$  and hence is neglected.

$$a_1 = \tau_x / \rho q^2$$

$$q^2 = \overline{u'^2} + \overline{v'^2} + \overline{w'^2} \quad (78)$$

$$L_x = \frac{|\tau_x / \rho|^{3/2}}{\epsilon}$$

where

$\epsilon$  = dissipation of turbulent kinetic energy

(79)

$$G_x = (\overline{p'v'}/\rho + 1/2 \overline{q^2 v'}) / |\tau_{\max}/\rho|^{1/2} \tau_x / \rho$$

where  $a_1$ ,  $L_x$ ,  $G_x$ , are Bradshaw's boundary layer parameters modified to include the effects of curvature and rotation.

Equations 68, 69, 71, 75 and 76 constitute a set of five differential equations for five unknowns,  $u$ ,  $v$ ,  $w$ ,  $\tau_x$ ,  $\tau_r$ . These equations have to be solved simultaneously with proper boundary conditions. Bradshaw's numerical analysis of three-dimensional boundary layers is based on a functional relationship for  $a_1$ ,  $L$ ,  $G$  based on two-dimensional boundary layer measurements. A preliminary attempt to modify these functions to allow for rotation and curvature is described below.

A stress Richardson number, ( $R_{ix}$ ) to account for the effects of curvature and rotation, is defined as the ratio of production of a Reynolds stress due to curvature and rotation to the production due to mean shear. Richardson number in  $x$  direction is therefore

$$R_{ix} = - \frac{(2\Omega_z + cu + \frac{\partial u}{\partial r}) \overline{w'v'}}{\frac{\partial u}{\partial z} \overline{v'^2}} \quad (80)$$

and in  $r$  direction is

$$R_{i_r} = \frac{(2\Omega_z + 2cu)}{\frac{\partial w}{\partial z}} \cdot \frac{\overline{u'v'}}{\overline{v'^2}} \quad (81)$$

In most of the turbulent boundary layer flows, the production of a turbulence quantity is balanced by the dissipation and the convective and diffusion terms are in order of magnitude smaller.

$$\text{Production} \approx \text{Dissipation} \quad (82)$$

For stationary boundary layers on flat surfaces we have

$$\text{Production due to Shear} = \text{Dissipation}$$

$$\therefore \frac{\tau_{x_0}}{\rho} \frac{\partial u}{\partial z} \Big|_0 = \dot{\epsilon} = \frac{(\tau_{x_0}/\rho)^{3/2}}{L_{x_0}} = \frac{(\tau_{x_0}/\rho)^{3/2}}{l_{x_0}} \quad (83)$$

where  $l_{x_0}$  is the mixing length at no rotation and is defined as

$$l_{x_0} = \frac{(\tau_{x_0}/\rho)^{1/2}}{\frac{\partial u}{\partial z} \Big|_0} \quad (84)$$

For boundary layers with rotation, the production term in the shear stress equations are modified by  $(1 - R_{ix})$  and  $(1 - R_{ir})$  respectively.

$$\therefore \frac{a_x}{a_{x_0}} \tau_x / \tau_{x_0} \approx 1 - R_{ix} \quad (85)$$

and

$$\tau_r / \tau_{r_0} \approx 1 - R_{ir}$$

Also the turbulent energy equation gives

$$\text{Production} = \frac{\tau_x}{\rho} \frac{\partial u}{\partial z} = \frac{(\tau_x/\rho)^{3/2}}{L_x} = \frac{(\tau_x/\rho)^{3/2}}{l_x} \approx \text{Dissipation} \quad (86)$$

$$\therefore \frac{l_x}{L_x} = \frac{l_{x_0}}{L_{x_0}} \quad (87)$$

Since dissipation is the same we have  $\frac{\tau_x^{3/2}}{L_x} \approx \frac{\tau_{x_0}^{3/2}}{L_{x_0}}$  (88)

Using equation (85), equation (88) can be expressed as

$$\frac{L_x}{L_{x_0}} = (1 - Ri_x)^{3/2} \quad (89)$$

Equations (85) and (89) can be used to modify  $a_1$ ,  $L_x$  and  $G_x$  as follows:

$$\begin{aligned} a_1 &= a_{10} (1 - Ri_x) \\ L_x &= L_{x_0} (1 - Ri_x)^{3/2} \\ G_x &= G_{x_0} / (1 - Ri_x) \end{aligned} \quad (90)$$

The Richardson number  $R_{ix}$  appears in equation (90) as the modification parameter. It can be related to a Rotation parameter  $R_o = \epsilon_w \delta / r$  where  $\epsilon_w$  is the limiting streamline angle at the wall and  $\delta$  is the boundary layer thickness as follows:

$$R_{ix} = - \left( \frac{2\Omega_z + cu + \frac{\partial u}{\partial r}}{\frac{\partial u}{\partial z}} \right) \frac{\overline{w'v'}}{\overline{v'^2}}$$

In rotating passages of axial flow turbomachines,  $\frac{\partial u}{\partial r} \sim \frac{u}{r}$ ,  $c \sim \frac{1}{r}$ ,

$\frac{\partial u}{\partial z} \sim \frac{u}{\delta}$ .  $\overline{w'v'}$  varies directly as the radial component of wall shear stress, and hence,

$$\frac{\overline{w'v'}}{v'^2} \sim -\frac{\epsilon_w}{v'^2} = -k \epsilon_w$$

$$\therefore R_{ix} \sim \left[ 2(\Omega_x r + u) \delta / ru \right] k \epsilon_w \approx 4k \epsilon_w \delta / r = \beta R_o \quad (91)$$

So  $a_1$ ,  $L_x$  and  $G_x$  can be approximated as

$$\begin{aligned} a_1 &= a_{10} (1 - \beta R_o) \\ L_x &= L_{x_o} (1 - \beta R_o)^{3/2} \\ G_x &= G_{x_o} (1 - \beta R_o)^{-3/2} \end{aligned} \quad (92)$$

This completes the theoretical formulation. An attempt will be made in the future to solve these equations by finite difference technique. This method predicts not only the velocity profiles, but also the shear stress distribution inside the boundary layer.



### 3. EXPERIMENTAL PROGRAM

#### 3.1 Facility Description:

The blade was made of the transparent plexiglass of constant thickness of 0.5 inch. Both the leading and trailing edges of the blade were shaped to form a symmetric airfoil shape to assure the smooth flow at both edges. The plexiglass plate was heated in the oil tub, then put on the mold and was cooled to give an axial advance of 10 inches. The blade has a circumferential extent of 300 degrees. The details of the blade are shown in Figure 3.

The reason for the use of the transparent plexiglass for the material is twofold. Since very little is known on the helical channel flow, application of various forms of flow visualization technique was considered. The use of the transparent material as the blade would make application of the particle tracing method possible. The other factor concerns with the roughness factor the blade surface. The blade surface would be considered hydraulically smooth when the surface roughness has less than a certain value. The often used criterion for the hydraulically smooth surface is given by  $U_T k/\nu < 2.5$ , where  $k$  is a height of the surface roughness. This condition gives the roughness to be less than 0.02 in. which would be rather difficult to achieve when the blade was made of, e.g., fiberglass.

Hub is essentially a circular cylinder, made of aluminum, of 18 in. in diameter and 23 in. in length, and 1/4 in. in thickness. Nose cone has a spherical shape of 18 in. in diameter, and was made of aluminum of 1.4 in. in thickness. First, the mold was constructed and molten aluminum was poured. This was later machined to give a smooth surface.

The rotor assembly was constructed by installing the four blades on the hub with an equal angular interval of 90 degrees. Each blade was fastened on the hub at eight positions by a screw of  $3/16$  in. in diameter. A  $1/4$  in. hole was drilled in the blade, and the screw was inserted from the hub. A circular hole of  $3/4$  in. in diameter was drilled on the blade surface at the end of the hole. This hole was filled by an aluminum disk of  $3/4$  in. in diameter and  $1/2$  in. in thickness, which was threaded. End of the screw inserted to the blade from the hub was in this aluminum disk, thus giving a firm support to the blade.

Detailed drawing of the rotor assembly is given in Figure 4. In this Figure, the probe traversing unit is also shown. This is used for the measurement of the velocity distribution across the channel by traversing the probe while the rotor assembly is in motion. Seen in this drawing are, the probe holder which is seated inside the hub, location of the slots where the probe is traversed, the step motor which traverses the probe while the rotor assembly is in motion, and the slip ring unit which allow for the step motor to be controlled from the stationary system.

### 3.2 Experimental Method and Instrumentation:

#### 3.2.1 Three Channel Pressure Transfer Device:

In the past, pressure transfer device was installed inside the rotor assembly. Pressure measured in the rotating system was led to the pressure transfer device from one end and then to manometer through a stationary conduit which came from the other end of the pressure transfer device. The conduit was fastened to a stationary system to

keep it from rotating. This arrangement, however, had inherent disadvantages. Due to vibration of the rotor assembly, excessive wear

experienced by the device led to occasional damage to the unit. Since it was installed inside the rotor assembly, inspection of the device meant removal of the unit from the rotor assembly, which was a time consuming process.

In view of these difficulties, a new pressure transfer device was constructed. Details of the newly constructed pressure transfer device are shown in Figure 4. The device has three channels, and each channel was made airtight by using the double sealed ball bearings. Pressure leakage along the cylinders was prevented by the use of the O-ring and the plastic sealers. The three channel pressure transfer device was installed on a stand outside the rotor assembly. Pressure from the rotating system was transferred to the pressure transfer device through a shaft which was fastened to the nose cone, and its value was evaluated by the manometer reading. In order to reduce the possible interference from the incoming flow, the pressure transfer device was housed inside the streamlined cowling.

In order to eliminate possible transmission of the rotor assembly vibration to the pressure transfer device, a coupling unit was constructed (Fig. 4). The shaft attached to the nose cone was connected to the shaft of the pressure transfer device through a coupling which consisted of the conduit of 1.625 inches in length and two disks of synthetic rubber of .25 in. in thickness. Test showed that the vibration of the rotor assembly was not transferred to the pressure transfer by the use of this coupling unit.

### 3.2.2 Ammonia Transfer Device:

Direction of the flow near the blade surface was determined by means of the ammonia streak method, i.e., by releasing a small amount of ammonia gas through the holes drilled on the blade surfaces. Ammonia transfer device is a means to transfer the ammonia gas from the stationary system to the rotating system. Details of this are given in Reference 5. The ammonia transfer device was mounted on the stand outside the rotor assembly. Details of the limiting streamline angle measurement are given in Section 3.6

### 3.2.3 RPM Counter:

The RPM counter consists of 4.5 in. diameter metallic disk fixed at the end of the rotating shaft. The disk has 60 notches at equal intervals on the circumference to allow light to pass from one side of the disk to a photocell on the other side. The photocell is connected to a digital counter which counts the pulses and thus the rpm to an accuracy of 1/10 rpm.

Figure 17 shows a schematic diagram of the instrumentation used for the measurement of the velocities inside the rotor passage. Details of the hardware and technique are described in Section 3.7.

All the measurements, with the exception of those described in Section 3.3, are carried out without the throttle at the exit.

### 3.3 Effect of Throttle:

In order to investigate the overall performance of the four bladed flat plate inducer at various flow coefficients, a throttle was installed

at the exit. The throttle clearance was varied and the annulus wall static pressure, stagnation pressure distribution at the exit were measured.

Figure 18 shows the static pressure distribution measured on the annulus wall with various throttle clearances. Numbers in the figure represent the throttle clearances in inches. The location of the leading edge of the blade is taken as the origin of the abscissa. It is seen that the annulus wall static pressure increases as the throttle clearance decreases. The negative pressure at the leading edge of the blade is considered to be caused by the blade blockage effect. Increase of the blade static pressure at the trailing edge is considered to be caused by the effect opposite to the blade blockage, i.e., by the increase of flow area due to the absence of the blade thickness. It is seen that the static pressure is constant downstream of the rotor assembly. It is interesting to note that the pressure gradient on the annulus wall decreases as the throttle clearance decreases.

The radial variation of stagnation pressure and angle distribution were measured 14 inches downstream of the trailing edge. The stagnation pressure rise coefficients at various throttle positions are plotted in Figure 19. Even at large throttle openings, appreciable pressure rise can be seen especially at the tip. This is caused by considerable boundary layer growth on the blades, and the shear pumping effect. The outlet angles, measured with respect to tangential direction, were derived using a cobra probe. The flow reversal, near the hub, occurs at flow coefficient of 0.0592 or less (Figure 20). The performance of the flat plate inducer, plotted in the form of  $\bar{\psi} - \bar{\phi}$  curve is shown in Figure 21.

### 3.4 Blade Static Pressures:

The flow in a channel differs from those around a single blade two aspects: (a) The pressure gradient that exists in a channel change the boundary layer behavior, local shear stress, limiting streamline angle etc. (b) The interaction between the boundary layers on the two adjoining surfaces gives rise to complicated profiles arising out of mixing. In view of this it is important to have a knowledge of the static pressure measurements on the blade.

The blade static pressure measurements were carried, with no throttle, at 11 radii and at five tangential locations,  $\theta = 30^\circ, 75^\circ, 150^\circ, 225^\circ$  and  $270^\circ$  on both leading and trailing surfaces of the blade. The results are plotted in Figures 22 and 23.

In Figure 22, radial variations of the blade static pressure coefficient at various tangential locations are shown. It is seen that  $\psi_s$  takes nearly a constant value except in the region near the tip where it changes considerably, especially near the trailing edge.

In Figure 23, chordwise variation of the blade static pressure coefficient at various radial positions are shown. It is interesting to note that the static pressure distributions on the leading surface behaves quite differently compared to that on the trailing surface. While  $\psi_s$  takes the minimum values at the midchord location on the trailing surface, it takes the maximum values on the leading surface.

The existence of finite loading on the blades can be explained on the basis that the boundary layer on the leading and trailing surfaces grow differentially giving rise to asymmetrical flow around the blade chord.

### 3.5 Limiting Streamline Angle Measurement:

The limiting streamline angles on a rotating body can be determined from the ammonia streak method described in Reference 5. Small amount of ammonia gas is released through the blade static pressure taps, while the rotor is in motion, and the trace of the gas is recorded on an ozalid paper. It is important to realize that, in order for the above procedure to be valid, the ammonia gas must remain in the collateral region, which means that the ammonia gas coming from the orifice on the blade surface must have a very low velocity. Typical traces of limiting streamlines derived by this method are given in Reference 5.

Measurements of the limiting streamline angle were carried out at the predetermined tangential locations which coincided with the locations of the blade static pressure taps. At each tangential location, more than two measurements are made. Variation between the two measurements is found to be very small.

In Figure 24 radial variations of the limiting streamline angle are shown for various tangential locations. It is seen from these figures that, except near the trailing edge, the limiting streamline angle on the leading blade surface behaves quite differently from that on the trailing blade surface. It is interesting to note that at  $\theta = 30$  degrees, the limiting streamline angles on the leading surface is nearly twice the value on the trailing surface. As  $\theta$  increases, this trend reverses itself, and at  $\theta = 150$  degrees, the limiting streamline on the leading surface becomes smaller than that on the trailing surface. Unlike the case for the rotating helical blade, the large values for the limiting streamline angles do not mean that the flow is laminar. The flow is found to be turbulent throughout the channel.

In Figure 25, tangential variations of the limiting streamline angle are shown for various radial locations. At  $r = 18$  in., the limiting streamline angle increases as  $\theta$  increases on the leading surface while it takes a nearly constant value on the trailing surface. For the radial distance less than 16 inches, the behavior of the limiting streamline angle is different from that of  $r = 18$ ". As  $\theta$  increases, it increases to reach a maximum value on the trailing surface while it decreases to reach a minimum value and then increases on the leading surface. This behavior is quite different from the behavior of the limiting streamline angle for the rotating helical blade which showed that the limiting streamline angle increased monotonically with increase in  $\theta$ .

It must be pointed out here that for the rotating helical blade (Reference 5) the tangential pressure gradient was considered to be zero, and the experimental investigation showed this to be the case. For the present investigation, experiment has shown that there exist the pressure gradients, as reported in Section 3.4. It is interesting to note that the behavior of the limiting streamline angle is similar to the behavior of the blade static pressure. This can be seen when Figures 25a-c are compared with Figure 23. This may be interpreted as the indication that the limiting streamline angle is closely related to the blade static pressure distribution. Thus, in order to evaluate the limiting streamline angle it is necessary that the pressure gradients be known. Dependency of the limiting streamline angle on the radial pressure gradient was reported in reference 9. Tangential variation of the limiting streamline angle can be predicted when the tangential pressure gradient is given.



### 3.6 Determination of the Wall Shear Stress:

One of the most important problems in the boundary layer flow investigation is the determination of the wall shear stress. In two-dimensional boundary layer flows, the wall shear stress has been determined by various direct and indirect methods. The frequently used direct methods include the Preston tube method, the heated element method (HEM) and the floating element method (FEM).

Because of the presence of the centrifugal force, vibration and rotation use of FEM and HEM methods are severely limited in its application for wall shear stress measurements on a rotating blade.

In this paper, the wall shear stress was evaluated by means of the Preston tube method. Validity of its use for three-dimensional boundary layer flows is discussed below.

#### 3.6.1 Law of the Wall:

For two-dimensional turbulent boundary layer flows, it has been well established that, near the wall there exists a region where the velocity is represented as a universal function of  $z^+$  by

$$\frac{U}{U_\tau} = f(z^+), \quad \text{where } z^+ = \frac{U_\tau z}{\nu} \quad (93)$$

The function  $f$  is represented by

$$f(z^+) = A \ln z^+ + B \quad (94)$$

where  $A$  and  $B$  are constants. This is known as the law of the wall.

When a total pitot tube (whose diameter is smaller than the extent of validity of the law of the wall) is used, the wall shear stress can

be related to the dynamic pressure  $\Delta P$  recorded by the pitot tube through the following relationship.

$$\frac{\tau_0 d^2}{\rho v^2} = F \left( \frac{\Delta P d^2}{\rho v^2} \right) \quad (95)$$

where  $d$  is the diameter of the Preston tube.

This shows that the wall shear stress can be determined by the local dynamic pressure, once the function  $F$  is known. Determination of the wall shear stress has been carried out by many (3,9,12). Experimental verification of the validity of this approach to three-dimensional turbulent boundary layer flows was carried out by Pierce and Krommenhoek (14). Results obtained by the Preston tube method were compared with those obtained by the floating element method which gave the direct measurement of the shear force, and good agreement was reported. This result is of considerable significance since this clearly shows that the two-dimensional similarity law was valid in the collateral region of the three-dimensional boundary layer flow. Since the thickness of the collateral region is about a few percent of the boundary layer thickness, the use of the Preston tube method is not considered appropriate when the boundary layer thickness is very small.

Work done by Pierce and Krommenhoek clearly shows that the law of the wall does exist for three-dimensional boundary layer flow. For the derivation of the collateral relation for the rotating type boundary layer flow, it is considered that the law of the wall is valid. The investigations reported in Ref. 9 confirm this.

### 3.6.2 Applicability to Three-Dimensional Flows:

It has been pointed out that, in order for the Preston tube method to be adequately applied to three-dimensional boundary layer flows, the diameter of the tube must be smaller than, or approximately the same as the thickness of the collateral region. In this case, the flow is regarded essentially as two-dimensional one and the law of the wall for the two-dimensional flow will be directly applied. Thus, in order to discuss the applicability of the Preston tube method to three-dimensional boundary layer flows, it is necessary to determine approximate thickness of the collateral region.

The extent of the collateral region, however, is not determined clearly. In the present paper, the collateral region was defined as a region where inertia terms are negligible and the viscous forces are balanced by the Coriolis forces. In this respect, the collateral region may be considered to correspond to the laminar sublayer of the two-dimensional boundary layer flows. Therefore, the extent of the collateral region may be roughly considered about a few percent of the total boundary layer thickness. This severely limits the application of the Preston tube method to many actual cases.

In the present investigation, it is found out that the directions of the maximum total pressure obtained by the Preston tube did not agree with the limiting streamline angles obtained by the ammonia streak method. It is noticed that the difference in angles increase with the increase in limiting streamline angle, i.e., the difference in angles determined by two methods is large when the skewness of the flow is large. This trend is observed in the entire experiment. Even

though the extent of the collateral region cannot be determined definitely, the existing difference in angles determined by two methods clearly indicates that the diameter of the tube is larger than the extent of the collateral region.

It is known that the pitot tube is insensitive to the direction of the flow up to a certain degree of angle. This means that the full amount (within  $\pm 1$  percent) of the total pressure is recorded by the pitot tube when it is placed in the flow in such a way that its direction deviates from the flow direction by a certain degree of angle. This angular deviation,  $\gamma$  degrees, is a characteristic of the individual pitot tube and is known as the sensitivity of the probe.

In the collateral region, the direction of the flow is given by the limiting streamline angle  $\alpha = \arctan \epsilon_0$ . As the distance from the surface increases, the flow angle, measured from the tangential direction, decreases.  $\alpha_0$  is defined as a flow angle at the distance  $d$  (diameter of the tube) away from the surface. The direction of the flow changes from  $\alpha$  degrees to  $\alpha_0$  degrees within the distance  $d$ . When the pitot tube is placed in the direction  $\alpha_0 + \gamma$  degrees, it reads the full values of the total pressure for the flow whose direction lies between  $\alpha_0$  to  $\alpha_0 + 2\gamma$  degrees. This means that, for the flow whose direction lies between  $\alpha_0$  and  $\alpha_0 + 2\gamma$ , as far as the total pressure is concerned, is identical to the flow without skewness, i.e., two-dimensional flow. Though the value of  $\gamma$  was not evaluated precisely, it is considered to be large enough to regard the two-dimensional calibration scheme to be an accurate one. This is the basis for the use of the two-dimensional calibration scheme for the wall shear stress evaluation of three-dimensional boundary layer flows.

### 3.6.3 Experimental Procedure:

For the evaluation of the local total pressure, two different sizes of the pitot tubes were used. One was a tube of .028 in. outside diameter with 0.6 diameter ratio, and the other .065 in. in outside diameter with 0.7 diameter ratio. Both are approximately 1.5 in. in length.

Measurements of the total pressure were carried out at five tangential locations,  $\theta = 30, 75, 150, 225,$  and  $270$  degrees on both leading and trailing surfaces of the blade. At each tangential location measurements were carried out at four radial positions,  $r = 11, 13, 15$  and  $17$  inches. The tip of the pitot tube was placed approximately  $1/8$  in. upstream of the blade static pressure hole. The tube was rigidly attached to the blade surface by a cellophane tape. The other end of the tube was connected to the plastic tube. This was also attached to the blade surface by the cellophane tape. The plastic tube was connected to the pressure transfer device through the hole on the hub. The total pressure was evaluated by the manometer. At each position, starting from the tangential direction, several straightlines were drawn, with a five degree interval, on the blade surface through the point where the tip of the tube was placed. The tube was placed on the surface along these straightlines, and the total pressure measured. When the total pressure thus obtained was plotted against the angle measured from the tangential direction it is seen that the total pressure takes a maximum value. This maximum value was taken as the total pressure at this position.

In Figure 26, the total pressures recorded by the manometer are plotted against the angle measured from the tangential direction. Since no centrifugal force correction was applied, the maximum total pressure is represented by the minimum value in these figures. The values of the limiting streamline angle obtained by the ammonia streak method are shown by the vertical dotted lines in these figures. It is seen that the difference between the limiting streamline angle and the angle that gives the maximum total pressure increases as the limiting streamline angle increases. It is also seen that the difference in angles decreases near the blade tip. This is considered to be the result of the increase in the boundary layer thickness.

Using the blade static pressure obtained previously, the local dynamic pressure was obtained. Following the calibration procedure given by Patel (12), the local dynamic pressure was related to the wall shear stress.

All measurements were carried out using both tubes, and the results were compared. They are shown in Figure 27. It is seen that the two probes give almost identical values. With an intention to investigate the possible effects of the size of the tube, a pitot tube of .125 in. outside diameter with 0.6 diameter ratio and 1.5 in. long was used at some selected locations for the evaluation of the wall shear stress. The results agreed very well with those obtained by two other tubes. It is concluded that the size of the tube used in the experiment has little effect on the determination of the wall shear stress. This conclusion is identical to the conclusion obtained for the two-dimensional turbulent boundary layer flows..

In Figure 27, local skin friction coefficients are plotted as a function of the Reynolds number based on the distance measured from the leading edge of the blade. The skin friction coefficient is defined by

$$C_f = \frac{\tau_o}{\frac{1}{2}\rho U^2}$$

where U represents the local potential velocity outside the boundary layer and is assumed to be equal to  $\Omega r$ . Since the velocity outside the boundary layer is not known, and since there exists the pressure gradient, it is not appropriate to compare the above results with the known expression given for the flat plate.

Detailed discussion of skin friction measurements and correlations will be dealt with in a later section.

### 3.7 Velocity Profiles Inside the Blade Passage:

#### 3.7.1 Method of Measurement:

The mean flow velocity profiles inside the rotor blade passage are obtained by measuring total pressure and radial flow angle with a three hole disk probe. Measuring grid is 5 x 5 x 40 in tangential, radial, and blade to blade directions respectively. Figures 4 and 17 show the schematic diagram of the experimental setup. The radial and axial positions of the probe are adjusted manually while the blade to blade traversing (tangential direction) is done by a traverse unit installed inside the rotating hub. The traverse indexing unit is stationary and keeps the traverse wheel and the step-motor of the traverse unit locked except when indexed. The flow is traversed at five axial stations (Fig. 29) and five radial stations and 40 stations across the channel in the tangential direction.

The disk type of probe has a number of advantages over a conventional yaw probe for measurements close to blade walls. It can be easily aligned parallel to a blade surface, produces less flow distortion and has a wide linear flow angle measuring range ( $\pm 20^\circ$ ) as shown in the calibration curve Fig. 28.

The mainstream velocity component  $u$  (parallel to blade surface) is obtained from measurements of the total pressure, flow angle and the static pressure interpolated linearly from blade static pressure measurements as follows:

$$\frac{U}{U_t} = \sqrt{\frac{(P_o - P_s)}{\frac{1}{2} \rho U_t^2}} \cdot \cos \alpha \quad (96)$$



The radial component of velocity is given by

$$\frac{w}{U_t} = \sqrt{\frac{(P_o - P_s)}{\frac{1}{2} \rho U_t^2}} \cdot \sin \alpha \quad (97)$$

Displacement and momentum thicknesses are obtained by integrating the velocity component across the boundary layer using equations (29). Shape factor  $H$  is then calculated as the ratio of displacement to momentum thickness.

### 3.7.2 Mainstream Velocity Profile:

Figs. 30a to 30e show the mainstream velocity component across the passage at various radial and circumferential locations. From the profile distribution at the 1st slot (Figures 29 and 30a) i.e.  $\theta = 30^\circ$ , it is evident that the flow has already become turbulent over most of the radial locations. The boundary layer is thicker on the suction side (as much as 1.0 in. near tip). This may be due to inlet flow incidence because the inducer channel is being operated at open throttle.

The boundary layer is thin and laminar near hub on the pressure side. (At hub, the Reynolds number based on peripheral velocity  $\Omega Y$  and distance from leading edge is  $\sim 0.8 \times 10^5$ ).

The profile distribution at subsequent downstream measuring stations, (Fig. 30 b-e) shows that the boundary layer is turbulent at all the radial locations on both the surfaces and grows rapidly downstream. At measuring stations 4 and 5, (i.e.  $\theta \geq 210^\circ$ ) the two blade boundary layers have merged into each other near the tip. The mutual interference effect appear in

form of decrease in mainstream velocity component in the middle of the passage and the radial inward flow. The inviscid flow region disappears with the result that no definite boundary layer characteristics can be obtained in terms of the various types of boundary layer thickness parameters; ( $\delta$ ,  $\delta^*$ ,  $\theta_{11}$ ,  $H$  etc. ). It is obvious that in this region momentum integral technique can only give a qualitative picture of the flow. A modified viscous solution based on Cooper's finite difference scheme or Bradshaw's Method, modified and outlined in Sec. 2.6, is essential to predict this flow behavior.

#### Comparison with Power Law Profile:

In Figs. 31a-c the mainstream velocity component ( $u$ ) normalized by the free stream velocity  $u_e$  is plotted against the distance from the blade wall normalized by the local boundary layer thickness ( $\delta$ ). Comparing this with the Power Law profile of appropriate index ( $\frac{u}{u_e} = (\frac{z}{\delta})^{1/n}$ ) it appears that the experimental data fits this representation reasonably well. The agreement is poor near the tip because the boundary layer near the tip is affected by the tip clearance and the annulus wall effects. The value of exponent varies from 1/6 to 1/11, except near hub at  $\theta = 90^\circ$ , where the values are 1/4 and 1/5. Here the boundary layer appears to be in transition (Reynolds Number based on peripheral velocity and distance from leading edge  $3 \times 10^5$ ). The value of exponent is different on suction side (from 1/8 to 1/11) than on the pressure side (from 1/6 to 1/8). From the plot of shape factor based on the exponent, it is seen that the shape factor increases slightly with  $\theta$  except near hub. The radial variation in the profile shape is large indicating that the radial pressure gradients are stronger than chordwise pressure gradients. This is true because the measurements were taken at open throttle, yielding mild chordwise pressure gradient.

Comparison with Cole's Profile: In Figs. 32a-c, the mainstream velocity component  $u$  is plotted in the form of Cole's Law,

$$\frac{u}{u_\tau} = \frac{1}{k} \left( \log \left( \frac{z u_\tau}{\delta} \right) + \pi W(z/\delta) \right) + C \left( \frac{z u_\tau}{\delta} \right) \quad (98)$$

where  $u_\tau$  is friction velocity defined as  $u_\tau = \sqrt{\tau_o/\rho}$ ,  $\tau_o$  is the local wall shear stress,  $W$  is a wake function and  $\pi$  is a parameter which takes into account the effect of imposed pressure gradients.

It is seen from the plots that there exist the law of the wall region  $\left( \frac{u}{u_\tau} = \frac{1}{k} \log \frac{z u_\tau}{\delta} + C \right)$  up to  $z^+ \leq 200-300$ , depending upon the nature of the blade surface (suction or pressure) and the location of the measuring station. The mean value of constants in the law of wall vary in the range of 5.60 - 5.80 for the slope constant  $(1/k)$  and 4.5 to 5.5 for the constant  $C$ . The wake component  $W(z/\delta)$  of the Cole's Law appears to have different form than the sinusoidal form for stationary two dimensional flows and may be due to the fact that entrainment process which is dominant in the outer part of the boundary layer is different for the boundary layer on an enclosed rotating surface than for a stationary two dimensional surface. Value of  $\pi$  which is characteristic of the imposed pressure gradients is found to vary from -0.6 to 1.35. It is large and positive on the suction side and has a small negative value on the pressure side of the blade. It decreases with  $\theta$  up to  $\theta \leq 150^\circ$  and later increases slowly. This is in accordance with the trend of the observed blade static pressure distribution, as shown in Figure 22. The value of  $\pi$  increases with radius continuously in accordance with the radial pressure gradients.

The experimental results, therefore, indicate that for the turbulent boundary layers in the rotating channel, the law of the wall fits the data well in the region close to the wall (i.e. inner layer  $30 \leq y^+ \leq 300$ ) and the power law fits the data well in the outerlayer.

#### Distribution of Passage Averaged Mainstream Velocity:

In Fig. 33 is shown the radial variation of mainstream velocity component averaged across the channel. The passage averaged value of  $\bar{u}$  is found to be lower than the free stream velocity that exists in an inviscid flow ( $u = \Omega r$ ). The difference increases as the flow proceeds further downstream of the channel, especially after 3rd station i.e.  $\theta > 150^\circ$ . The largest difference is near the tip where the two surface boundary layers have interacted and for  $\theta > 150^\circ$  it extends up to midradius ( $R \sim 0.8$ ).

This large reduction in mainstream velocity near the tip is probably due to the mutual interference of the boundary layers on the two surfaces of the annulus wall boundary layer, which are now completely submerged into each other and also due to the observed radial inward flow in this region. This is in confirmity with the increase in radial pressure gradients observed near the tip region. As explained earlier, the value of shear stress is not negligible near the center of the passage and the turbulence level in this region is maintained at the expense of mainstream velocity gradient in the normal direction. This results in smaller mean mainstream velocities. Also from the local continuity considerations (over a cross-section) since the radial velocity component is increasing downstream of the passage, both in magnitude and extent, the mainstream velocity is bound to decrease as the flow proceeds downstream of the blade passage, till it leaves the rotor.

### 3.7.3 Radial Velocity Profile:

Figures 34a-e show the observed radial velocity distribution across the blade passage. The radial velocity increases on approach to the wall, indicating the extent of boundary layer on the blade surface. The radial velocity should decrease very close to the wall, but since the measurements could not be taken for values of  $y^+ < 100$  (due to finite size of the probe and this traversing unit), only the outer-region of the boundary layer flow has been scanned and the measurements are consistent with the expected behavior.

Near the center line of the channel, the radial velocities are small of the order of (ft/sec). However, qualitatively, it can be said that the radial velocity in this region is higher near the tip region where stronger radial pressure gradients exist. It is seen that for  $\theta = 30^\circ$  and  $90^\circ$ , the radial velocity is positive and implies more negative radial pressure gradient than predicted by simplified radial equilibrium theory. (Fig. 35)

The suction and pressure surface boundary layers near the tip have merged resulting in interaction with each other as well as the boundary layer on the annulus wall. The observed radial pressure gradient is more than that predicted by the simplified radial equilibrium theory

( i.e.  $\frac{\partial \psi_s}{\partial R} \geq \frac{2}{R} \left( R - \frac{\bar{U}}{u_t} \right)^2$  ) and this implies the presence of radial inward flow near the mid passage. This is evident from the velocity profiles shown for  $\theta > 90^\circ$  (Figures 34a-d). The inward flow increases both in magnitude and extent as the blade trailing edge is approached.

### Comparison with Mager's Profile:

The observed radial velocity component is plotted in Fig. 36a-c. as streamline angle (local radial to mainstream velocity ratio ) versus distance from the wall, normalized by the boundary layer thickness ( $\delta$ ).

A comparison with theoretical Mager's Model based on the limiting stream line angle (obtained from momentum integral solution (Section 2.4) and Mager's Profile (equation 31) indicates that the experimental data fits this form quite well except near the hub or tip. The agreement would have been better if the observed limiting streamline angle data were used in Mager's profile. However, in the tip region where radial inward flows are present, Mager's representation fails because of the reversal of radial velocity (S type of profile) inside the boundary layer. In fact any form of similarity in velocity profile in this region is expected to fail, because of the interaction of annulus wall boundary layer and boundary layers from the adjacent blade surfaces.

### Hodograph Representation:

The radial velocity inside the boundary layer is plotted in a hodographic form (local radial velocity ( $W$ ) against local mainstream component ( $u$ ) both of which are normalized by the local free stream velocity at the edge of boundary layer) in Figures 37a-g. The measurements at  $R = 0.56$ ,  $0.71$ ,  $0.866$  are shown in Figures 37a-d and for the tip radii ( $R = 0.93$ ,  $0.986$ ) in Figure 37e-g. It is interesting to note that in the region where the two boundary layers have not merged ( $R = 0.5$  to  $0.866$ ) the measurements in the outer region fall in a narrow band, thus indicating the existence of similarity in velocity profiles. The discrepancies, especially in Figure 3b, can be attributed partly to the experimental inaccuracy. The boundary

layers are very thin which thus introduces appreciable error in the measurement taken from a probe whose thickness is about 1/5 of the boundary layer thickness. Even near the trailing edge (Station #5) on the trailing side the boundary layer near the hub is thin.

The polar plot near the tip (37e-g) shows no similarity in velocity profiles. The interaction between blade and annulus wall boundary layers in this region makes the profile characteristics unique.

Plotted in Figs. 38a and 38b are the hodograph plots of velocities on leading and trailing surfaces respectively. The data appears to fall in a very narrow band for the leading surface (except the data very near the hub or tip). and fits the parabolic curve given by,

$$\frac{W}{U} = 0.3 \sqrt{\frac{U}{U_e} \left(1 - \frac{U}{U_e}\right)}$$

This equation has been derived in Ref. 9 for a single rotating blade on the basis of negligible pressure gradients and shear stresses in the outerpart of the boundary layer. This shows that the pressure gradients on the leading surface in the mainstream direction are very small except near the hub and tip. The data for the trailing surface shown is in Figure 38b has more scatter.

Polar plot of the velocity profiles near the tip surfaces are shown in Figure 39. The radial inward velocities are comparatively small at  $\theta = 210^\circ$ . The polar plot of the outer layer seem to fall on vertical line. Since the radial velocities in this region are small, no definite conclusion can be drawn with regard to the shape or trend, since the experimental inaccuracy may be large. However, at  $\theta = 270^\circ$  the radial

inward velocities seem to decrease the mainstream velocity. The radial inward velocity subsist only in the outer layer adjacent to the midpassage. This phenomena in the interaction zone is different and intrinsically more complex than those occurring near the blade surfaces. In view of the limited data in the inward velocity region, no definite conclusion can be drawn. Predictions based on asymptotic analysis do fit the data well at  $\theta = 270^\circ$ .

In Fig. 40 a,b,c are shown a similar polar plot, the abscissa being the velocity defect in the mainstream.

#### Passage Averaged Radial Velocity:

In Fig. 41 is shown the radial distribution of root square mean radial velocity, averaged across the channel width. The plot shows that the radial velocity increases downstream of the passage, the increase is very large near the hub region. Near the tip region, the value is nearly the same at all tangential locations. Higher radial velocities in the boundary layer imply higher values of the limiting streamline angle and from the above trend we find that this angle should increase as the flow proceeds downstream and decrease with radius when the RMS radial velocity is normalized with respect to local mainstream velocity, averaged across the passage width.

#### 3.7.4 Boundary Layer Characteristic Parameters ( $\theta_{11}$ , $H$ , $\epsilon_w$ ):

In this section the boundary layer characteristic parameters (i.e. the momentum thickness in the mainstream direction ( $\theta_{11}$ ), the shape parameter  $H$  and the limiting streamline angle ( $\epsilon_w$ )) derived from the experimental measurements are compared with the predictions based on momentum integral equations (Sec. 2.4 of this report).



The observed values of  $\theta_{11}$  (Fig. 42a,b) is found to increase slowly further downstream.  $\theta_{11}$  increases with increase in radius. The values on the suction side are higher than those on the pressure side. The predictions agree well with the measured values except near the leading edge, where the extent of laminar boundary layer growth is assumed to be known. The transition from laminar to turbulent boundary layer is assumed to occur instantaneously at a critical Reynolds Number  $3 \times 10^5$  (based on peripheral velocity and distance from the leading edge.) Compared to the boundary layer growth on a single blade rotating in stationary fluid, the boundary layer growth is much smaller in a channel due to the presence of radial and chordwise pressure gradients. The difference between the observed and predicted boundary layer growth is partly due to an error in estimating the extent of initial laminar boundary layer and partly due to an error in estimating the momentum thickness  $\theta_{11}$  from measurements.

The observed values of the limiting streamline angle  $\epsilon_w$  (Fig. 42d & c) first increase in chordwise ( $\theta$ ) direction reaching an asymptotic value at  $\theta \sim 2$  radians.

The value of  $\epsilon_w$  decreases with increase in radius and reaches a minimum at the tip. The magnitude of  $\epsilon_w$  is higher on the leading side indicating that the boundary layer is more skewed and that the cross flow is larger compared to that on the trailing side of the channel. The predictions agree reasonably well except near transition. The value of  $\epsilon_w$  in the laminar region is obtained from the approximate solution of Banks and Gadd and asymptotic value obtained by Cochran. The numerical results are liable to some error because the transition is assumed to be sudden and there is an order of magnitude of difference in the value of limiting streamline angle ( $\epsilon_w$ ) for laminar and turbulent boundary layers respectively.

An important difference between the single blade results of reference 9 and the rotating channel is that the values are higher in a rotating channel and there is a radial variation due to presence of varying radial pressure gradient.

The distribution of shape factor  $H$  obtained from the measurements is plotted in Figure 43. The value of  $H$  is higher on the pressure side (1.30 to 1.50) compared to the suction side of the channel (1.10 to 1.30). Its value is nearly constant near the midradius but changes rapidly at hub and tip due to the interference effects of hub or annulus wall boundary layers. The value is more at higher radii due to larger radial pressure gradient. A plot of shape factor based on power law fitting of the experimental data (Fig. 44) also shows that the shape factor is almost constant, except near hub or tip regions. Since the experimental data has been obtained by running the four-bladed channel at open throttle and hence with mild pressure gradients, the above results show that it is valid to take  $H$  constant in  $\theta$  direction in predicting  $\theta_{11}$  and  $\epsilon_w$  in this case but it would be necessary to include its ( $H$ ) variation for future experiments with stronger pressure gradients as outlined in section 2.4 of this report.

### 3.7.5 Skin Friction Correlation:

Skin friction coefficients derived from preston tube measurements are plotted against Reynolds number (based on mainstream velocity and local radius) in Figure 45. In the earlier plot (Figure 27) the Reynolds number is based on the distance from the leading edge.

The skin friction coefficient for the rotating channel is shown compared with those of a stationary channel (fully developed) with the same mean velocity in Figure 45. The correlation for a stationary channel is given by

$$C_{fo} = \frac{0.0791}{\left(\frac{\bar{U} d_h}{\nu}\right)^{0.25}} \quad (99)$$

where  $d_h$  = hydraulic diameter, which is equal to twice the normal distance between the blades at any radius. The skin friction coefficient for a rotating channel is higher than those of a stationary channel on both the pressure and suction surfaces.

The skin friction coefficients derived from the velocity profile, using clausner chart, are shown in Figures 46 a and b. These values are in close agreement with the values derived from direct measurement (Figures 45 a and b).

#### 4. FUTURE MEASUREMENTS

Measurements of static pressure, limiting streamline angle and skin friction at the blade surface and the mean velocity profiles inside the blade passage will be performed on the four-bladed flat plate inducer at 450 rpm and at a throttle opening of (0.75 inch) corresponding to a flow coefficient  $\phi = .05$ . In addition, hot wire measurements would be made to derive the turbulent intensity and turbulent stress components inside the rotor passage. The method of measuring static pressure, limiting streamline angle and mean velocity profiles has been described in Section 3.7. The skin friction would be measured by using hot film sensors on the surface at selected locations and the hot wire measurements would be done by using a three wire sensor described below.

##### 4.1 Hot Wire Measurements:

Since the flow inside the inducer is highly three-dimensional, a three sensor hot wire probe will be used for the measurement of turbulent quantities. Also, the asymptotic analysis developed in Section 2.5 is valid if shear stress gradient varies radially only in the interference region. Since this region is far away from the solid boundaries, only turbulent shear stresses are expected to exist and therefore measurement of the turbulent stresses inside the rotor are necessary to check the validity of the above assumption.

A special probe configuration shown in Figure 47 would be used to obtain the turbulent quantities from the direct measurement of the three mean sensor output voltages  $\bar{E}_1, \bar{E}_2, \bar{E}_3$  and the six products of fluctuating voltages  $(\overline{e_1^2}, \overline{e_2^2}, \overline{e_3^2}, \overline{e_1 e_2}, \overline{e_1 e_3}, \overline{e_2 e_3})$ . The orientation of the sensors is shown in Figure 47.  $x, z, r$  are the directions

of blade chord, blade normal and radial directions respectively. Sensors 1 and 2 are in the xz plane and are orthogonal to each other. Sensor 1 makes an angle  $\alpha_1$  with the x axis. Sensor 3 is located midway between 1 and 2 and is at angle  $\gamma_1$  to the xz plane (or plane of the sensors 1 and 2).

The constitutive equations of the hot wire and a method of deriving the turbulent quantities from the hot wire voltage measurements are given below.

Effective cooling velocity on hot wire 1 (shown in Figure 47) is,

$$V_{e_1}^2 = [(\bar{U} + u') \sin \alpha_1 - (\bar{V} + v') \cos \alpha_1]^2 + k^2 [(\bar{U} + u') \cos \alpha_1 + (\bar{V} + v') \sin \alpha_1]^2 + [\bar{W} + w']^2 \quad (100)$$

where k is a function of wire parameters i.e.,  $\ell/d$  ratio.

Since  $k^2 \ll 1$  and  $\bar{U} > u, u, w, \bar{v}, \bar{w}$  we have from equation (100)

$$V_{e_1}^2 \approx \bar{U}^2 \sin^2 \alpha_1 \left[ 1 + \frac{2(u' \sin \alpha_1 - v' \cos \alpha_1 - \bar{V} \cos \alpha_1)}{\bar{U} \sin \alpha_1} + k^2 \cot^2 \alpha_1 + \frac{(\bar{W} + w')^2}{\bar{U}^2 \sin^2 \alpha_1} \right] \quad (101)$$

$$\therefore V_{e_1} \approx \bar{U} \sin \alpha_1 \left[ 1 + \frac{k^2}{2} \cot^2 \alpha_1 + \frac{1}{2} \left( \frac{\bar{W} + w'}{\bar{U} \sin \alpha_1} \right)^2 + \frac{(u' \sin \alpha_1 - v' \cos \alpha_1 - \bar{V} \cos \alpha_1)}{\bar{U} \sin \alpha_1} \right] \quad (102)$$

Using Reynolds averaging;  $V_{e_1} = \bar{V}_{e_1} + v_{e_1}$  where  $\bar{V}_{e_1}$  and  $v_{e_1}$  are mean and fluctuating components.

$$\bar{V}_{e_1} = \bar{U} \sin \alpha_1 \left[ 1 + \frac{k^2}{2} \cot^2 \alpha_1 - \frac{\bar{V}}{\bar{U}} \cot \alpha_1 + \frac{1}{2} \left( \frac{\bar{W}}{\bar{U} \sin \alpha_1} \right)^2 \right] \quad (103)$$

$$v_{e_1} = u' \sin \alpha_1 - v' \cos \alpha_1 + \frac{w'}{\bar{U} \sin \alpha_1} \quad (104)$$

Similarly we have,

$$\overline{V_{e_2}} = \overline{U} \cos \bar{\alpha}_1 \left[ 1 + \frac{k^2}{2} \tan^2 \bar{\alpha}_1 + \frac{\overline{V}}{\overline{U}} \tan \bar{\alpha}_1 + \frac{1}{2} \left( \frac{\overline{W}}{\overline{U} \cos \bar{\alpha}_1} \right)^2 \right] \quad (105)$$

$$\text{and } v_{e_2} = u' \cos \bar{\alpha}_1 + v' \sin \bar{\alpha}_1 + \frac{\overline{W}}{\overline{U} \cos \bar{\alpha}_1} \cdot w' \quad (106)$$

And

$$\overline{V_{e_3}} = \overline{U} \cos \gamma_1 \left[ 1 + \frac{k^2}{2} \cot^2 \gamma_1 + \frac{\overline{W}}{\overline{U}} \cot \gamma_1 + \frac{1}{2} \left( \frac{\overline{W}}{\overline{U}} \cot \gamma_1 \right)^2 \right] \quad (107)$$

and

$$v_{e_3} = u' \cos \gamma_1 - w' \sin \gamma_1 \quad (108)$$

The hot wires to be used have  $\alpha_1 = \gamma_1 = 45^\circ$ , therefore,

$$\overline{V_{e_1}} = \frac{\overline{U}}{\sqrt{2}} \left[ 1 + \frac{k^2}{2} + \frac{\overline{V}}{\overline{U}} + \left( \frac{\overline{W}}{\overline{U}} \right)^2 \right]$$

$$\overline{V_{e_2}} = \frac{\overline{U}}{\sqrt{2}} \left[ 1 + \frac{k^2}{2} - \frac{\overline{V}}{\overline{U}} + \left( \frac{\overline{W}}{\overline{U}} \right)^2 \right] \quad (109)$$

$$\overline{V_{e_3}} = \frac{\overline{U}}{\sqrt{2}} \left[ 1 + \frac{k^2}{2} + \frac{\overline{W}}{\overline{U}} + \frac{1}{2} \left( \frac{\overline{W}}{\overline{U}} \right)^2 \right]$$

From King's law for heat transfer in hot wire, the voltage E is given by

$$E_i^2 = E_{oi}^2 + B_i V_i^{n_i} \quad (i = 1, 2 \text{ or } 3) \quad (110)$$

where  $n_i$  and  $B_i$  are wire constants, with  $n_i = 0.45$  to  $0.50$  and  $V_i$  is the effective cooling velocity. Applying Reynolds' averages.

$$\overline{E_i^2} = \overline{E_{oi}^2} + B_i \overline{V_i^{n_i}} \quad (111)$$

$$e_i = \frac{n_i B_i \overline{V_i^{n_i}}}{2 \overline{E_i} \overline{V_i}} v_i = \frac{n_i (\overline{E_i^2} - \overline{E_{oi}^2})}{2 \overline{E_i} \overline{V_i}} v_i \quad (112)$$

Substitution of equations 104, 106 and 108 in 112 results in,

$$\begin{aligned}\frac{e_1}{K_1} &= u' - v' + w' \frac{2\bar{W}}{\bar{U}} \\ \frac{e_2}{K_2} &= u' + v' + w' \frac{2\bar{W}}{\bar{U}} \\ \frac{e_3}{K_3} &= u' - w'\end{aligned}\tag{113}$$

where

$$K_i = \frac{n_i B_i}{2\sqrt{2} \bar{E}_i \bar{V}_i^{(1-n_i)}}\tag{114}$$

Solving for fluctuating velocity components  $u'$ ,  $v'$ , and  $w'$ :

$$\begin{aligned}u' &= \frac{1}{2(1+\alpha)} \left( \frac{e_1}{K_1} + \frac{e_2}{K_2} + 2\alpha \frac{e_3}{K_3} \right) \\ v' &= \frac{1}{2} \left( \frac{e_2}{K_2} - \frac{e_1}{K_1} \right) \\ w' &= \frac{1}{2(1+\alpha)} \left( \frac{e_1}{K_1} + \frac{e_2}{K_2} - \frac{2e_3}{K_3} \right)\end{aligned}\tag{115}$$

where  $\alpha = 2\bar{W}/\bar{U}$

Therefore, various correlations  $\overline{u'^2}$ ,  $\overline{v'^2}$ ,  $\overline{w'^2}$ ,  $\overline{u'v'}$ ,  $\overline{v'w'}$ ,  $\overline{u'w'}$  can be derived from equation (115). A technique of deriving the turbulence intensities and correlations from the hot wire data is described below:

From  $u'$ ,  $v'$  and  $w'$  in equation 115, making desired products and averaging,

$$\overline{u'^2} = \frac{1}{4(1+\alpha^2)} \left[ \frac{\bar{e}_1^2}{K_1^2} + \frac{\bar{e}_2^2}{K_2^2} + 4\alpha^2 \frac{\bar{e}_3^2}{K_3^2} + 2 \frac{\bar{e}_1 \bar{e}_2}{K_1 K_2} + 4\alpha \left( \frac{\bar{e}_1 \bar{e}_3}{K_1 K_3} + \frac{\bar{e}_2 \bar{e}_3}{K_2 K_3} \right) \right]\tag{116}$$

$$\overline{v'^2} = \frac{1}{4} \left[ \frac{\bar{e}_1^2}{K_1^2} + \frac{\bar{e}_2^2}{K_2^2} - 2 \frac{\bar{e}_1 \bar{e}_2}{K_1 K_2} \right]\tag{117}$$

$$\overline{w'^2} = \frac{1}{4(1+\alpha)^2} \left[ \frac{\overline{e_1^2}}{k_1^2} + \frac{\overline{e_2^2}}{k_2^2} + 4\alpha \frac{\overline{e_3^2}}{k_3^2} + \frac{2\overline{e_1 e_2}}{k_1 k_2} - 4\left( \frac{\overline{e_1 e_3}}{k_1 k_3} + \frac{\overline{e_2 e_3}}{k_2 k_3} \right) \right] \quad (118)$$

$$\overline{u'v'} = \frac{1}{4(1+\alpha)} \left[ \frac{\overline{e_2^2}}{k_2^2} + 2\alpha \frac{\overline{e_2 e_3}}{k_2 k_3} - 2\alpha \frac{\overline{e_1 e_3}}{k_1 k_3} - \frac{\overline{e_1^2}}{k_1^2} \right] \quad (119)$$

$$\overline{vw'} = \frac{1}{4(1+\alpha)} \left[ \frac{\overline{e_2^2}}{k_2^2} - 2 \frac{\overline{e_2 e_3}}{k_2 k_3} + 2 \frac{\overline{e_1 e_3}}{k_1 k_3} - \frac{\overline{e_1^2}}{k_1^2} \right] \quad (120)$$

$$\overline{u'w'} = \frac{1}{4(1+\alpha)^2} \left[ \frac{\overline{e_1^2}}{k_1^2} + \frac{\overline{e_2^2}}{k_2^2} + \frac{2\overline{e_1 e_2}}{k_1 k_2} - 2(1-\alpha) \left( \frac{\overline{e_1 e_3}}{k_1 k_3} + \frac{\overline{e_2 e_3}}{k_2 k_3} \right) - 4\alpha \frac{\overline{e_3^2}}{k_3^2} \right] \quad (121)$$

Since all the quantities on the right-hand side of equations 116-121 are known combinations of the measured values  $\overline{e_1^2}$ ,  $\overline{e_2^2}$ ,  $\overline{e_3^2}$ ,  $\overline{e_1 e_2}$ ,  $\overline{e_2 e_3}$ ,  $\overline{e_1 e_3}$ , the turbulent quantities  $\overline{u'^2}$ ,  $\overline{v'^2}$ ,  $\overline{w'^2}$ ,  $\overline{uv'}$ ,  $\overline{vw'}$  and  $\overline{uw'}$  can be determined. A schematic of the circuitry consisting of a four channel constant temperature hot wire anemometer, Model 420A wide-band multiplier and available averaging circuits to be used in this program, is shown in Figure 48. The hotwire probe would traverse by the traversing mechanism described in Section 3 the signals would be transmitted to stationary system using MSD #6, a six channel mercury slipring unit, as shown in Data Transmission Assembly (Figure 4).



#### 4.2 Wall Shear Stress Measurements:

Skin friction measurements at selected locations (5 radial x 5 tangential locations) would be obtained by mounting a disk probe with two heated skin friction gauges as described in an earlier report (Reference 21). Measurements would be transmitted to a four-channel constant hot wire anemometer through the mercury slip ring unit. The probe will be calibrated in a wind tunnel with the use of a Preston tube to provide a known value for the skin friction stress.

## REFERENCES

1. Coles, D., "The Law of the Wake in the Turbulent Boundary Layer", Jour. Fluid Mech. Vol. 1, Part 2, 1956.
2. Eichelbrenner, E. A., and Peube, J., "Theoretical and Experimental Investigations on Three-Dimensional (Laminar and Turbulent) Boundary Layers in Particular on Problems of Transition, Separation and Reattachment", Laboratoire de Mechanique des Fluides, Universite de Portier, 1966.
3. Head, M. R., and Rechenberg, I., "The Preston Tube as a Means of Measuring Skin Friction", Jour. Fluid Mech. Vol. 14, Part 1, 1962.
4. Hornung, H. G., and Joubert, P. N., "The Mean Velocity Profile in Three-Dimensional Turbulent Boundary Layers", Jour. Fluid Mech., Vol. 15, 1963.
5. Jabbari, A., "Turbulent Boundary Layer Characteristics on a Rotating Helical Blade", MS Thesis, Dept. of Aerospace Engineering, The Pennsylvania State University, 1969.
6. Johnston, J. P., "A Wall Trace, Flow Visualization Technique for Rotating Surfaces in Air", ASME, J. Basic Eng., 1964.
7. Johnston, J. P., "On Three-Dimensional Turbulent Boundary Layer Generated by Secondary Flow", J. Basic Eng., Trans. ASME Vol. 82, 1960.
8. Klinksiek, W., and Pierce, F. J., "Simultaneous Lateral Skewing in a Three-Dimensional Boundary Layer Flow", ASME Paper 69-FE-24, 1969.
9. Lakshminarayana, B., Jabbari, A., and Yamaoka, H., "Turbulent Boundary Layer on a Rotating Helical Blade", Jour. Fluid Mech., Vol. 51, p. 547, 1972.
10. Lakshminarayana, B., "Experimental and Analytical Flow Through a Rocket Pump Inducer", NASA SP 304, 1973.
11. Mager, A., "Generalization of Boundary Layer Momentum Integral Equations to Three Dimensional Flow Including Those of Rotating System", NACA Rep. 1067, 1952.
12. Patel, V. C., "Calibration of the Preston Tube and Limitations on its Use in Pressure Gradients", Jour. Fluid Mech., Vol. 23, Part 1, 1965.
13. Pierce, F. J., "The Law of the Wake and Plane of Symmetry Flows in Three-Dimensional Turbulent Boundary Layers", J. Basic Eng., Trans. ASME, Series D. Vol. 88, 1966.

14. Pierce, F., and Krommenhoek, D., "Wall Shear Diagnostics in Three-Dimensional Turbulent Boundary Layers," ARO-D Tech. Report No. 2, VPI, 1968.
15. Poncet, A., and Lakshminarayana, B., "Three Dimensional Analysis and Measurement of the Flow in the Three Bladed Rocket Pump Inducer", NASA CR 2290, 1973.
16. Prandtl, L., "On Boundary Layers in Three-Dimensional Flow", Report and Trans., No. 64, British M.A.P., 1946.
17. Preston, J. H., "The Determination of Turbulent Skin Friction by Means of Pitot Tubes", J. Roy. Aero. Soc. 58, 1954.
18. Ruden, P., "Investigation of Single Stage Axial Flow Fan", NACA TM 1062, 1944.
19. Shanebrook, J. R., "An Approximate Method of Treating the Three-Dimensional Boundary Layer Equations When Cross Flow is Small", Ph.D. Dissertation, Syracuse University, 1965.
20. Velkoff, H. R., et al, "Exploratory Study of the Nature of Helicopter Rotor Blade Boundary Layer", USAAVLABS Tech. Report 69-50, Fort Eustis, Virginia 1969.
21. Yamoako, H., Lakshminarayana, B., Anand A. K., "Investigations and Analysis of Flow Phenomena in Axial Flow Inducer", Progress Report to NASA, July 1971.
22. B. Lakshminarayana, "Three Dimensional Flow Field in Rocket Pump Inducers", Part I, ASME Paper 73 FE 33 (To be published in Journal of Fluids Engineering).
23. B. Lakshminarayana and A. K. Anand, "Effect of Solidity on Rocket Pump Inducer", Second JSME Symposium on Fluid Machinery and Fluidics" p. 157-166, September 1972.
24. B. Lakshminarayana, "Visualization Study of Flow in Axial Flow Inducer", Transactions ASME, Journal of Basic Engineering, December, 1972, p. 777-787.
25. W. H. Banks & G. E. Gadd, "A Preliminary Report on Boundary Layers on Screw Propellers and Simpler Rotating Bodies", NPL Report SH R 27/62, March, 1962.
26. A. E. Von Doenhoff and N. Tetervin NACA TR 772, 1943.
27. J. F. Nash & V. C. Patel, "Three Dimensional Turbulent Boundary Layers", published by SBC Books, Inc. 1972.

28. P. Bradshaw et al., "Calculation of Boundary Layer Development Using the Turbulent Energy Equations", J. Fluid Mech., 28, p. 593, 1967.
29. P. Bradshaw, "Calculation of Three Dimensional Turbulent Boundary Layers," J. Fluid Mech. 46, p. 417, 1971.
30. B. Lakshminarayana, A. K. Anand, H. Yamaoka, "Investigation of Flow Phenomena in Axial Flow Inducers," Progress Report to NASA, November 1971.

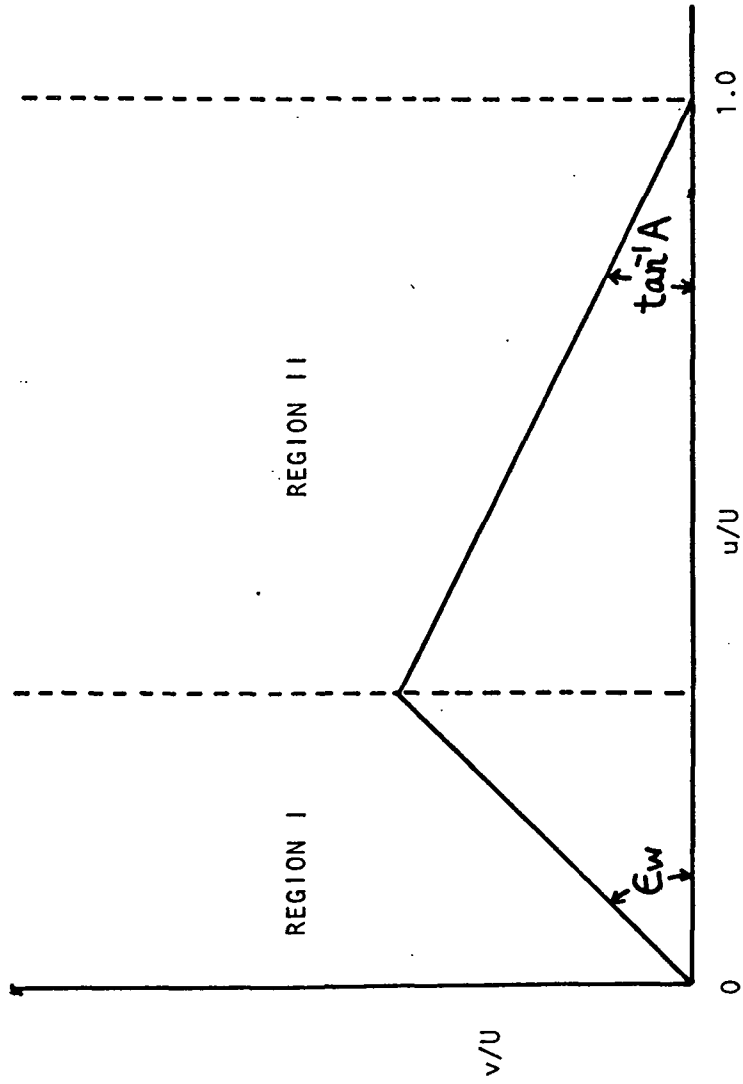


Figure 1 The triangular model

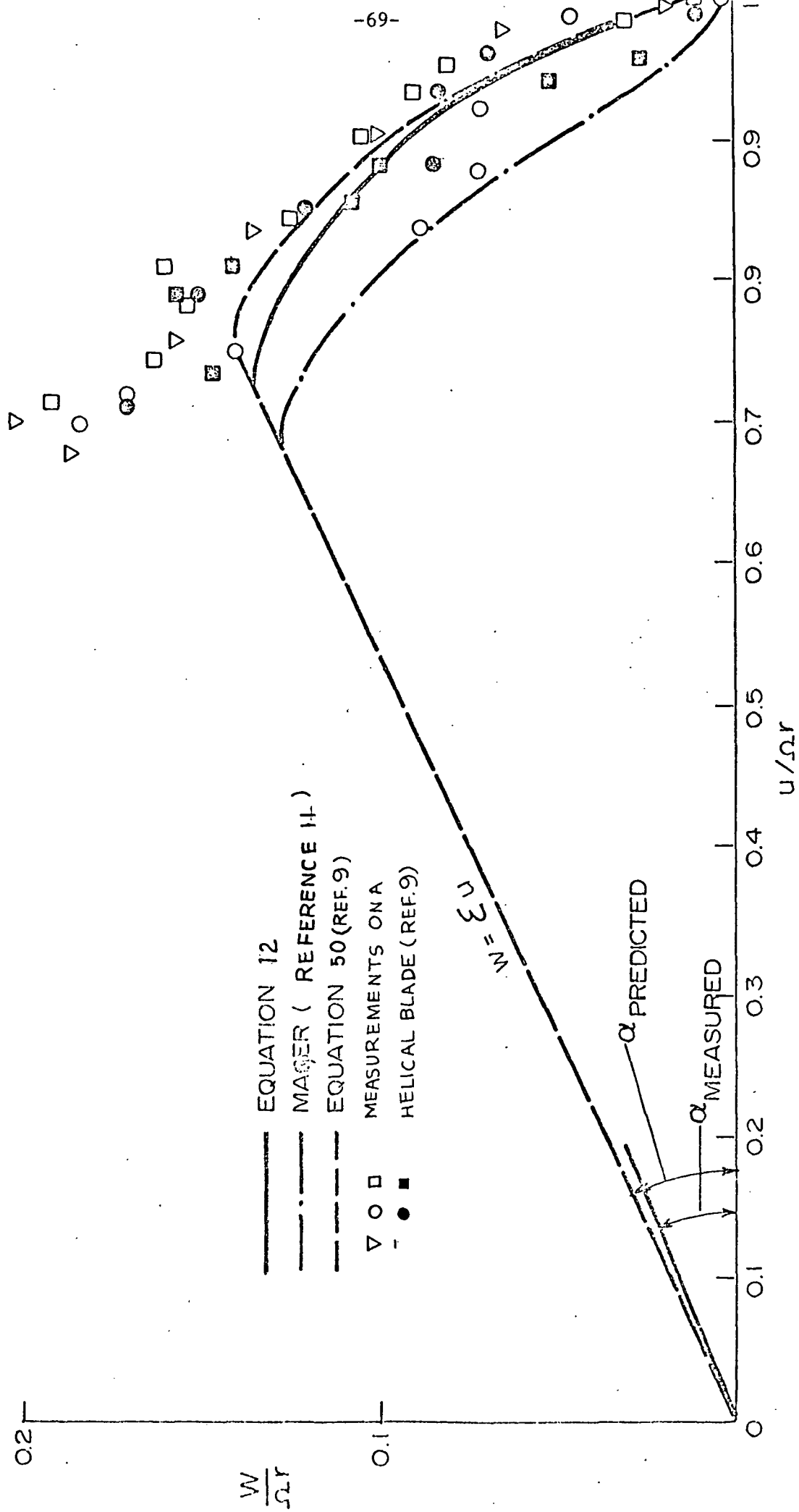


FIG 2 : THE HODOGRAPH PLOT

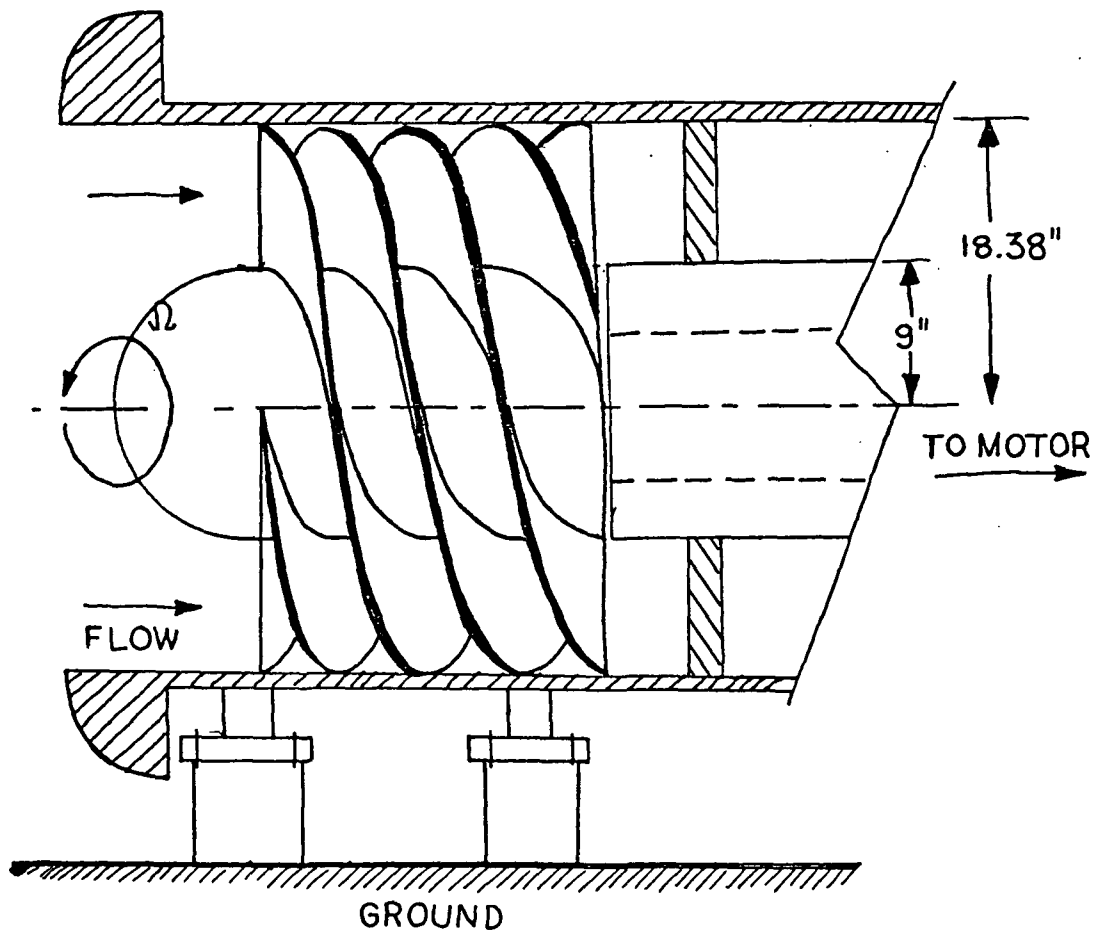


FIG3: 4 BLADED INDUCER CONFIGURATION





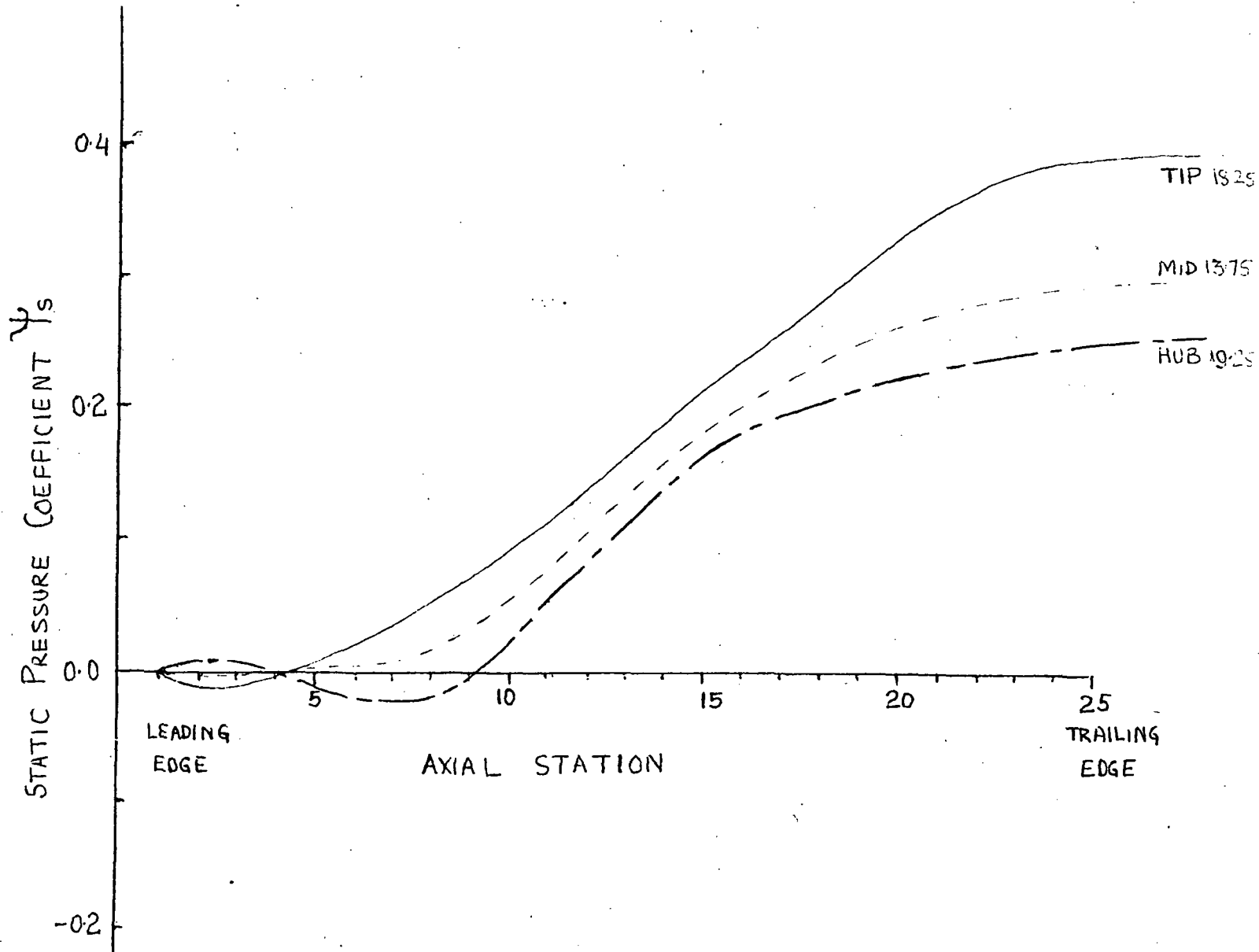


FIG5: STATIC PRESSURE DISTRIBUTIONS FOR 3BLADED-INDUCER  
AT THE MIDPASSAGE (REF.15)

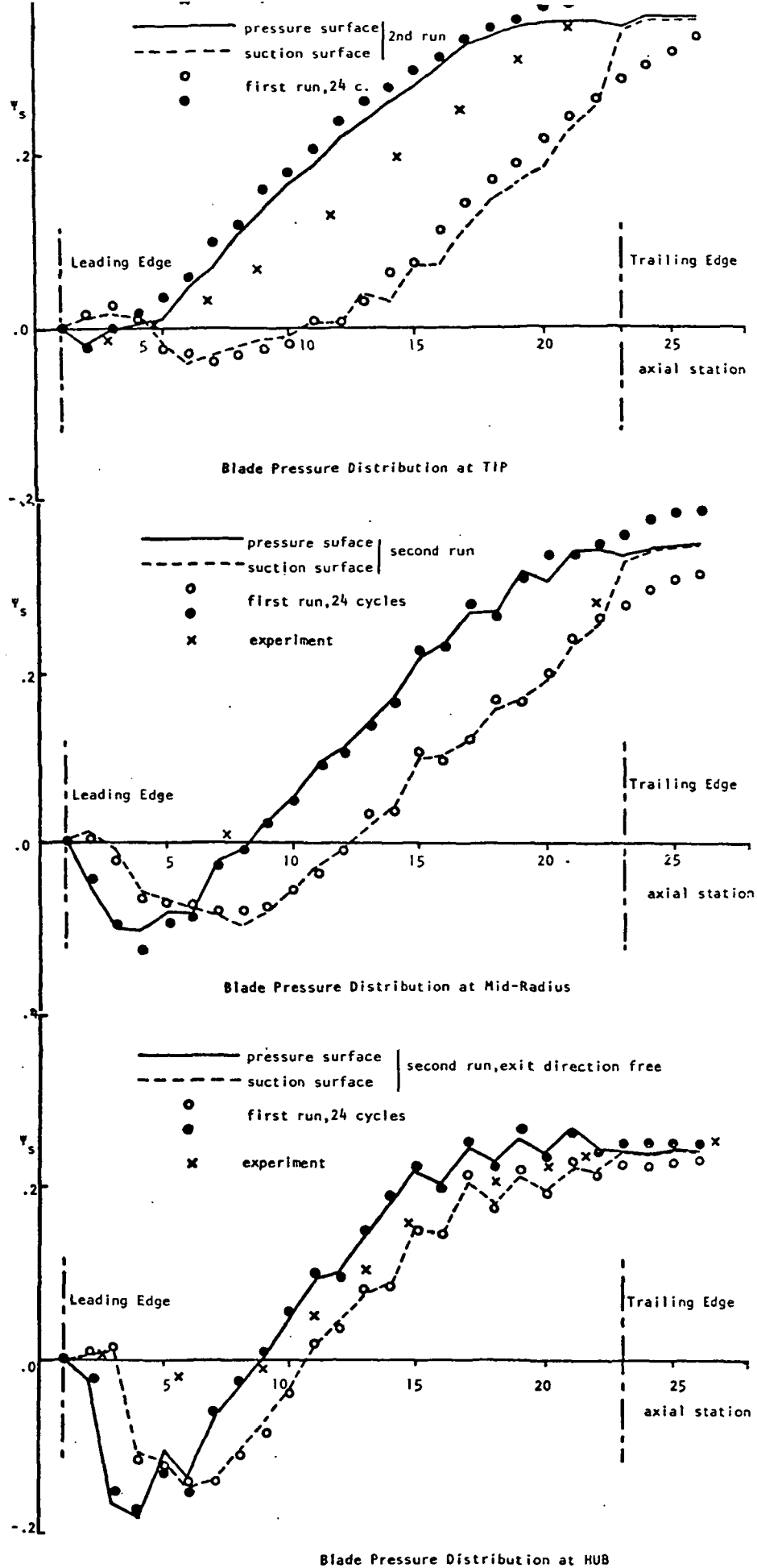


FIG6: RADIAL & CHORDWISE DISTRIBUTION OF BLADE STATIC PRESSURE  
ON 3 BLADED INDUCER ( REF.15)

FIG7: RADIAL VARIATION OF K

SYMBOL

$\theta$

0.5 RAD.

1.0 RAD.

3.0 RAD.

2.0 RAD.

5.0 RAD.

$\circ$

$+$

$\square$

$\times$

$\Delta$

$\theta = 0.5 \text{ RAD.}$

$\theta = 1.0 \text{ RAD.}$

$\theta = 3.0 \text{ RAD.}$

$\theta = 4.0 \text{ RAD.}$

$\theta = 5.0 \text{ RAD.}$

0.5 RAD.

1.0 RAD.

2.0 RAD.

3.0 RAD.

4.0 RAD.

5.0 RAD.

$K = \frac{1}{R} \frac{dR}{d\theta}$

$\rightarrow R \text{ RADIUS} \rightarrow$

GRAPH PAPER

PRINTED IN U. S. A.

FIG 8: CHORDWISE VARIATION OF  $R_g$

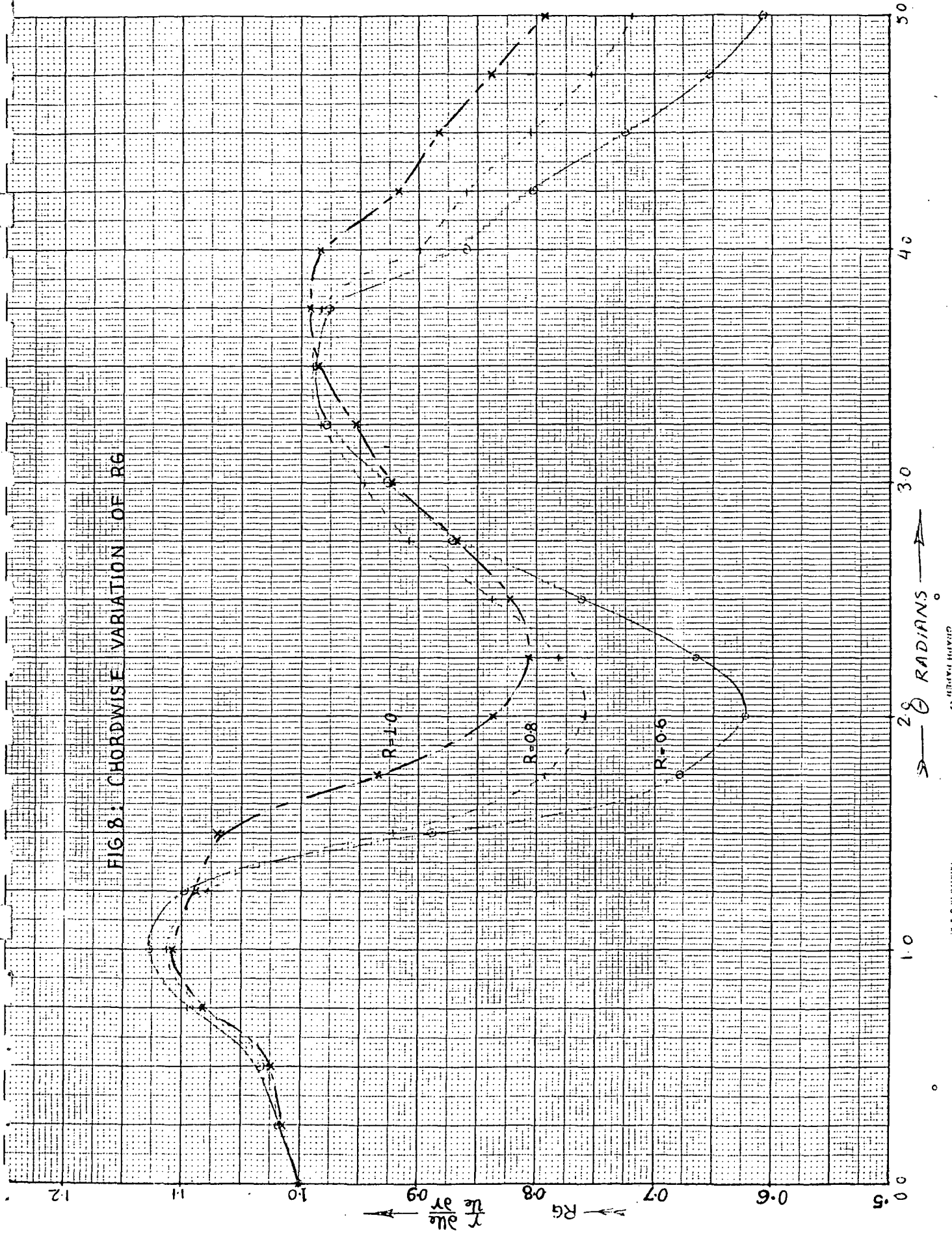
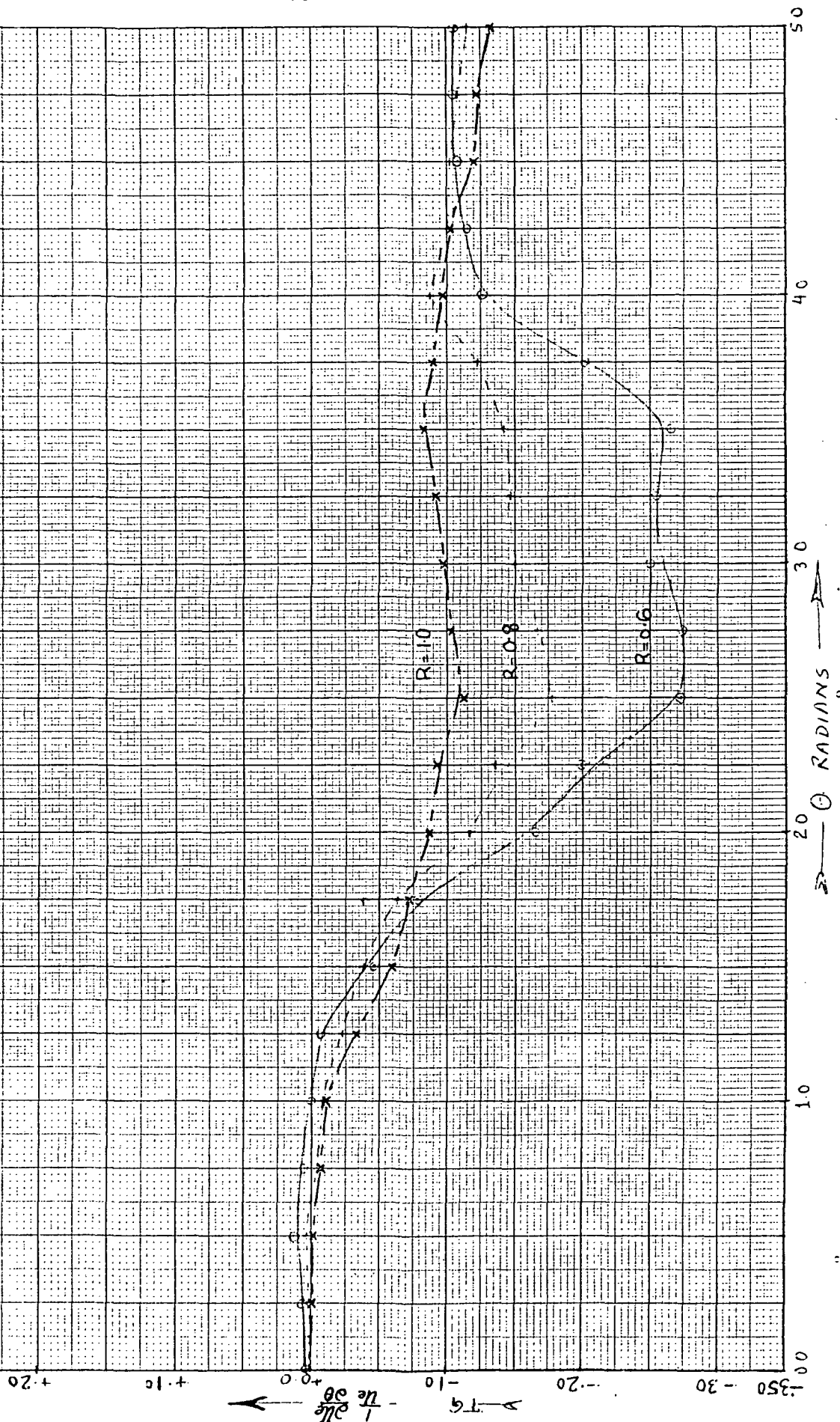


FIG. 9: CHORDWISE VARIATION OF  $T_g$



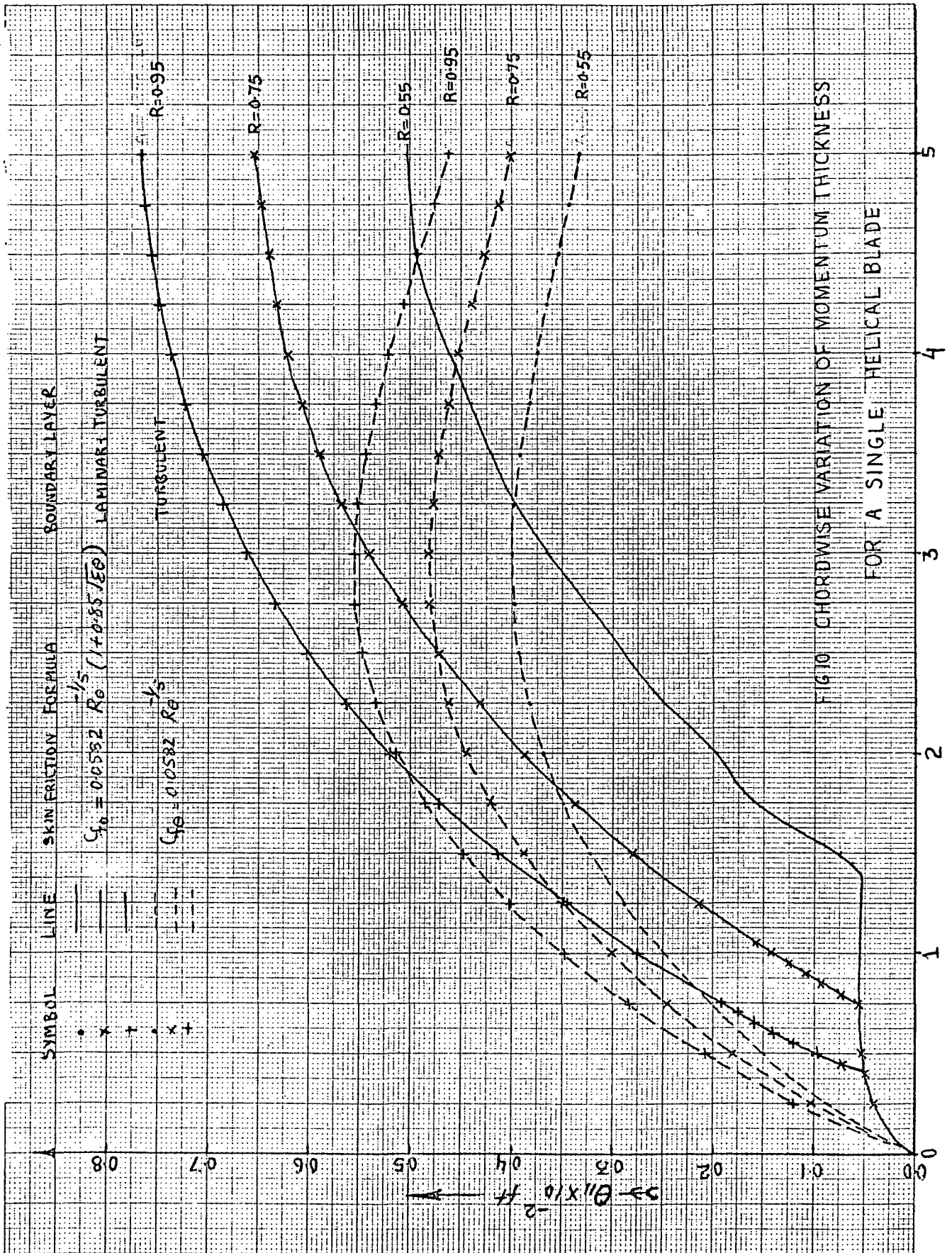


FIG. 10 CHORDWISE VARIATION OF MOMENTUM THICKNESS FOR A SINGLE HELICAL BLADE



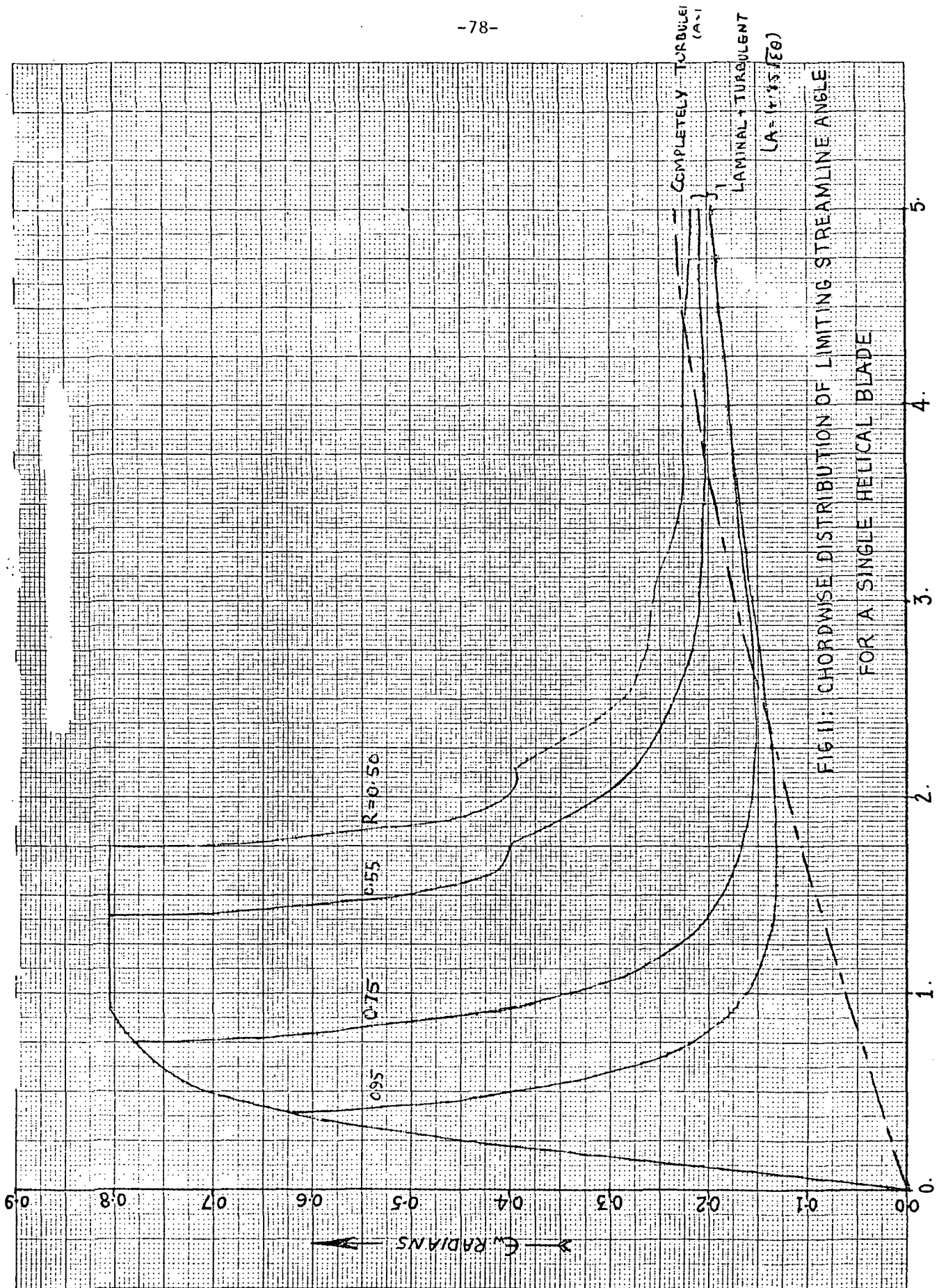
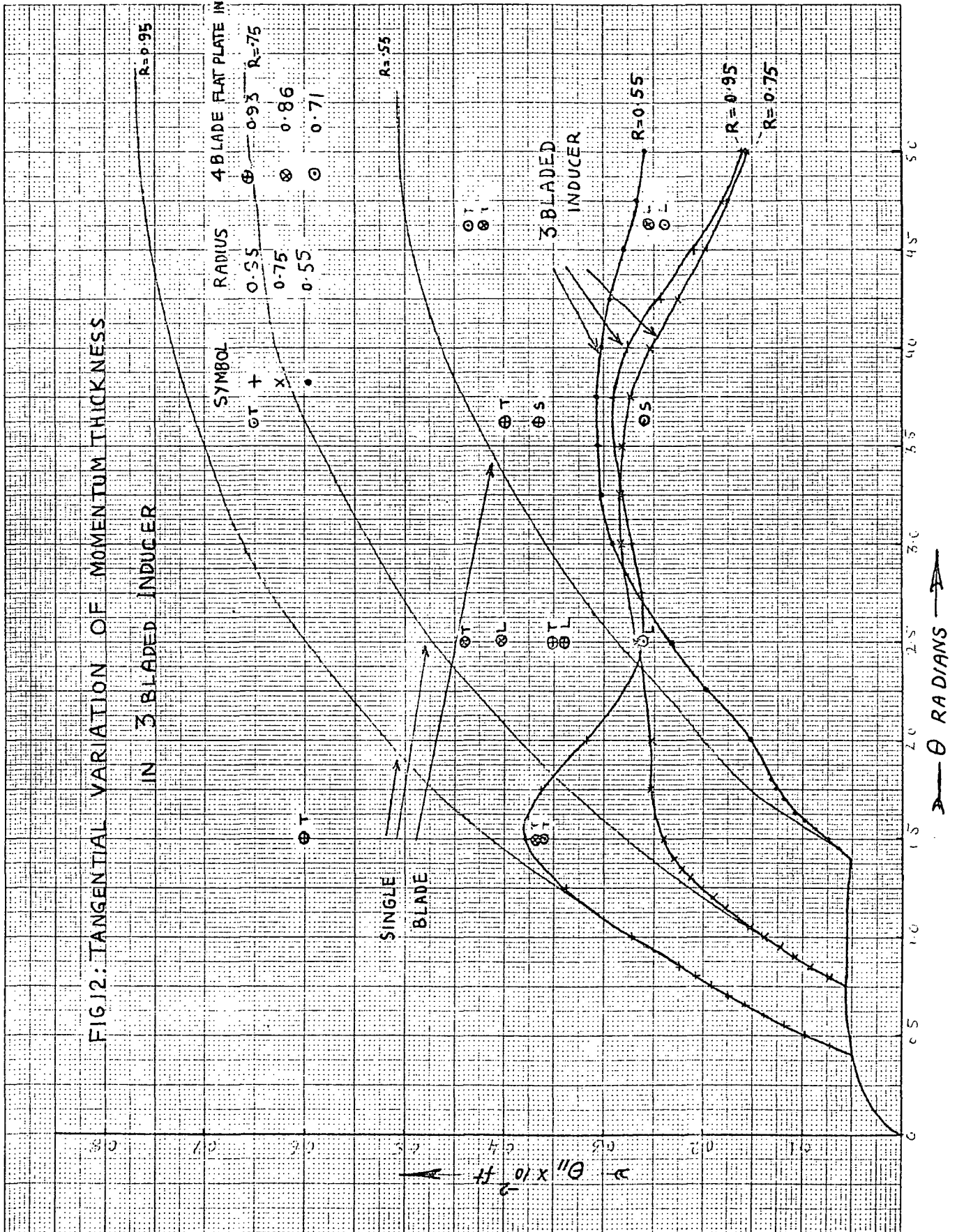
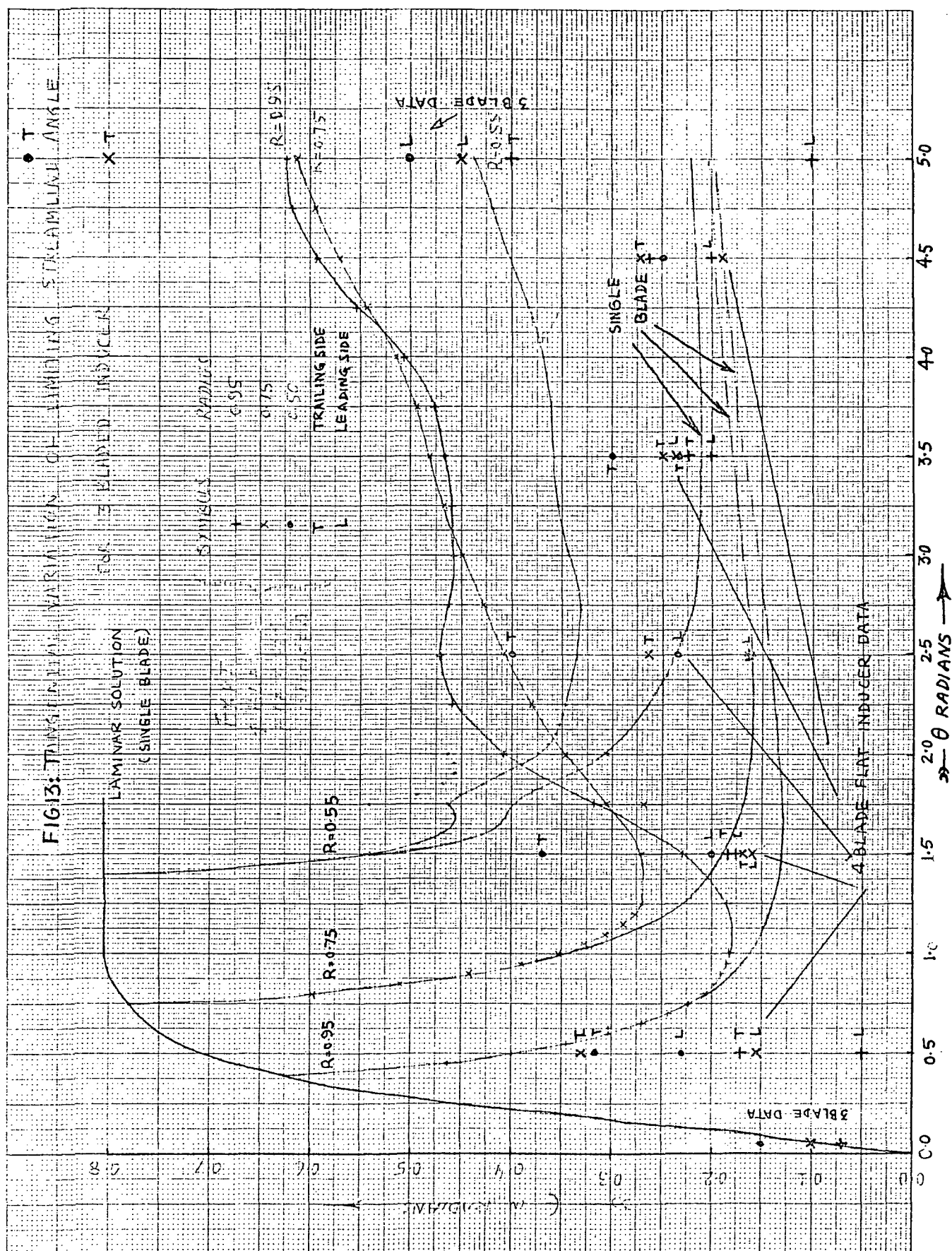


FIG. 11: CHORDWISE DISTRIBUTION OF LIMITING STREAMLINE ANGLE FOR A SINGLE HELICAL BLADE

FIG12: TANGENTIAL VARIATION OF MOMENTUM THICKNESS









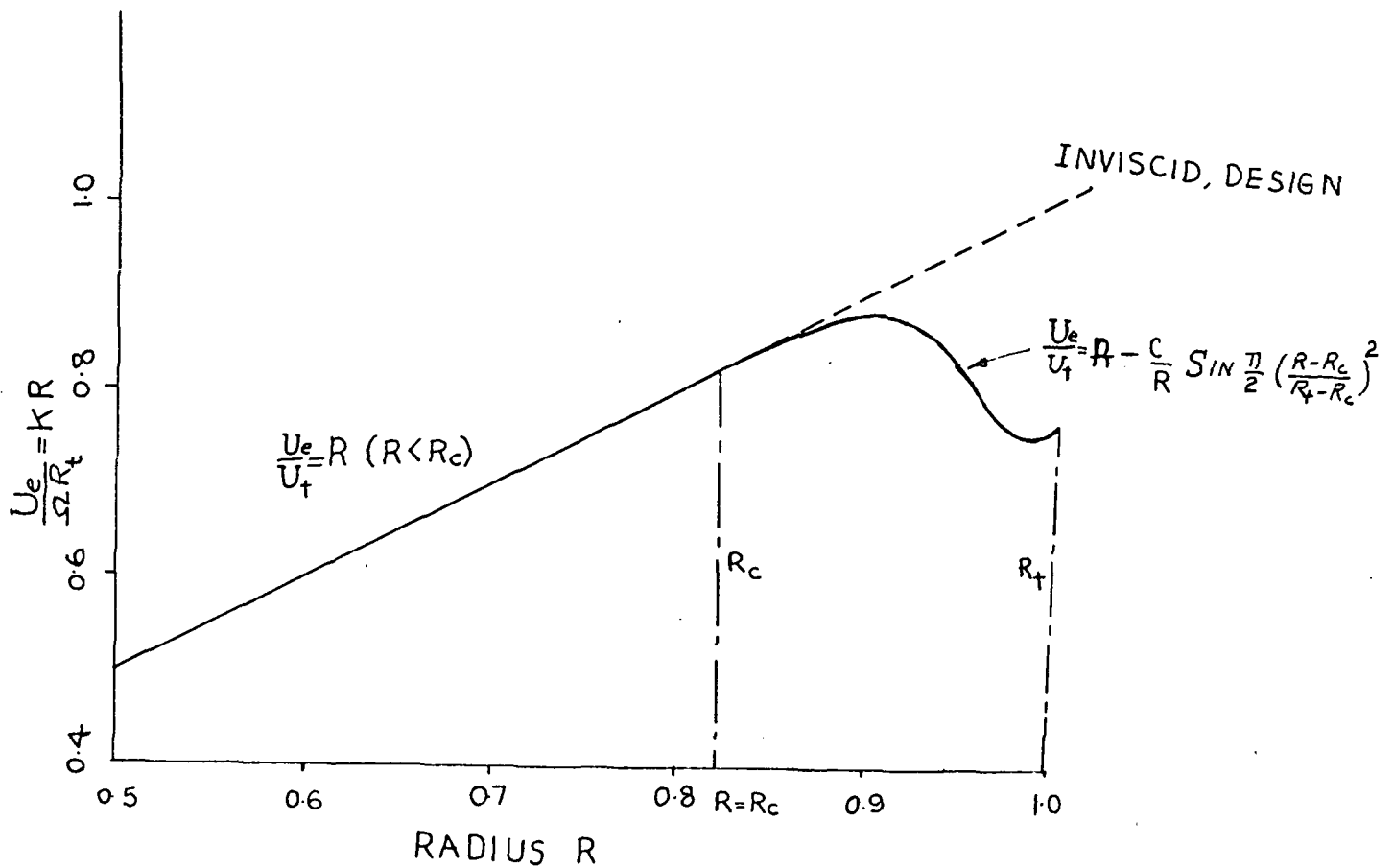
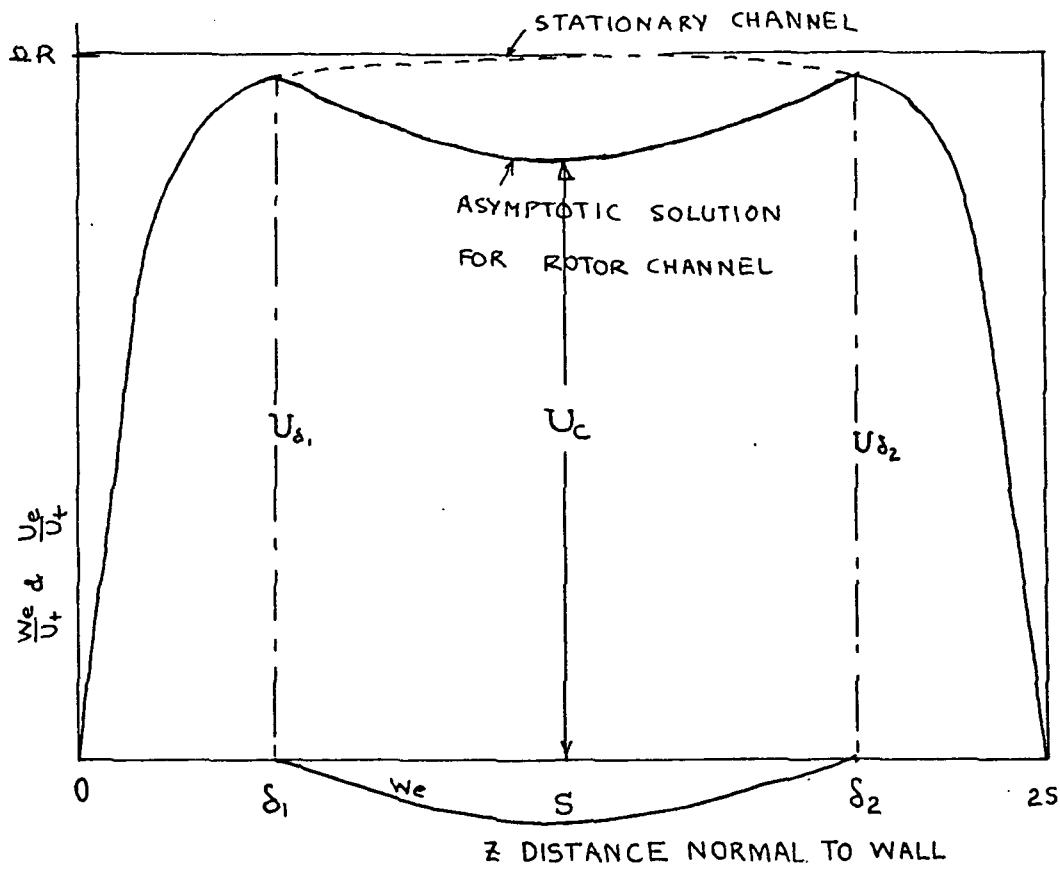


FIG 15: NATURE OF VELOCITY PROFILES IN ASYMPTOTIC REGION

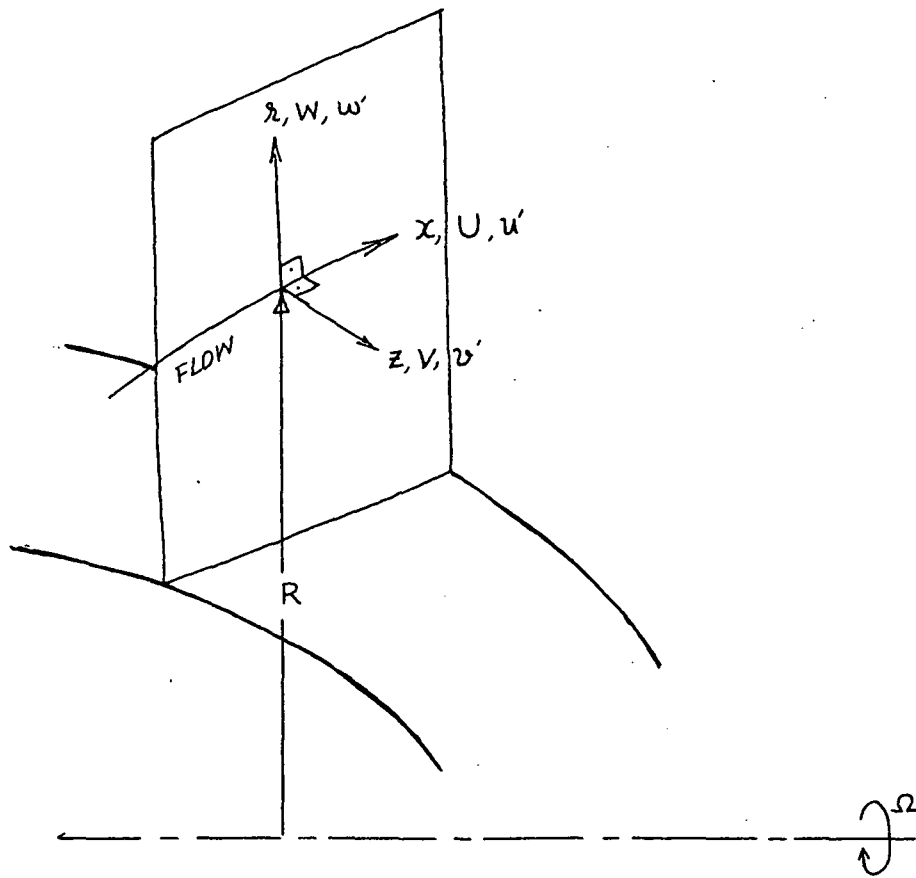


FIG 16 : COORDINATE SYSTEM FOR TURBULENT FIELD METHOD

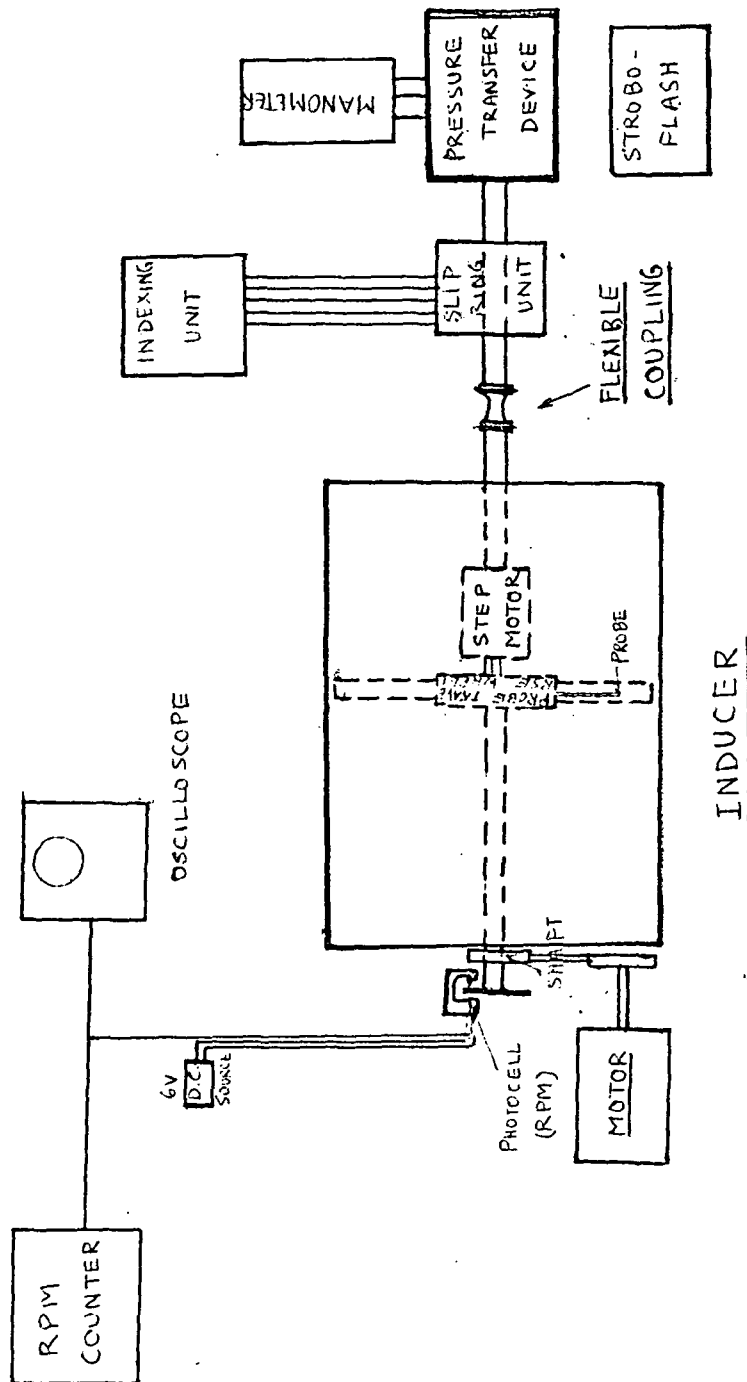


FIG 17: SCHEMATIC DIAGRAM OF EXPERIMENTAL SET-UP

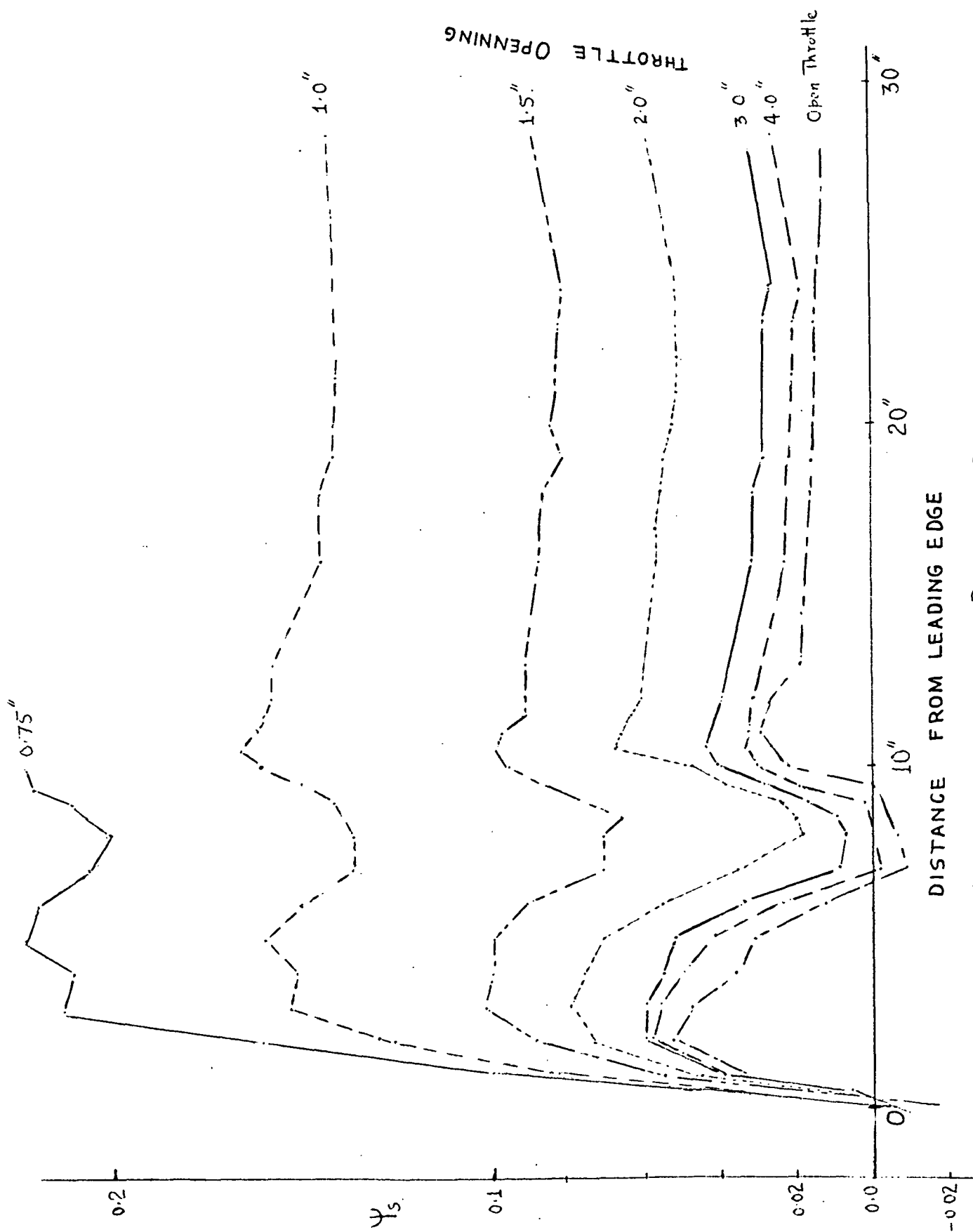


FIG18: ANNULUS WALL STATIC PRESSURE DISTRIBUTION

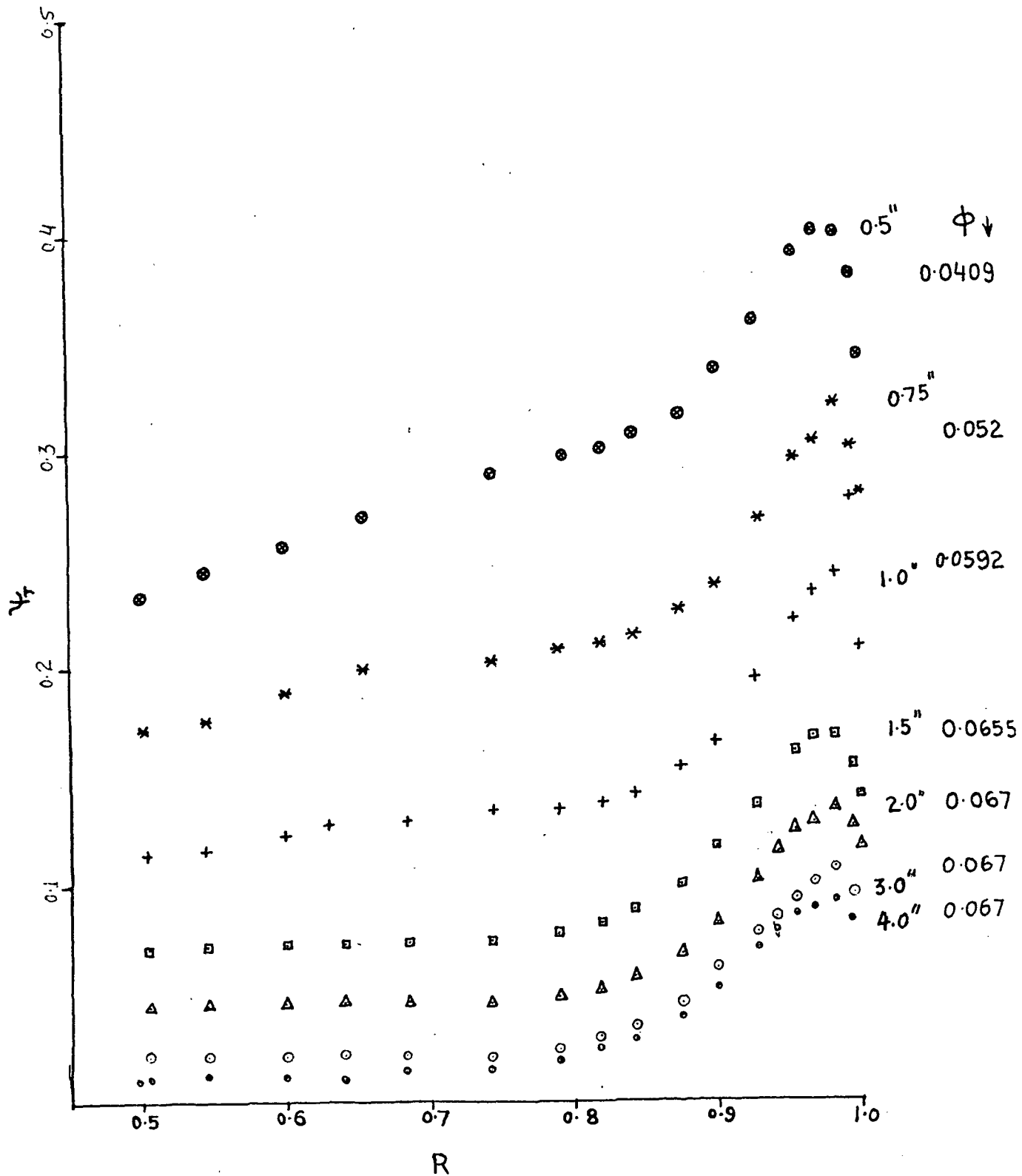


FIG 19: DISTRIBUTION OF STAGNATION PRESSURE COEFFICIENT  $\Psi_t$   
AT THE INDUCER EXIT AT DIFFERENT THROTTLE POSITIONS

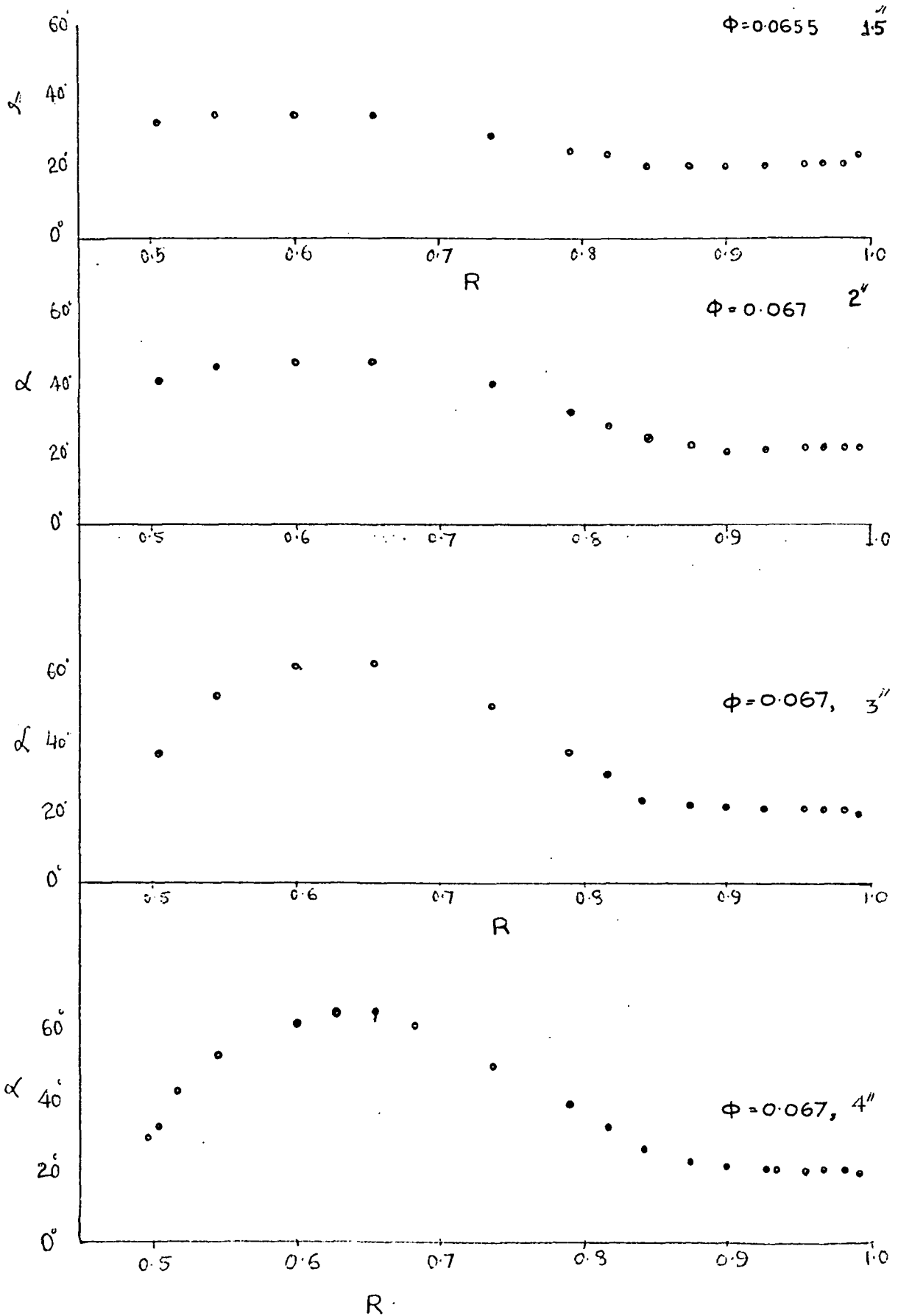


FIG20 : RADIAL DISTRIBUTION OF OUTLET ANGLE  $\alpha$   
AT THE EXIT OF 4BLADED FLAT PLATE INDUCER



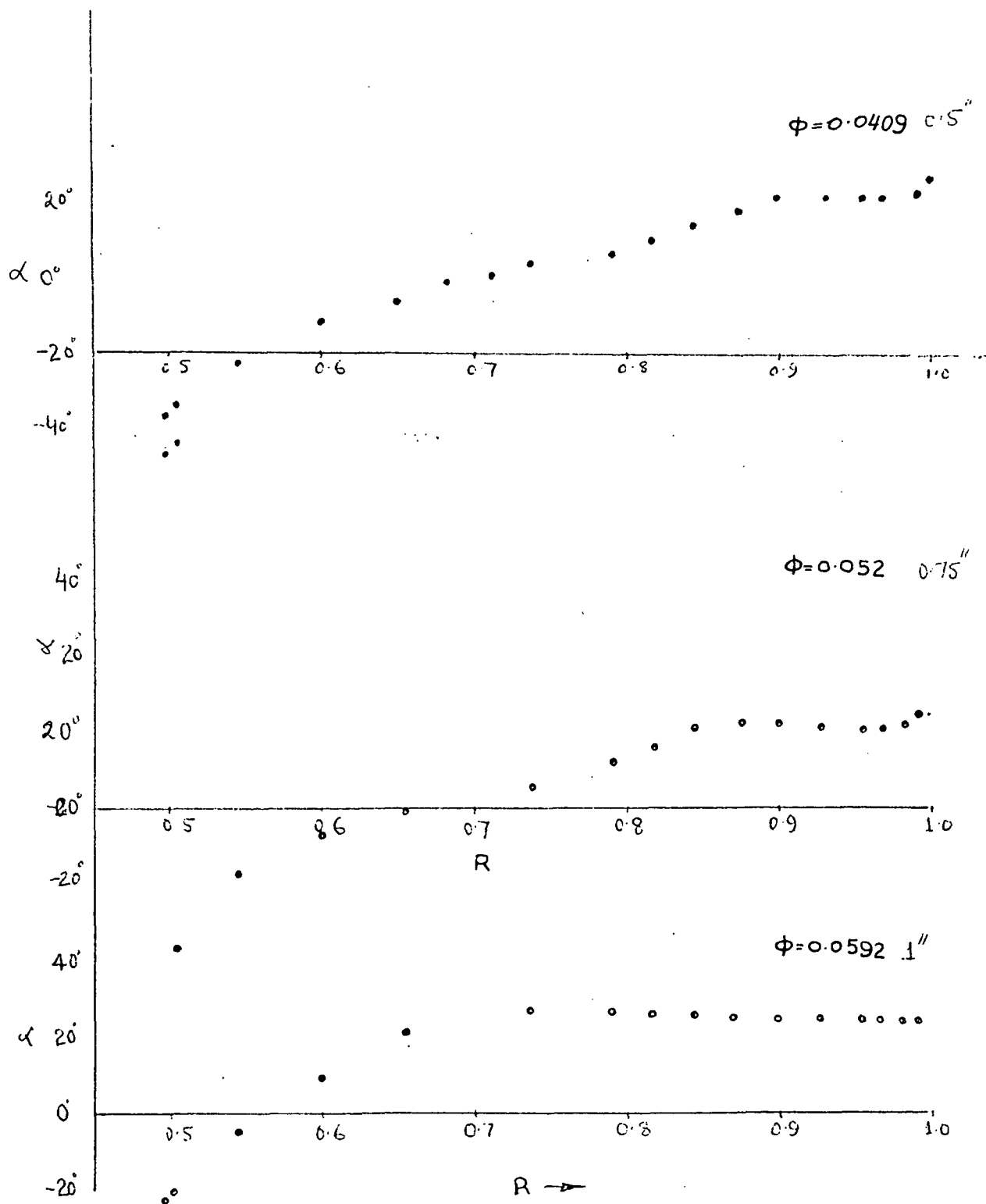


FIG 20 (a)

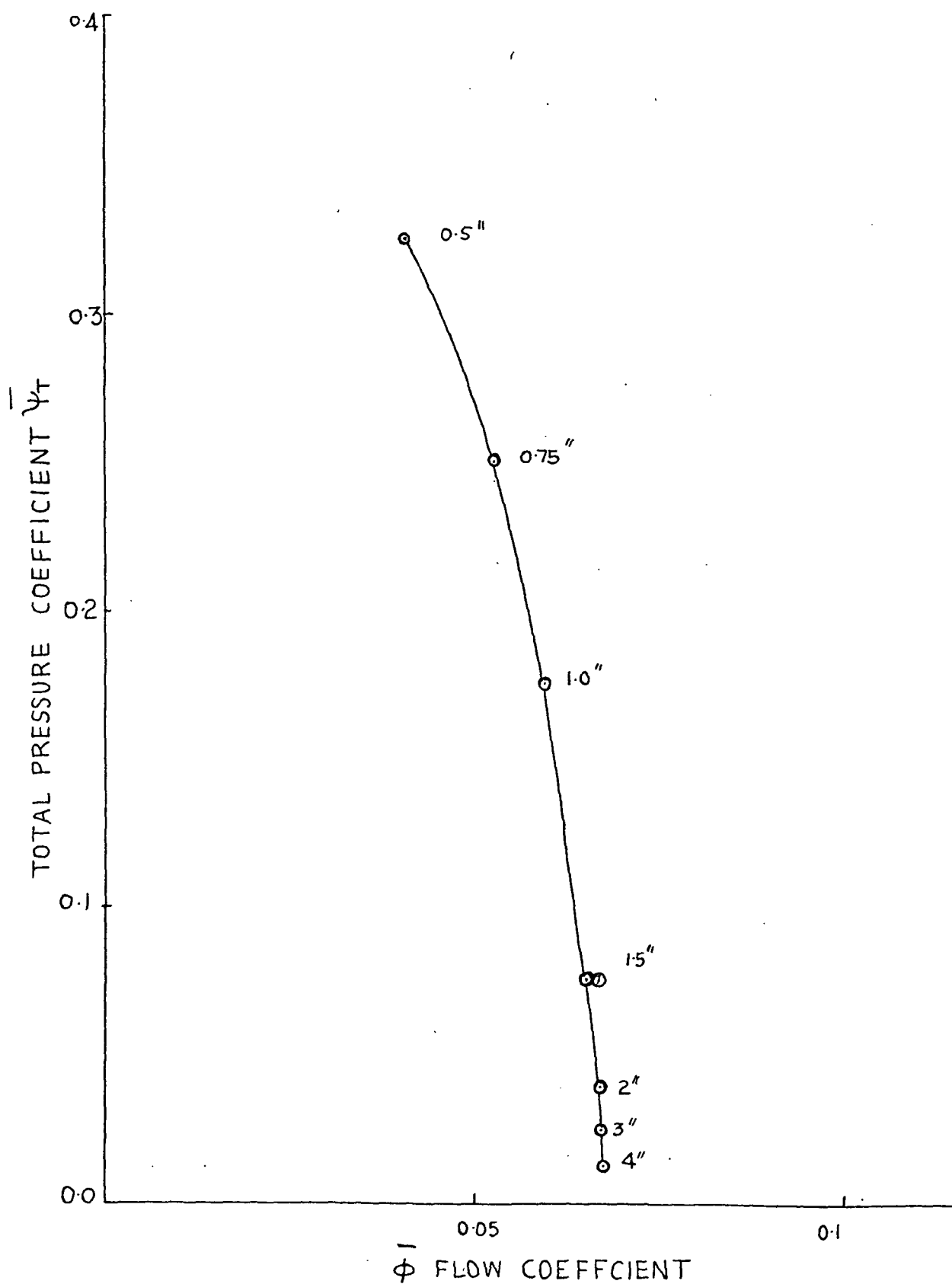
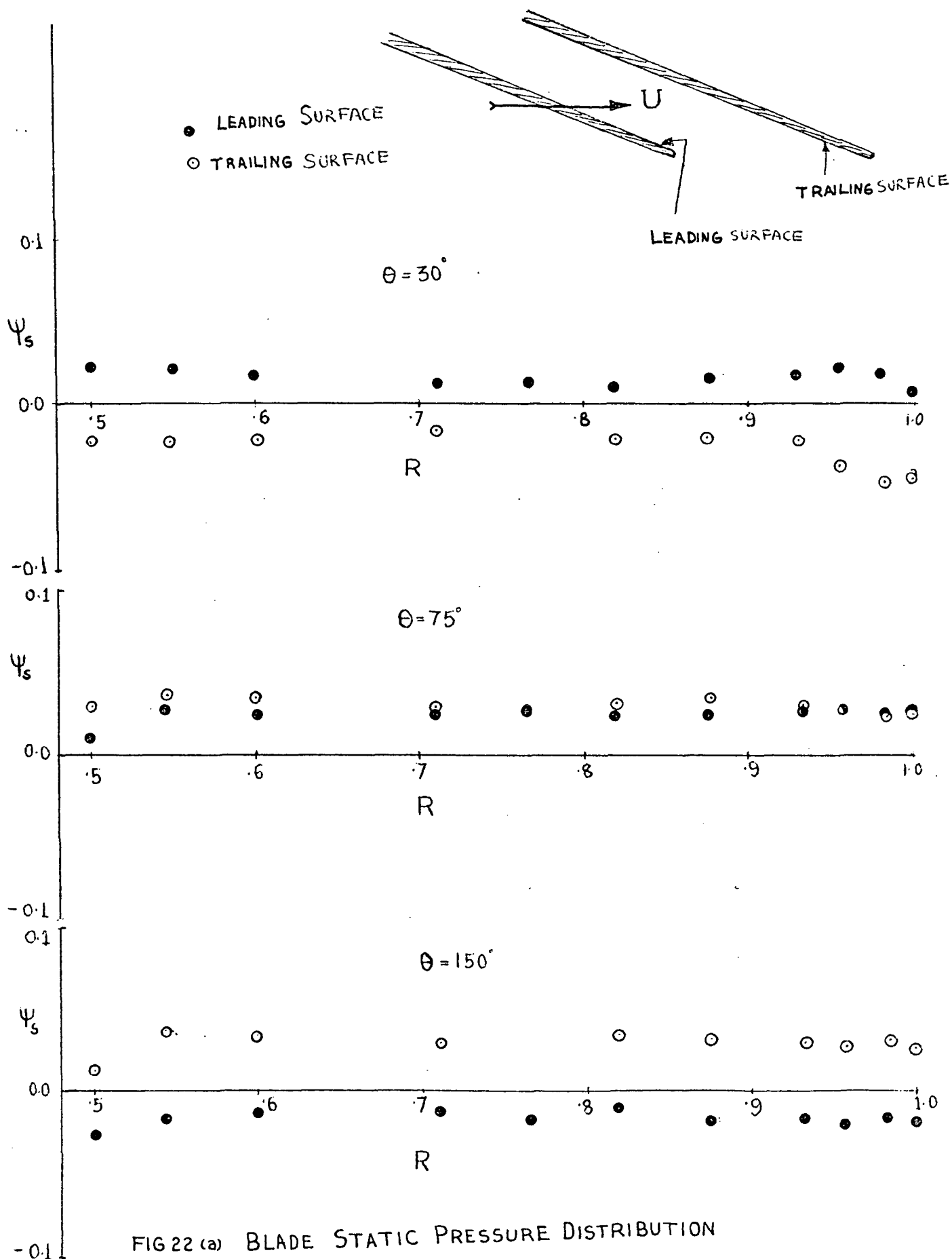
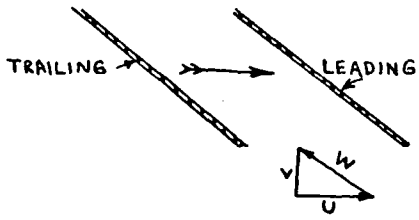


FIG 21 PERFORMANCE CHARACTERISTICS OF 4-BLADED INDUCER





● LEADING SURFACE

○ TRAILING SURFACE

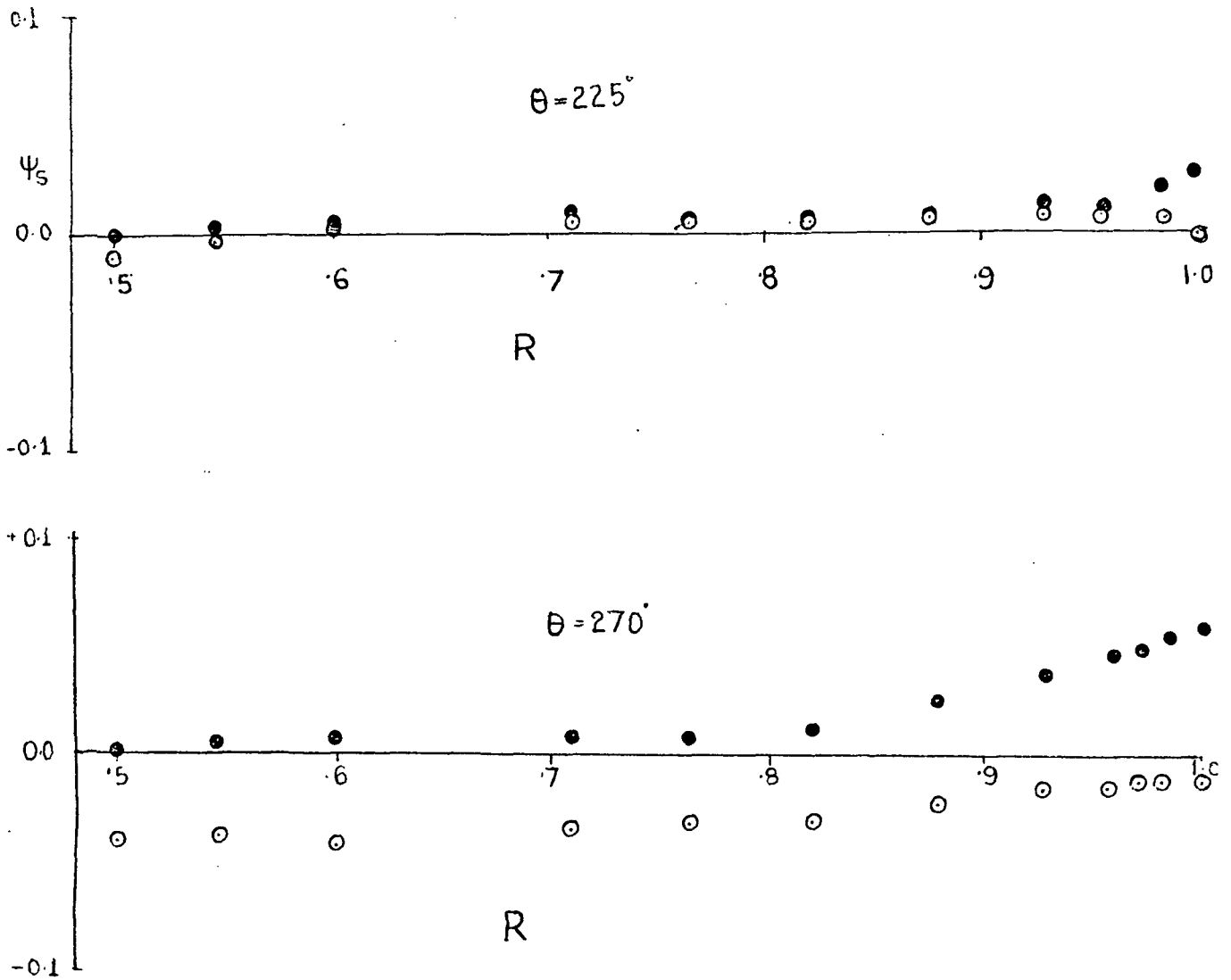
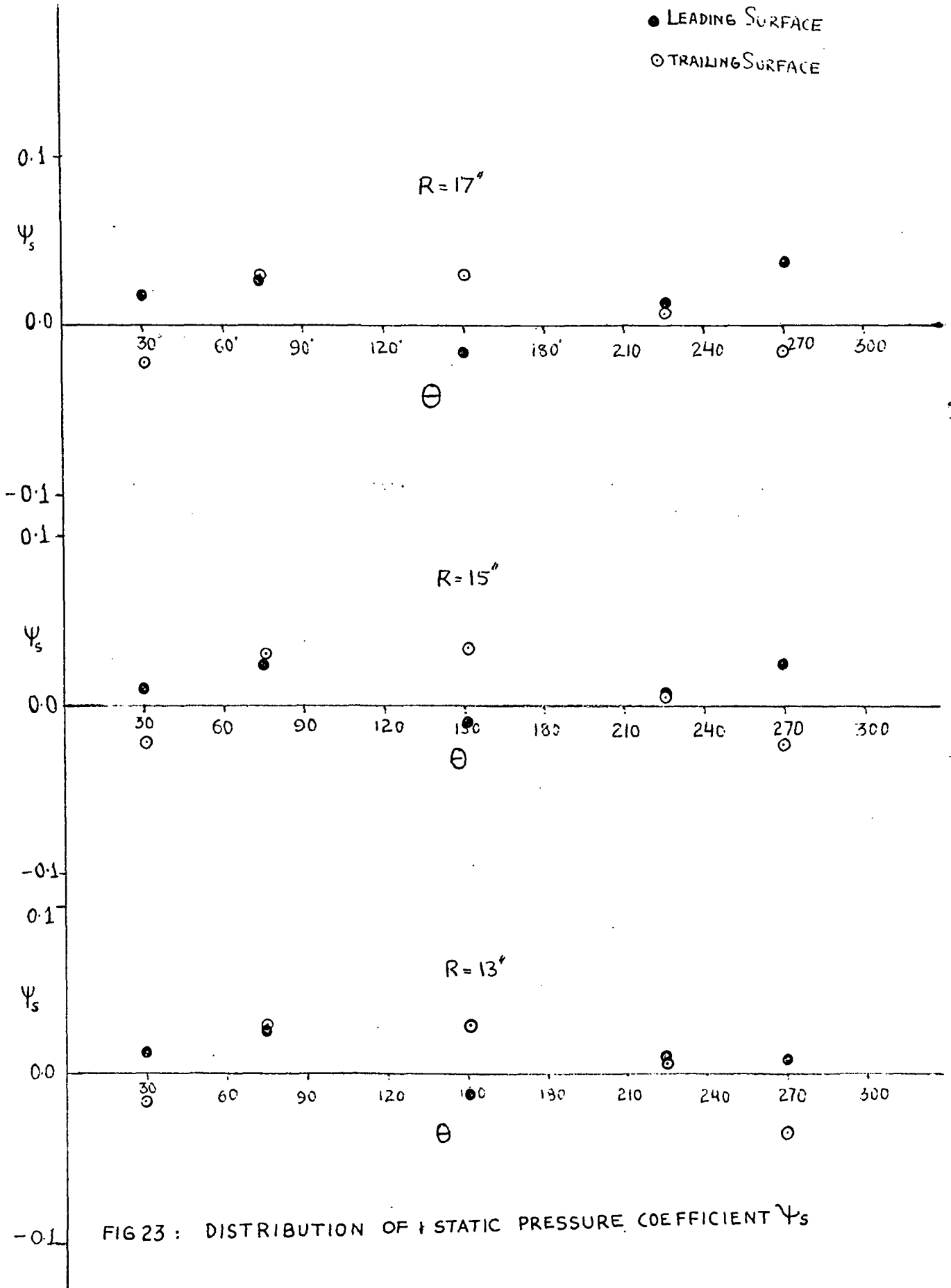


FIG 22(b) BLADE STATIC PRESSURE DISTRIBUTION



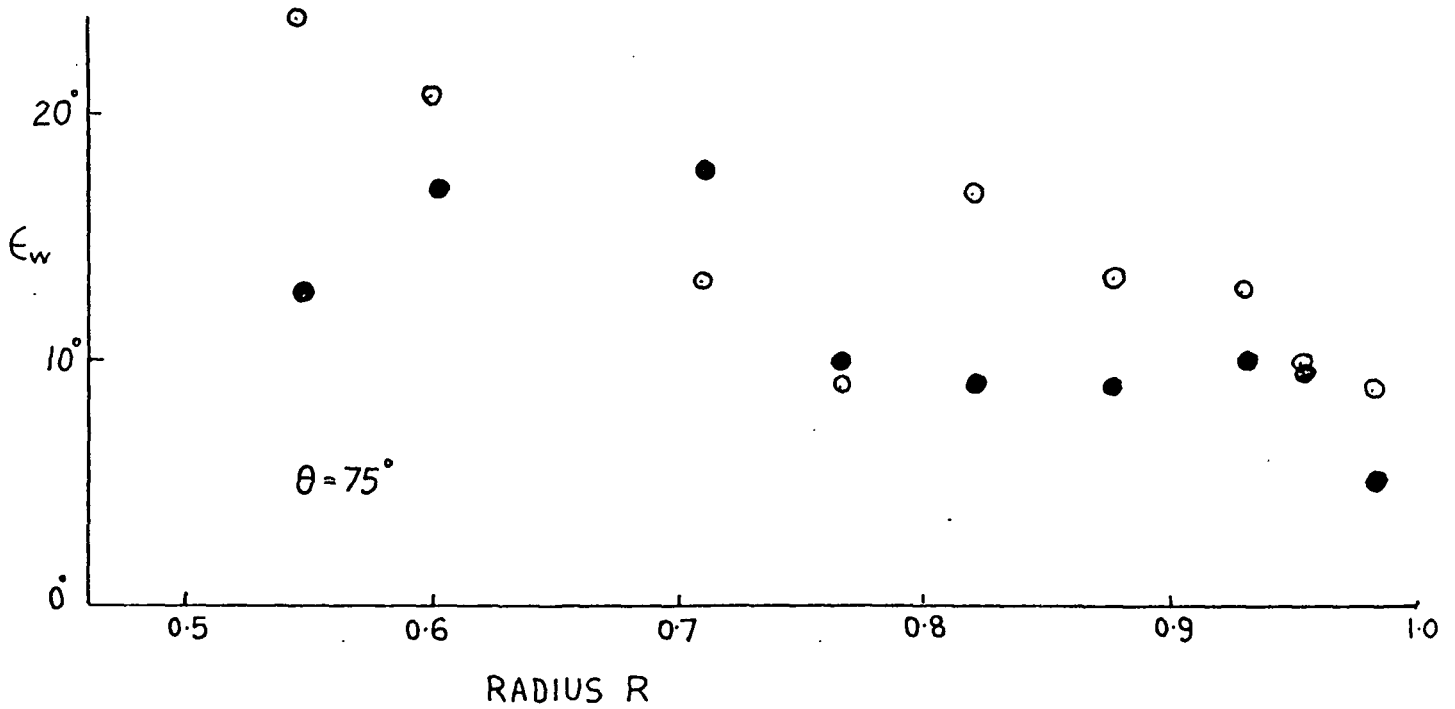
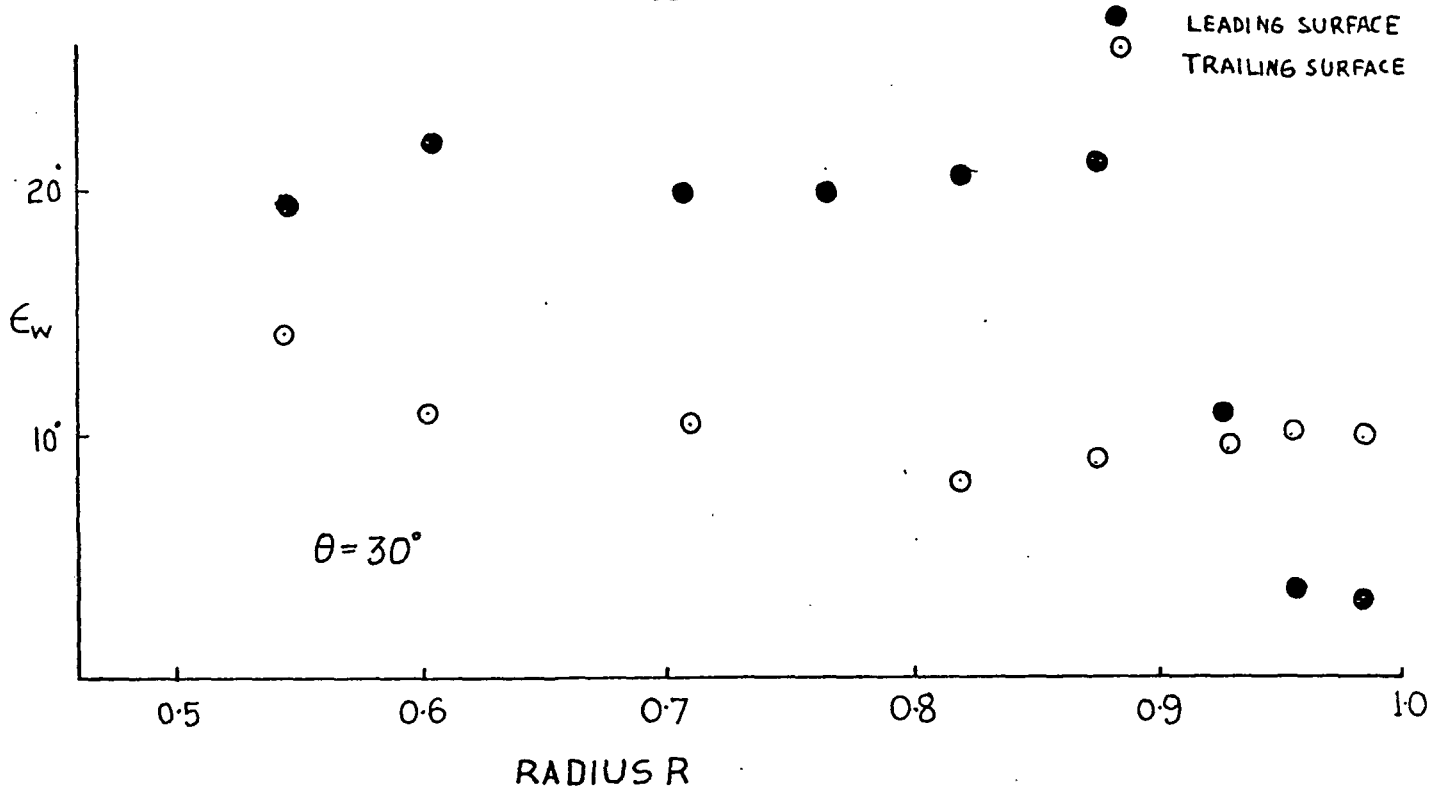


FIG 24(a) RADIAL VARIATION OF LIMITING STREAMLINE ANGLE  $\epsilon_w$

● LEADING SURFACE  
○ TRAILING SURFACE

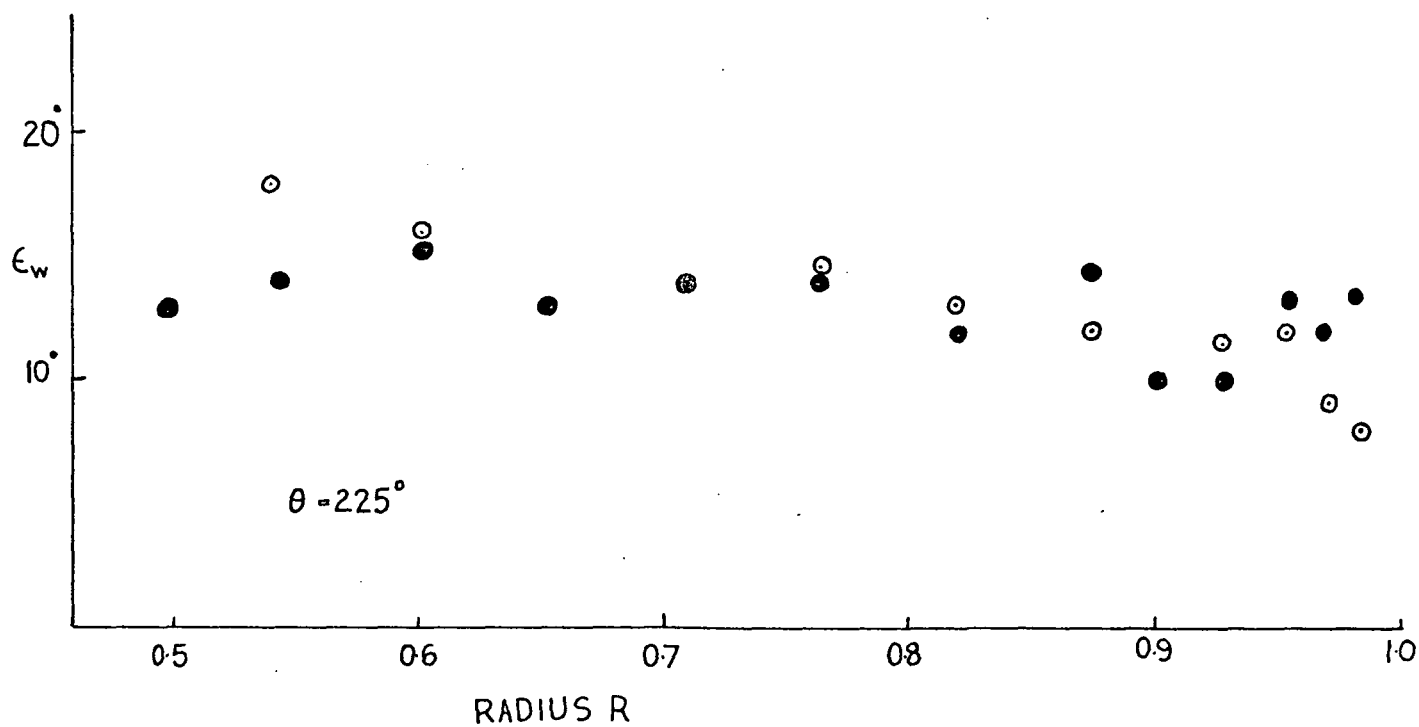
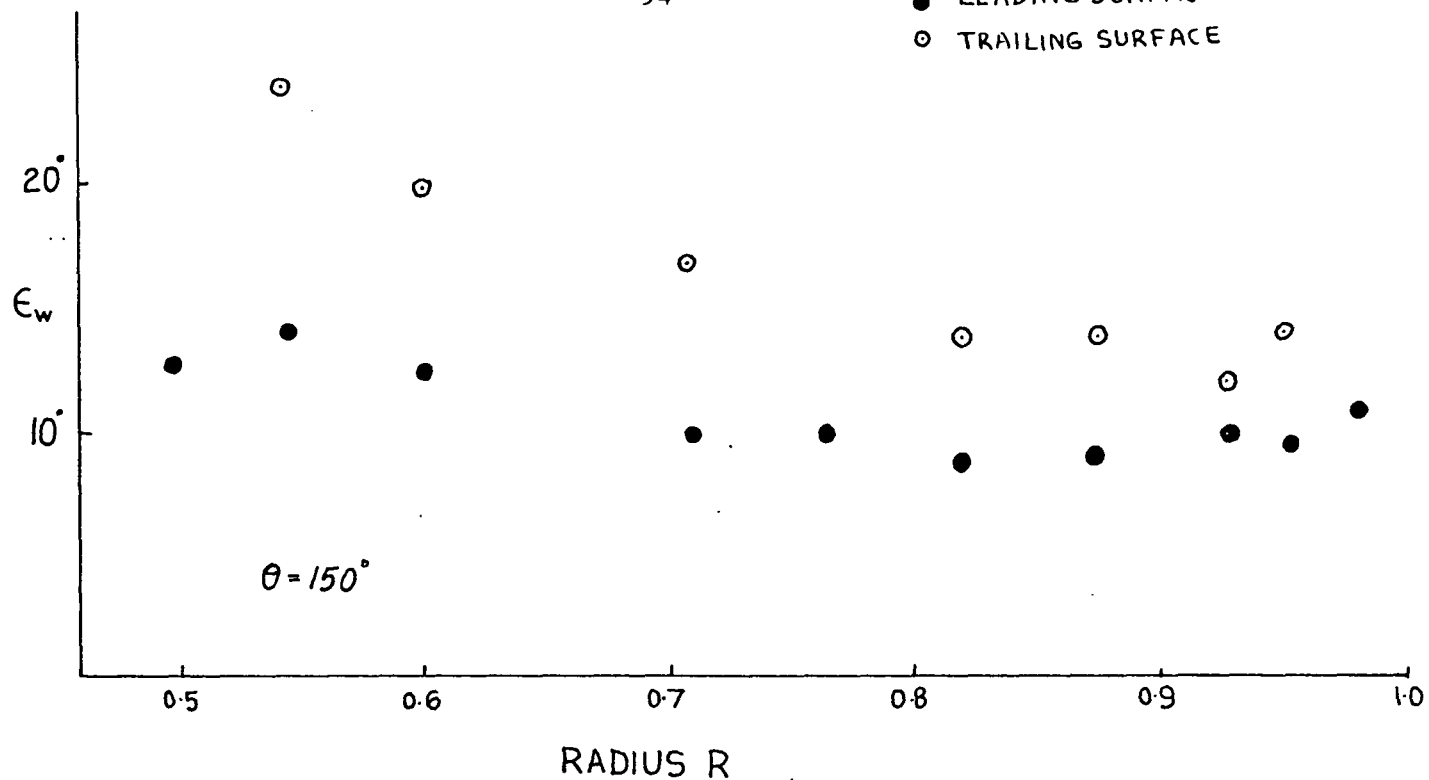


FIG 24(b) RADIAL VARIATION OF LIMITING STREAMLINE ANGLE  $\epsilon_w$

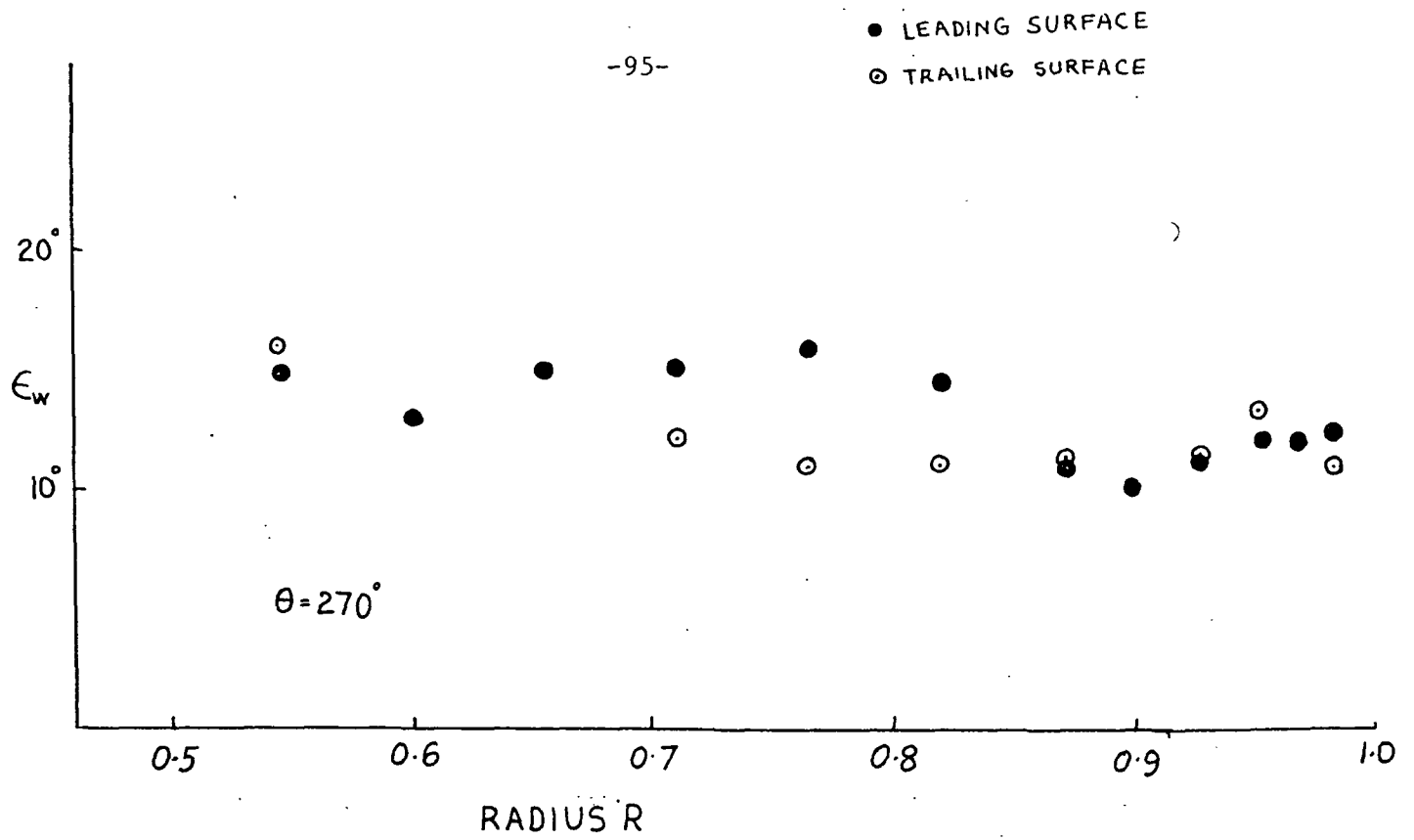


FIG 24(c) RADIAL VARIATION OF LIMITING STREAMLINE ANGLE  $\epsilon_w$



FIG 25(a) CHORDWISE VARIATION OF LIMITING STREAMLINE ANGLE  $\epsilon_w$

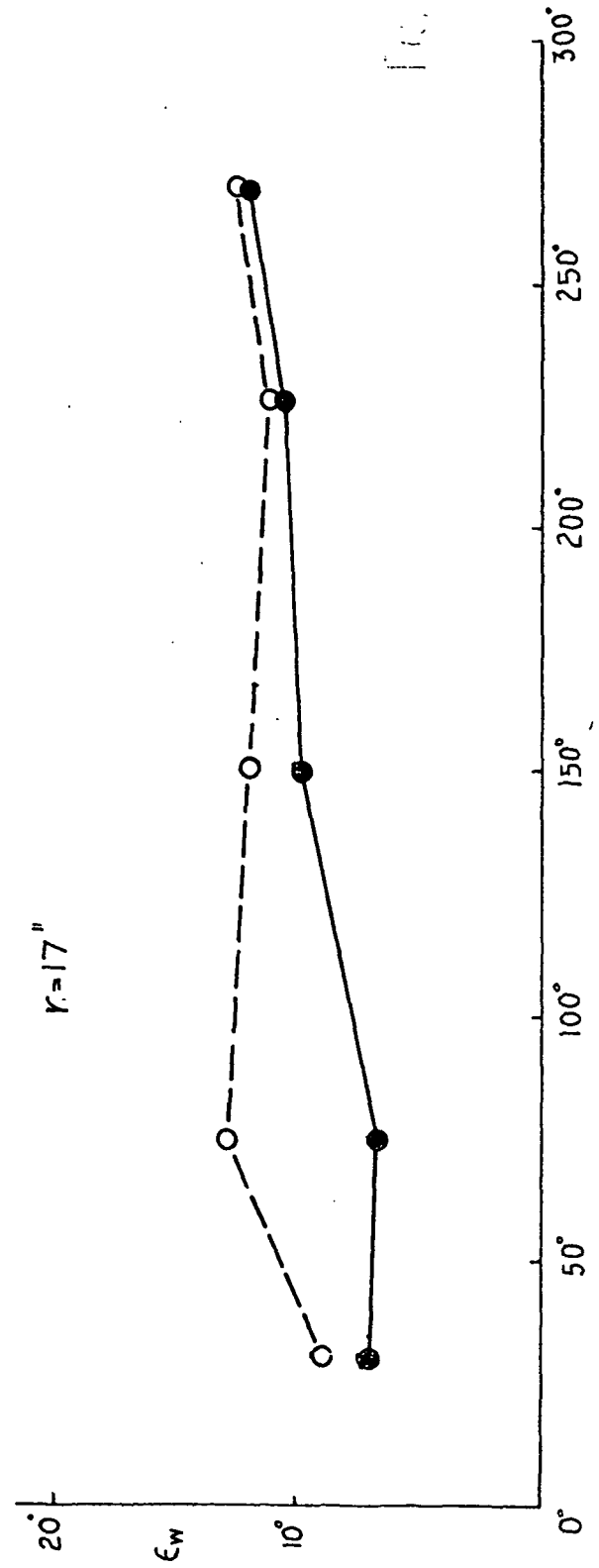
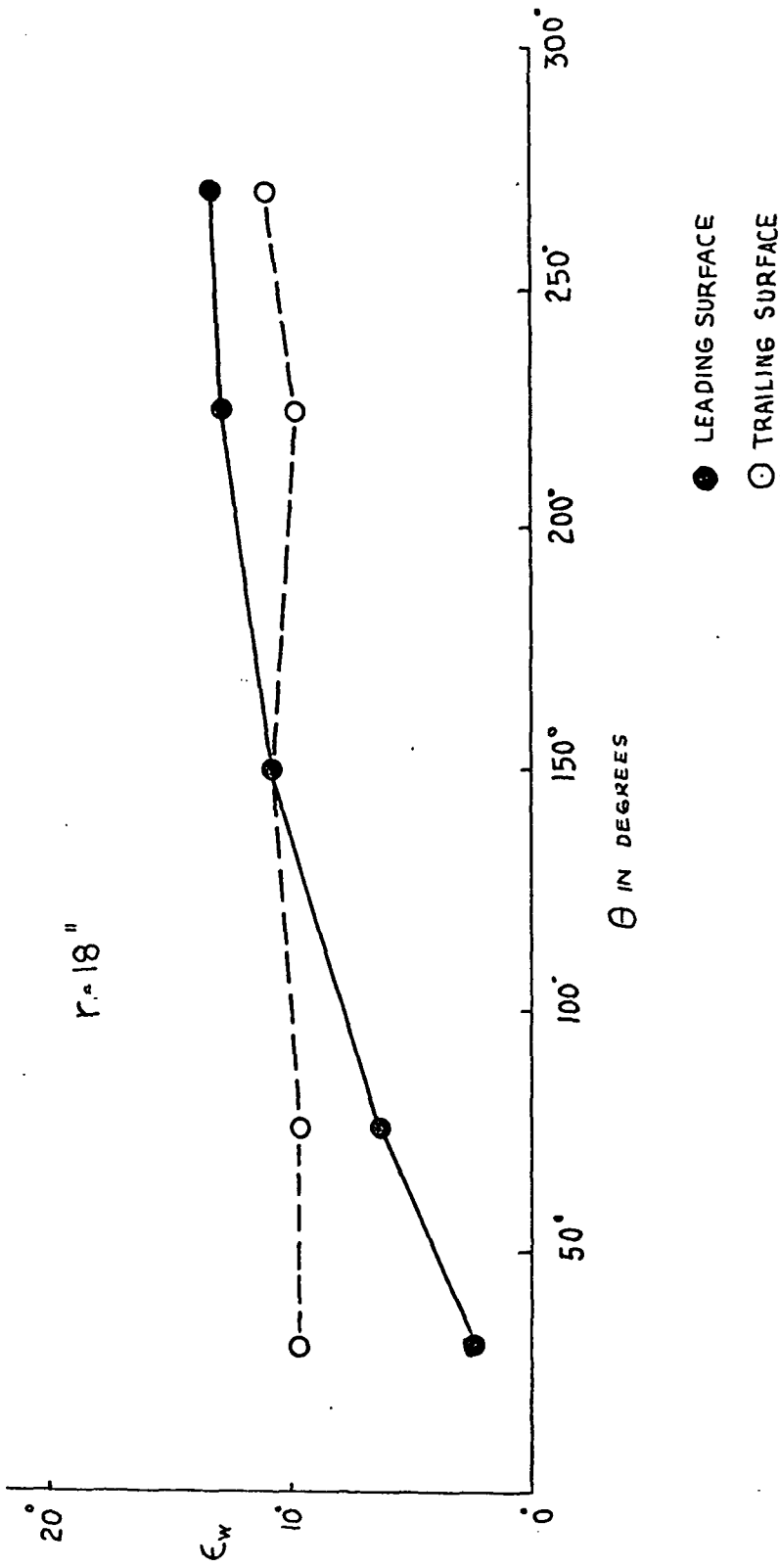


FIG 25

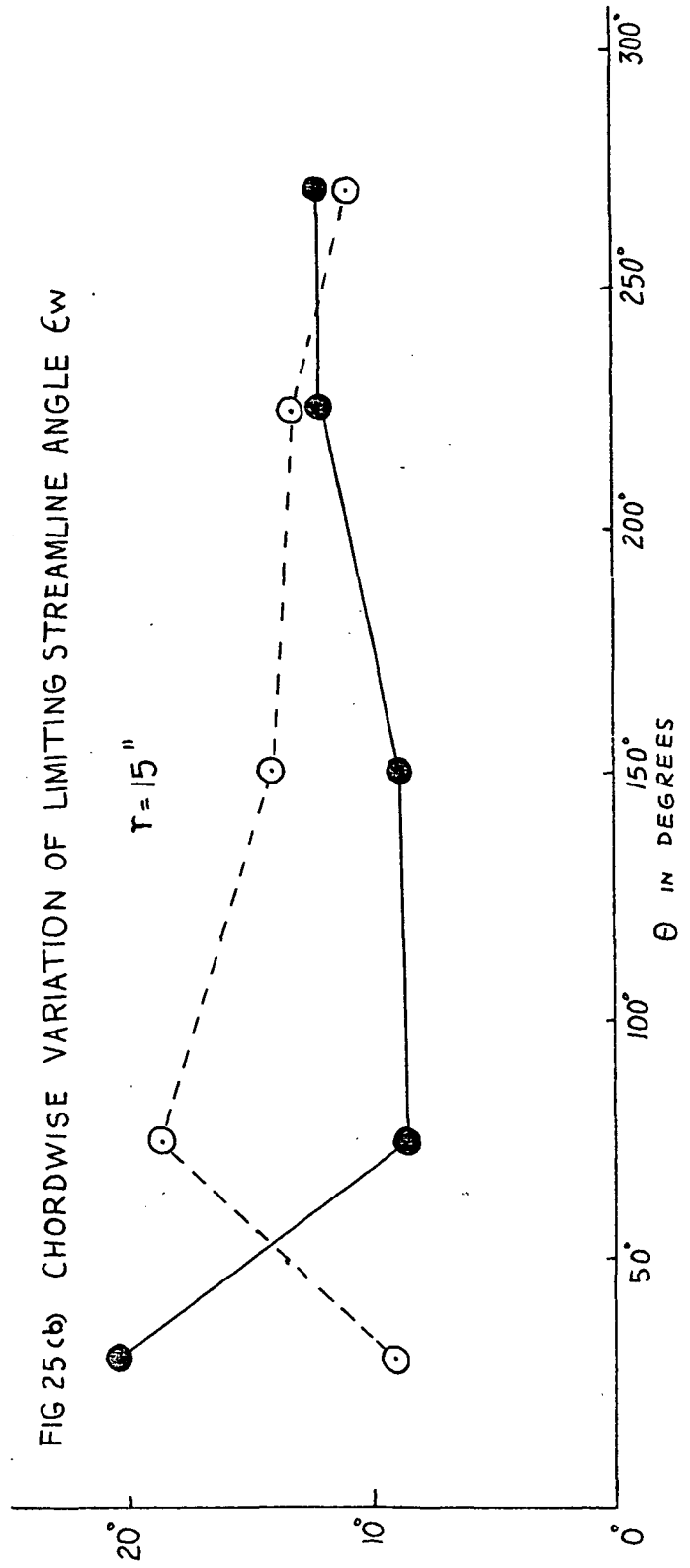
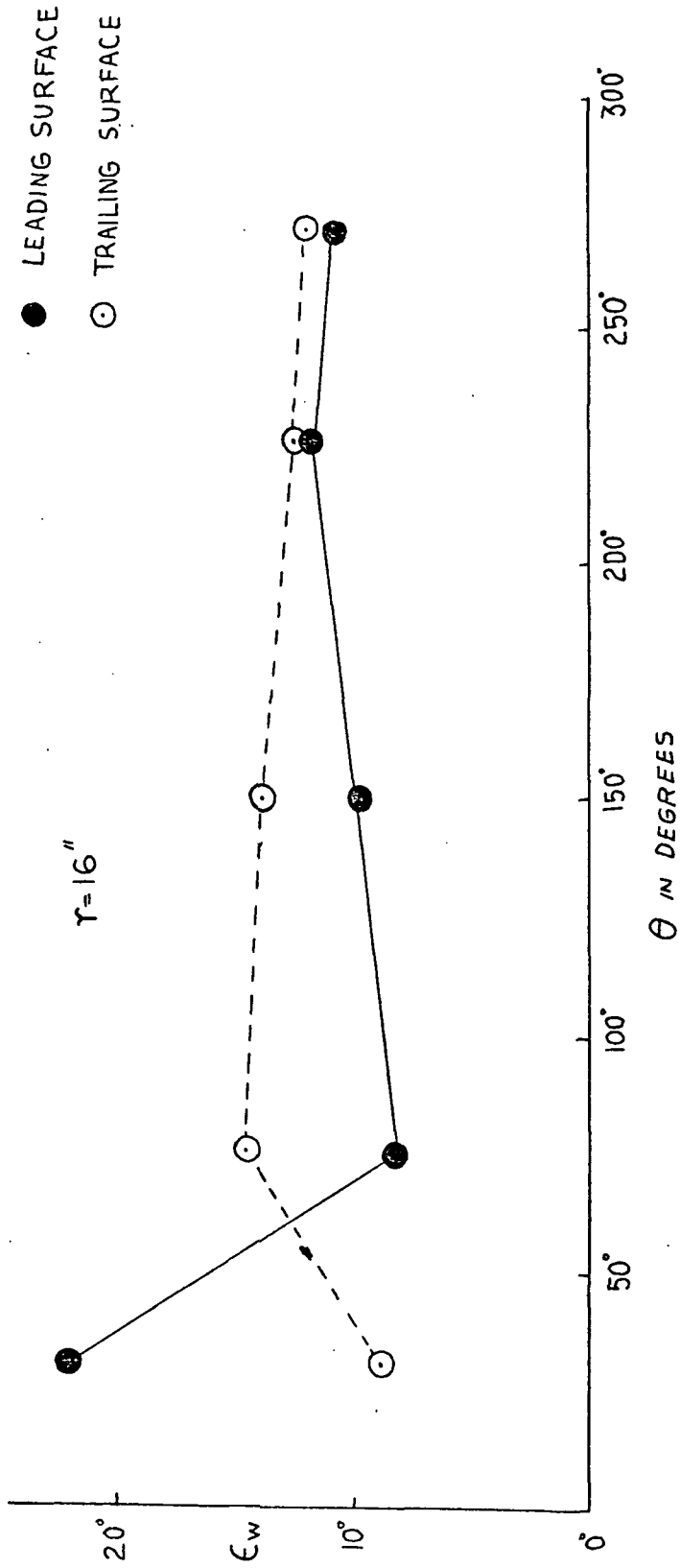


FIG 25(b) CHORDWISE VARIATION OF LIMITING STREAMLINE ANGLE  $\epsilon_w$

FIGURE 25b

FIG25(c) CHORDWISE DISTRIBUTION OF LIMITING STREAMLINE ANGLE  $\epsilon_w$

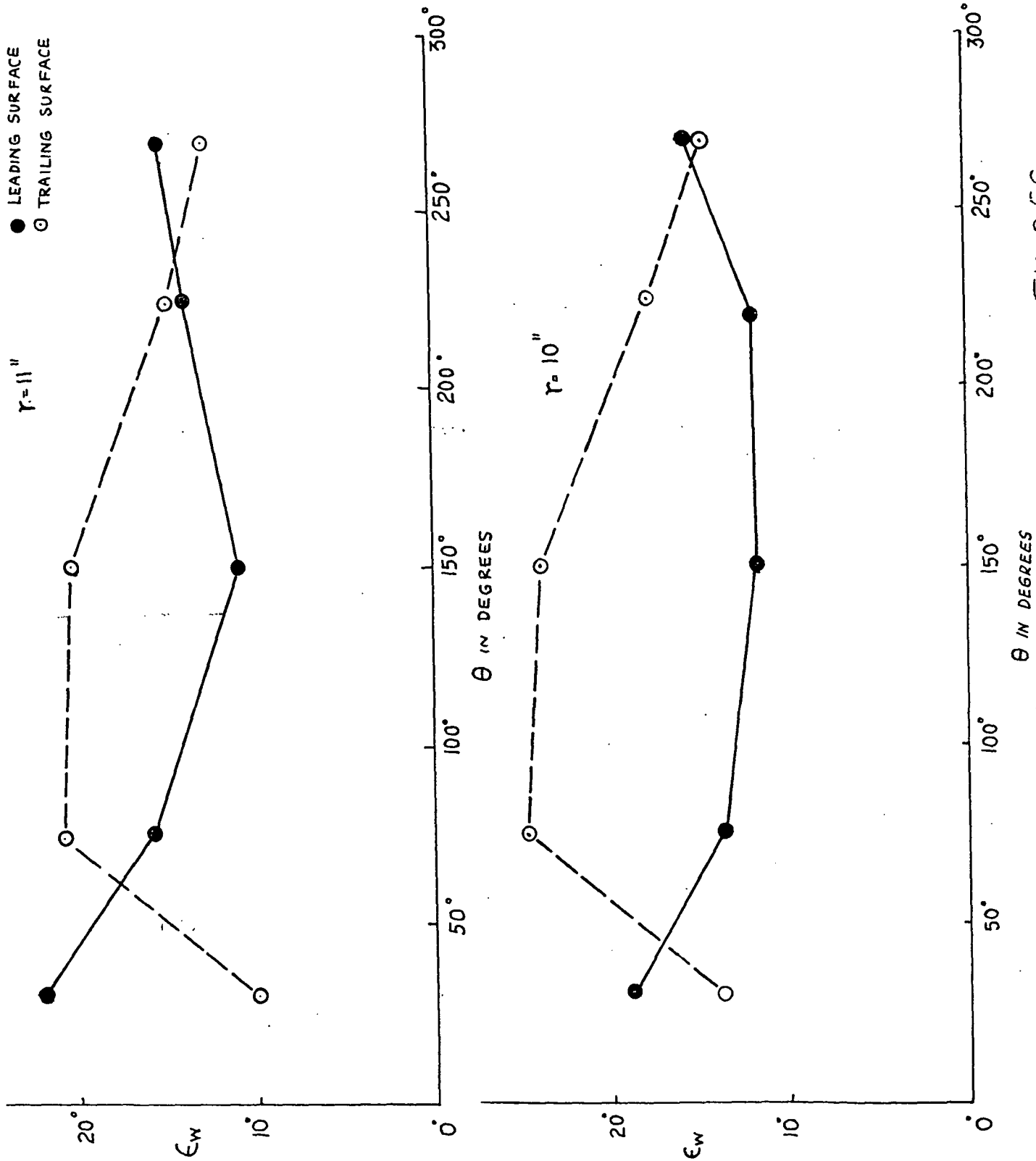


FIG 25C

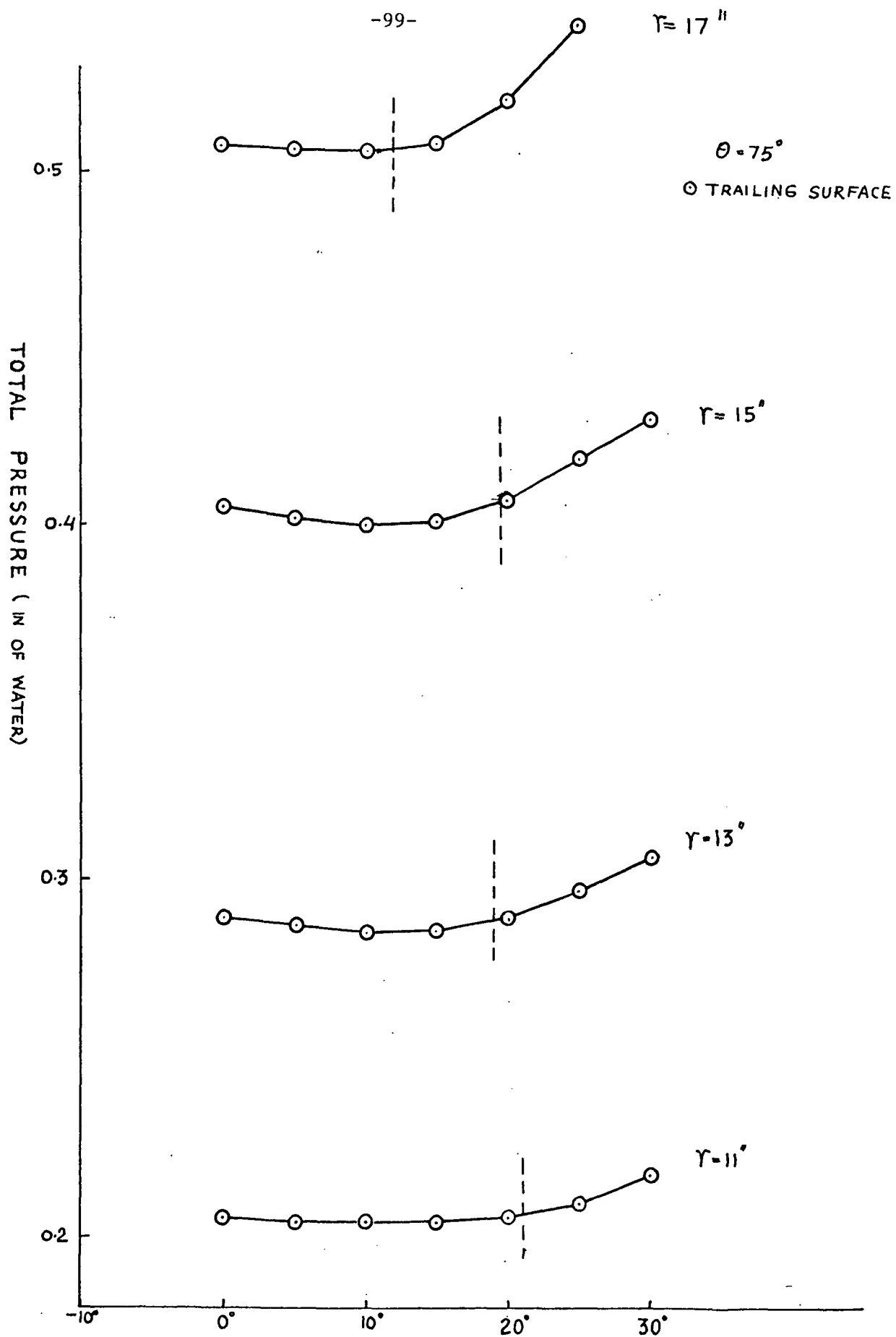


FIG26: VARIATION OF TOTAL PRESSURE WITH PROBE ANGLE

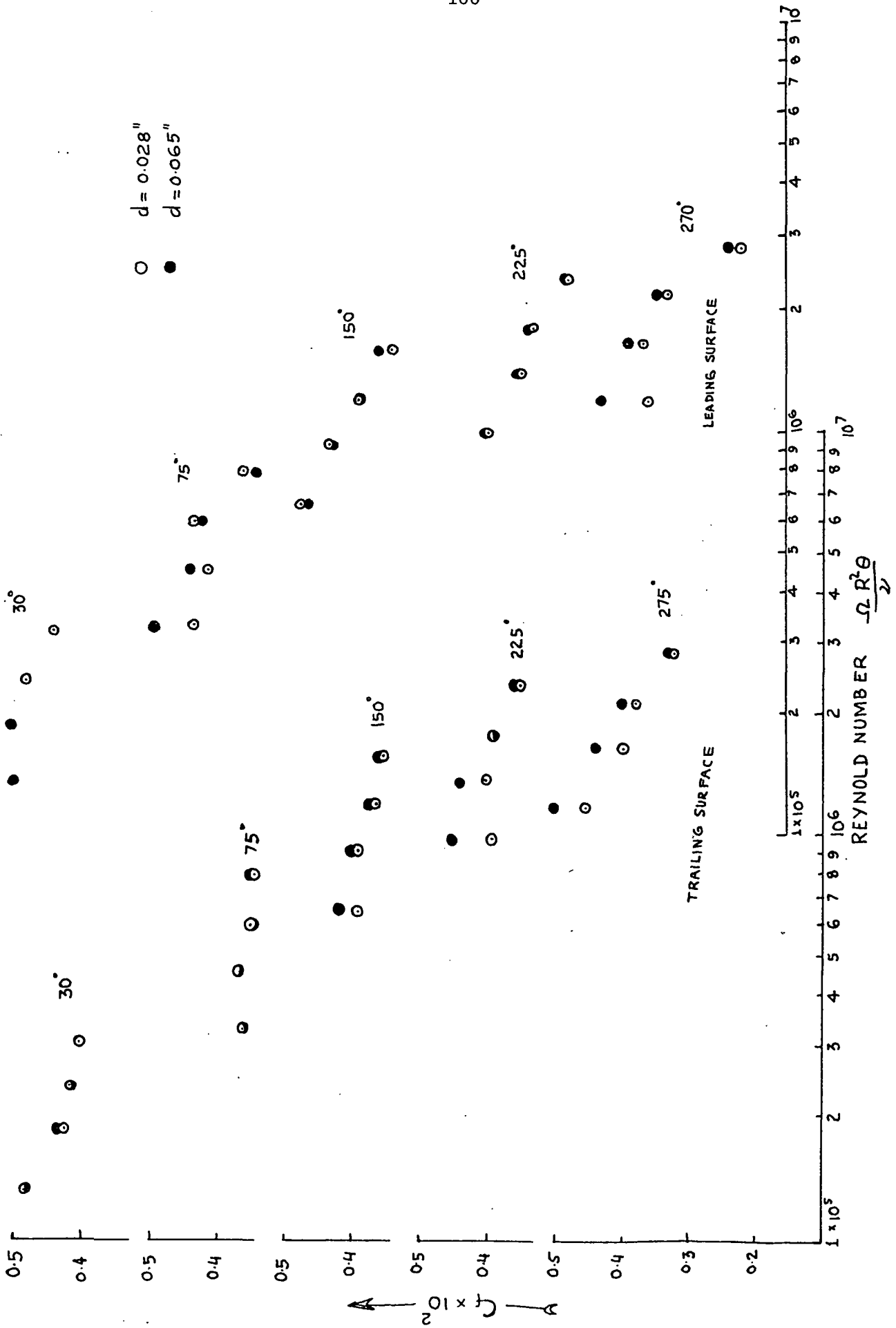


FIG27: VARIATION OF SKIN FRICTION COEFFICIENT  $C_f$  WITH REYNOLD'S NUMBER

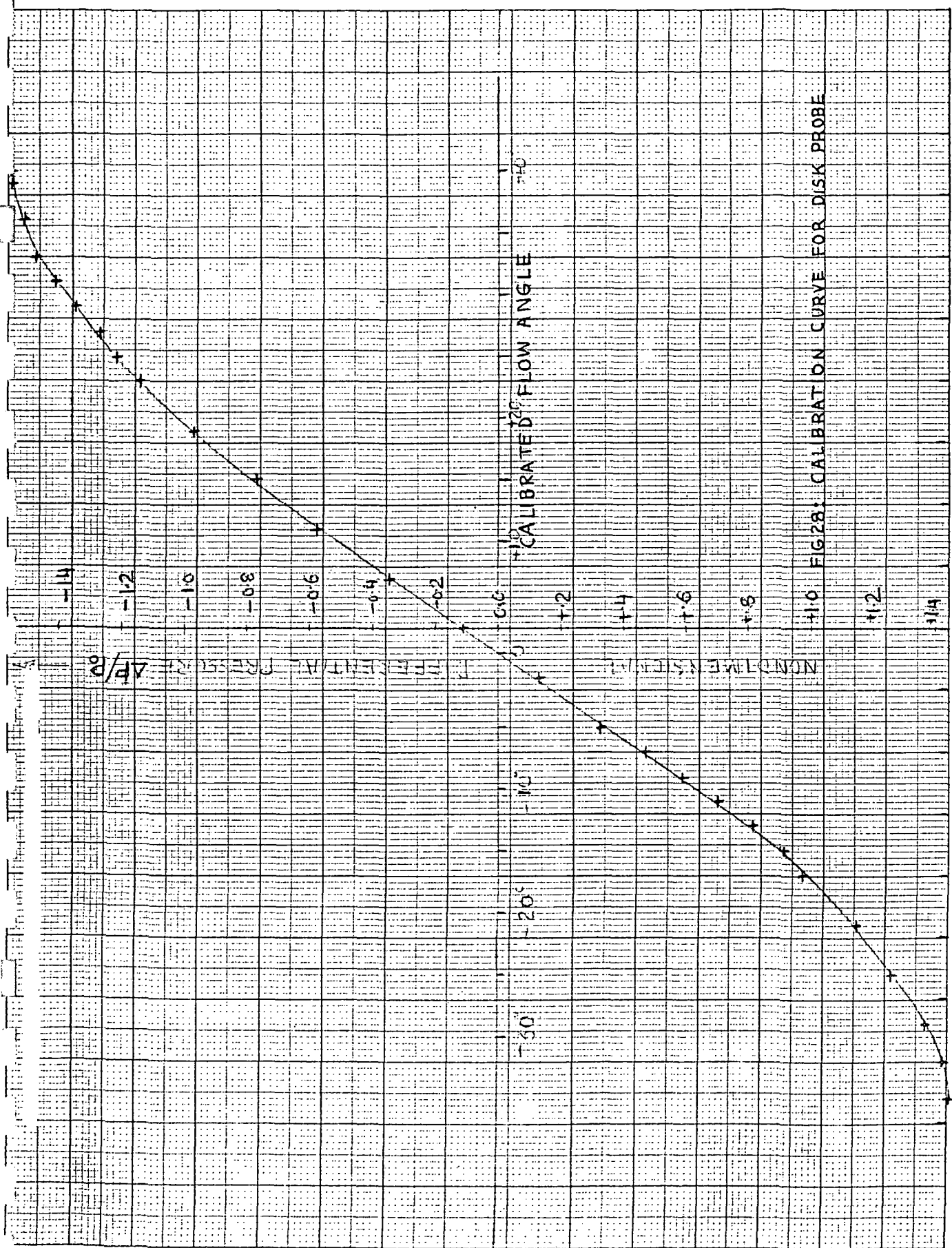


FIG 28: CALIBRATION CURVE FOR DISK PROBE

INDICATED FLOW ANGLE

GRAPH PAPER

W. B. M. 101

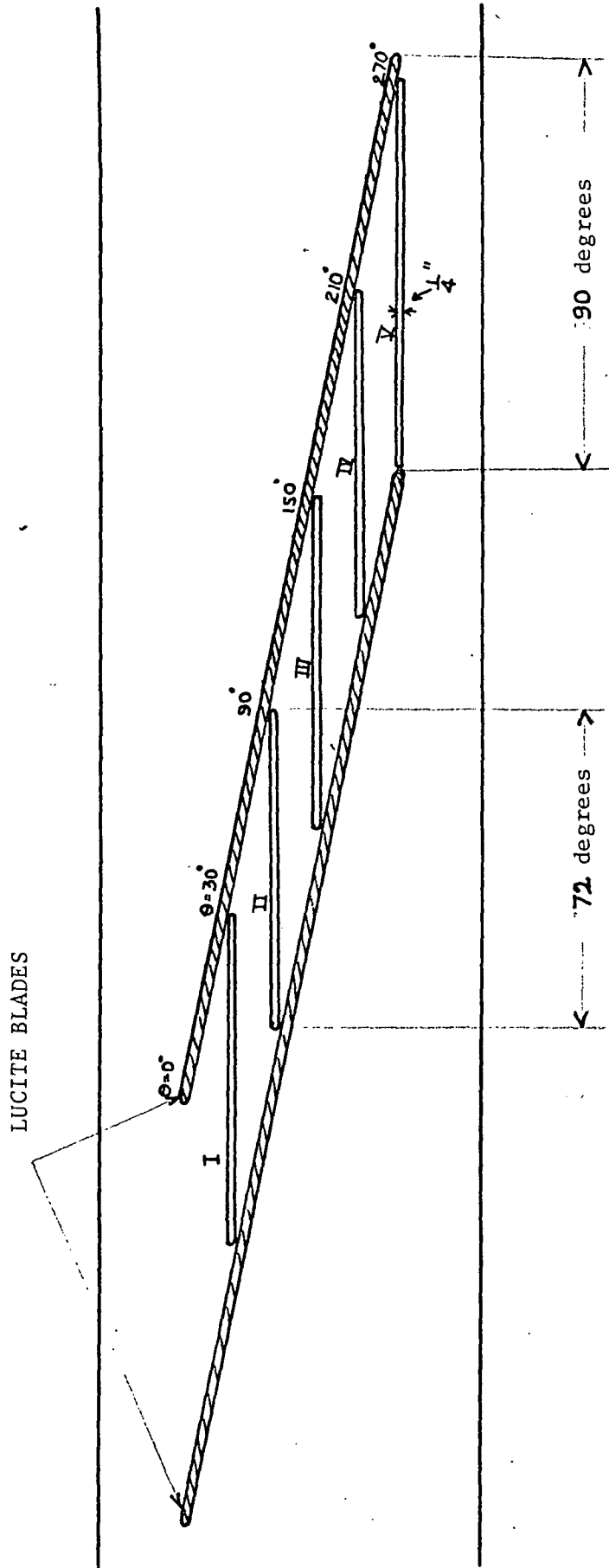


Figure 29: Developed view of the hub

NONDIMENSIONAL VELOCITY  $U/U_*$

-103-

$R=0.98$

$R=0.93$

$R=0.86$

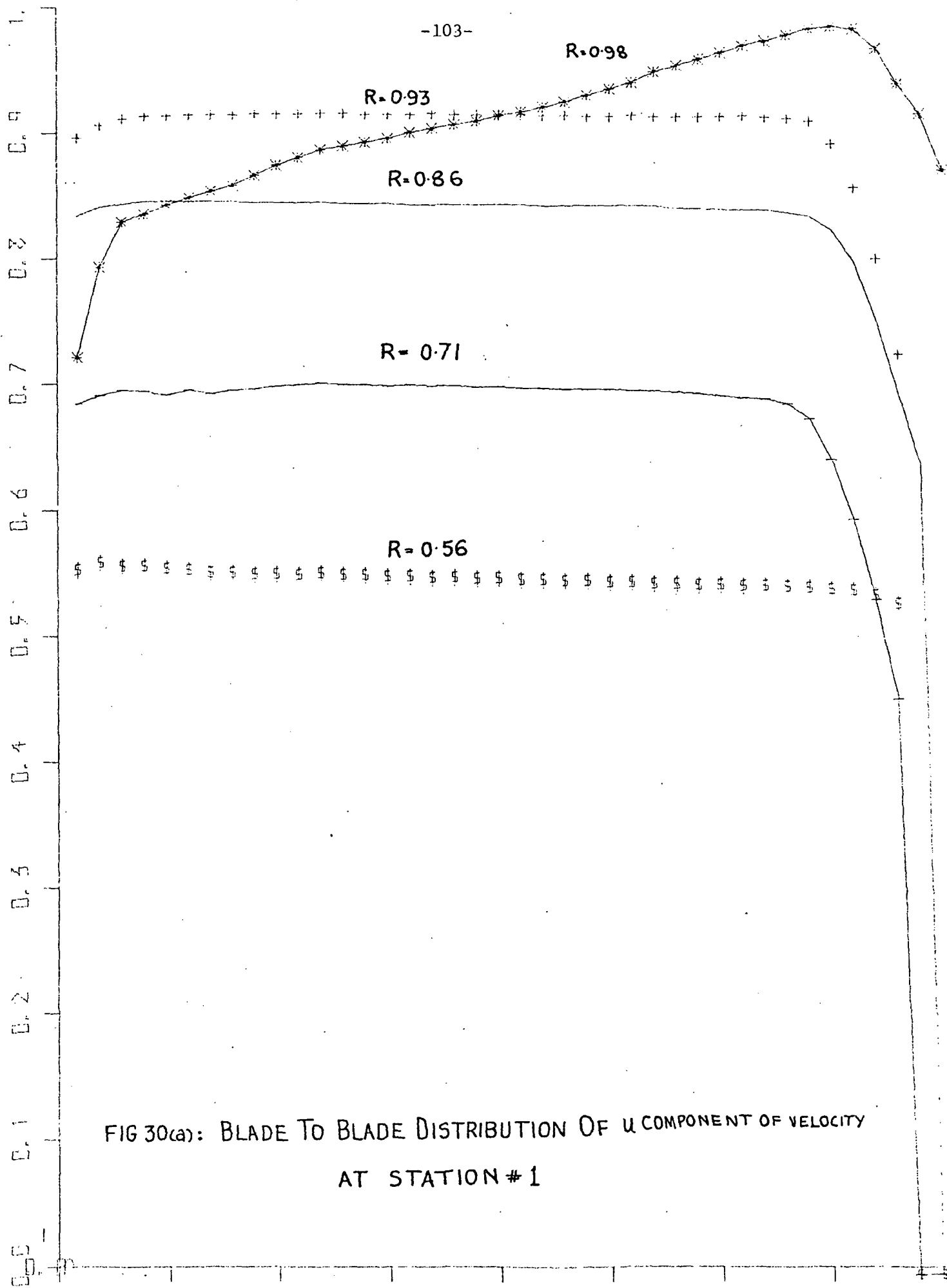
$R=0.71$

$R=0.56$

FIG 30(a): BLADE TO BLADE DISTRIBUTION OF  $u$  COMPONENT OF VELOCITY  
AT STATION #1

0.0 9.0 18.0 27.0 36.0 45.0 54.0 63.0 72.0

TRAILING





NONDIMENSIONAL VELOCITY  $U/U_1$

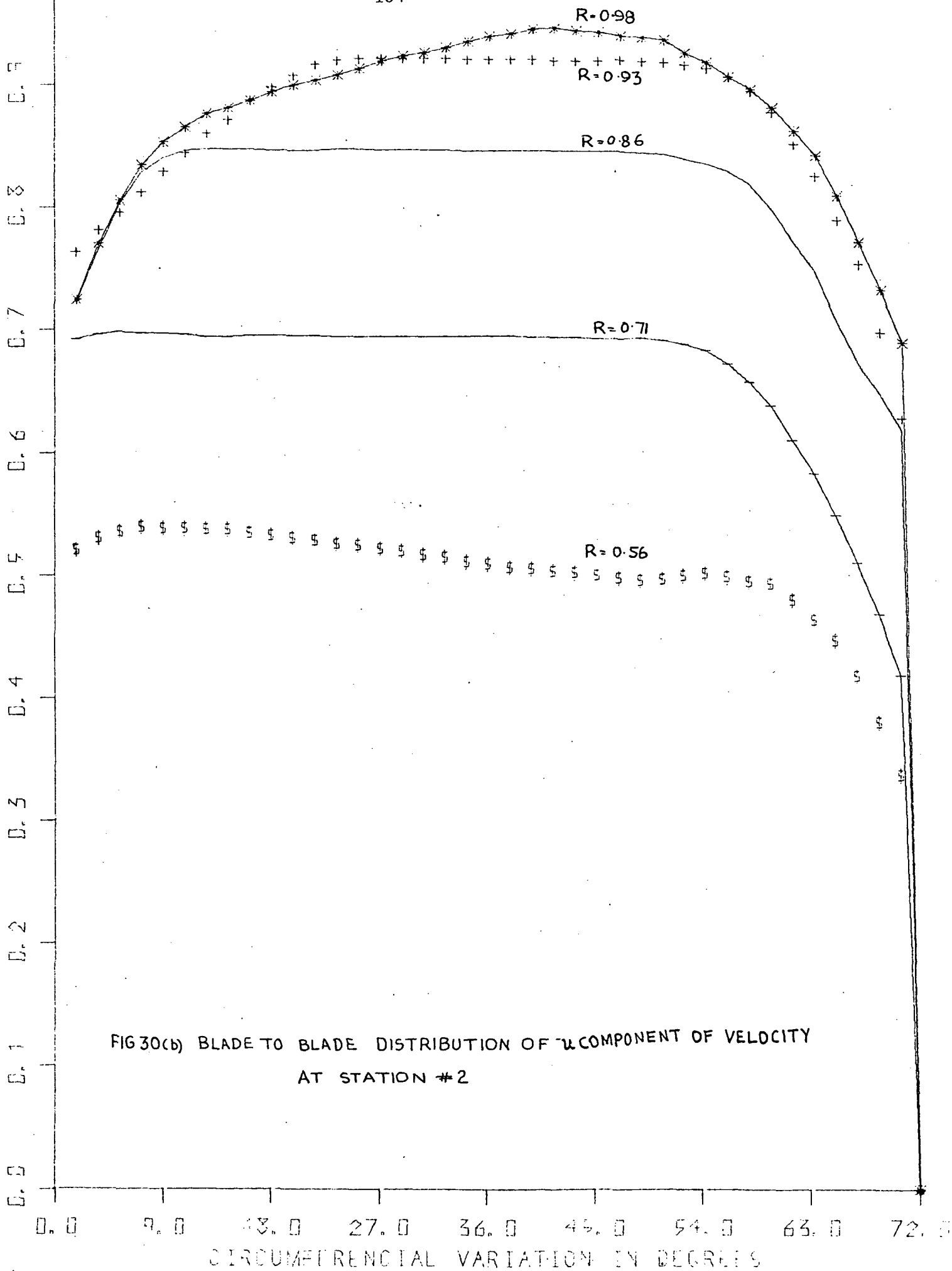
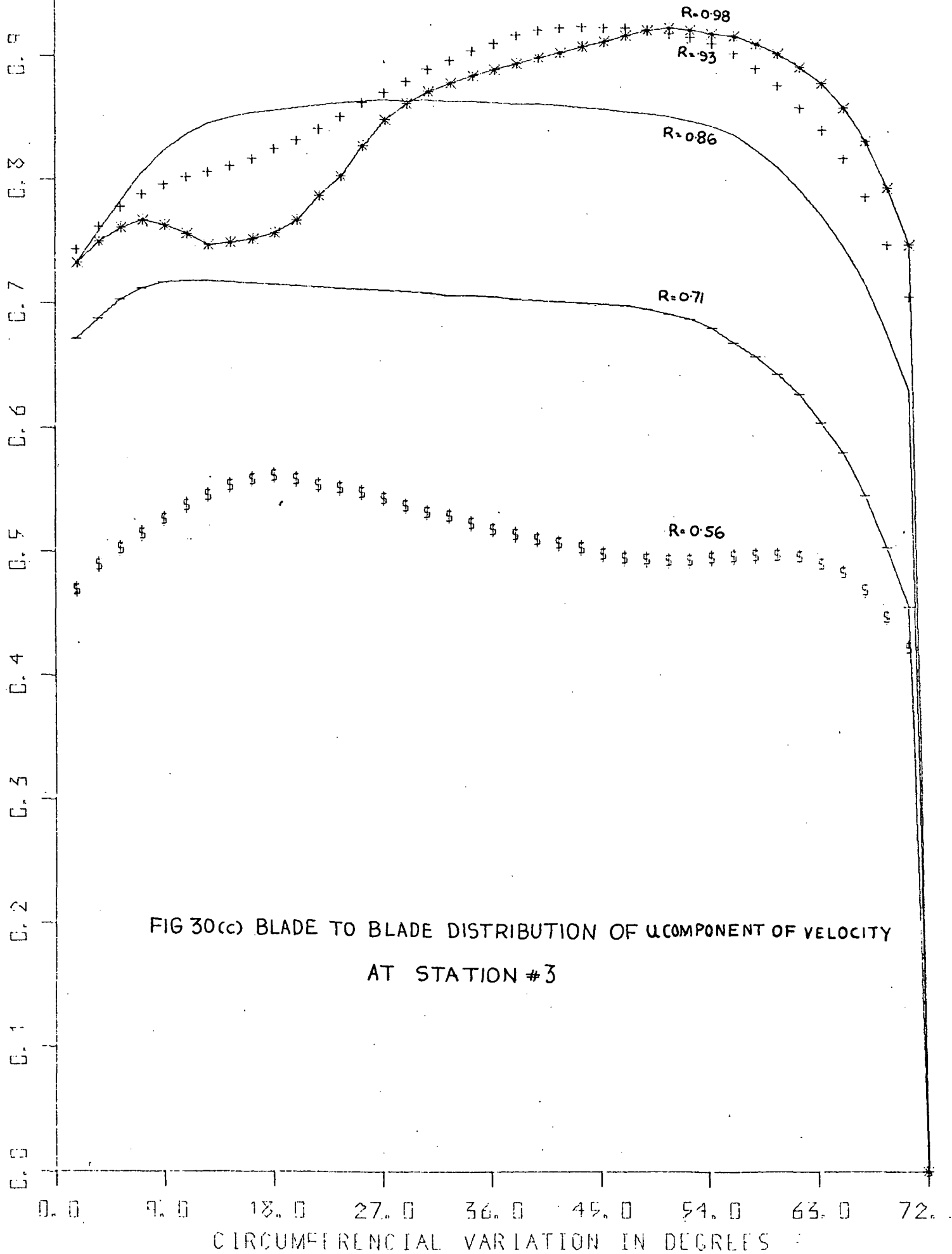
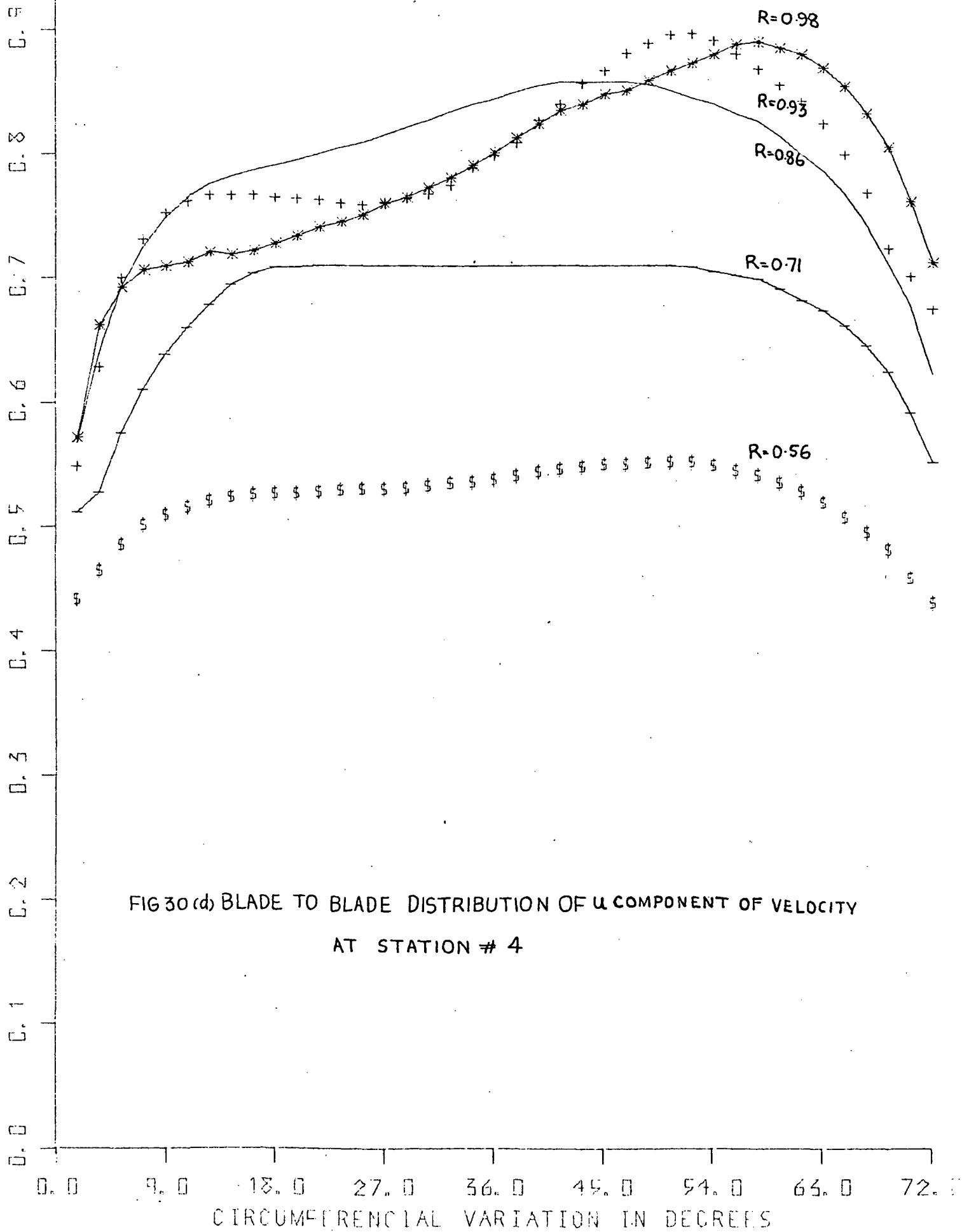


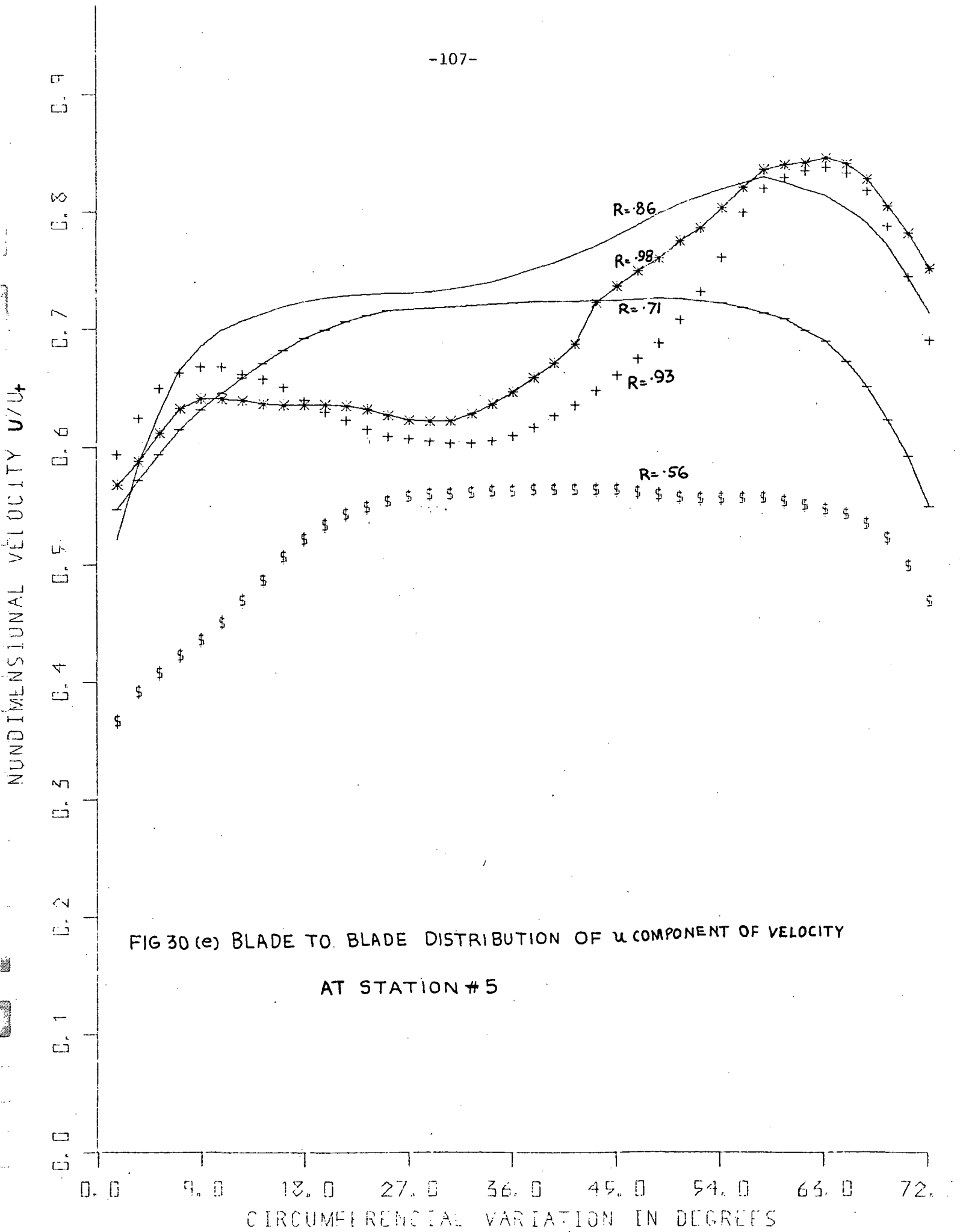
FIG 30(b) BLADE TO BLADE DISTRIBUTION OF  $u$  COMPONENT OF VELOCITY  
AT STATION #2

NUNDIMENSIONAL VELOCITY  $V/U_t$



NON DIMENSIONAL VELOCITY  $V/U_1$





6/2/73 FIG 31(a) COMPARISON OF EXPERIMENTAL VELOCITY PROFILES

WITH "POWER LAW PROFILES"

AT 2<sup>ND</sup> SLOT

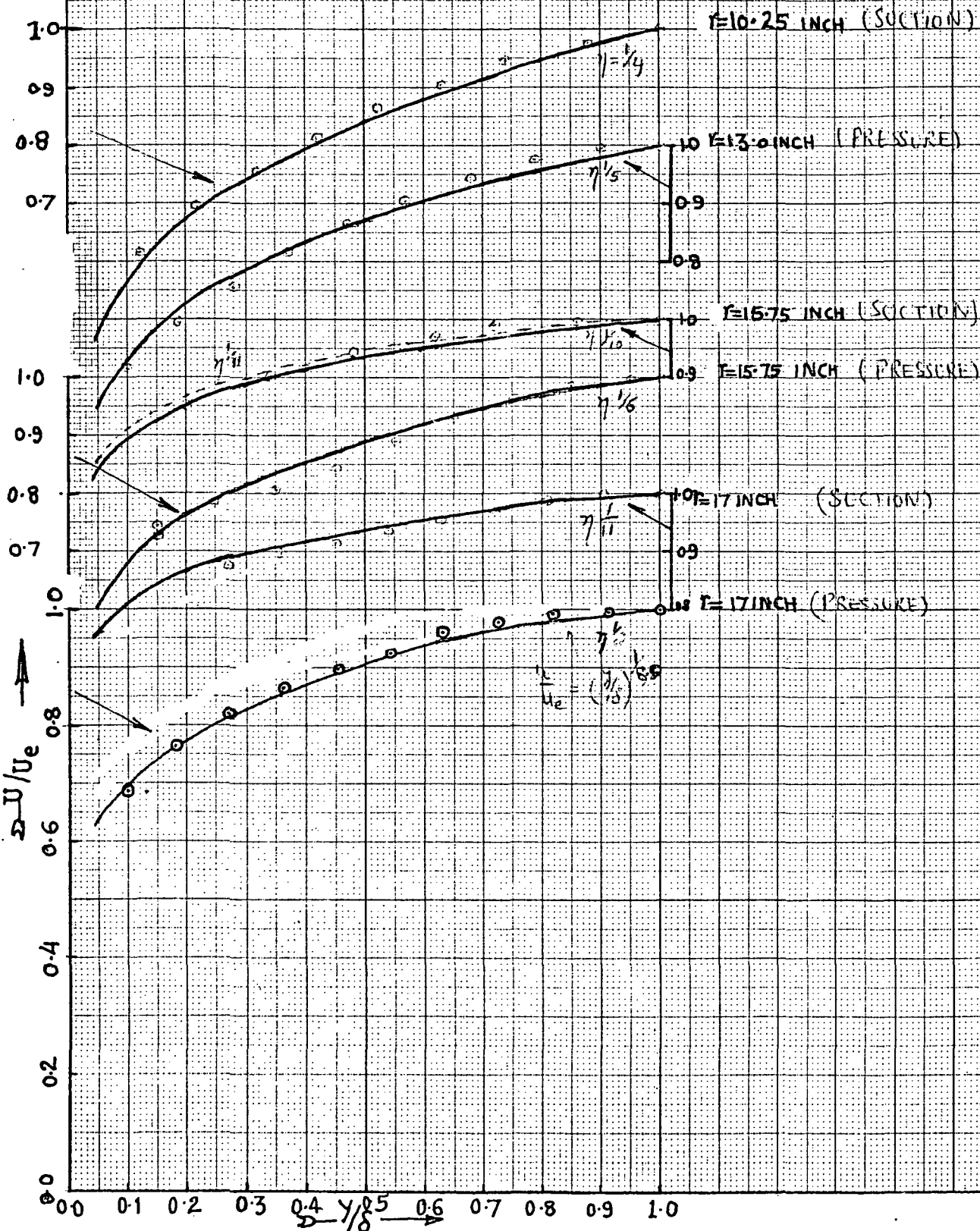


FIG 31(b) COMPARISON OF EXPERIMENTAL VELOCITY PROFILES

POWER LAW PROFILES  
AT STATION # 3

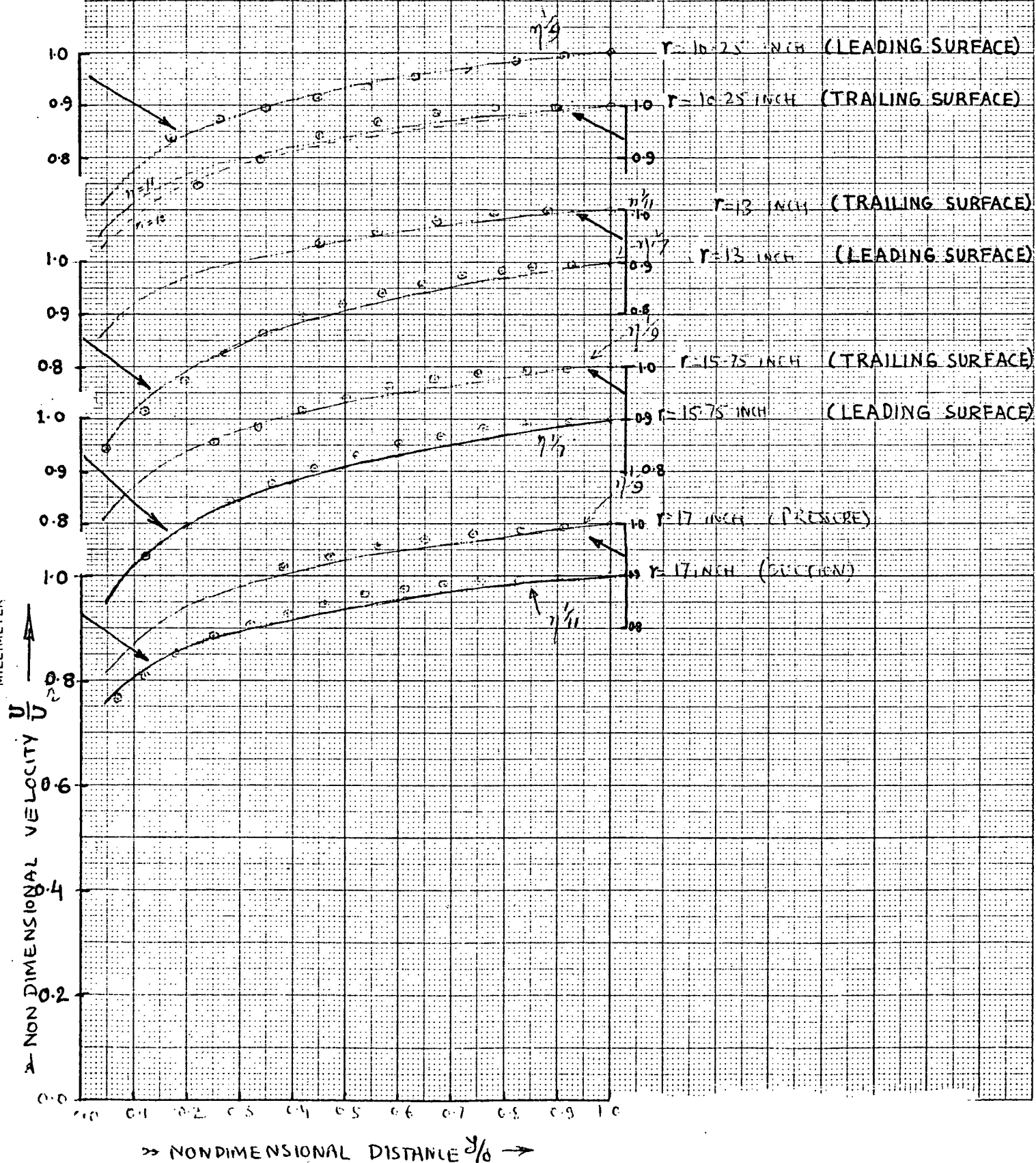


FIG 31 (c) COMPARISON OF EXPERIMENTAL VELOCITY PROFILES

WITH POWER LAW PROFILES AT STATION #4

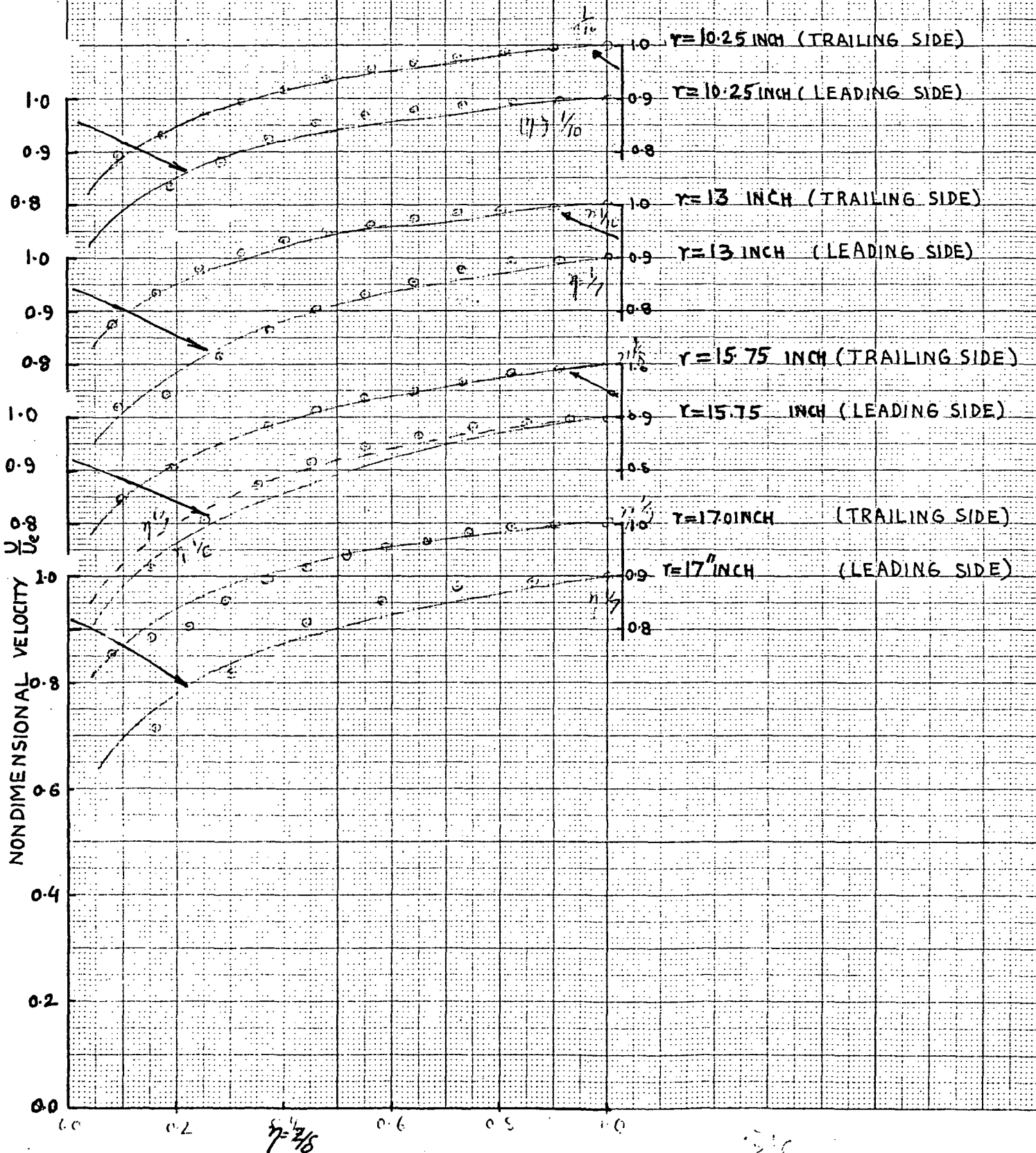
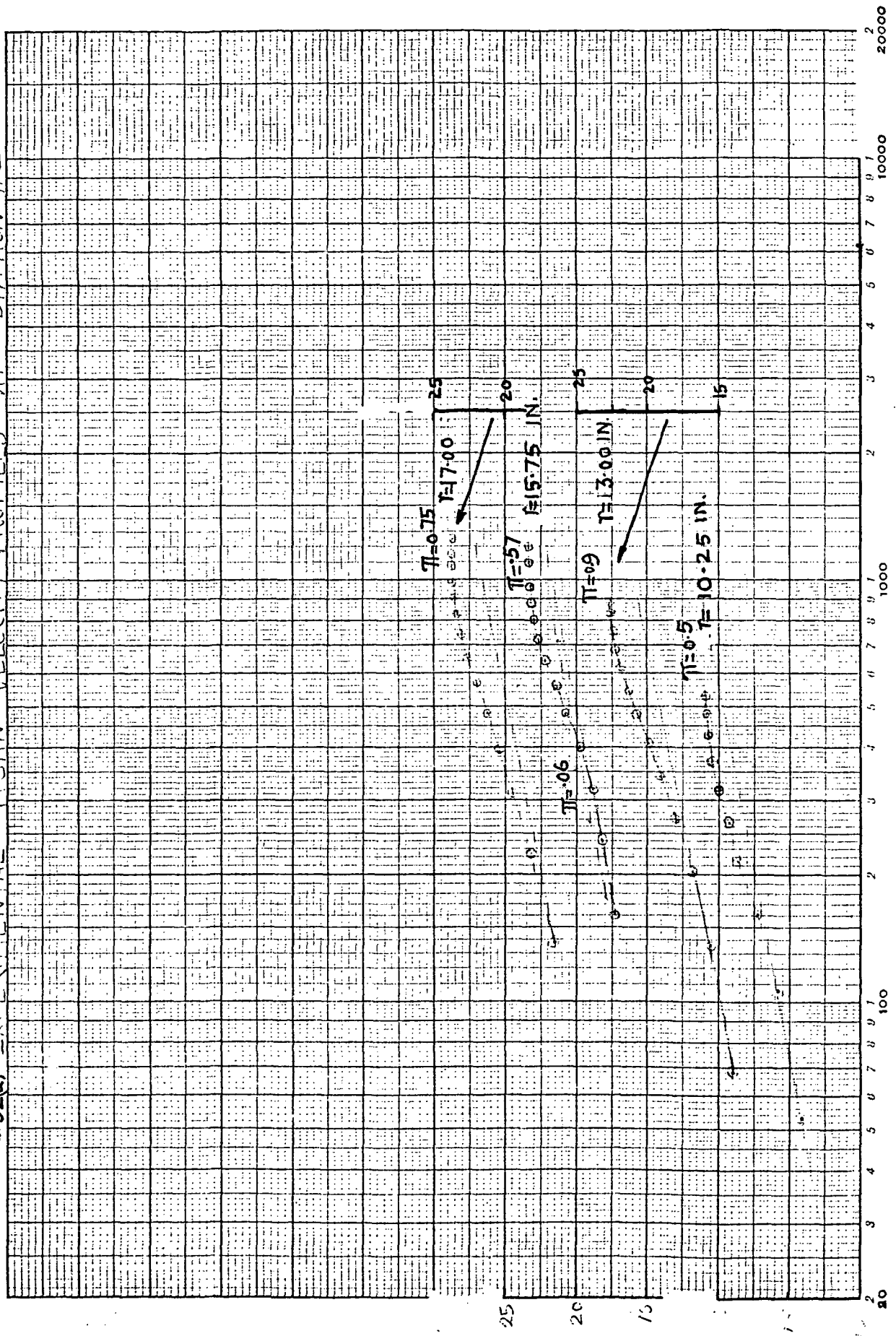
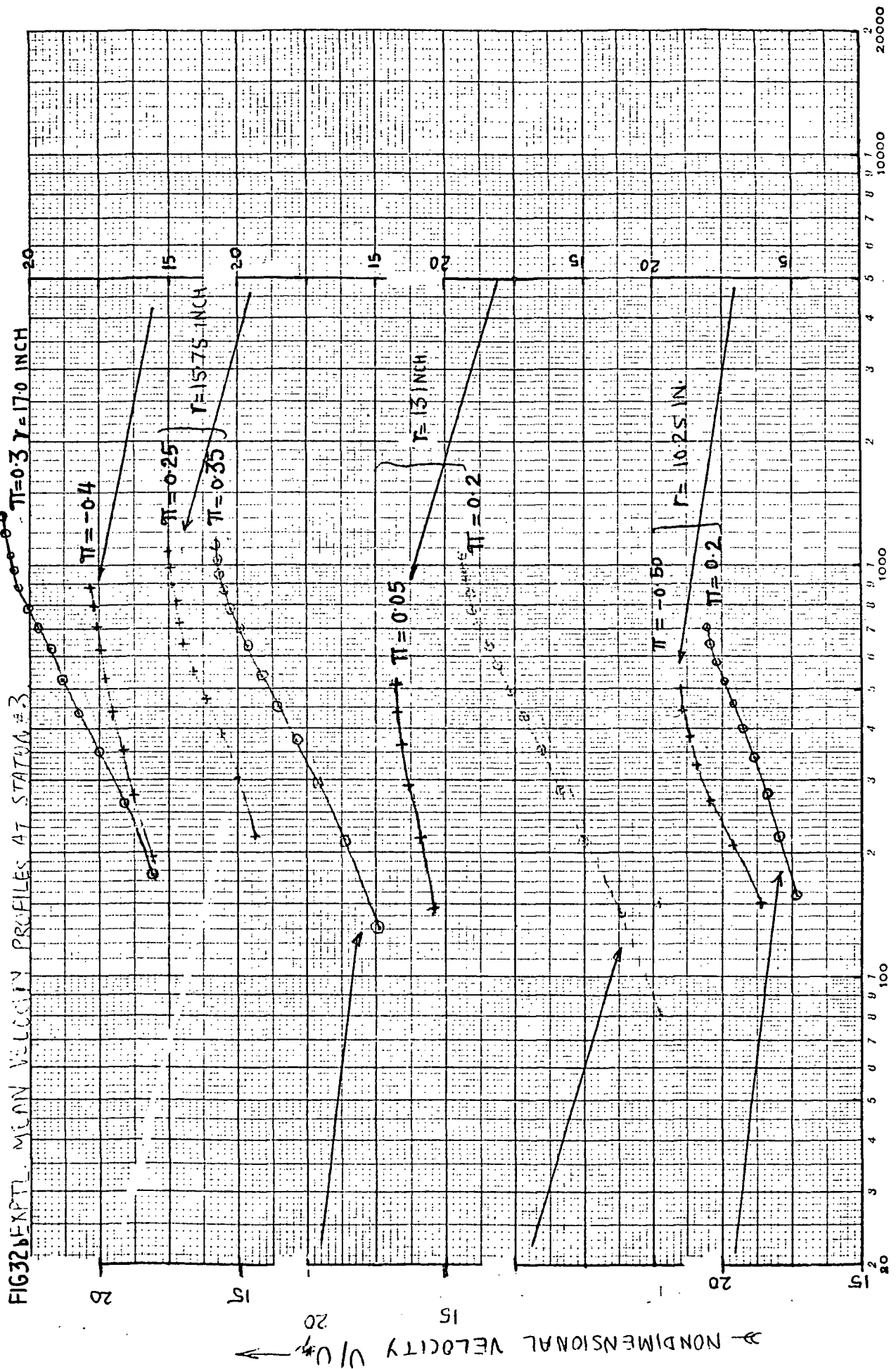


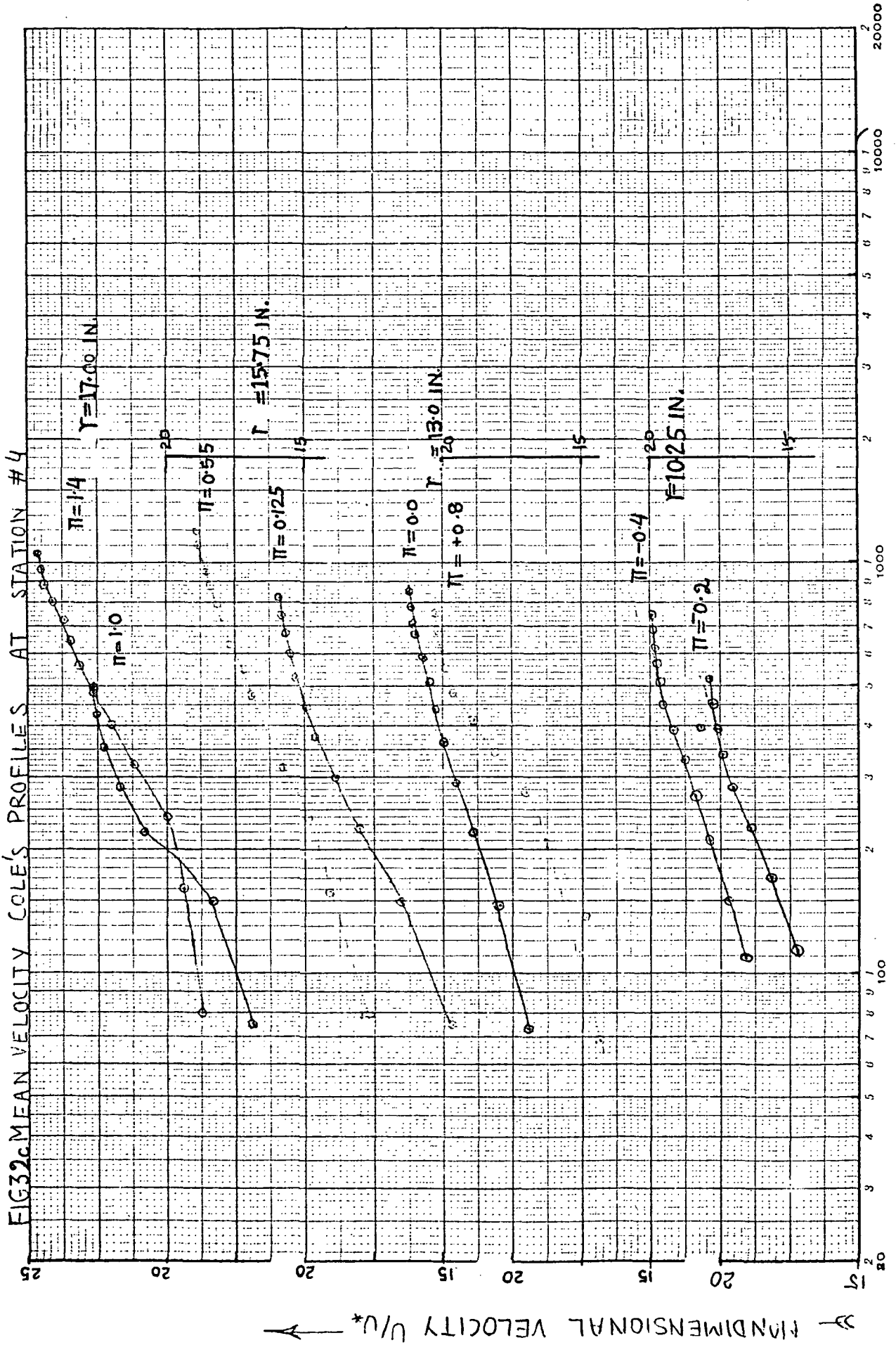
FIG 32(a) EXPERIMENTAL MEAN VELOCITY PROFILES AT STATION #2



3-- REYNOLD'S NUMBER.  $z_{up}/D$







REYNOLD'S NUMBER  $U^*Z/\nu$

FIG 33 A PLOT OF PASSAGE AVERAGED MEAN VELOCITY  $\bar{u}$

\* 1<sup>ST</sup> SLOT  $\theta=30^\circ$   
 + 2<sup>ND</sup> SLOT  $90^\circ$   
 • 3<sup>RD</sup> SLOT  $150^\circ$   
 o 4<sup>TH</sup> SLOT  $210^\circ$   
 □ 5<sup>TH</sup> SLOT  $270^\circ$

INVISCID FREE STREAM

0.7 0.8 0.9 1.0  
 R — RADIUS

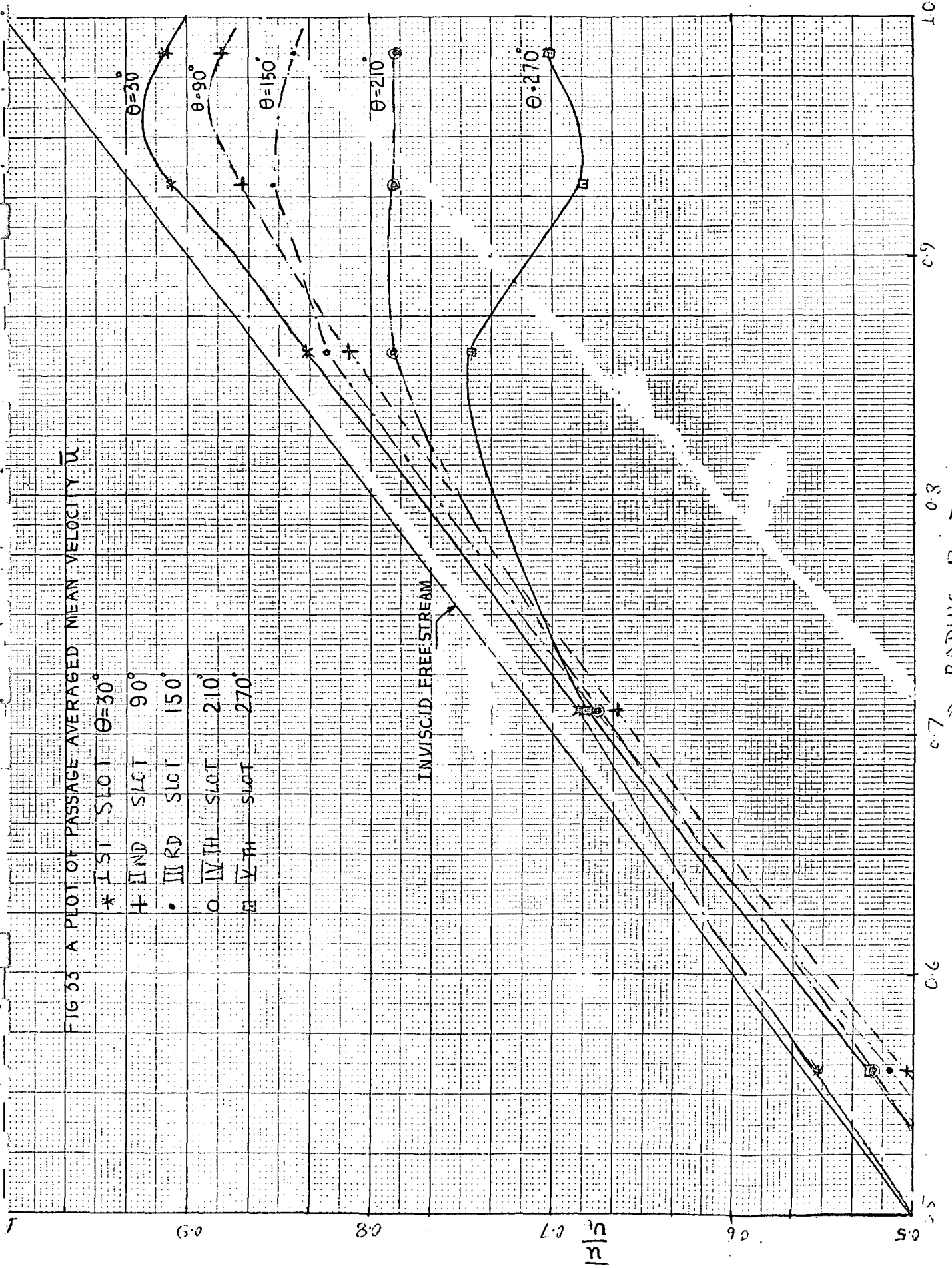


FIG 34(a)- BLADE TO BLADE DISTRIBUTION OF RADIAL VELOCITY  
AT STATION # 1

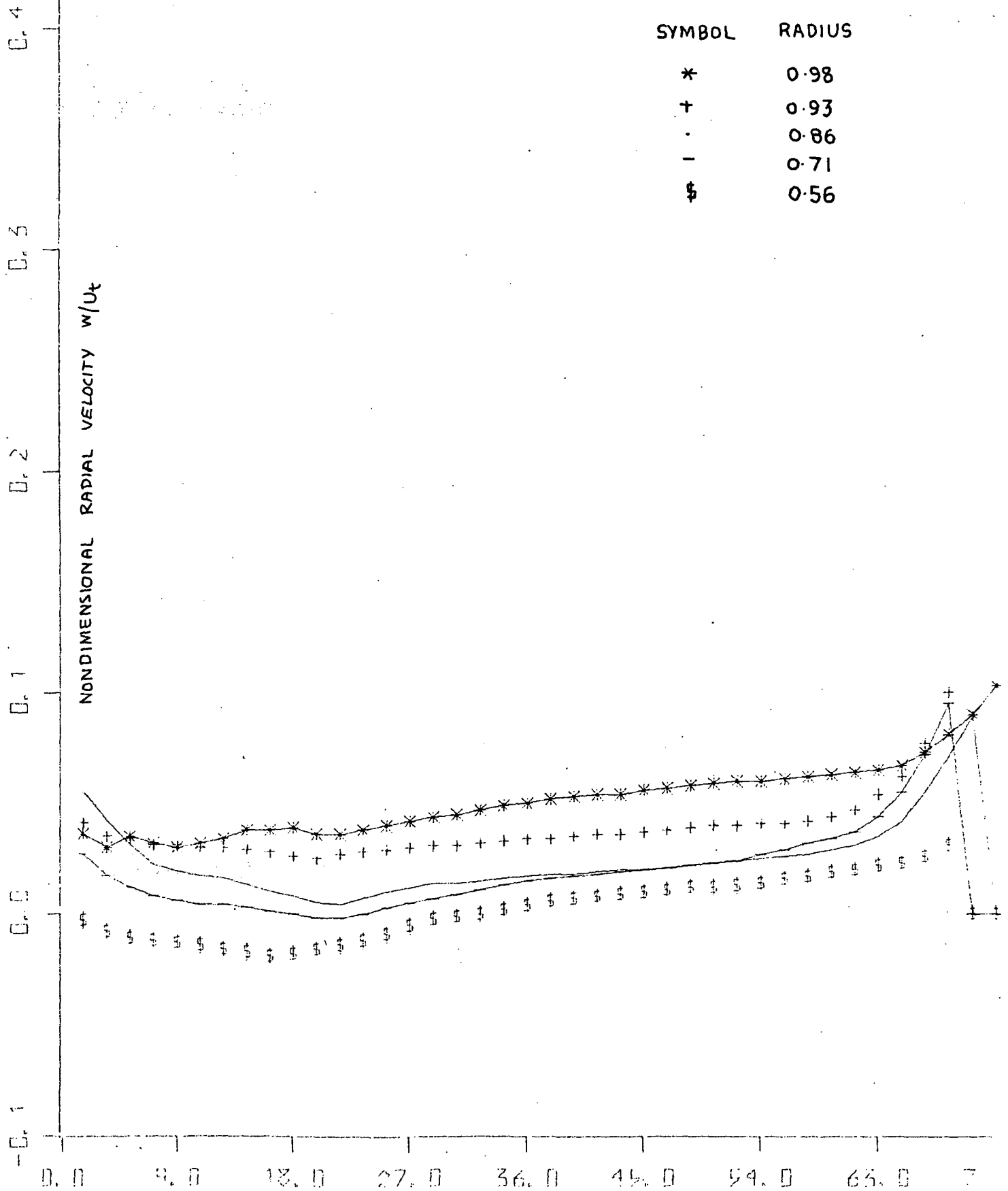


FIG34(b)- BLADE TO BLADE DISTRIBUTION OF RADIAL VELOCITY  
AT STATION #2

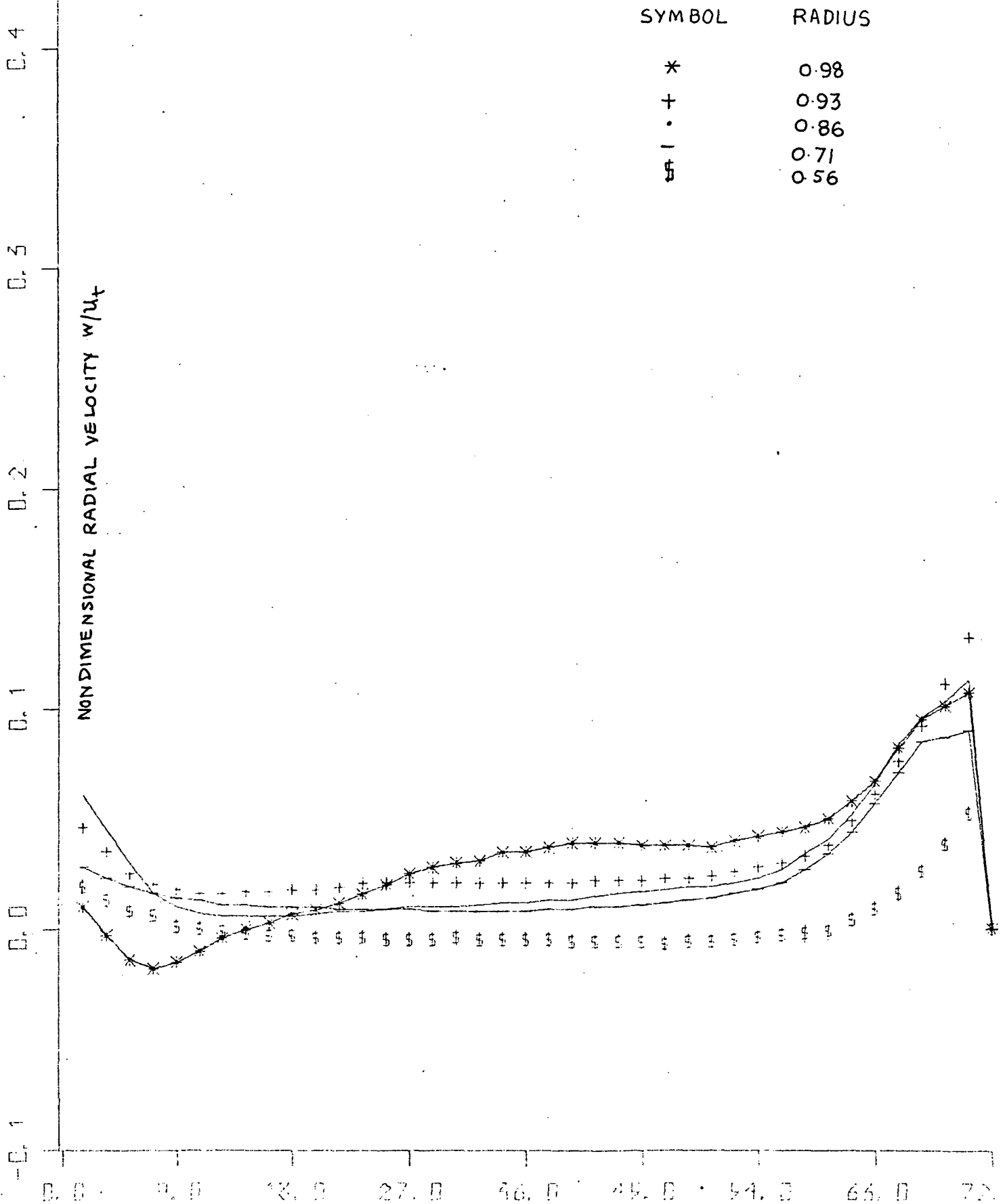


FIG 34(c): BLADE TO BLADE DISTRIBUTION OF RADIAL VELOCITY  
AT STATION #3

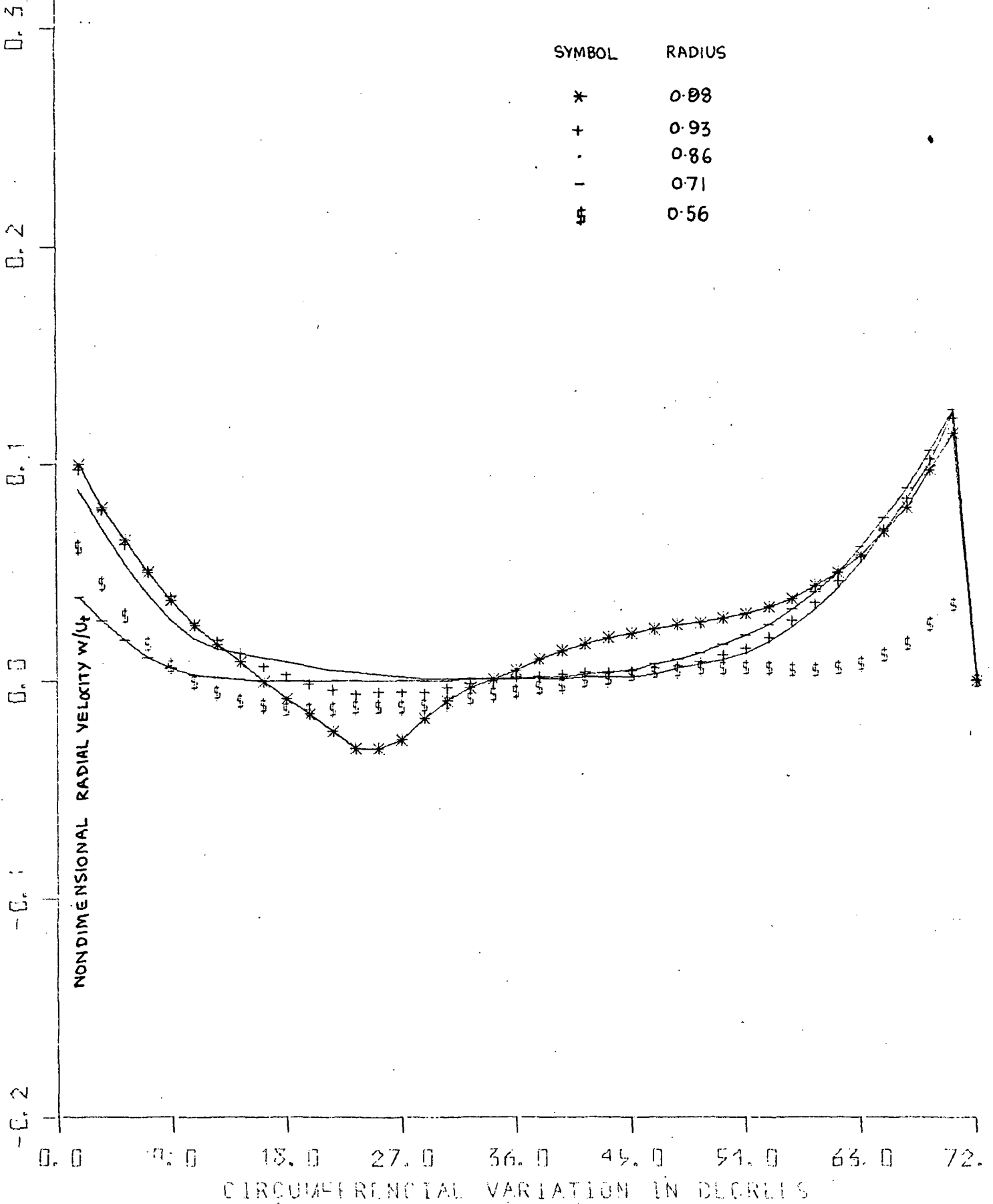


FIG 34(d): BLADE TO BLADE DISTRIBUTION OF RADIAL VELOCITY  
AT STATION #4

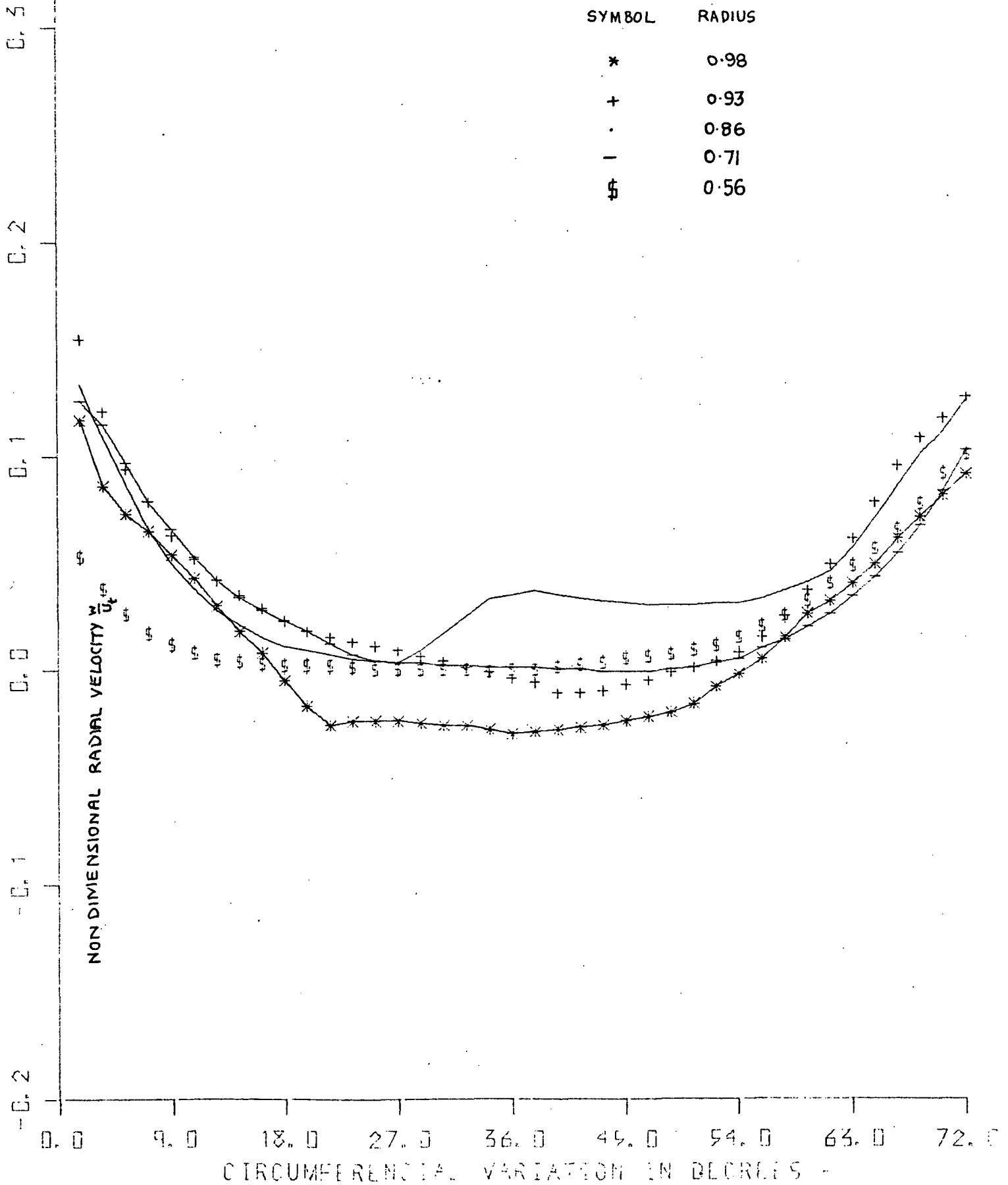


FIG 34(e): BLADE TO BLADE DISTRIBUTION OF RADIAL VELOCITY

AT STATION #5

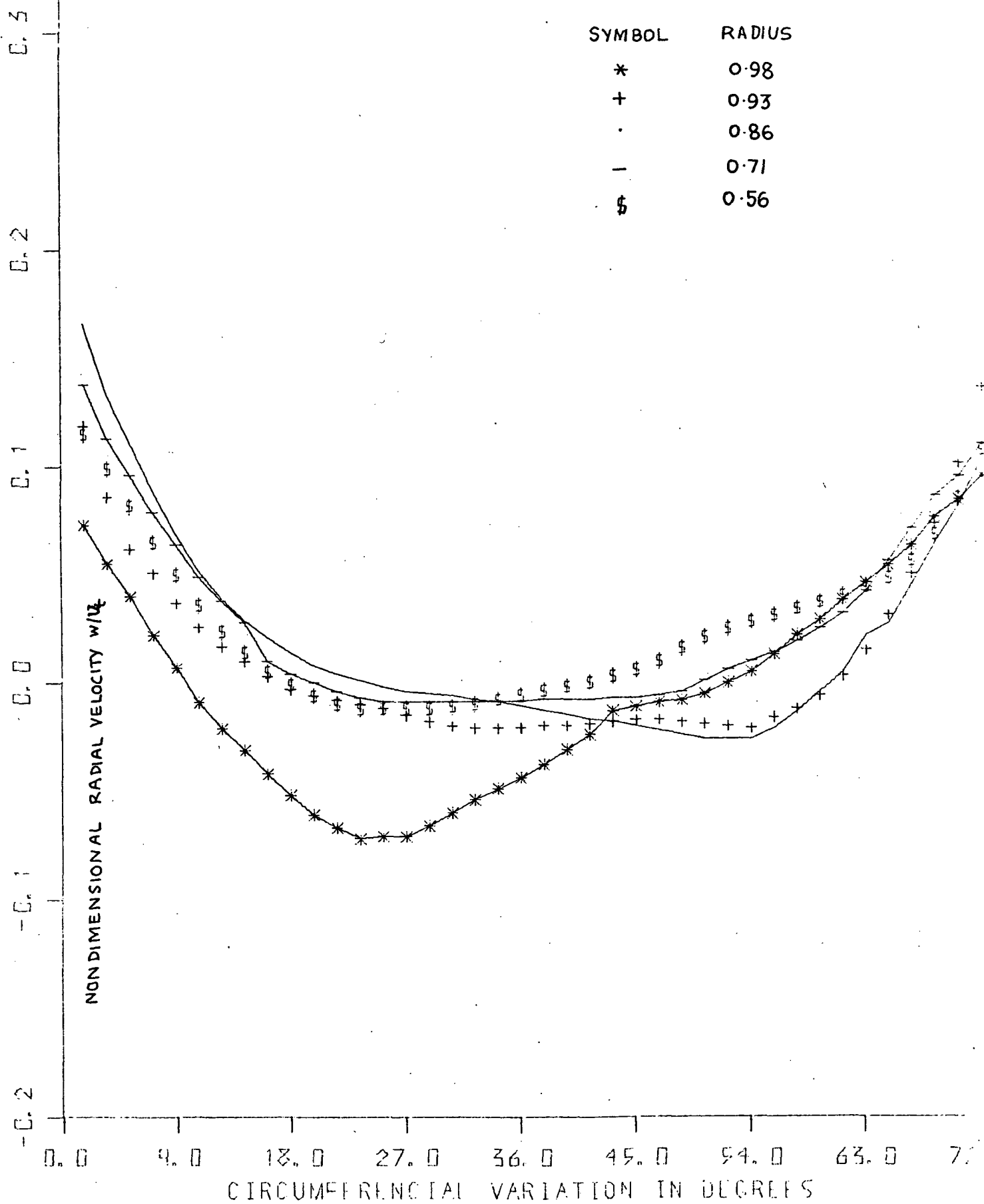




FIG 35 COMPARISON OF RADIAL PRESSURE GRADIENTS AT THE MID PASSAGE  
DERIVED FROM SIMPLIFIED RADIAL EQUILIBRIUM EQUATION  
AND THE MEASURED VALUES AT STATION #1

SYMBOL	LINE
$\frac{\partial p}{\partial R}$	X
$\frac{(\frac{V}{U})^2}{R^2} - \frac{1}{2} \frac{\partial^2 p}{\partial R^2}$	O

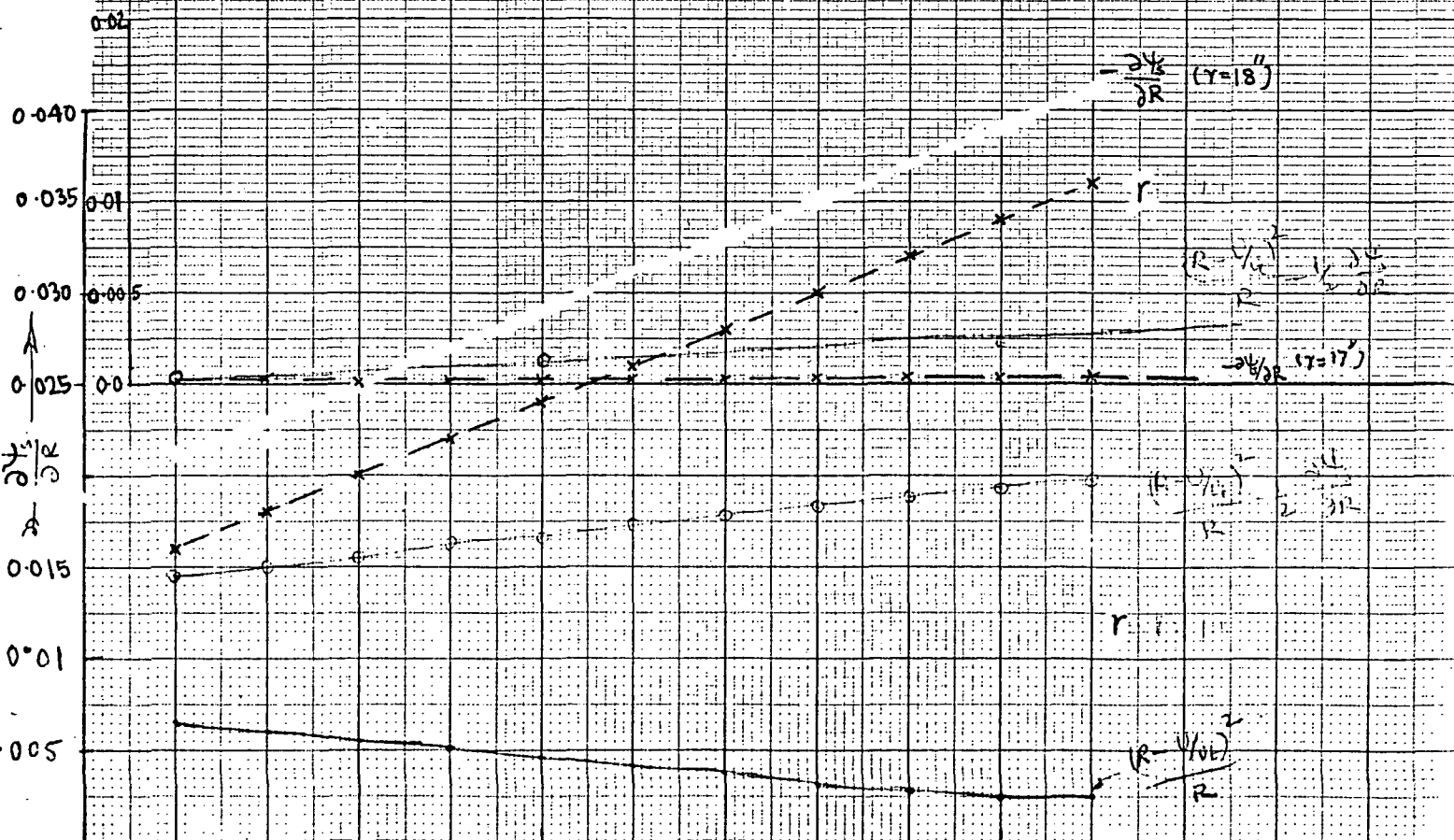


FIG36(a): MAGER'S PLOT OF RADIAL VELOCITY PROFILES AT

STATION # 2 ( $\theta = 90^\circ$ )

THEORETICAL  
EXPERIMENTAL

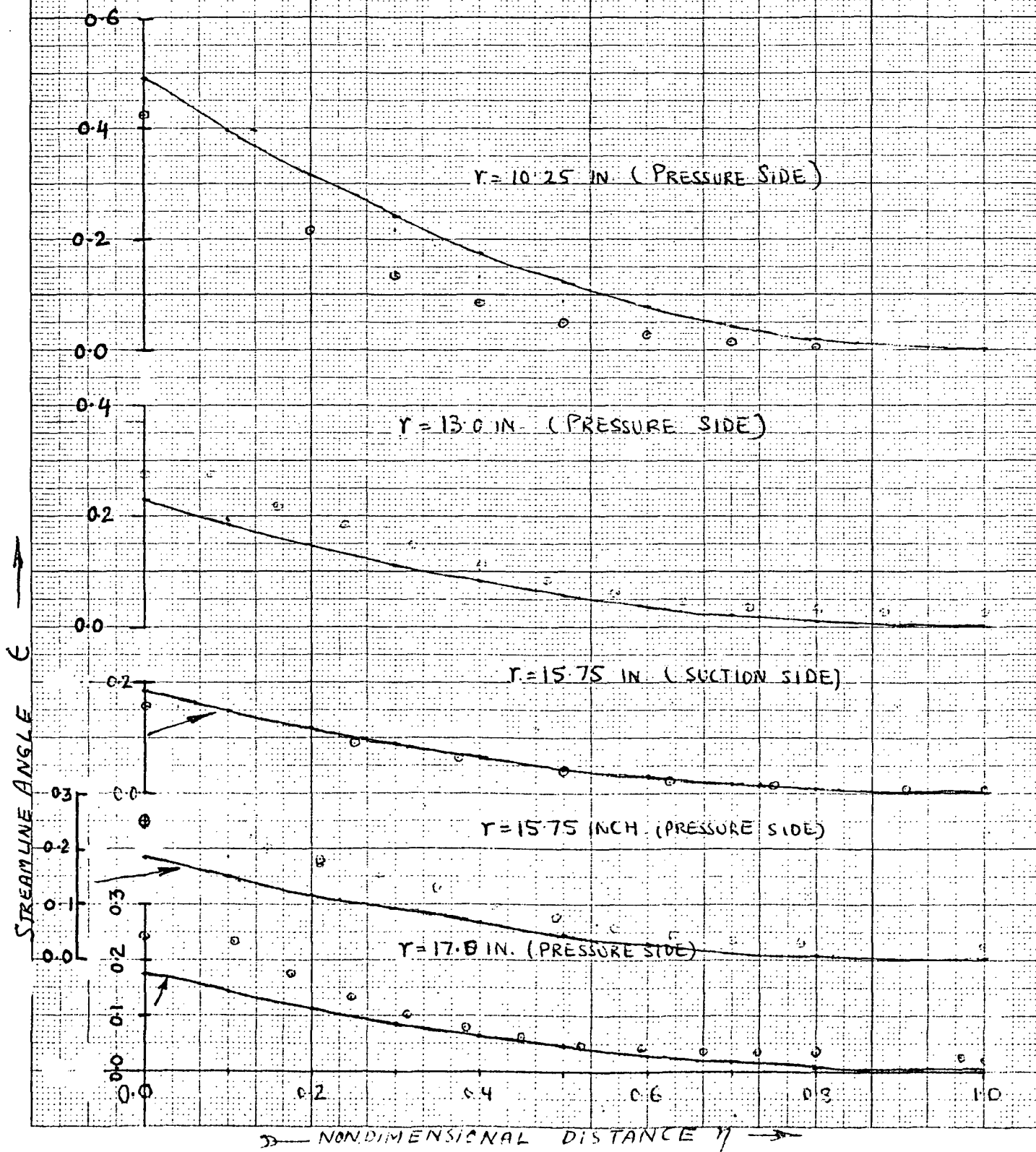


FIG36(b): MAGER'S PLOT OF RADIAL VELOCITY AT STATION #3 (150°)

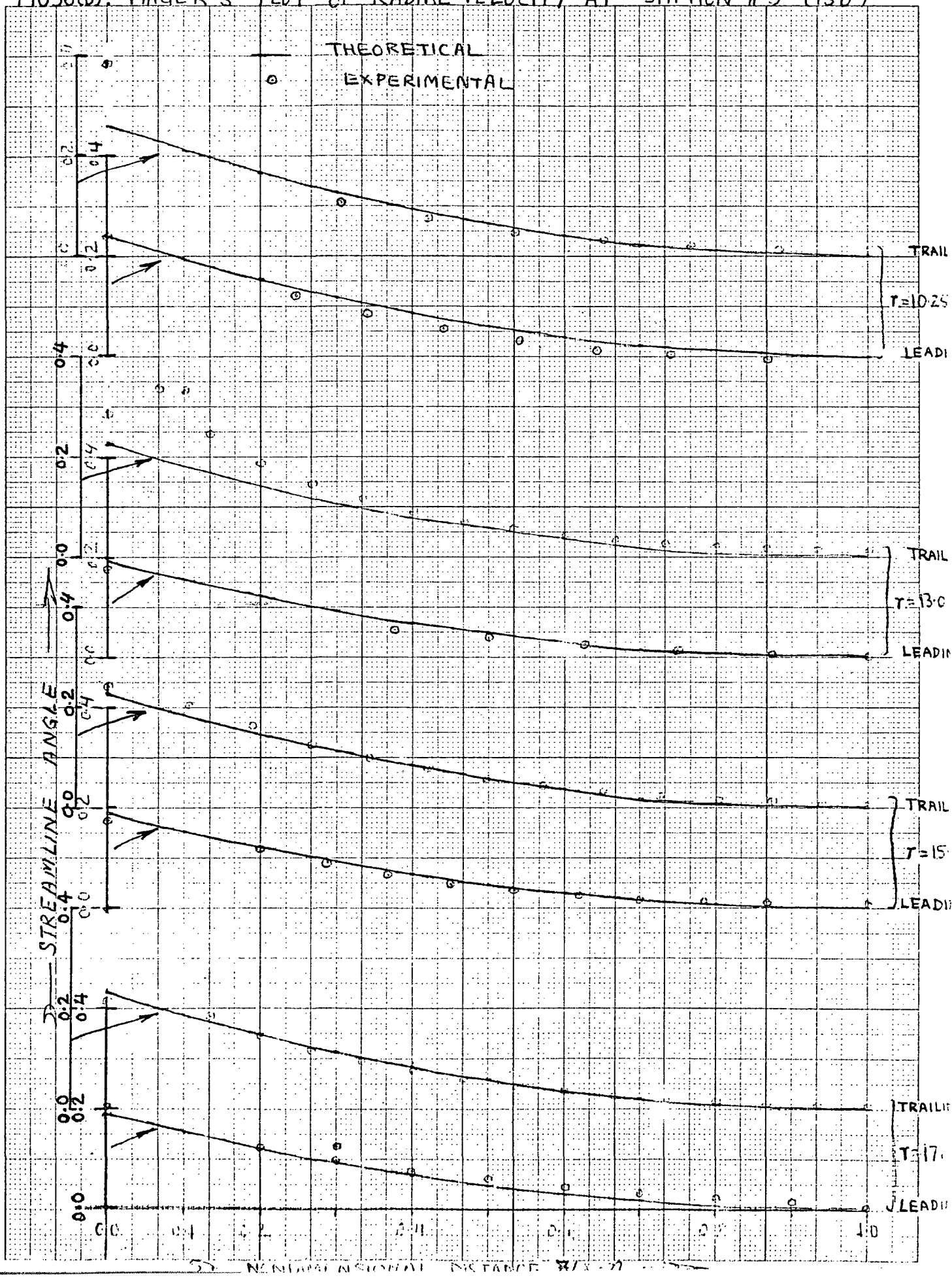


FIG 36 (a) MAGER'S PLOT OF RADIAL VELOCITY AT STATION # 4 (210')

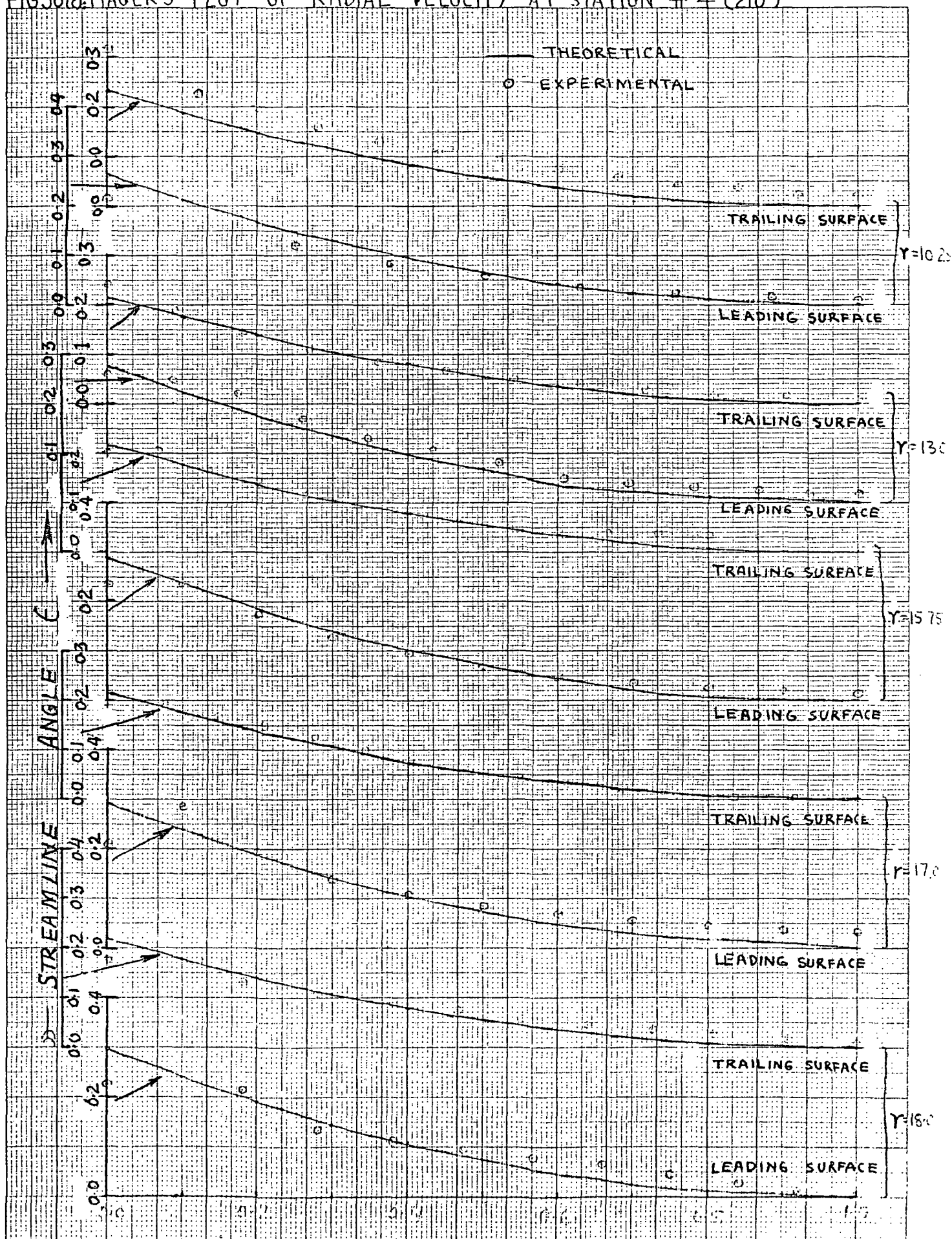


FIG 37(a) HODOGRAPH PLOTS AT STATION # 2

SIDE	SYMBOL	RADIUS
LEADING	*	0.86
	+	0.71
	.	0.56
TRAILING	-	0.86
	\$	0.71
	o	0.56

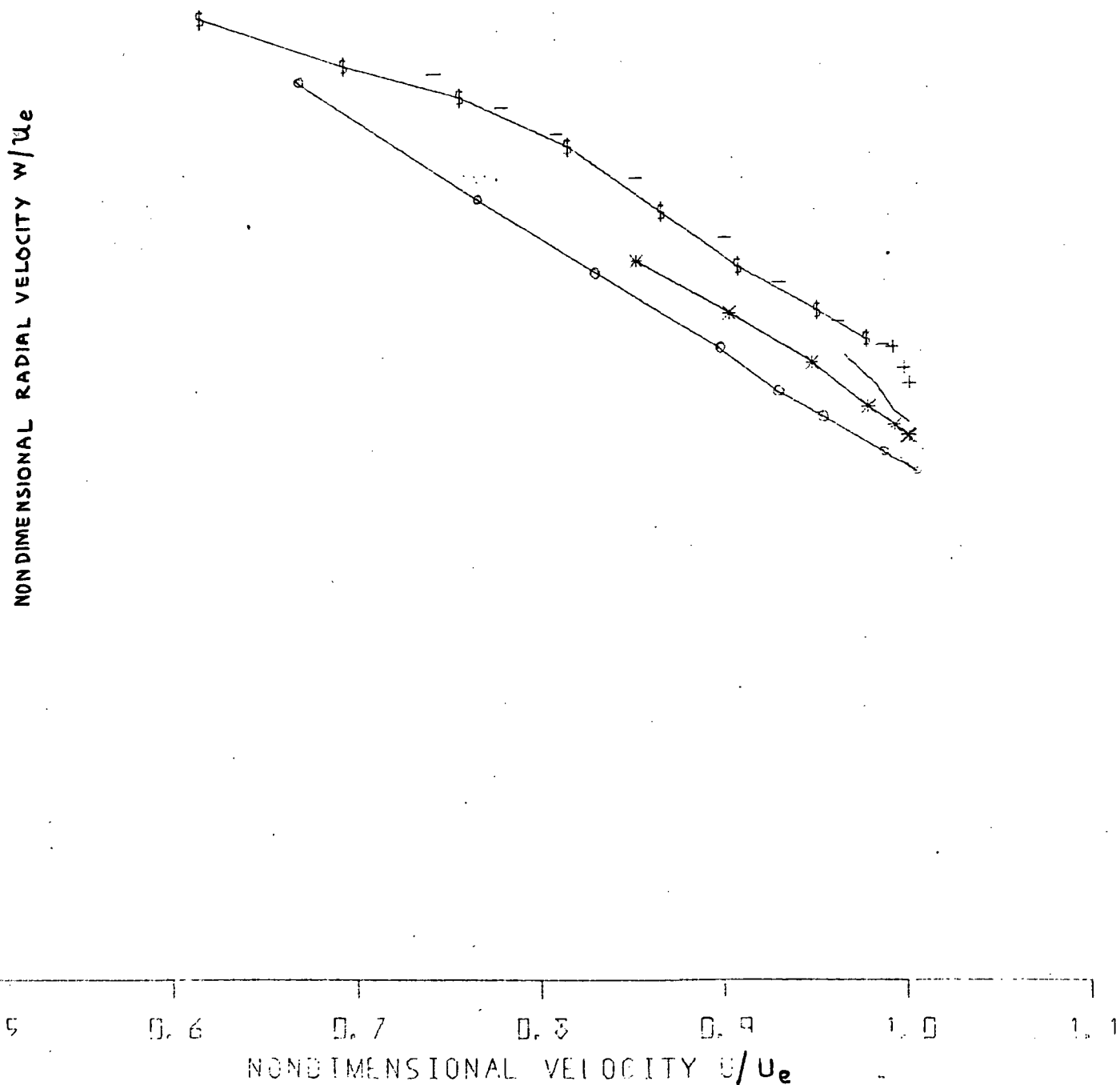


FIG 37(b) HODOGRAPH PLOTS AT STATION #3

SIDE	SYMBOL	RADIUS
LEADING	*	0.88
	+	0.71
	.	0.56
TRAILING	-	0.86
	\$	0.71
	o	0.56

NONDIMENSIONAL RADIAL VELOCITY  $w/u_e$

NONDIMENSIONAL VELOCITY  $U/u_e$

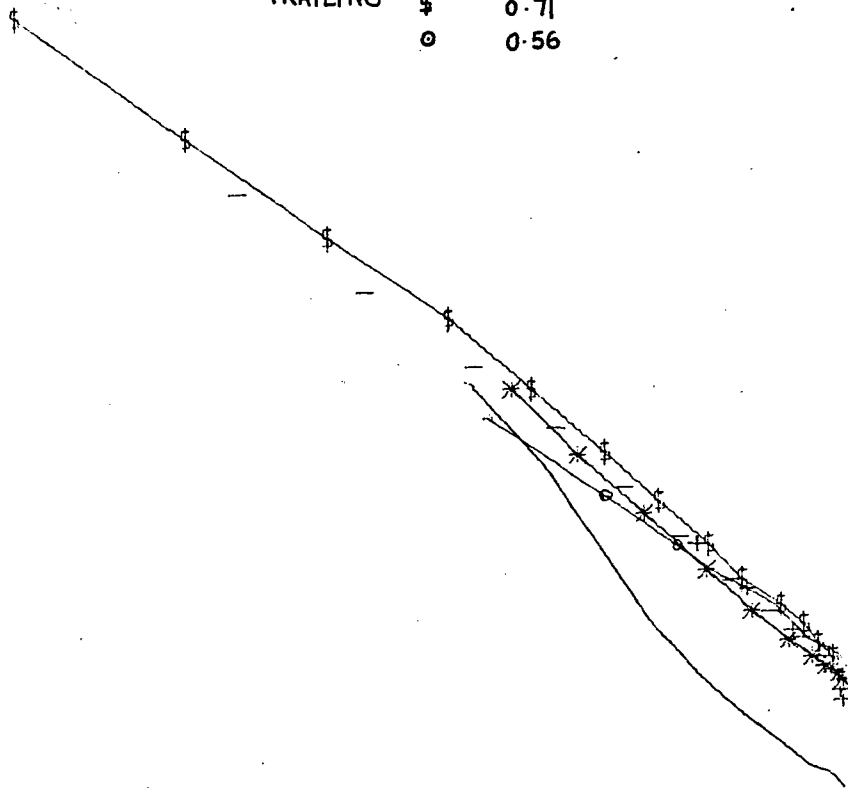


FIG 37(c): HODOGRAPH PLOTS AT STATION # 4

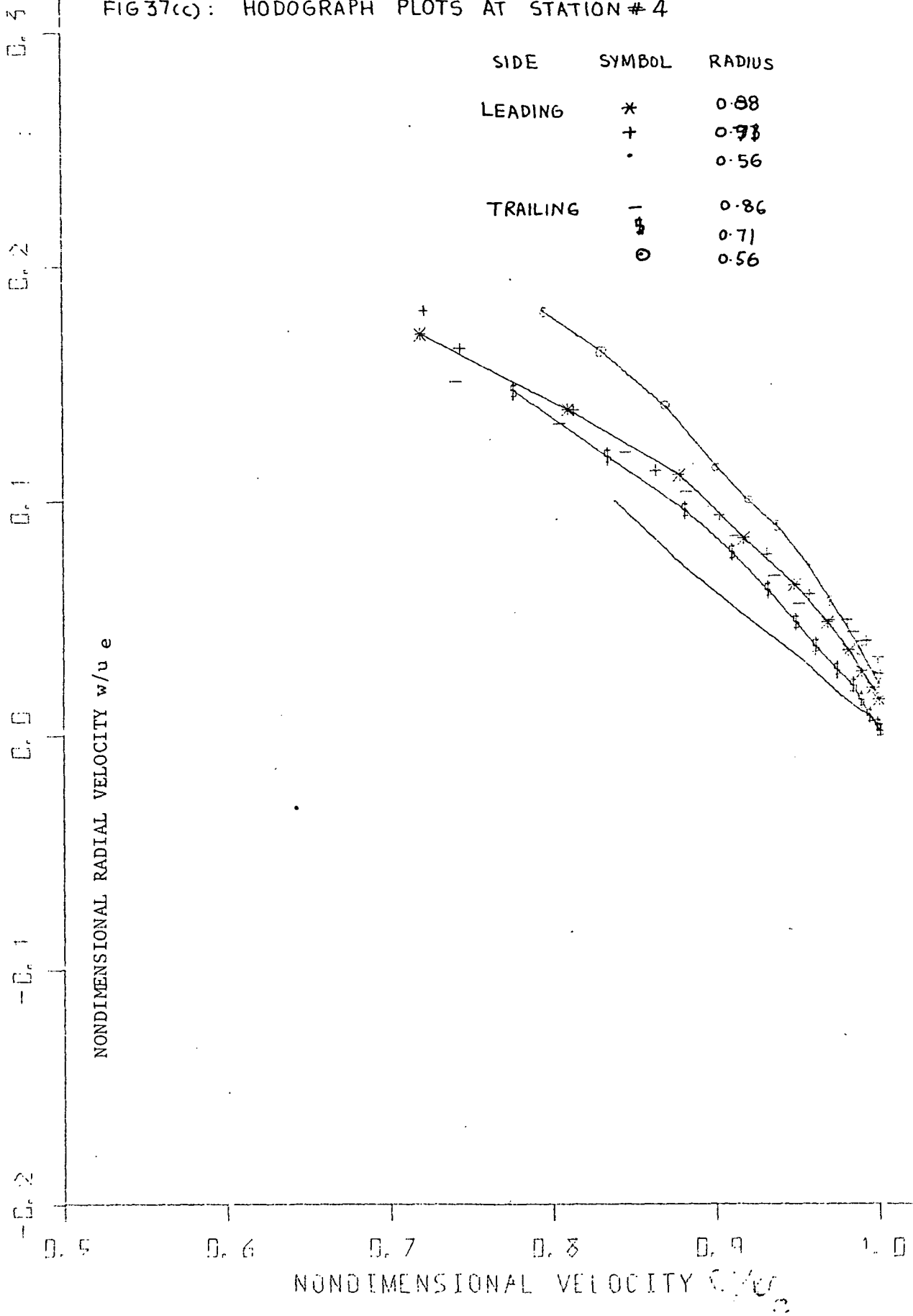


FIG 37(d): HODOGRAPH PLOTS AT STATION #5

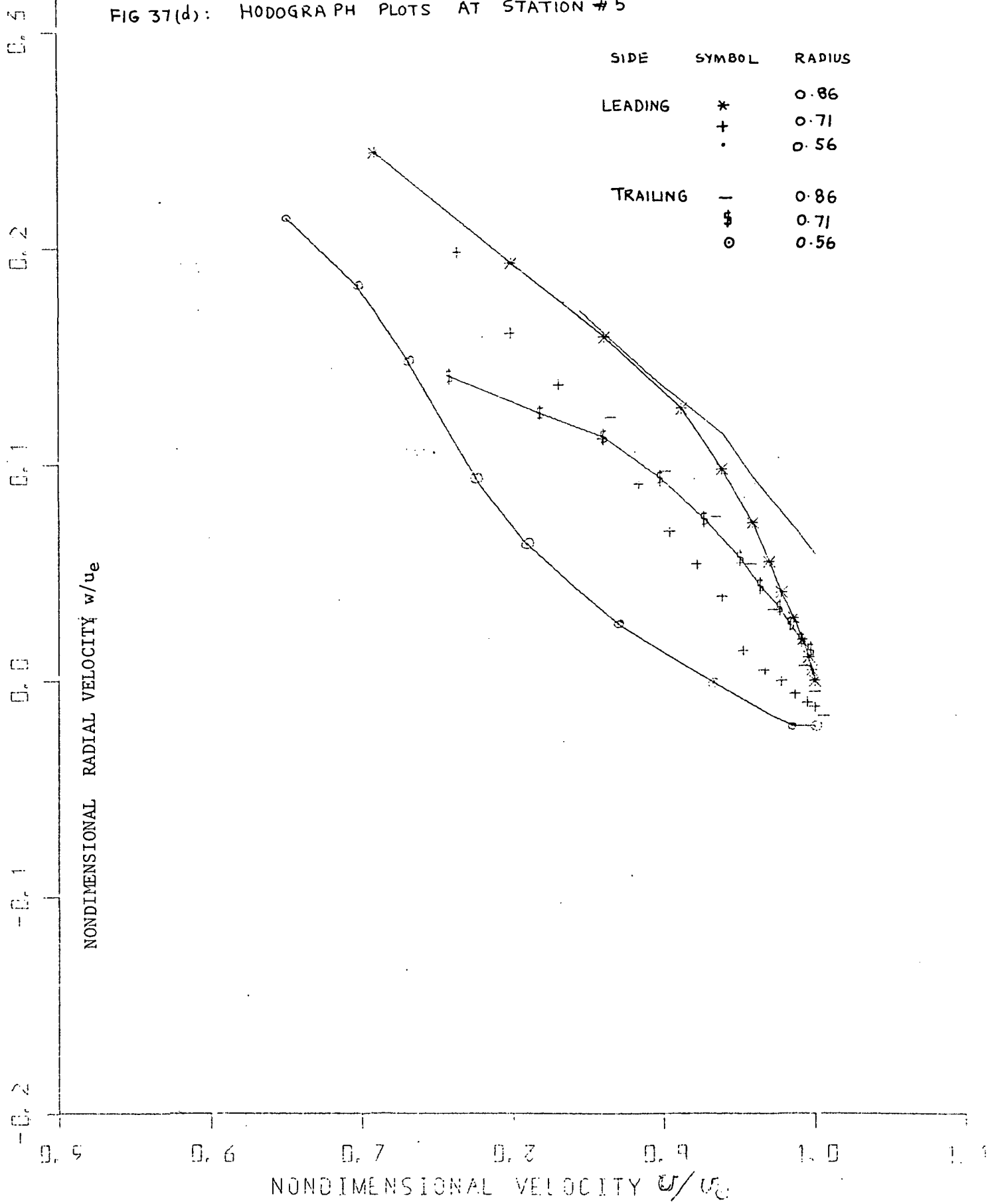




FIG 37(e): HODOGRAPH PLOTS AT STATION #2

SIDE	SYMBOL	RADIUS
LEADING	*	0.98
	+	0.93
TRAILING	-	0.98
	.	0.93

NONDIMENSIONAL RADIAL VELOCITY  $w/u_e$

NONDIMENSIONAL VELOCITY  $u'/u_e$

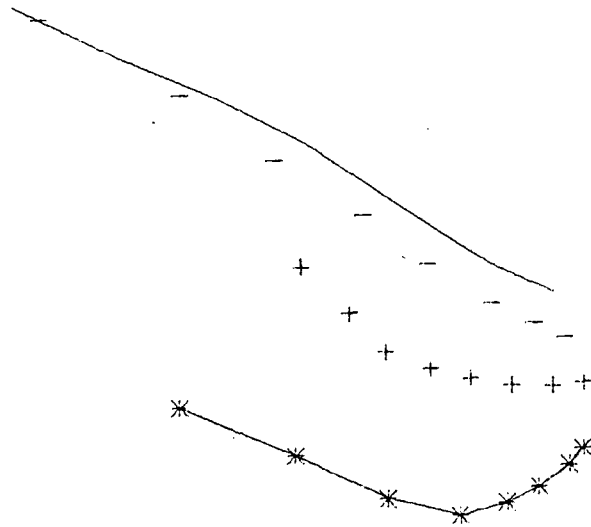


FIG 37(f) HODOGRAPH PLOTS AT STATION # 4

SIDE	SYMBOL	RADIUS
LEADING	*	0.98
	+	0.93
TRAILING	.	0.98
	-	0.93

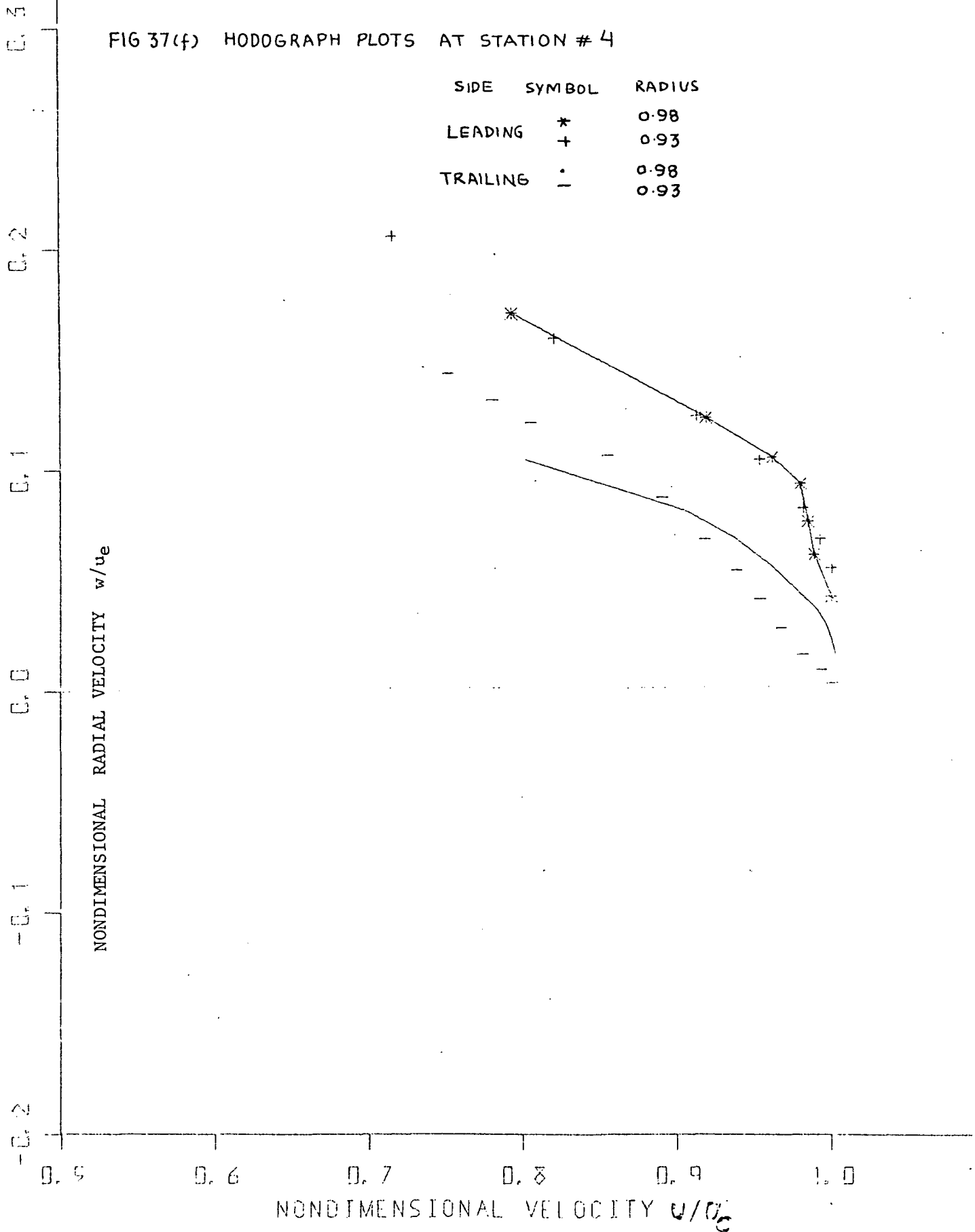
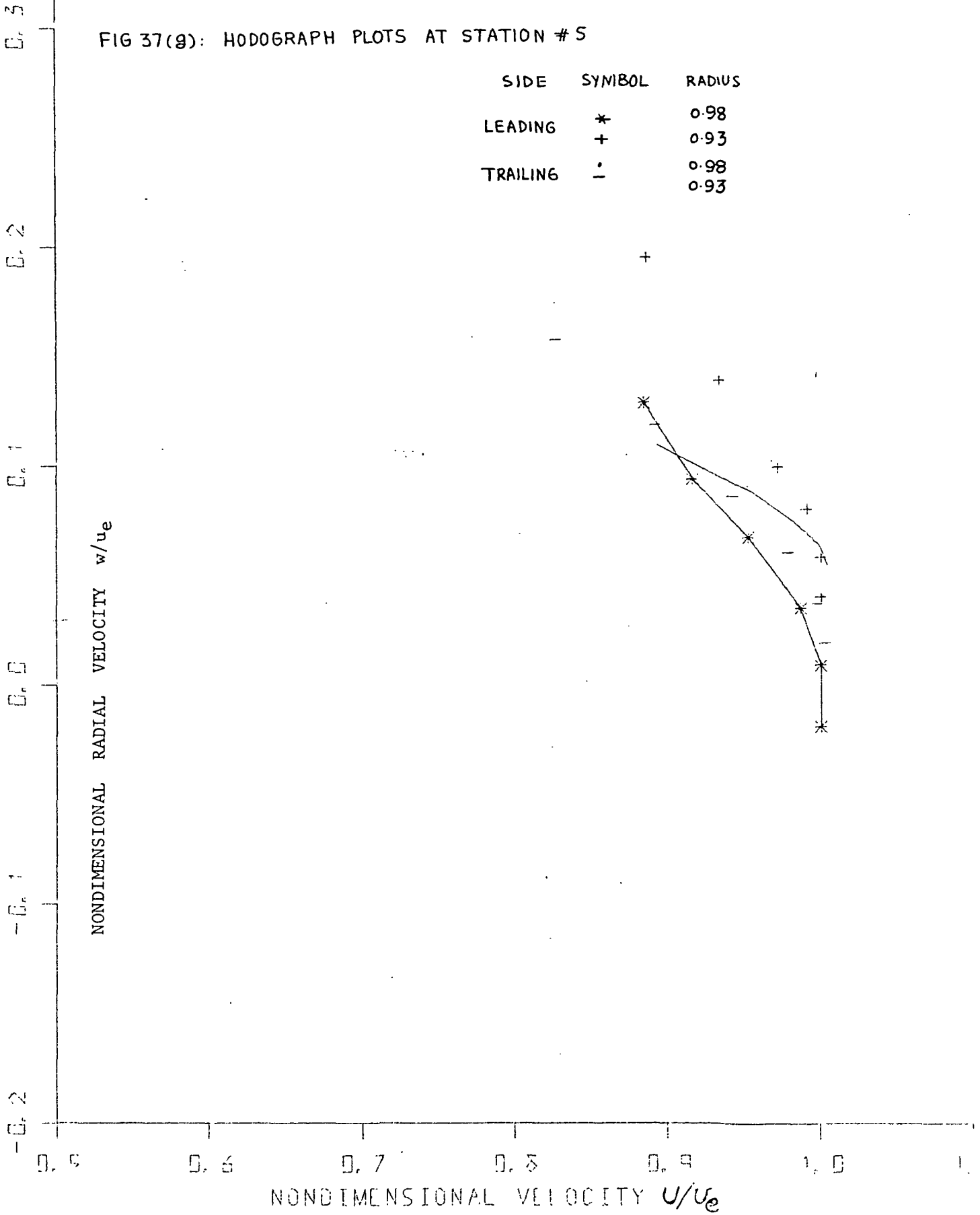


FIG 37(g): HODOGRAPH PLOTS AT STATION #5



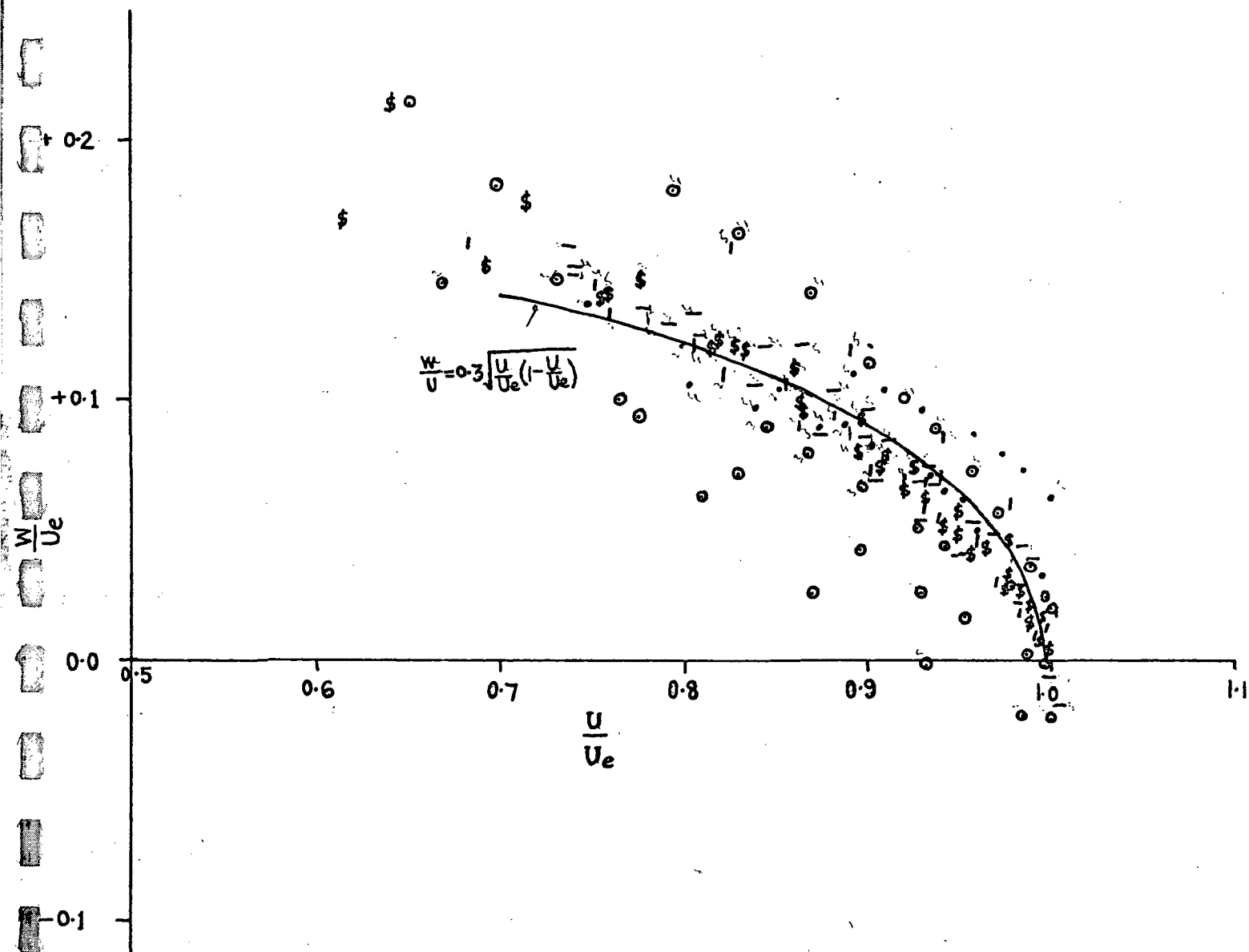


FIG 38 (a) HODOGRAPH PLOT REPRESENTATION FOR VELOCITY COMPONENTS  
ON TRAILING SIDE BOUNDARY LAYER

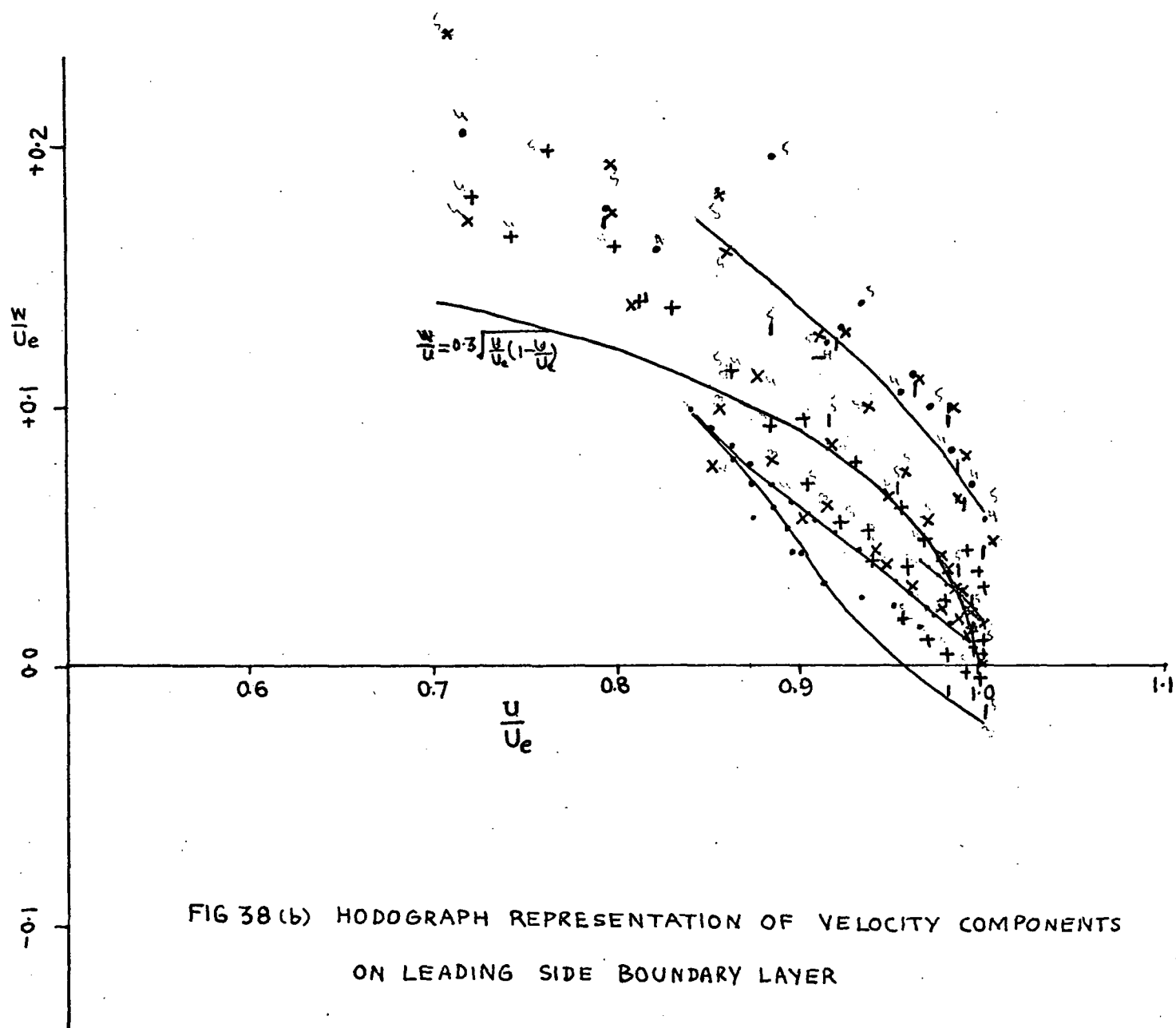


FIG 38 (b) HODOGRAPH REPRESENTATION OF VELOCITY COMPONENTS  
ON LEADING SIDE BOUNDARY LAYER

4<sup>TH</sup> STATION

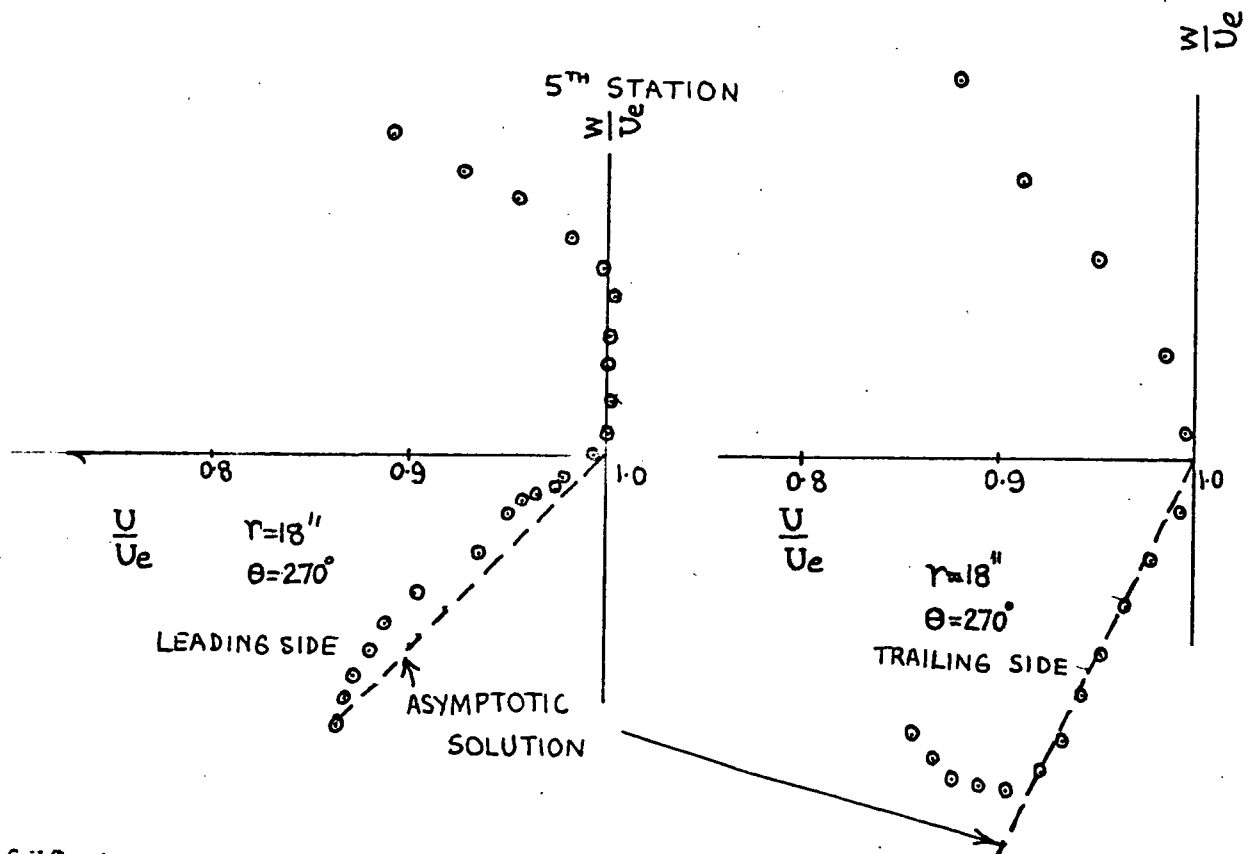
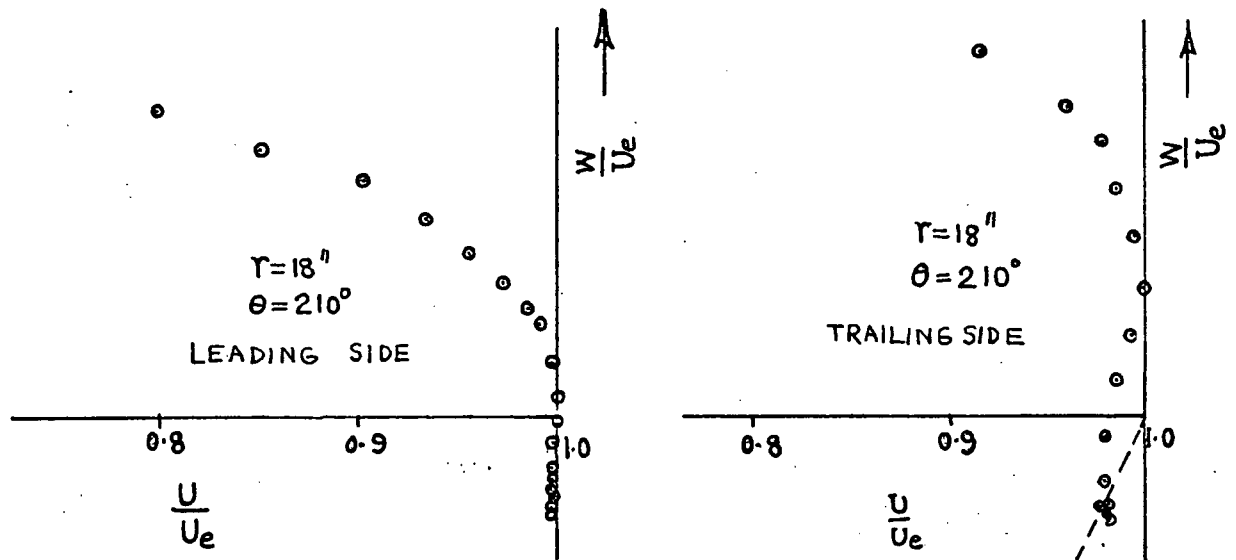


FIG39: HODOGRAPH PLOT FOR CROSS FLOW IN THE OUTER LAYER

FIG 40(a): VELOCITY DEFECT REPRESENTATION OF

$r = 18''$

$r = 17''$

INTERFERENCE REGION AT STATION #5

0.1

0.0

$u/u_e$

0.1

TRAILING SIDE

LEADING SIDE

TRAILING SIDE

LEADING SIDE

$u-u_e/u_e$

FIG 40(b): VELOCITY DEFECT REPRESENTATION OF INTERFERENCE REGION

AT STATION # 4

$r = 18''$   
 $r = 17''$

$\frac{W}{U_e}$

0.10

0.05

0.0

-0.05

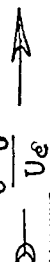




FIG. 40(C): VELOCITY DEFECT REPRESENTATION OF INTERFERENCE REGION

AT STATION #3

○  $\gamma = 18''$

x  $\gamma = 17''$

$\Delta \cdot W/u_e \rightarrow$

$\Delta \cdot \frac{u - \bar{u}}{u_e}$

GRAPH PAPER (C)

MADE IN U.S.A.

+01

0.02

0.0

0.4

0.6

0.8

1.0

1.2

1.4

1.6

1.8

2.0

-0.06

-0.04

-0.02

0.0

0.02

0.04

0.06

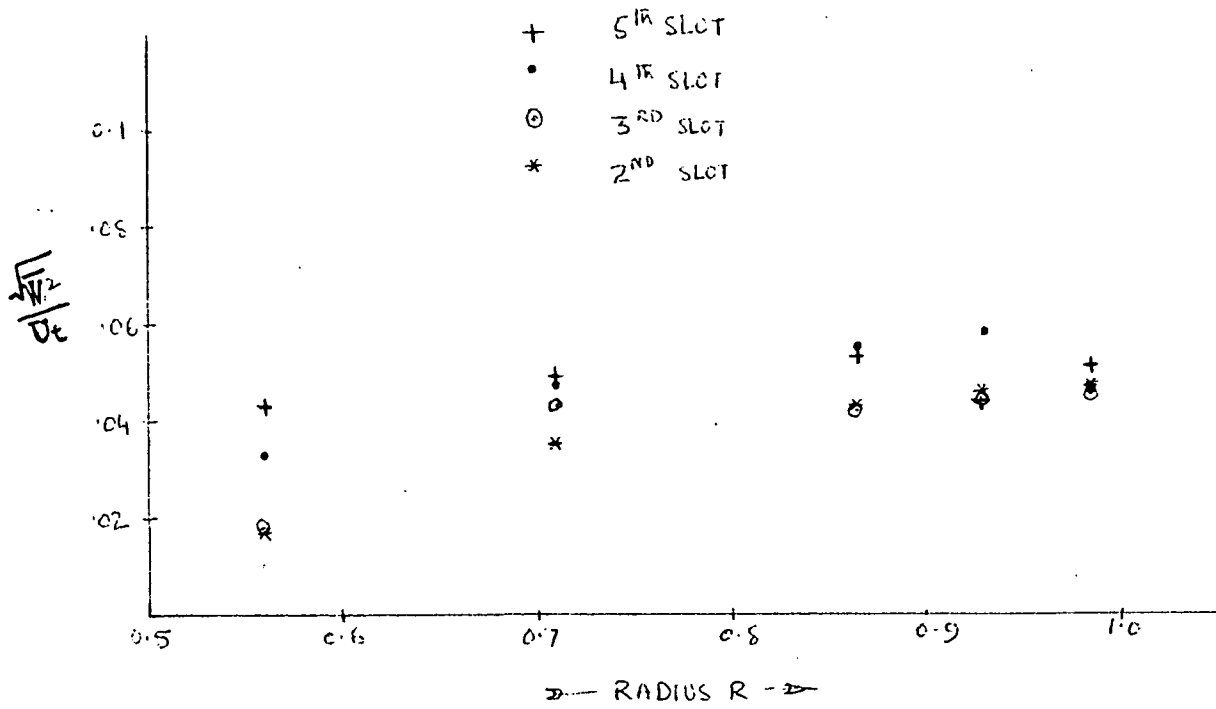
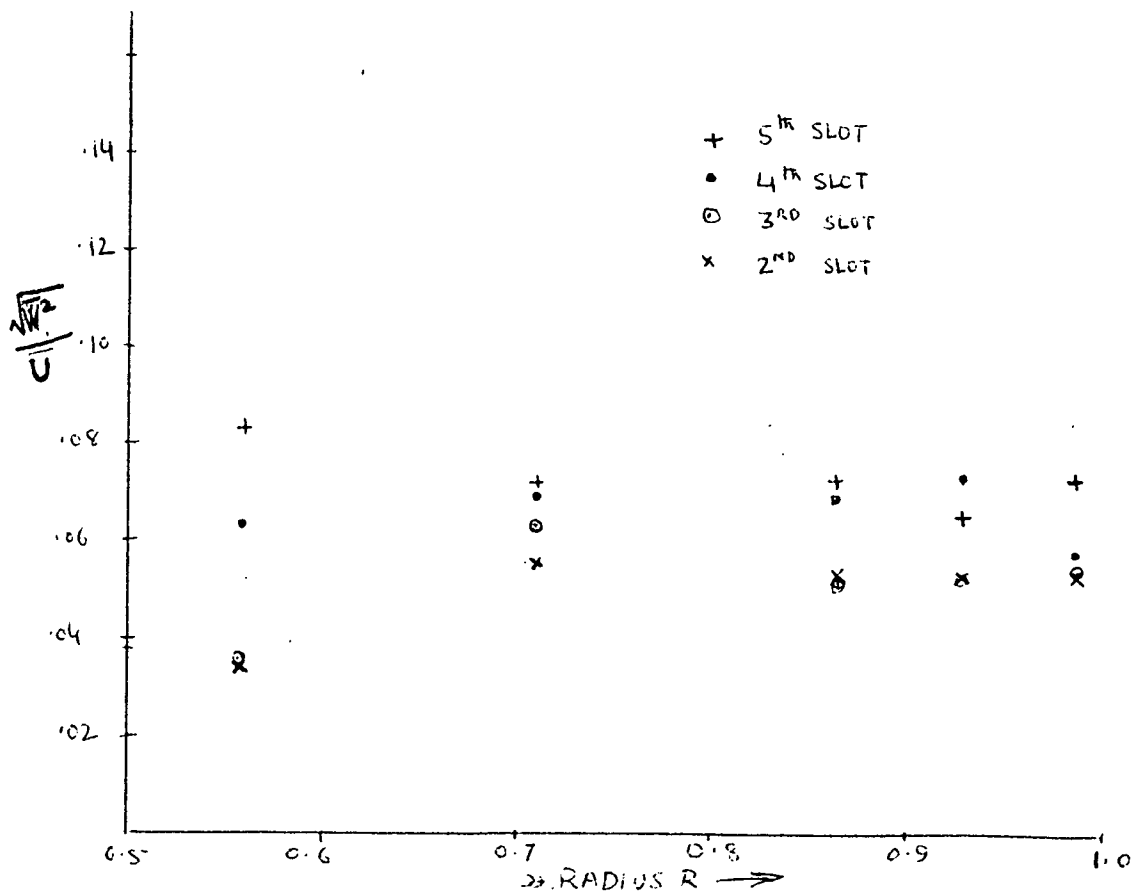
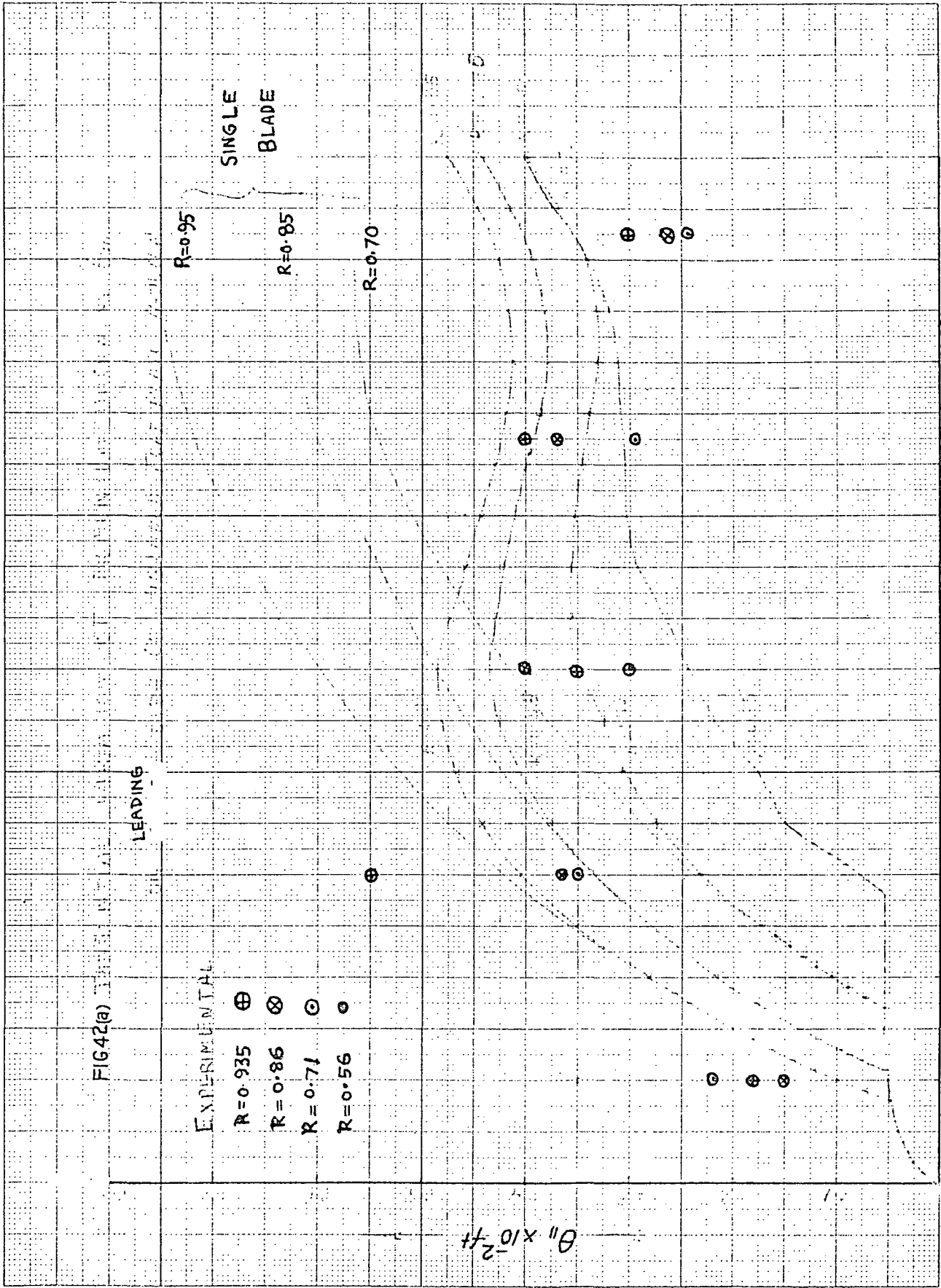


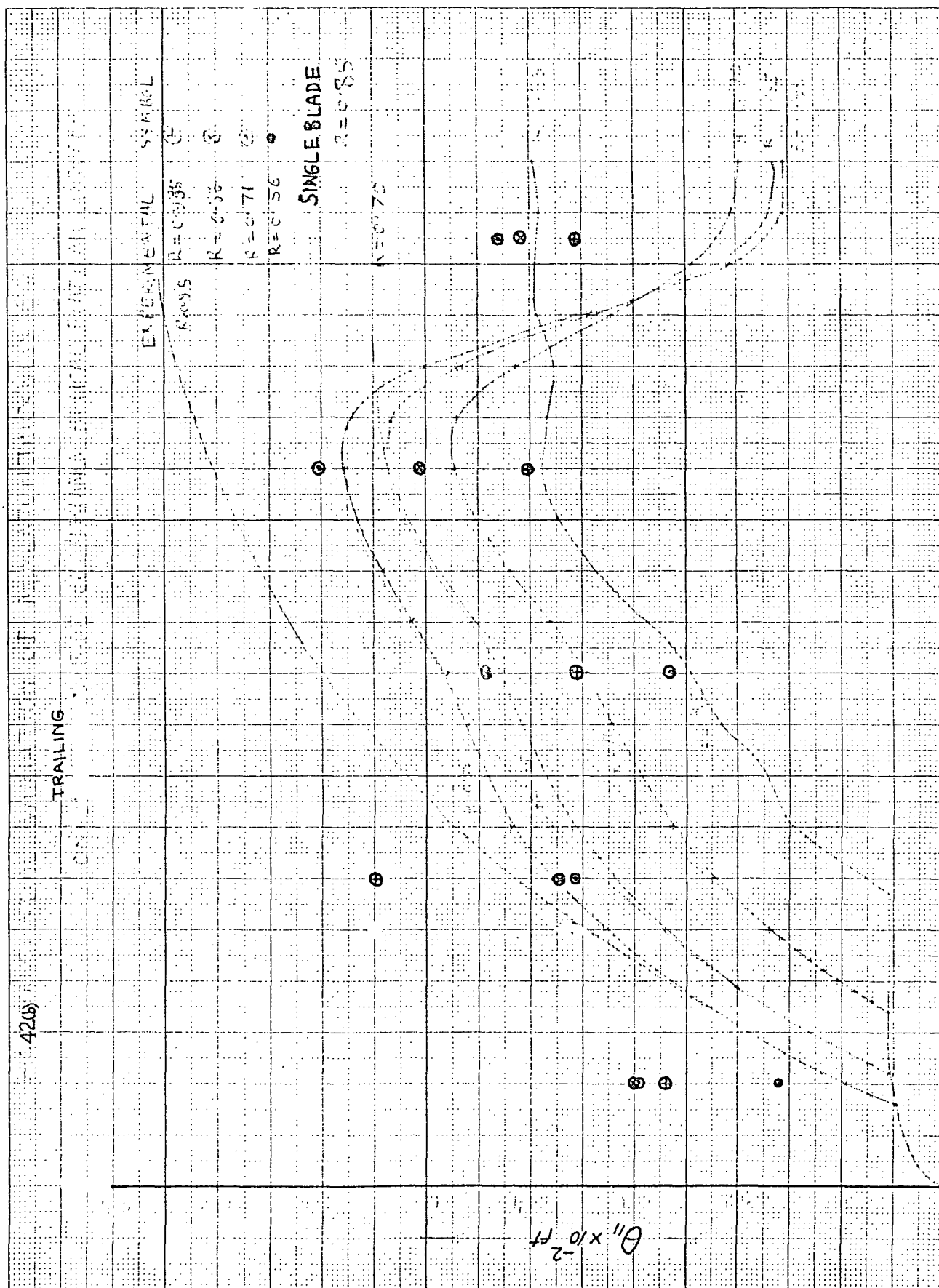
FIG41: RADIAL DISTRIBUTION OF RMS RADIAL VELOCITY

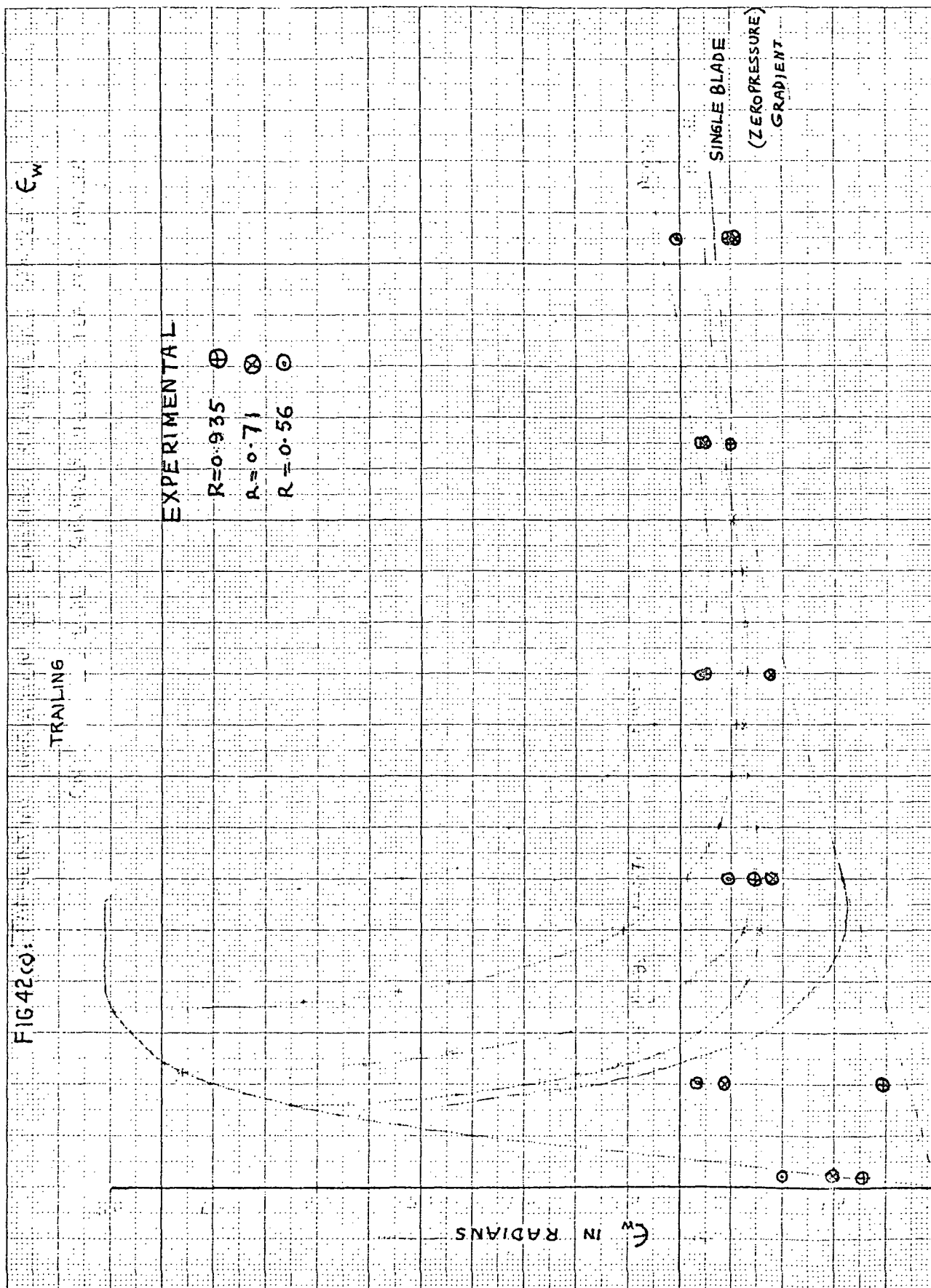




NO. 100000 DIFFERENTIAL CALCULATOR

MADE IN U.S.A.

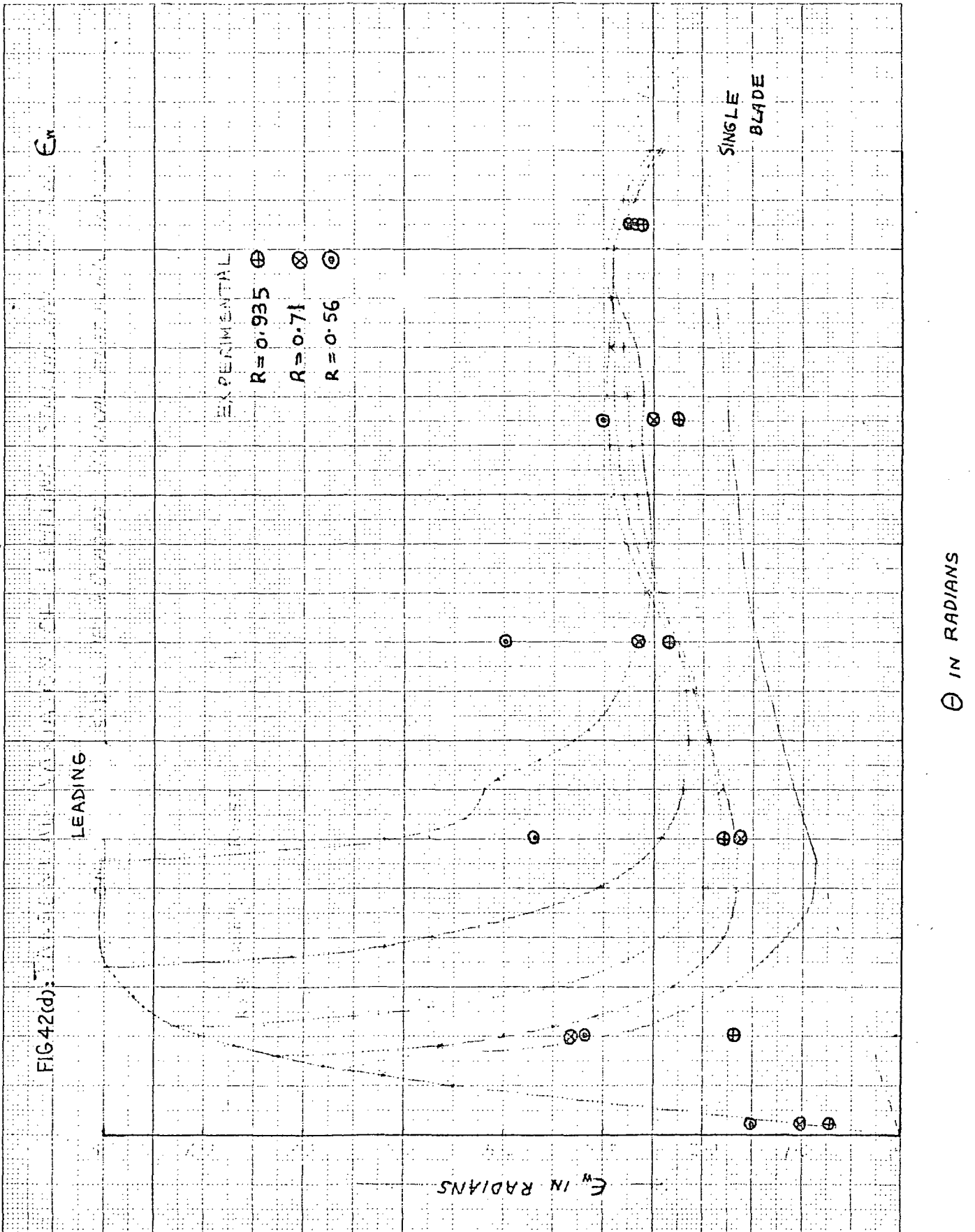


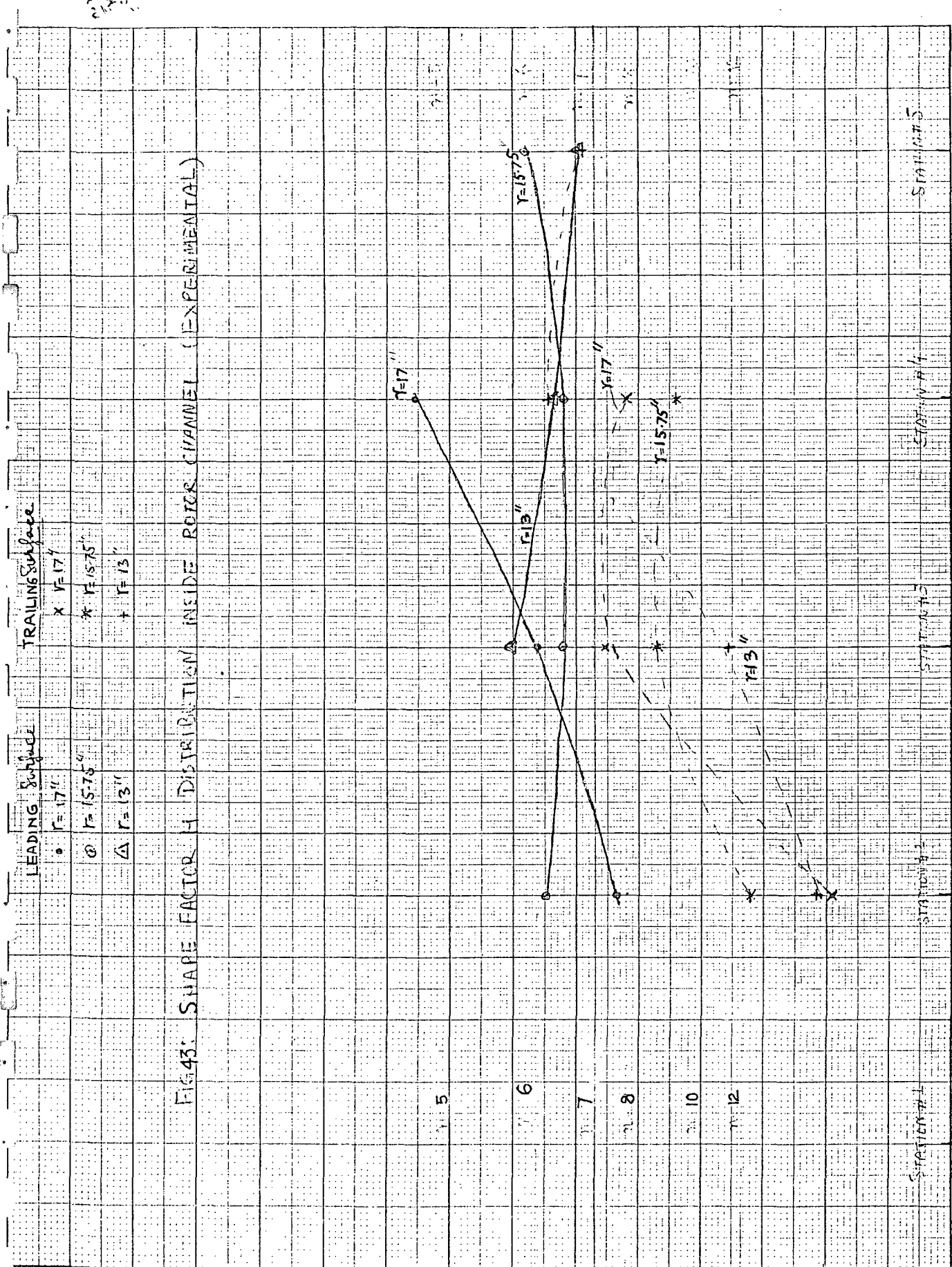


100-MICRON LINEAR  
MILLIMETER

LEUJENT, DITZON CO.  
MADE IN U. S. A.

 $\theta$  IN RADIANS





CHORDWISE DISTANCE,  $\theta$  IN RADIANS

FIG 44: DISTRIBUTION OF SHAPE FACTOR (H) OBTAINED FROM

POWER LAW FIT OF EXPERIMENTAL DATA

SYMBOLS POSS. SUCES.

H=2.5 IN +

H=3.0 IN x

H=3.75 IN o

H=4.5 IN •

LEADING SIDE

TRAILING SIDE

$r=10.75$

$r=13$

$r=15.75$

$r=17.0$

$r=15.75$

$r=17.0$

$\theta$  IN DEGREES



$C_f$  PLOT TRAILING SIDE

STATION	2	3	4	5
SYMBOL	○	●	□	△
EQ. STATIONARY	$C_{f0}$ ----			

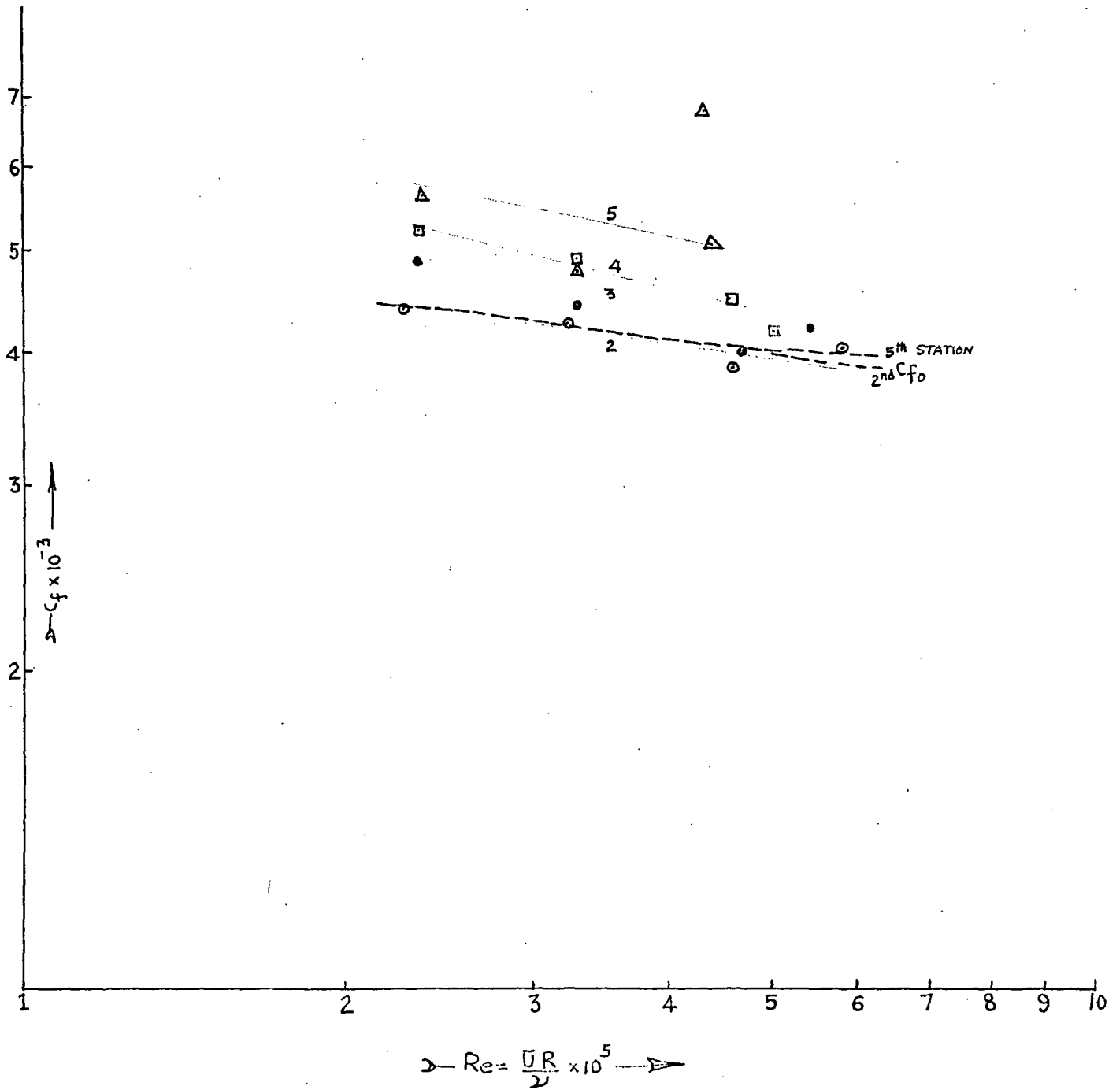


FIG 45(a) SKIN FRICTION VARIATION IN THE ROTOR PASSAGE AT TRAILING SIDE

$C_f$  PLOT LEADING SIDE

STATION 2 3 4 5

SYMBOL x \* ⊕ +

Eq. STATIONARY  $C_{fo}$  -----

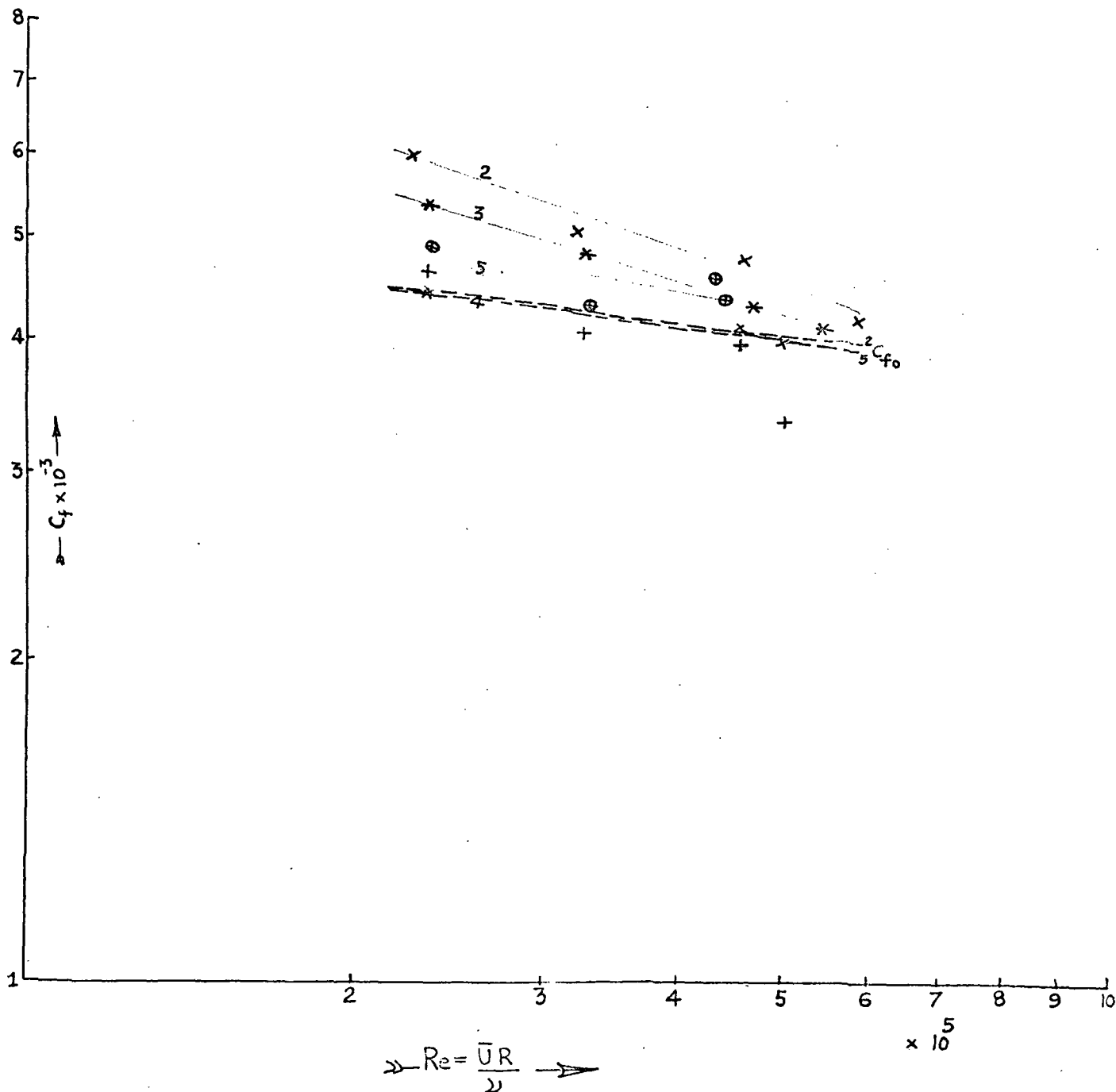


FIG 45(b) SKIN FRICTION VARIATION INSIDE ROTOR PASSAGE AT LEADING SIDE

NO. 3113 20 DIVISIONS PER INCH (1/20 DIVISIONS) OF THREE-DIGIT CIRCULAR RATIO NUMBER



RADIUS .98 .93 .86 .71 .56

LEADING SIDE \* + Δ ○ Δ

TRAILING SIDE ? ○ □

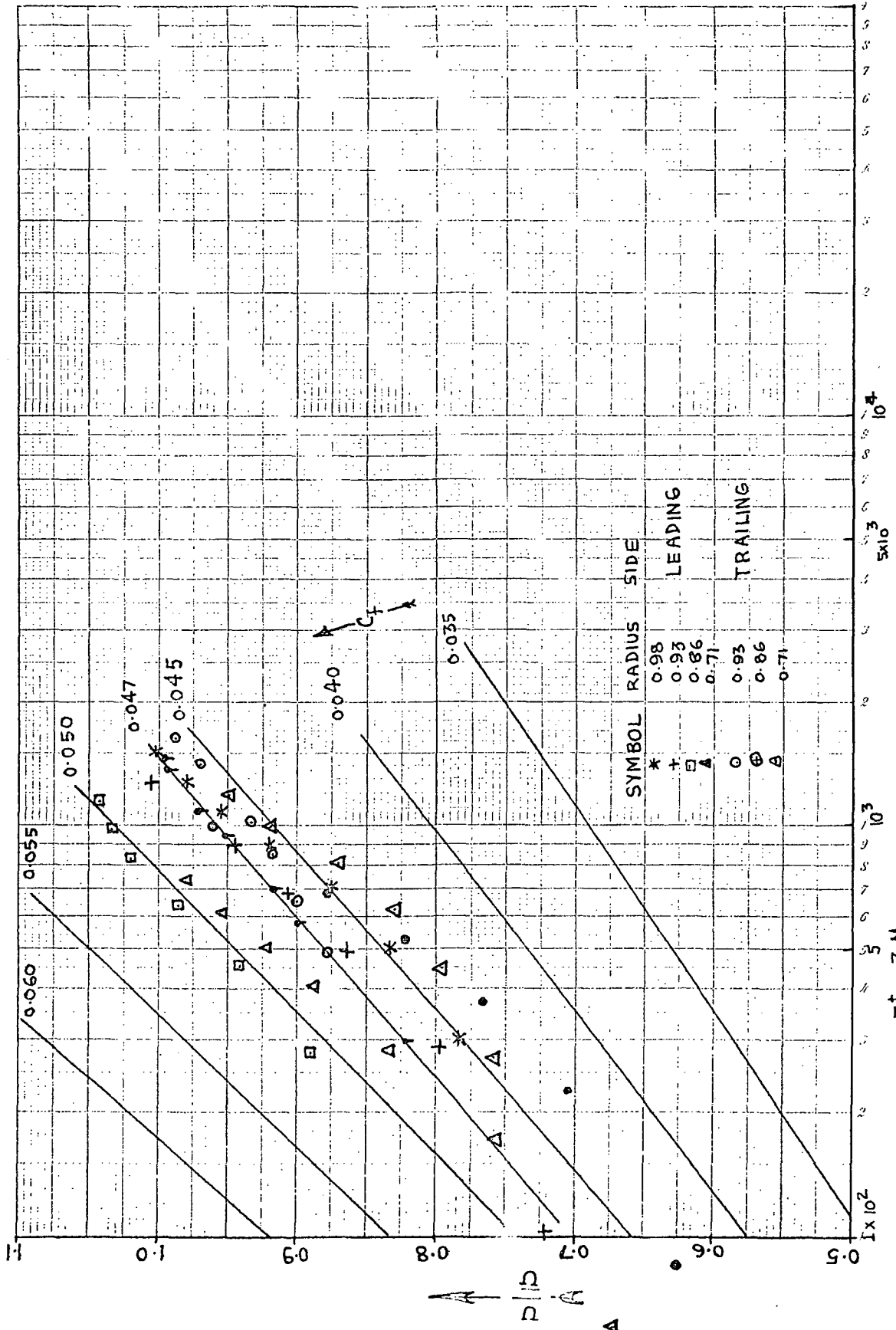


FIG 46' : SKIN FRICTION PLOT AT STATION #2

RADIUS 0.98 0.93 0.86 0.71 0.56  
 LEADING SIDE ○ ⊕ Δ  
 TRAILING SIDE \* + ▢ ▲ ■

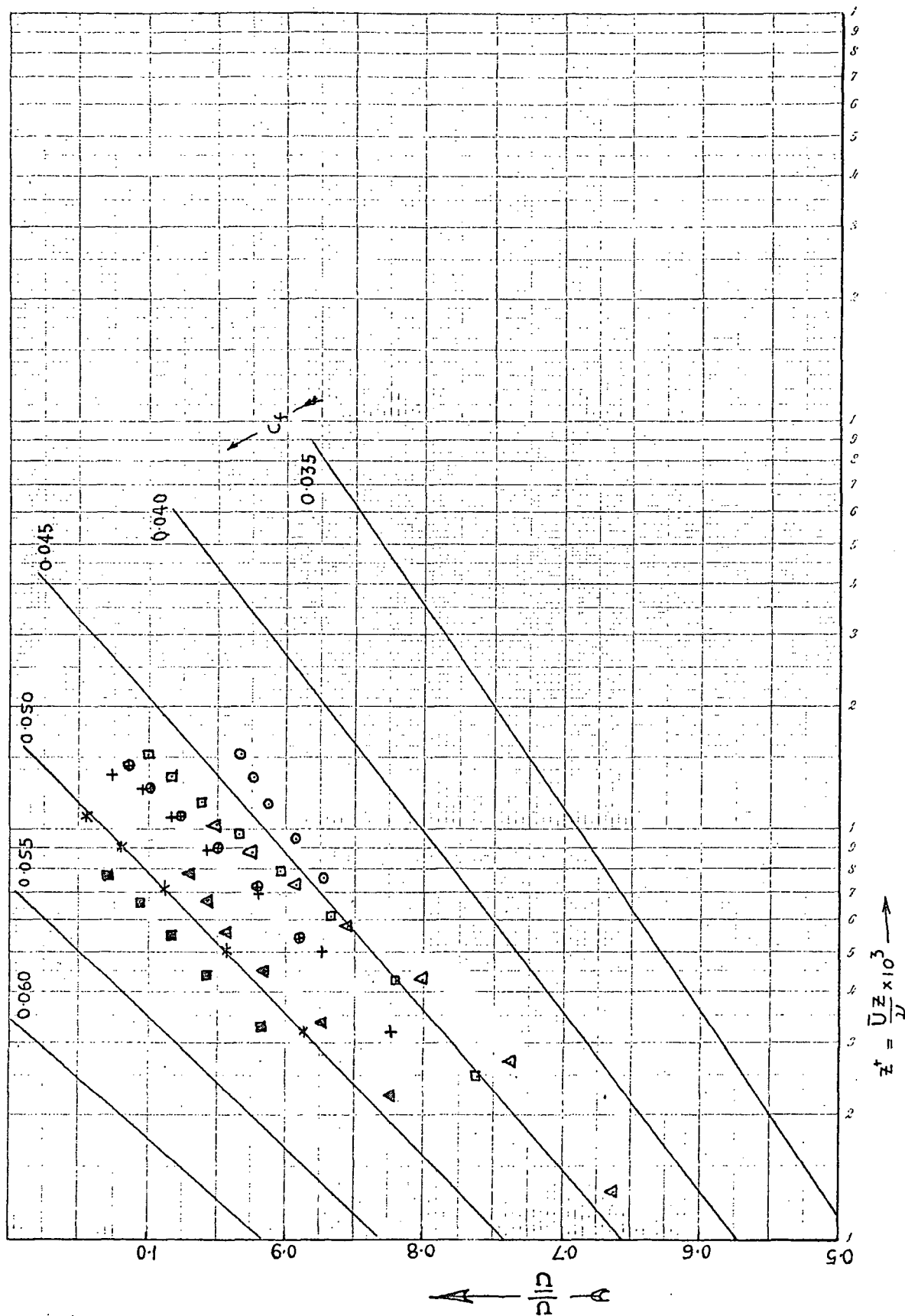
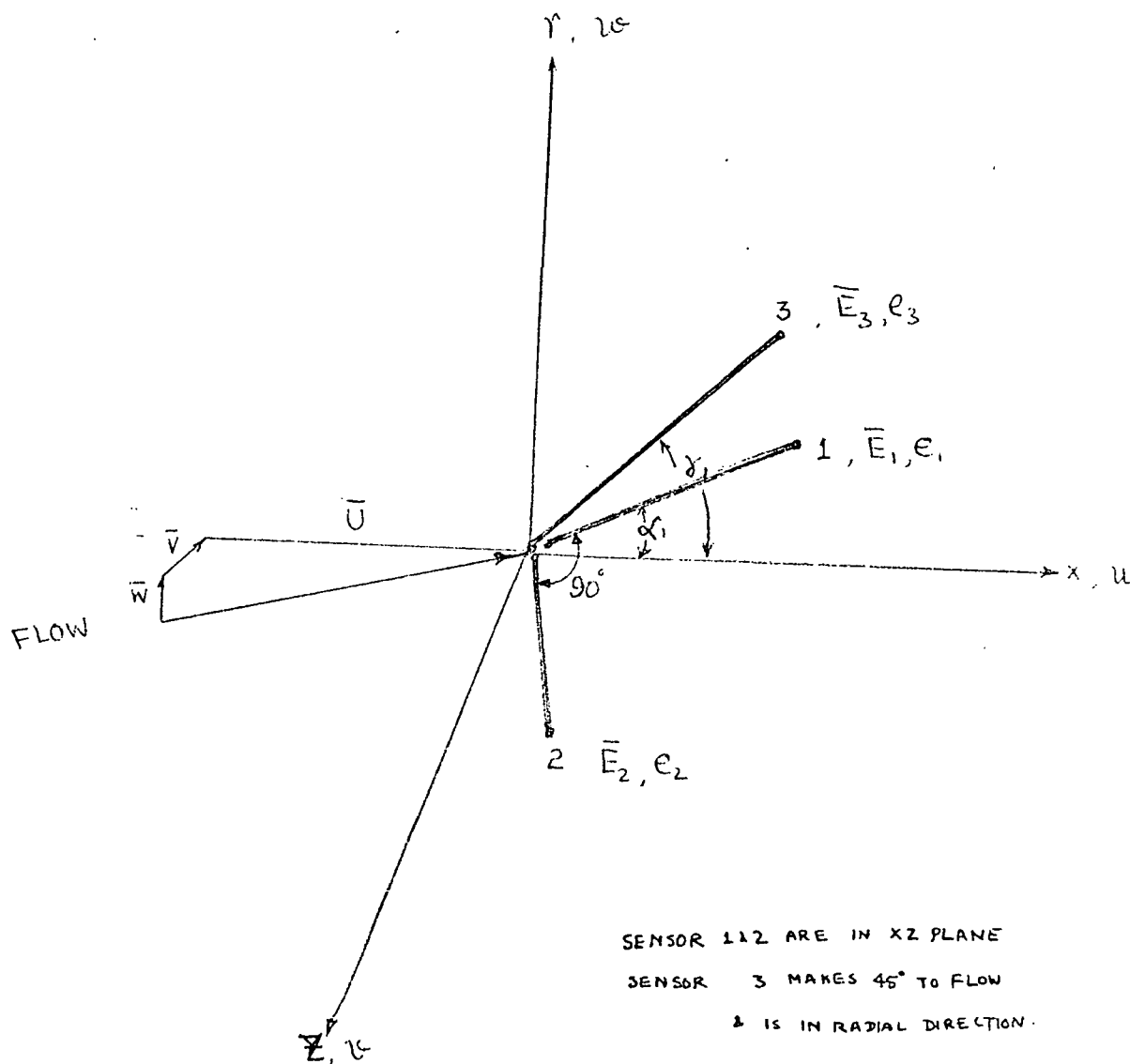


FIG 46 CLAUER PLOT OF MAIN VELOCITY PROFILE AT STATION #3



$x - y - z$  Orthogonal coordinate ~~the~~ system

$\bar{U}, \bar{V}, \bar{W}$  Mean velocity component vectors in respective directions.

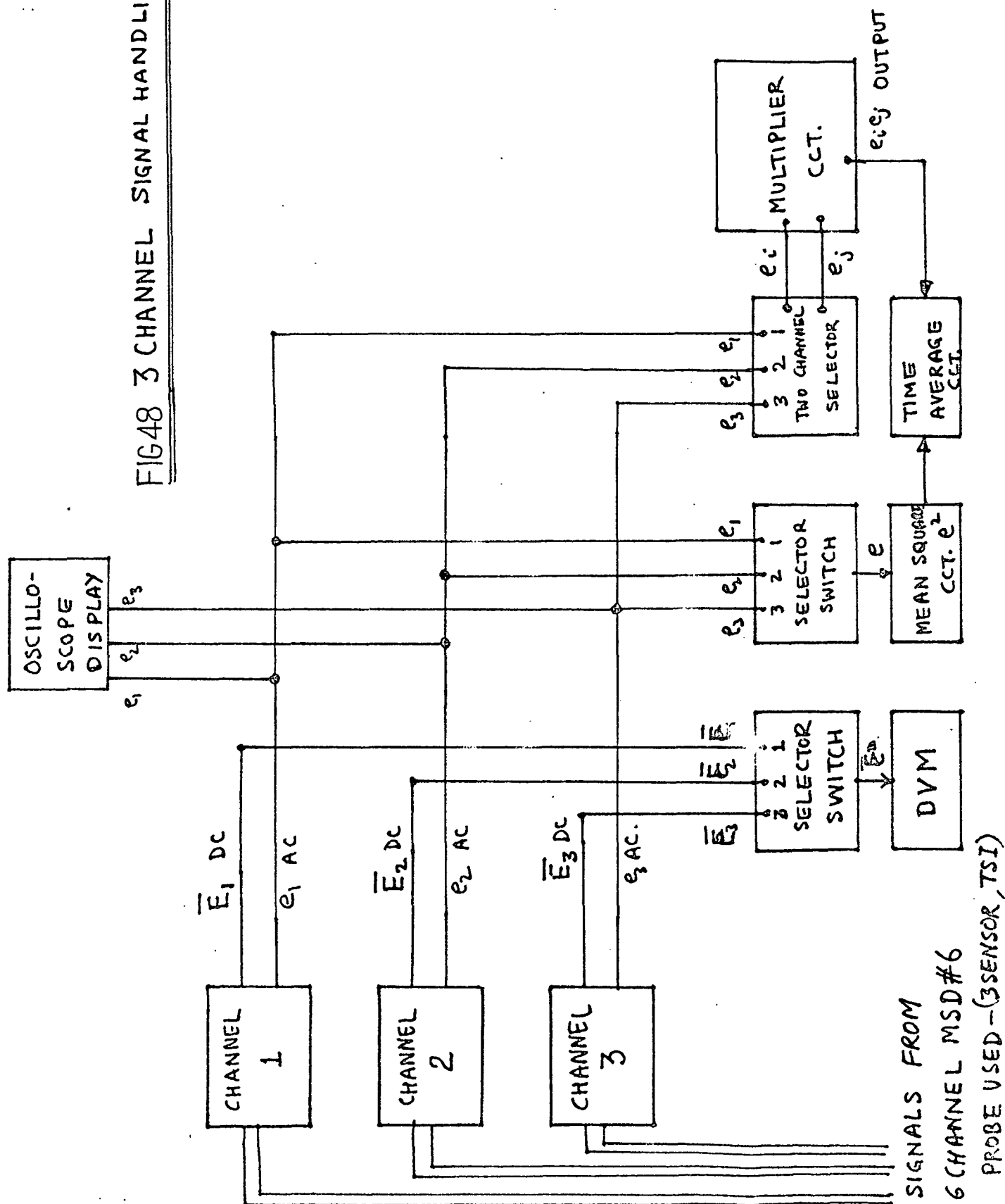
$u, v, w$  Fluctuating velocity components in same directions.

$\bar{E}_1, \bar{E}_2, \bar{E}_3$  Mean or D.C. component of sensor signal voltages in ~~directions~~  
 for the respective wires

$e_1, e_2, e_3$  Fluctuating sensor signal voltages of the three wires

FIG 47. ORIENTATION OF THREE SENSOR PROBE

FIG48 3 CHANNEL SIGNAL HANDLING SYSTEM



## Part II

### ANALYTICAL AND EXPERIMENTAL STUDY OF FLOW THROUGH A THREE-BLADED AXIAL FLOW INDUCER

## Table of Contents

	Page
List of Figures	150
List of Tables	152
Nomenclature	153
1. Introduction . . . . .	155
2. Theoretical Analysis . . . . .	156
2.1 Numerical Solution of the Inducer Flow Field. . . .	156
2.2 Initial Input to the Exact Solution Program . . . .	158
2.2.1 Grid Geometry. . . . .	158
2.2.2 Douglas Neumann Analysis . . . . .	159
2.2.3 Quasi-Three-Dimensional Analysis . . . . .	160
2.2.4 Velocity and Pressure Input Parameters . . . .	161
2.3 Exact Solution of the Inducer Flow Field. . . . .	162
2.3.1 Inviscid Solution. . . . .	164
2.3.2 Viscid Solution. . . . .	165
3. Experimental Analysis and Discussion . . . . .	168
3.1 Three-Bladed Inducer . . . . .	168
3.2 Blade Static Pressure Measurements. . . . .	170
3.2.1 Equipment Used . . . . .	170
3.2.2 Procedures and Techniques. . . . .	171
3.2.3 Blade Static Pressure Distribution . . . . .	173
3.3 Three-Sensor Hotwire Probe Measurements . . . . .	173
3.3.1 Equipment Used . . . . .	174
3.3.2 Procedure and Techniques . . . . .	176
3.3.3 Mean Velocity Profiles . . . . .	177
3.3.4 Turbulence Intensities and Stresses. . . . .	180
4. Conclusions . . . . .	181
Appendix 1: Fortran Listing of Input Program to Define Grid Geometry and Initialize Velocity and Pressure Parameters	
Appendix 2: Fortran Listing of Exact Method of Solution Incorporating Inviscid and Viscid Modifications	
Appendix 3: Derivation of the Three-Sensor Hotwire Equations	
References . . . . .	183



List of Figures

<u>Figure</u>	<u>Title</u>	<u>Page</u>
1a	Inducer Test Facility	184
1b	Inducer Inlet and Outlet Angle	184
2a	Blade Pressure Distribution at the Tip	185
2b	Blade Pressure Distribution at Mid Passage	186
2c	Blade Pressure Distribution at the Hub	187
2d	$V_{\theta}/U_t$ , $V_z/U_t$ Comparison of Results - Station 5	188
3	Inducer Geometry for Numerical Analysis	189
4	Reynolds Number vs. Skin Friction Coefficient	190
5	Location of Experimental Flow Measuring Stations	191
6	Schematic Diagram of Blade Static Pressure Test Setup	192
7a	Scanivalve	193
7b	Scanivalve Mounted in Inducer Hub	193
7c	Blade Static Pressure Test Setup	194
8a	Blade Static Pressure Distribution - Radial Station 1	195
8b	Blade Static Pressure Distribution - Radial Station 2	196
8c	Blade Static Pressure Distribution - Radial Station 3	197
8d	Blade Static Pressure Distribution - Radial Station 4	198
8e	Blade Static Pressure Distribution - Radial Station 5	199
9	Schematic Diagram of Rotating Hotwire Test Setup	200
10	Sub-miniature Triaxial Probe for Boundary Layer Flow	201
11a	Triaxial Hotwire Probe and Support	202

List of Figures (Con't)

<u>Figure</u>	<u>Title</u>	<u>Page</u>
11b	Hotwire Calibration Tunnel	202
11c	Triaxial Probe Mounted in Inducer Hub (Station 2)	202
12	Multi-Sensor Anemometer Circuit Diagram	203
13	Rotating Hotwire Test Setup	204
14a	Total Relative Velocity vs Passage Width - Station 1	205
14b	Tangential Relative Velocity vs Passage Width - Station 1	206
14c	Axial Relative Velocity vs Passage Width - Station 1	207
14d	Radial Relative Velocity vs Passage Width - Station 1	208
15	Comparison of Rotating Hotwire and Pressure Probe Measurements	209
16	Total Relative Velocity vs $r/r_t$ - Station 1	210
17a	Total Relative Velocity vs Passage Width - Station 2	211
17b	Axial Velocity vs Passage Width - Station 2	211
17c	Tangential Relative Velocity vs Passage Width - Station 2	212
17d	Radial Velocity vs Passage Width - Station 2	212
18a	Tangential Turbulence Intensity Isocontour - Station 2	213
18b	Radial Turbulence Intensity Isocontour - Station 2	214
18c	Axial Turbulence Intensity Isocontour - Station 2	215
19a	$\overline{u_\theta u_r}$ Isocontour - Station 2	216
19b	$\overline{u_\theta u_z}$ Isocontour - Station 2	217
19c	$\overline{u_r u_z}$ Isocontour - Station 2	218

List of Tables

<u>Table</u>	<u>Title</u>	<u>Page</u>
1	Percentage Chord of Blade Static Pressure Measurement Stations	219
2	Radial Location ( $r/r_t$ ) of Blade Static Pressure Measurement Stations	220

# Nomenclature

$AX, N1, N2$	=	Orthogonal coordinate system along hotwire axis
$\{a, b, c, d, e, f\}_{i=1,9}$	=	Coefficient constants in derivation of hotwire equations (Appendix 3)
$B$	=	Slope of hotwire calibration curve
$C_f$	=	Skin friction coefficient ( $= \tau \cdot 1/2 \rho \bar{w}^2$ )
$E$	=	Output D.C. voltage of hotwire anemometer
$E_o$	=	D.C. voltage of hotwire anemometer at zero velocity
$e$	=	Output A.C. voltage of hotwire anemometer
$F$	=	Body force including viscous terms
$g_o$	=	Gravitational acceleration
$h$	=	Static head
$k$	=	Correction factor for the deviation from the cosine law
$L$	=	Constant used to relate hotwire voltage and velocity
$N$	=	Number of blades
$n$	=	Unit normal to blade surface
$O(\epsilon)$	=	Terms of small order
$p$	=	Static pressure
$R$	=	Non-dimensionalized radius ( $= r/r_t$ )
$R, \theta, Z$	=	Rotating cylindrical coordinate system
$R_e$	=	Reynolds number ( $= \bar{w}r/\nu$ )
$r$	=	Local radius
$U$	=	Local blade speed ( $= R\Omega$ )
$V$	=	Resultant absolute velocity
$W$	=	Resultant relative velocity
$u, v, w$	=	Relative velocity components in the $R, \theta, Z$ directions
$Z$	=	Non-dimensional axial location ( $= z/r_t$ )
$z$	=	Local axial location

# Nomenclature (con't)

$\beta$	=	Angle of the flow with inducer axis
$\gamma$	=	Angle of the blade with inducer axis
$\theta$	=	Local tangential location
$\nu$	=	Kinematic viscosity
$\rho$	=	Fluid density
$\sigma$	=	Normal Stress
$\tau$	=	Shear stress
$\phi$	=	Inlet flow coefficient
$\psi_s$	=	Static head coefficient ( $= 2g_o h/U_t^2$ )
$\Omega$	=	Angular velocity of inducer

## Superscripts

-	=	Time averaged or passage-averaged quantity
$\rightarrow$	=	Vector quantity
'	=	Fluctuating quantity

## Subscripts

$ax, n1, n2$	=	Components along AX, N1, N2 directions
$eff$	=	Effective cooling value sensed by hotwire anemometer
$m$	=	Refers to manometer values
$r, \theta, z$	=	Components along R, $\theta$ , Z directions
$t$	=	Refers to values at the inducer tip
$1, 2, 3$	=	Refers to hotwire sensor values

## 1. INTRODUCTION

The complexity of the flow in axial inducers makes meaningful predictions extremely difficult. The long and narrow flow passages between the blades generate thick three-dimensional boundary layers, often fully developed, with large turbulence levels. The secondary motions in these inducers are not confined to thin regions at the blades, but extend over the entire cross section of the flow region.

However, in order to understand the extent of these three-dimensional effects, it is essential that there be a thorough understanding of the three-dimensional inviscid effects such as blade blockage, flow turning, etc. on the flow region. A method of obtaining the exact solution to the inducer flow field has been developed by Cooper and Bosch in Reference 1. This three-dimensional analysis employs an iterative numerical procedure to solve the equations of motion expressed in finite difference flow. The use of this procedure for the three-bladed Penn State inducer (Figure 1a) and the current analysis being undertaken to reduce the necessary computational time and incorporate the dominant viscous terms is reflected in Section 2.

Section 3 is devoted to the experimental program being conducted in the three-bladed inducer. The experimental data is used to supplement the theoretical analysis being undertaken, and vice versa, in an attempt to gain a thorough knowledge of all aspects of the inducer flow field. An extensive survey of the blade static pressures is presented, as well as preliminary results on hotwire measurements within the rotating flow passage.

A comprehensive report on these investigations is currently under preparation and will be submitted when completed.

## 2. THEORETICAL ANALYSIS

A thorough knowledge of all significant inviscid effects (blade blockage, flow turning, finite hub/tip ratio, etc.) and viscid effects (boundary layer growth, energy dissipation, etc.) is essential in the accurate prediction of the flow in all turbomachinery. Cooper and Bosch (Reference 1) have made an important contribution toward the three-dimensional inviscid flow solution. Application of this method of analysis to the Penn State inducer is given in Section 2.3. In addition, Section 2.3 includes modifications to the Cooper-Bosch method which are attempted to help reduce convergence time of the solution and provide a viscid solution capability based on empirically determined blade skin friction coefficients. A method of initializing blade flow parameters as input to the Cooper-Bosch method in a further attempt for a faster solution convergence rate is given in Section 2.2.

### 2.1 Numerical Solution of the Inducer Flow Field:

The availability of modern computers with large storage capacities and fast computation times greatly enhance the possibility of numerically solving the complete equations of motion. One of the early investigations in this area was made by Cooper and Bosch (Reference 1) for the case of the three-dimensional inviscid flow through axial flow inducers.

The application of this method to the solution of the flow in the three-bladed Penn State inducer has been reported by Poncet and Lakshminarayana in Reference 2. Because of the iterative techniques employed in the Cooper-Bosch program, a large amount of computer time is usually required to converge to a satisfactory solution. An investigation of available

mathematical methods to solve the four simultaneous nonlinear partial differential equations governing the inducer flow revealed that there was no alternate method which would solve the equations more efficiently or effectively with a minimum of programming effort than the exact method described by Reference 1. The next available approach for the speedier solution of the governing flow equations is the optimization of the input parameters of velocity and pressure which would allow faster convergence to the three dimensional solution. Cooper and Bosch have derived an approximate analysis solution to be used as an initial input to the exact program. This method derives the blade-to-blade average quantities using axisymmetric equations, then uses these quantities in a blade-to-blade solution of an integrated form of the scalar momentum equation in the tangential direction. The flow parameters derived by this method were used in Reference 2. However, a different method of developing the initial input flow parameters has been attempted in the present analysis (Section 2.2).

In addition to the development of the flow parameters, a numerical procedure to generate the axial, radial, and tangential coordinates for the three-dimensional mesh grid points required in the Cooper-Bosch analysis has been developed, allowing for easier and more accurate flow geometry input to the exact program.

The above features have been incorporated in a computer program, written in Fortran IV and run on an IBM 370/165, which produces the complete set of input parameters in the correct data format used by the Cooper-Bosch program. It is hoped that the present analysis, being



performed at Penn State, will provide a more accurate and less time consuming method for initializing the necessary input flow parameters, thus significantly reducing the convergence time required in the solution of the three-dimensional exact problem.

## 2.2 Initial Input to the Exact Program:

The input program developed in the present analysis is divided into two basic parts: the derivation of the thorough-flow mesh grid coordinate system used for the Cooper-Bosch exact analysis, and the generation of initial velocity and static pressure parameters at each three-dimensional grid point describing the flow region.

### 2.2.1 Grid Geometry

The input data required for the generation of the three-dimensional grid coordinate system include:

1. The blade profile coordinates of up to three reference blade sections defined at constant radii.
2. The thorough flow geometry mesh coordinates ( $r/r_t$  and  $z/r_t$ ) in the axial-radial plane.
3. The design values of air flow angles (Figure 1b).

Within the blade passage (between leading edge and trailing edge), the values of the tangential coordinates are generated by interpolation between the pressure and suction surfaces of the reference blade profiles. The tangential coordinates are determined at any radius (or, more precisely, the radii associated with the thorough-flow (R,Z) coordinates) by the interpolation between or extrapolation from two adjacent reference radii.

Tangential coordinates are expressed in radians, while axial and radial coordinates are nondimensionalized with respect to tip radius.

### 2.2.2 Douglas-Neumann Analysis

An initial estimation for the velocity and static pressure distribution throughout the inducer flow passage is calculated by the two-dimensional Douglas-Neumann program described in detail in Reference 3. The technique employed by the Neumann program to solve a particular fluid flow problem is to use source distributions of appropriate strength on the surface of the blade profile in such a way that the flow normal to the surface of the body is either zero or prescribed. When the Neumann boundary condition is applied, an integral equation in source strength  $\sigma$  is obtained

$$-\bar{V}_{\infty} \cdot \bar{n} = \sigma(s) + \int_{\text{body}} \sigma(q) A(q,s) dq \quad (1)$$

where  $A(q,s) = \bar{n} \cdot \bar{V}(q,s)$  and  $V_{\infty}$  is the onset flow.  $\bar{V}(q,s)$  is the velocity at a surface point  $s$  due to a unit source at  $q$ .

The solution for the general case of a lifting cascade at any angle of attack is calculated by superposition of three "basic flows" in such a way that the correct angle of attack is obtained and the Kutta condition is satisfied. The "basic" flows are: flow at zero angle of attack, flow at  $90^\circ$  angle of attack, and circulatory flow for each cascade. Superposition of solutions is possible because the potential equation is linear and the boundary condition on the cascade blade is homogeneous. In the Douglas-Neumann results, velocities and static pressure coefficients are normalized with the modulus of the average onset flow velocity

$$\frac{V_{\text{inlet}} + V_{\text{exit}}}{2} \quad (2)$$

### 2.2.3 Quasi-Three-Dimensional Modification

The investigation of the flow around an isolated airfoil in a contracting or diverging stream is presented in Reference 4. This analysis provides a simple method of modifying the two-dimensional Douglas-Neumann flow solutions to account for the three-dimensional effect of the converging or diverging streamlines. An expression for static pressure coefficient on the airfoil surface is derived as a function of channel slope, two-dimensional static pressure coefficient, and the Fourier coefficients of the blade profile. The analysis utilizes thin airfoil theory approximations and assumes that thickness effects are the same as in plane flow. The mean flow is assumed to be inviscid, steady, and incompressible, and the variation of channel height is assumed to vary linearly from leading to trailing edge while the length of the contracting section is assumed to be the same as the axial projection of the blade.

In the present application, the expression for static pressure coefficient has been modified in an attempt to represent the flow about a row of two-dimensional infinite cascades. This quasi-three-dimensional approach has been applied to the two-dimensional results obtained from the Douglas-Neumann analysis of 2.2.2 for each of the three reference blade profiles used to describe the Penn State inducer. The effect of the converging channel as determined by the above analysis on the Neumann solution for the Penn State inducer is essentially to decrease the blade static pressure near the trailing edge.

#### 2.2.4 Velocity and Pressure Input Parameters

Once all values of static pressure coefficient are calculated at three constant radii reference blade profiles by the previous analysis, the values of  $\psi_s$  at the necessary grid locations specified by the three-dimensional Cooper-Bosch input geometry are interpolated between or extrapolated from these reference values. Thus, especially at the hub inlet where  $r/r_t = .25$  (the minimum reference radius is  $r/r_t = .50$ ), the calculated  $\psi_s$  distributions are not exact and may appear distorted. One possible remedy is to run the Douglas-Neumann program for each of the flow streamlines used in the Cooper input, with blade profiles found by projection of the reference blade profiles to the required grid locations. This may be attempted at a later date. Nevertheless, using the present method of analysis, the static pressure coefficients are determined for each three-dimensional grid coordinate of the Cooper-Bosch system.

Values of radial, axial, and tangential velocities are then derived with the aid of the Douglas-Neumann program, the quasi-three-dimensional results, and the grid geometry. Thus, all the flow parameters necessary for the Cooper-Bosch analysis can be calculated. The pressure and velocity values, along with other necessary input parameters, are placed by the input program onto 9 track, 1600 BPI (Bits per inch) computer tape for acceptance by the Cooper-Bosch three-dimensional exact solution program.

Figures 2a, 2b, and 2c compare the pressure distribution derived in this analysis with design values, experimental results of Section 3.2, and previous solution results of Reference 2.

A comparison of the radial variation of axial and tangential velocities calculated by the above method with the experimental results of Reference 2 shows close agreement (Figure 2d). The agreement between the measured  $\frac{v}{U_t}$  and inviscid prediction may be fortuitious, since the axial velocity predicted at the same locations is considerably different from the measured values.

A preliminary listing of the input computer program is given in Appendix 1. The listing of the Douglas Neumann program is given in Reference 3 and is not reproduced here.

### 2.3 Exact Three-Dimensional Solution:

A method of obtaining the exact solution of the inducer flow field has been developed by Cooper and Bosch (Reference 1). This three-dimensional analysis employs an iterative numerical procedure to solve the equations of motion expressed in finite difference form. The nonlinear partial differential equations governing the flow in a rotating cylindrical coordinate system  $R, \theta, Z$  are:

$$\text{R Momentum: } \frac{g_o}{\rho} \frac{\partial p}{\partial r} + u \frac{\partial u}{\partial r} + \frac{v}{r} \frac{\partial u}{\partial \theta} + w \frac{\partial u}{\partial z} - \frac{1}{r} (v + r\Omega)^2 + F_r = 0 \quad (3)$$

$$\theta \text{ Momentum: } \frac{g_o}{\rho} \frac{\partial p}{\partial \theta} + u \frac{\partial v}{\partial r} + \frac{v}{r} \frac{\partial v}{\partial \theta} + w \frac{\partial v}{\partial z} + \frac{uv}{r} + 2u\Omega + F_\theta = 0 \quad (4)$$

$$Z \text{ Momentum: } \frac{g_o}{\rho} \frac{\partial p}{\partial z} + u \frac{\partial w}{\partial r} + \frac{v}{r} \frac{\partial w}{\partial \theta} + w \frac{\partial w}{\partial z} + F_z = 0 \quad (5)$$

$$\text{Continuity: } \frac{u}{r} + \frac{\partial u}{\partial r} + \frac{1}{r} \frac{\partial v}{\partial \theta} + \frac{\partial w}{\partial z} = 0 \quad (6)$$

Where  $w$ ,  $v$ ,  $u$  are velocities in axial, tangential and radial directions respectively. These equations are rearranged to give residuals which are reduced to zero by a relaxation procedure.

In applying this method to the Penn State inducer, the flow is assumed to be incompressible, and a grid of  $7 \times 7 \times 26$  is chosen to represent the blade passage. The flow geometry is shown in Figure 3.

The boundary condition to be satisfied on the hub, annulus walls, and the blade surfaces is  $\bar{W} \cdot \bar{n} = 0$ , where  $\bar{n}$  is the direction normal to the channel boundaries.

The first of the 26 axial stations corresponds to the upstream thorough-flow boundary where the initial conditions are applied. For the boundary value problem to be consistent, these initial upstream conditions must specify the three components of velocity and pressure, and the tangential velocity on the second axial station (which thus defines the swirl at the inlet of the inducer).

The last four axial stations correspond to the downstream flow through boundary, and extend about one-fifth of the chord length downstream of the trailing edge. With  $\bar{W} \cdot \bar{n} = 0$  to be satisfied on these stagnation stream surfaces, the set of boundary conditions for the problem is complete.

The Cooper-Bosch program has been suitably modified for use on the IBM 370/165 system at The Pennsylvania State University. For increased efficiency, the program has been compiled under a Fortran IV H level optimization procedure which shortens the time required for repetitive calculations, and production runs were submitted using the resulting object card deck.

### 2.3.1 Inviscid Solution

Using the input parameters of velocity and pressure derived from the analysis of section 2.2, preliminary results of the exact inviscid program confirm that a lower total rms (root mean square) residual is obtained than with the previous method of initializing the input variables.

As an example, the final rms residual for the inviscid results of Reference 2 was 0.12450 after 68 relaxation cycles, whereas a similar value is obtained using the present analysis in 10 relaxation cycles. This amounts to a considerable saving in computer time. Twenty-five iteration cycles has reduced the rms residual to 0.10579, indicating that a faster convergence to the solution should be possible. Further investigation should be carried out to confirm the effectiveness of the input analysis as an alternative to the Cooper-Bosch approximate solution method.

In a further attempt to decrease the convergence time, the exit flow angle was allowed to change depending upon the tangential and axial velocities calculated at the inducer trailing edge. Since the exact downstream boundaries are not known in this type of problem, it was hoped that by allowing the downstream boundaries to adjust themselves and thereby unload the blade trailing edge, a more exact definition of the downstream streamlines would result in lower rms residuals. Cooper and Bosch suggest a similar technique as a means of reducing rms residuals in their recommendations for future work.

Since the extension of the stagnation stream surfaces downstream have been constructed to be uniformly periodic with a spacing of  $2\pi/N$

(N being the number of blades), the values of velocity and pressure at the downstream tangential channel boundaries would be equal. This condition is applied at the blade trailing edge after each iteration cycle, resulting in an outlet angle defined by  $\beta = \tan^{-1} \frac{v}{w}$ . The change in outlet air angle, if any, is then used to recalculate the downstream stagnation stream surfaces.

This method also has the advantage of automatically forcing the Kutta-Joukowski condition for the blade pressure distribution to be satisfied. Changes made to the original Cooper-Bosch program can be seen in Appendix 2 and are concentrated in subroutine "Main".

As yet, this analysis has been untested.

### 2.3.2 Viscid Solution

In addition to the attempts to improve the convergence of the exact inviscid solution, a method of incorporating viscous effects into the governing equations of motion has also been investigated. The viscous equations of motion are:

R Momentum:

$$\frac{1}{\rho} \frac{\partial p}{\partial r} + v \frac{\partial u}{r \partial \theta} + u \frac{\partial u}{\partial r} + w \frac{\partial u}{\partial z} - (v + r\Omega)^2 = \frac{1}{\rho} \left[ \frac{\partial \tau_{r\theta}}{r \partial \theta} + \frac{\partial \tau_{rz}}{\partial z} + \frac{\partial \sigma_{rr}}{\partial r} + \frac{\sigma_{rr} - \sigma_{\theta\theta}}{r} \right] \quad (7)$$

$\theta$  Momentum:

$$\frac{1}{\rho r} \frac{\partial p}{\partial \theta} + v \frac{\partial v}{r \partial \theta} + u \frac{\partial v}{\partial r} + w \frac{\partial v}{\partial z} + \frac{uv}{r} + 2\Omega u = \frac{1}{\rho} \left[ \frac{\partial \sigma_{\theta\theta}}{r \partial \theta} + \frac{\partial \tau_{\theta z}}{\partial z} + \frac{\partial \tau_{\theta r}}{\partial r} + \frac{2}{r} \tau_{\theta r} \right] \quad (8)$$



Z Momentum:

$$\frac{1}{\rho} \frac{\partial p}{\partial z} + \frac{v}{r} \frac{\partial w}{\partial \theta} + u \frac{\partial w}{\partial r} + w \frac{\partial w}{\partial z} = \frac{1}{\rho} \left[ \frac{\partial \tau_{z\theta}}{r \partial \theta} + \frac{\partial \sigma_{zz}}{\partial z} + \frac{\partial \tau_{rz}}{\partial r} + \frac{\tau_{rz}}{r} \right] \quad (8)$$

Where

$$\begin{aligned} \sigma_{\theta\theta} &= -\overline{v'^2}, \quad \tau_{\theta z} = -\overline{v'w'} = \tau_{z\theta} \\ \sigma_{rr} &= -\overline{u'^2}, \quad \tau_{rz} = -\overline{u'w'} = \tau_{zr} \\ \sigma_{zz} &= -\overline{w'^2}, \quad \tau_{\theta r} = -\overline{v'u'} = \tau_{r\theta} \end{aligned} \quad (9)$$

Molecular viscosity terms have been neglected in these equations.

Comparing these equations with the momentum equations used by Cooper and Bosch, the following expressions for FR, FT, and FZ (the exact program variables for viscous loss terms) can be given as:

$$FR = -\frac{1}{\rho} \left[ \frac{\partial \tau_{r\theta}}{r \partial \theta} + \frac{\partial \tau_{rz}}{\partial z} + \frac{\partial \sigma_{rr}}{\partial r} + \frac{(\sigma_{rr} - \sigma_{\theta\theta})}{r} \right] \quad (10)$$

$$FT = -\frac{1}{\rho} \left[ \frac{\partial \sigma_{\theta\theta}}{r \partial \theta} + \frac{\partial \tau_{\theta z}}{\partial z} + \frac{\partial \tau_{\theta r}}{\partial r} + \frac{2}{r} \tau_{\theta r} \right] \quad (11)$$

$$FZ = -\frac{1}{\rho} \left[ \frac{\partial \tau_{z\theta}}{r \partial \theta} + \frac{\partial \sigma_{zz}}{\partial z} + \frac{\partial \tau_{rz}}{\partial r} + \frac{\tau_{rz}}{r} \right] \quad (12)$$

Since the stagger angle is very large, these viscous terms can be approximated at the blade surface by neglecting second order terms as well as normal shear stresses to the following expressions:

$$FR = - \frac{1}{\rho} \frac{\partial \tau_{rz}}{\partial z} \quad (13)$$

$$FT = - \frac{1}{\rho} \frac{\partial \tau_{\theta z}}{\partial z} \quad (14)$$

$$FZ = - \frac{1}{\rho} \frac{\partial \tau_{z\theta}}{r \partial \theta} \quad (15)$$

The distribution of wall shear stress is assumed to be linear across the flow passage from pressure surface to suction surface. The values of wall shear stress are assumed to be known from previous experimentation. Skin friction coefficient  $C_f$  for a four blade flat plate helical channel is given in reference 5. The results, summarized in Figure 4, are considered to be valid for the three blade inducer under consideration. Interpolation of the curves in Figure 4 for a given blade surface grid location under consideration gives a value of shear stress  $\tau = C_f \cdot \frac{1}{2} \rho \bar{W}^2$  for the appropriate Reynolds number  $R_e = \frac{\bar{W} R}{\nu}$  of the flow at that point, where  $\bar{W}$  is the average relative velocity across the flow passage. Calculation of  $\tau$  at each grid location within the flow passage allows the derivatives of equations (13)-(15) to be calculated by finite difference methods.

The changes to the original Cooper and Bosch exact program necessitated by the inclusion of the viscous loss terms are made in subroutines "Main", "Dloss", and "Resid" and are shown in Appendix 2.

The effect of the viscous loss terms in the exact three-dimensional analysis is, as yet, untested.

### 3. EXPERIMENTAL PROGRAM AND DISCUSSION

The primary goal of performing the following experimental program is to investigate the flow characteristics such as velocity, turbulence, and static pressure of the relative flow inside a three bladed inducer. The importance of this experimental data for a better understanding and prediction of the flow is mentioned in section 1.

A secondary goal is the determination of the effectiveness of triaxial rotating hotwire as a method of measuring mean and fluctuating velocities and turbulence stresses within the inducer blade passage.

#### 3.1 Three Blade Inducer:

The experimental investigation is performed on a three foot diameter axial flow inducer with three equally spaced blades. The test facility is pictured in Figure 1a. Design of the blades are by the mean streamline method of Wislicenus (Reference 6). The inducer is operated at 450 rpm, which is determined to an accuracy of 0.1 rpm by means of a photocell circuit with rotating calibrated disk and displayed on an electronic counter.

Important parameters of the inducer are as follows:

Number of Blades	3
Hub Tip Ratio at Outlet	0.50
Hub Tip Ratio at Inlet	0.25
Radial Clearance	0.0625"
Inlet Flow Coefficient (Design)	0.065
Blade Chord at $r/r_t = 1.0$	82.96"
Blade Chord at $r/r_t = 0.75$	63.18"
Blade Chord at $r/r_t = 0.50$	49.94"

Solidity at $r/r_t = 1.0$	2.15	
Solidity at $r/r_t = 0.75$	2.21	
Solidity at $r/r_t = 0.50$	2.61	
Reynolds Number Based on Tip Radius	$7.0 \times 10^5$	
Maximum Deviation of Camber Line	$r/r_t = 1.0$	.00637
from Mean Streamline	$r/r_t = 0.75$	.01075
$(\frac{\Delta n}{L})_{\max}$	$r/r_t = 0.50$	.020

The design blade and flow angles are given in Figure 1b.

The use of the three bladed inducer for the continued experimental investigation defined in this report is a result of conclusions reached by prior analysis and detailed in Reference 2; namely, it has appreciably better performance than a similar four bladed inducer tested at the same flow coefficient.

Blade static pressure measurements were obtained with use of hypodermic steel tubing of .063" ID imbedded in the blade at ten separate pressure and suction surface locations. The pressure measurements were carried out at five radii from taps of .063" diameter drilled at equally spaced intervals from tip to hub. The chordwise location of these stations are given in Table 1. The radial location of the stations are given in Table 2.

Velocity and turbulence measurement stations within the blade passage have been previously used (Reference 2) and were constructed by cutting tangential slots in the hub wall at the locations described in Figure 5.

The inducer is statically and dynamically balanced at facilities in the Garfield Thomas Water Tunnel of The Pennsylvania State University.

### 3.2 Blade Static Pressure Measurement:

An extensive experimental investigation of the blade static pressure distribution has been undertaken to help provide a check on prior theoretical analyses and provides information useful in formulation of future theoretical development.

#### 3.2.1 Equipment Used:

A schematic diagram of the blade static pressure test setup is shown in Figure 6. The equipment used to measure the blade static pressure distribution of the three bladed inducer described in detail in Section 3.1 is as follows:

1) Scanivalve - The scanivalve (Figure 7a), a scanning type pressure sampling valve for measuring multiple pressures was mounted in the rotating hub section of the inducer. The scanivalve incorporates a fluid wafer switch for time sharing one pressure lead with up to twenty four (24) unknown pressures, and is stepped by a ratchet-gear solenoid.

2) Solenoid Controller - A solenoid controller uses push button pulse length feedback and increased drawing voltage to step the solenoid driven scanivalve. The controller was equipped with a 24-division indicator dial which allowed monitoring of the static pressure station under consideration.

3) Three Channel Pressure Transfer Device (PTD) - A 3-channel pressure transfer device, constructed by the Penn State Aerospace Department, is used to transfer the static pressure measurements from the rotating reference frame of the three bladed inducer to the stationary

reference frame. Each channel is made airtight by the use of double sealed ball bearings, and pressure leakage is prevented by use of O-rings and plastic sealers. The PTD is mounted on a stand outside the rotor assembly and is housed in a streamlined cowling to reduce any interference on the incoming flow.

4) Slip Ring Unit - An eight-channel slip ring unit, constructed by the Penn State Aerospace Department, is used to conduct electrical signals from the stationary reference frame to the rotating reference frame of the scanivalve. Electrical continuity is provided by carbon brushes in contact with a rotating commutator aligned along the inducer's rotational axis. The slip ring unit is mounted on the pressure transfer device, and all electrical and pressure connections are transferred through a hollow shaft and flexible couplings to the nose cone of the inducer.

5) Peripheral Equipment - A transistorized 30 volt D.C. power supply was used to provide voltage to the scanivalve and solenoid controller units. A micromanometer graduated in 0.001" divisions was used to measure the blade static pressure.

### 3.2.2 Experimental Procedure and Techniques:

Flexible vinyl tubing of 0.063" inside diameter was used to connect the ten suction and ten pressure surface stations to the available tubes on the scanivalve (Figure 7b). The vinyl tubing was also used to connect the collection tubulation of the scanivalve to the measurement channel of the pressure transfer device. The manometer was similarly joined to this

channel. Electrical connections from the scanivalve were transferred through the slipring unit to the solenoid controller and power supply (Figure 7c). Masking tape was used to cover the radial pressure taps not under consideration in a particular run.

Once the inducer speed was adjusted to 450 rpm, the static pressures associated with the ten pressure and ten suction surface stations at a particular radial passage location could be measured by stepping the scanivalve through its range of operation. The dial on the solenoid controller would indicate which station pressure was being measured. Each step provided the blade static pressure of a different chordwise station. Pressure readings were measured on the micromanometer to 0.001". Once all readings for a particular radial passage location were obtained, the inducer was brought to rest and the next radial passage location was considered by uncovering the static pressure taps associated with it and covering the previous tap locations.

Since the blade static pressure measurements were taken on the rotating blade, it is necessary to apply a centrifugal force correction to obtain the static head. If  $h_m$  is the height of the water column measured by the manometer, the actual static head is given by

$$h_s = \frac{\rho_m}{\rho} h_m + \frac{\Omega^2}{2g} (r^2 - r_o^2) \quad (16)$$

where  $\rho_m$  is the density of the manometer liquid,  $r_o$  is the radius of the rotating shaft used in the pressure transfer device, and  $r$  is the radius of the static pressure tap under consideration.

From this, the blade static pressure coefficient is defined by

$$\psi_s = \frac{2gh_s}{U_t^2} \quad (17)$$

and is calculated for all pressure measurement stations.

### 3.2.3 Blade Static Pressure Results:

Experimental results are plotted in Figures 8a-8e for the various radial passage locations. Comparison of these results with the exact analysis results of Reference 2 show close agreement, especially in the tip region (Figure 2a). The Cooper-Bosch program, however, predicts negative  $\psi_s$  for the pressure surface near the leading edge for all passages considered, when in fact this result was not noticed during experimentation. Near the blade tip,  $\psi_s$  is positive near the suction surface leading edge and becomes negative at approximately 20 percent chord. The magnitudes of  $\psi_s$  agree favorably, especially at the trailing edge where little discrepancy is noted.

The values of  $\psi_s$  obtained from the Douglas-Neumann approach of Section 2.2 agree favorably at the tip and mid passage, but is noticeably different at the hub, due perhaps to the method of extrapolation used in the construction of that curve, as mentioned in Section 2.2.4. The quasi-three-dimensional approach has been intended, however, only as a means of closely approximating input flow parameters for the Cooper-Bosch analysis and, thus, is shown in Figures 2a-2c only to indicate its relative proximity to the experimental and exact solutions.

### 3.3 Three Sensor Rotating Hotwire-Measurements:

Initial feasibility investigation into the use of the hotwire anemometer in the rotating flow passage of the three blade Penn State inducer has been mentioned in Reference 5. One problem experienced has been the inability of the relatively crude slipring unit to maintain



the continuity of the hotwire circuitry. It did not allow suitable operation of the hotwire for extended periods of time to allow meaningful measurements to be obtained. The present study is an attempt to improve upon the accuracy and longevity of the initial investigation and prove the suitability of hotwires in the measurement of the relative mean and fluctuating velocities in a rotating environment.

### 3.3.1 Equipment Used:

A schematic diagram of the rotating hotwire test setup is given in Figure 9. A detailed description of the equipment used in the measurement of the relative mean and fluctuating velocities within the rotating passage of the three bladed inducer follows:

1) Triple Sensor Hotwire Probe - A subminiature triaxial probe designed for boundary layer flows was used in the experimentation (Figure 10). The wire is 3  $\mu\text{m}$  diameter copper plated tungsten with a length/diameter ratio of approximately 300. The probe is attached to a specifically designed probe support for use in traversing the inducer flow passage (Figure 11a).

2) Three-Channel Constant Temperature Hotwire Anemometer - Two dual channel constant temperature hotwire anemometers are being used to provide the three channel capability necessary for these measurements. The original circuitry is shown in Figure 12, but is modified slightly for higher output voltage levels.

3) Mercury Slip Ring Unit - A ten-channel mercury slip ring unit was utilized in the rotating hotwire measurements conducted on the three bladed inducer. The slip ring unit exhibits the smallest and most stable

resistance in the transfer of measuring signals from the rotating electrical elements to the stationary electrical conductors. Contact between the rotating wires and the stationary contact screws is made through a round contact disc to which the rotating wire is connected, rotating in mercury. Triple distilled mercury is used to provide the greatest conductivity and the lowest noise level distortion possible.

4) Peripheral Equipment - The A.C. voltage signals obtained from the hotwire anemometer are visualized on a four-channel storage Tektronix-600 oscilloscope. Instantaneous mean velocity D.C. voltage readings from the anemometers are displayed on a digital voltmeter.

The fluctuating voltage (A.C.) signals are processed through a 5.0 KHZ low-pass filter driven by a 15-volt regulated power supply, which is used to cut off the high frequency noise which may have entered the circuit.

Mean square values of the A.C. voltages are obtained by passing the signals through a true rms voltmeter and subsequently through a manually controlled signal integrator. The mean squared voltage is displayed on a digital voltmeter.

A sum-and-difference circuit is utilized to obtain the sum and difference between the three hotwire signals needed for the turbulence intensity calculations (Section 3.3.2).

A wave analyzer is used for sinewave signal generation to determine gains throughout the hotwire circuitry and the accuracy of the associated peripheral equipment.

5) Calibration Equipment - A low turbulence calibration tunnel is used for the hotwire calibration. The horizontal wind tunnel has a

test cross-section of 1 1/2" x 1 1/2" and operates within the range of air velocities of 0 to 300 feet per second (Figure 11b). The calibration velocities were measured with a nonshielded pitot tube and the micro-manometer of section 3.2.1.

### 3.3.2 Experimental Procedures and Techniques:

Measurements were taken at two axial stations, corresponding to approximately 33 percent and 90 percent of the blade chord (Figure 5). Various velocity measurements have previously been performed at these stations (Reference 2) and thus a comparison of hotwire experimental results with these prior investigations are possible.

Six radial stations (corresponding to  $r/r_t$  values of .973, .945, .890, .781, .671, .548) at station 1 and five radial stations ( $r/r_t$  locations of .973, .945, .890, .781, .671) at station 2 are traversed at several tangential intervals in an attempt to get an accurate and detailed appraisal of the flow velocities, turbulence intensities and stresses in these regions.

The three sensor probe is attached to a ten-inch section of aluminum tubing and fixed in a particular radial and tangential locations by a coupling mounted in the inducer hub (Figure 11c). The probe is accurately aligned in the tangential direction with the aid of the guide vane attached to the probe's adjustable protection pin. Orientation of the three individual hotwires was measured with respect to the  $(r, \theta, z)$  coordinate system by utilizing a linearly calibrated scale eyepiece in a 30-X Bosch and Lomb microscope. The direction cosines of this orientation was then calculated, as was direction cosines

of the two arbitrary normals to each wire. These values were used in the governing hotwire equations derived in Appendix 3.

The experimental setup for the hotwire measurements is shown in Figure 13. With the probe in position, the inducer is started and rotated to 450 rpm. The corresponding mean D.C. voltages of the three hotwire channels  $E_1$ ,  $E_2$ ,  $E_3$  are recorded, in addition to the A.C. fluctuation voltage values of  $\overline{e_1'^2}$ ,  $\overline{e_2'^2}$ ,  $\overline{e_3'^2}$ ,  $\overline{(e_1' + e_2')^2}$ ,  $\overline{(e_1' - e_2')^2}$ ,  $\overline{(e_1' + e_3')^2}$ ,  $\overline{(e_2' + e_3')^2}$ ,  $\overline{(e_2' - e_3')^2}$ ,  $\overline{(e_1' - e_3')^2}$ .

Mean voltages are obtained over an integration of 100 seconds. The inducer is then stopped, the probe is moved to another location, and the procedure repeated until the flow field is entirely surveyed. Station 1 and Station 2 are surveyed similarly, except that no turbulence measurements were recorded at station 1.

The resultant voltage measurements from the three channel rotating hotwire experiment are converted to mean velocities  $u$ ,  $v$ ,  $w$  and turbulence quantities  $\overline{u'^2}$ ,  $\overline{v'^2}$ ,  $\overline{w'^2}$ ,  $\overline{u'v'}$ ,  $\overline{u'w'}$ ,  $\overline{v'w'}$  from the appropriate calibration curves and the applicable equations derived from the hotwire orientation as explained in Appendix 3.

The data reduction was accomplished in a computer program written to solve, for all flow stations considered, the resulting three simultaneous mean velocity equations and six simultaneous turbulence velocity equations. The IBM 370/165 of the Penn State computation was used in this task.

### 3.3.3 Mean Velocity Profiles:

The mean velocity profiles of  $W/U_t$ ,  $u/U_t$ ,  $v/U_t$  and  $w/U_t$  are plotted versus percentage of passage width for station 1 in Figures 14a-14d and for station 2 in Figures 17a-17d. The variation of these profiles with various  $r/r_t$  can readily be seen.

Measurements at Station 1:

Total Relative Velocity - Figure 14a shows the tangential variation of total velocity  $W/U_t$ . Comparison of this profile with the results of Reference 2 obtained by pressure probe measurements show good agreement at two similar radii (Figure 15). A velocity deficiency is noted in Figure 14a at approximately 55 percent passage width for all radial stations, but it is especially pronounced near the tip. This seems to indicate a concentration of high turbulence intensities in this region and, indeed, qualitative measurement of the A.C. fluctuating voltages confirm this fact. From the passage measurements of Figure 14a, the suction surface boundary layer can be discerned, appearing to grow in thickness near the tip. The effects of tip losses are apparent from Figure 16 where total relative velocity is plotted versus radius. The deviation of the flow from ideal conditions is apparent near the tip. As no evidence can be detected of the pressure surface boundary layer, it indicates that the suction surface boundary layer is larger than that of the pressure surface. It should be remarked here that no measurements are taken close to the wall. Since the blade element is not radial, the probe could not be located very close to the wall.

Axial Velocity - Figure 14c shows axial velocity  $w/U_t$  versus percentage of passage width. The general trend for the tangential variation of axial velocity at the radii considered shows an increase toward the pressure surface. The radial variation of the axial velocity shows the largest values near the hub, decreasing consistently towards the tip. This tends to indicate the effect of blade blockage on the axial velocity distribution.

Radial Velocity - Figure 14d depicts the tangential variation of the radial velocity  $u/U_t$ . Large values are shown to exist near the suction surface at radii close to the hub, indicating higher radially outward flow in this region. Near the tip regions, the profiles show a contour change at mid passage which may be interpreted as an indication of radially inward flow.

Measurements at Station 2:

Total Relative Velocity - The tangential variation of total velocity  $W/U_t$  is shown in Figure 17a. Again, as in station 1, a velocity deficiency is noticed at approximately 40 percent passage width. A growth in the dimensions of the eddy near the trailing edge can be seen by comparison with Figure 14a. The relative velocity distribution from  $R = 0.781$  to  $0.973$  are similar with very nearly same average values. Furthermore, the average values  $(\bar{w}/U_t)$  are considerably less than the design values.

Axial Velocity - Figure 17b gives the tangential variation of axial velocity  $w/U_t$ . Overall magnitudes, of course, are higher than station 1 due to the converging annulus. Again, as in station 1, the radial distribution of axial velocity show larger values toward the hub to indicate the continuing presence of the blade blockage effect. In comparison, the opposite trend was found in Reference 2 at downstream locations where no blade blockage effects should be present. The pressure surface boundary layer is evident near the hub and displays a greater thickness in this region than near the tip.

Radial Velocity - The variation of radial velocity  $u/U_t$  across the passage is shown in Figure 17d. The overall magnitudes appear

larger than at station 1. The radial variation of velocity show higher values of radial velocity near the hub, with smaller magnitudes progressing toward the tip. No evidence of radially inward flow is noticed at midpassage, although the large change in velocity at approximately 25 percent passage width near the tip indicates perhaps some change of direction may be occurring there.

### 3.3.4 Turbulence Intensities and Reynolds Stresses:

The turbulence intensities  $\sqrt{u'^2}/W$ ,  $\sqrt{v'^2}/W$ ,  $\sqrt{w'^2}/W$  are plotted in iso-contour form in Figures 18a-18c. The contours for all three intensity components are essentially the same, showing a pocket or core of high turbulence centered at 40 percent passage width and this agrees with the total velocity deficiency noted in Section 3.3.3 in this region. Turbulence levels are generally higher near the tip, whereas magnitudes of the hub are generally constant across the blade passage.

Relative magnitudes of turbulence intensities rank  $\sqrt{w'^2}/W$  highest, with  $\sqrt{u'^2}/W$  and  $\sqrt{v'^2}/W$  following in order. Maximum turbulence intensities of 25 percent are measured, which are considered high for the linear assumptions made in the derivation of the hotwire equations. Hence, some error is expected in the evaluation of intensity from the hotwire equations.

The isocountour Reynolds stress distributions,  $\overline{u'v'}/W^2$ ,  $\overline{u'w'}/W^2$  and  $\overline{v'w'}/W^2$  within the blade passage are given in Figures 19a-19c. Concentrations in stress intensities are similar to the previous turbulence intensity contours, but with slightly different passage locations.

#### 4. CONCLUSIONS

A brief summary of conclusions reached by the investigation recorded in this report are as follows:

1) The input program derived in Section 2.2 appears to provide a better initialization of velocity and pressure parameters needed for the Cooper Bosch exact solution. Evidence of this is shown by initial exact solution inviscid results which indicate a reduction of total RMS residual after a similar number of relaxation cycles from results of Reference 2.

2) Modifications to the Cooper Bosch program to automatically unload the trailing edge station and incorporate dominant viscid effects have been made in subroutines "Main", "Dloss", and "Resid". These modifications have yet to be tested, but significant improvements are expected and will be presented in the comprehensive report to follow.

3) A method to obtain velocity and turbulence measurements in the rotating blade channel has been tested. The triaxial hotwire probe in rotation utilized in this study have yielded satisfactory velocity profiles and turbulence intensity measurements. Comparison of velocities derived from rotating hotwire with those derived by rotating pressure probe measurements of Reference 2 show good agreement. It can be concluded that hotwire anemometry can be an extremely useful tool in the experimental determination of relative flow parameters in a rotating environment.

4) Turbulence levels within the blade passage, indicated from the experimental results of this report, are generally high near the tip regions and, in particular, a growing core of high turbulence is evident at mid passage. This necessarily indicates the significant extent of flow mixing due to boundary layer interaction, radially outward flow, annulus wall effect, etc. which is prevalent within the long narrow passages of the inducer channel.

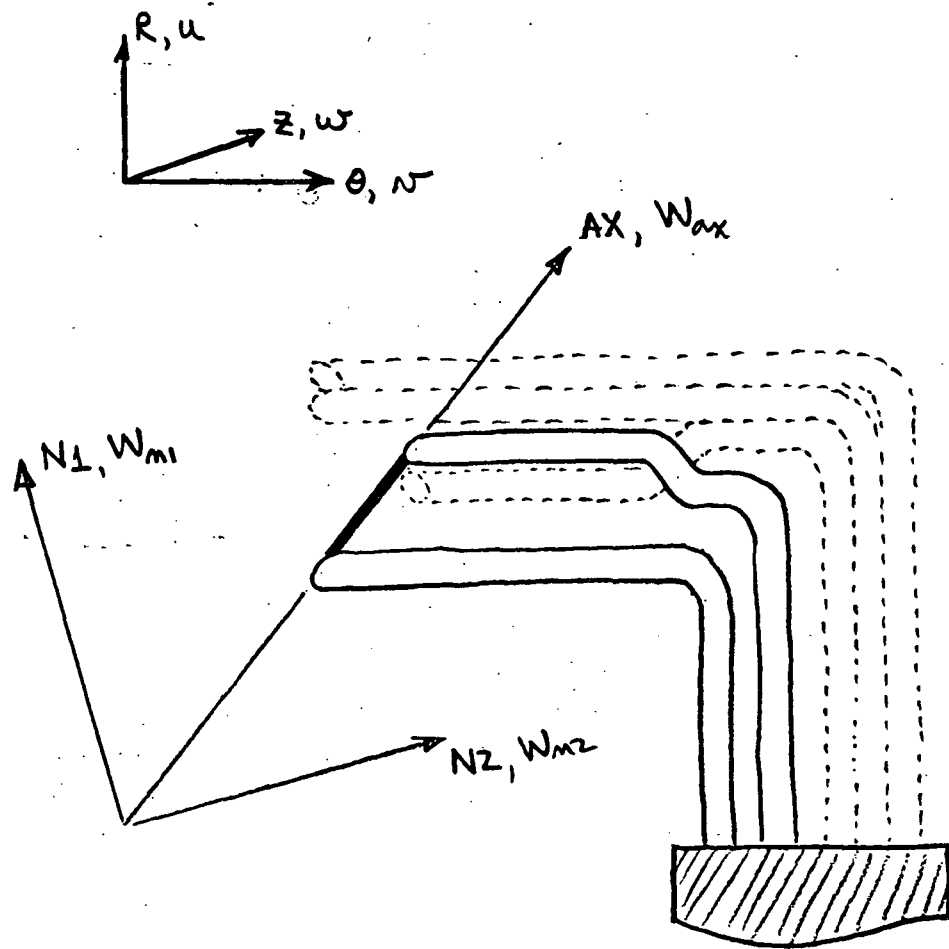


5) Overall agreement between all velocity components and pressure distributions obtained by present experimentation, prior experimentation, present theoretical analysis, and prior theoretical investigations is good. Detailed comparison will be presented in the later report.

# APPENDIX 3: Derivation of Equations for A Three-Sensor Probe

## A3.1 Direction Cosine Method for Non-Orthogonal Probes:

Consider one hotwire sensor with respect to the  $(R-\theta-z)$  coordinate system.



Hotwire (1) has an orthogonal coordinate system associated with its position  $(AX, N1, N2)$ . This  $(AX, N1, N2)$  coordinate system can be transformed to the  $(R-\theta-z)$  coordinate system by:

$$W_{ax} = a_1 v + b_1 u + c_1 w \quad (1)$$

$$W_{m1} = a_2 v + b_2 u + c_2 w \quad (2)$$

$$W_{m2} = a_3 v + b_3 u + c_3 w \quad (3)$$

where  $a_1, b_1, c_1$ , etc. are the associated direction cosines between  $(AX, N1, N2)$  and  $(R-\theta-Z)$ . The effective cooling velocity is known (Reference 7) to be

$$W_{eff}^2 = W_{m1}^2 + W_{m2}^2 + k^2 W_{ax}^2$$

or

$$W_{eff} = (W_{m1}^2 + W_{m2}^2 + k^2 W_{ax}^2)^{1/2} \quad (4)$$

Considering instantaneous quantities, equations (1) - (3) can be rewritten as

$$W_{ax} = \bar{W}_{ax} + W'_{ax} = a_1(\bar{v} + v') + b_1(\bar{u} + u') + c_1(\bar{w} + w') \quad (5)$$

$$W_{m1} = \bar{W}_{m1} + W'_{m1} = a_2(\bar{v} + v') + b_2(\bar{u} + u') + c_2(\bar{w} + w') \quad (6)$$

$$W_{m2} = \bar{W}_{m2} + W'_{m2} = a_3(\bar{v} + v') + b_3(\bar{u} + u') + c_3(\bar{w} + w') \quad (7)$$

Substituting equation (5) - (7), into (4), we get

$$W_{eff} = \bar{W}_{eff} + W'_{eff} = \left[ a_4(\bar{v}^2 + v'^2 + 2\bar{v}v') + b_4(\bar{u}^2 + u'^2 + 2\bar{u}u') + c_4(\bar{w}^2 + w'^2 + 2\bar{w}w') + d_4(\bar{v}\bar{u} + v'u' + \bar{u}v' + \bar{v}u') + e_4(\bar{v}\bar{w} + v'w' + \bar{v}w' + \bar{w}v') + f_4(\bar{u}\bar{w} + u'w' + \bar{u}w' + \bar{w}u') \right]^{1/2} \quad (8)$$

where the constants are defined as

$$a_4 = a_2^2 + a_3^2 + k^2 a_1^2$$

$$d_4 = 2(a_2 b_2 + a_3 b_3 + k^2 a_1 b_1)$$

$$b_4 = b_2^2 + b_3^2 + k^2 b_1^2$$

$$e_4 = 2(a_2 c_2 + a_3 c_3 + k^2 a_1 c_1)$$

$$c_4 = c_2^2 + c_3^2 + k^2 c_1^2$$

$$f_4 = 2(b_2 c_2 + b_3 c_3 + k^2 b_1 c_1)$$

Equation (8) can be linearized by  $(1 + \delta)^{1/2} = 1 + \frac{\delta}{2}$ , where  $\delta$  is considered negligibly small, to the following expression:

$$W_{eff} = \sqrt{a_4}(\bar{v} + v') + \frac{d_4}{2\sqrt{a_4}}(\bar{u} + u') + \frac{e_4}{2\sqrt{a_4}}(\bar{w} + w') + O(\epsilon) \quad (9)$$

Taking the time average of equation (9), we get

$$\overline{W_{eff}} = \sqrt{a_4} \overline{v} + \frac{a_4}{2\sqrt{a_4}} \overline{u} + \frac{a_4}{2\sqrt{a_4}} \overline{w} \quad (10)$$

Subsequently, the difference between equation (9) and (10) is the fluctuating velocity  $W'_{eff}$

$$W'_{eff} = \sqrt{a_4} v' + \frac{a_4}{2\sqrt{a_4}} u' + \frac{a_4}{2\sqrt{a_4}} w' \quad (11)$$

### A3.2 Relating Voltages and Velocities:

Apply King's Law for instantaneous velocities (Reference 8)

$$E_1^2 = (\overline{E}_1 + e'_1)^2 = E_0^2 + B \sqrt{\overline{W}_1 + W'_1} \quad (12)$$

then

$$\overline{E}_1^2 + 2\overline{E}_1 e'_1 + e'^2_1 = E_0^2 + B \sqrt{\overline{W}_1 + W'_1}$$

Assume  $e'^2_1$ , and  $\frac{W'_1}{\overline{W}_1}$  are small. Linearize the equation to get

$$2\overline{E}_1 e'_1 = B \frac{W'_1}{2\sqrt{\overline{W}_1}}$$

or

$$W'_1 = \left( \frac{4\overline{E}_1 \sqrt{\overline{W}_1}}{B} \right) e'_1$$

Rewriting,  $W'_1 = L_1 e'_1$ , then

$$\left\{ \begin{array}{l} \overline{W_1'^2} = L_1^2 \overline{e_1'^2} \\ \overline{W_2'^2} = L_2^2 \overline{e_2'^2} \\ \overline{W_3'^2} = L_3^2 \overline{e_3'^2} \end{array} \right\} \quad \text{AND} \quad \left\{ \begin{array}{l} \overline{W_1' W_2'} = L_1 L_2 \overline{e_1' e_2'} \\ \overline{W_1' W_3'} = L_1 L_3 \overline{e_1' e_3'} \\ \overline{W_2' W_3'} = L_2 L_3 \overline{e_2' e_3'} \end{array} \right\} \quad (13)$$

The value of  $\overline{e_1'^2}$ ,  $\overline{e_2'^2}$ ,  $\overline{e_3'^2}$  are obtained directly from the

hotwire measurement of Section 3.3.2. The values of  $\overline{e_1' e_2'}$ ,  $\overline{e_1' e_3'}$  and

$\overline{e_2' e_3'}$  are derived as follows:

$$\begin{aligned}
\overline{e'_1 e'_2} &= \frac{1}{4} \left[ \overline{(e'_1 + e'_2)^2} - \overline{(e'_1 - e'_2)^2} \right] \\
\overline{e'_1 e'_3} &= \frac{1}{4} \left[ \overline{(e'_1 + e'_3)^2} - \overline{(e'_1 - e'_3)^2} \right] \\
\overline{e'_2 e'_3} &= \frac{1}{4} \left[ \overline{(e'_2 + e'_3)^2} - \overline{(e'_2 - e'_3)^2} \right]
\end{aligned}
\tag{14}$$

Where the mean-squared voltage within the bracket are obtained directly from the sum and difference circuit measurements of section 3.3.2.

### A3.3 Mean Velocity Calculation

Equation (10) for hotwire channel 1 and similar equations derived for channels 2 and 3 form a set of three linear equations in three unknowns.

$$\begin{aligned}
\overline{W}_1 &= a_5 \overline{v} + b_5 \overline{u} + c_5 \overline{w} \\
\overline{W}_2 &= a_6 \overline{v} + b_6 \overline{u} + c_6 \overline{w} \\
\overline{W}_3 &= a_7 \overline{v} + b_7 \overline{u} + c_7 \overline{w}
\end{aligned}
\tag{15}$$

where constants  $a_5$ ,  $b_5$ , etc. reflect the appropriate combination of direction cosines,  $k$  factor, etc.

Values of  $\overline{W}_1$ ,  $\overline{W}_2$ ,  $\overline{W}_3$  are known from application of equation (12) to the D.C. hotwire voltage obtained in Section 3.3.2. Solution of equation (15) thus give  $\overline{u}$ ,  $\overline{v}$ ,  $\overline{w}$  for each measurement location considered.

### A3.4 Fluctuating Velocities, Turbulence Intensities, and Turbulence Stresses

Equation (11) is squared and time-averaged to give the following expression:

$$\begin{aligned}
\overline{W_{eff}^2} &= (a_4)^2 \overline{v'^2} + \left( \frac{d_4^2}{4a_4} \right) \overline{u'^2} + \left( \frac{e_4^2}{4a_4} \right) \overline{w'^2} + d_4 \overline{u'v'} \\
&\quad + e_4 \overline{v'w'} + \left( \frac{d_4 e_4}{2a_4} \right) \overline{u'w'} + O(\epsilon)
\end{aligned}$$

or

$$\overline{W_1^2} = a_8 \overline{v'^2} + b_8 \overline{u'^2} + c_8 \overline{w'^2} + d_8 \overline{u'v'} + e_8 \overline{v'w'} + f_8 \overline{u'w'} \quad (16)$$

where  $a_8, b_8$ , etc. are the appropriate constants.

Similar equations exist for hotwire channels 2 and 3. Equation (11) can then be multiplied by the corresponding expression for  $\overline{W_2'}$  and averaged to obtain

$$\overline{W_1'W_2'} = a_9 \overline{v'^2} + b_9 \overline{u'^2} + c_9 \overline{w'^2} + d_9 \overline{u'v'} + e_9 \overline{v'w'} + f_9 \overline{u'w'} \quad (17)$$

where  $a_9, b_9$ , etc. are the appropriate constants. Similar expressions can be derived for  $\overline{W_1'W_3'}$  and  $\overline{W_2'W_3'}$ .

The values of  $\overline{W_1'^2}, \overline{W_2'^2}, \overline{W_3'^2}, \overline{W_1'W_2'}, \overline{W_1'W_3'}$  and  $\overline{W_2'W_3'}$  are obtained from the analysis of Section A3.2

Thus the equations (16) and (17) form a set of six equations in six unknowns, which can be solved simultaneously to give the quantities  $\overline{u'^2}, \overline{v'^2}, \overline{w'^2}, \overline{u'v'}, \overline{v'w'}$  and  $\overline{u'w'}$ .

REFERENCES

1. Cooper, P. and Bosch, H. "Three-Dimensional Analysis of Inducer Fluid Flow", NASA CR-54836, TRW ER-6673A, February 1966.
2. Poncet, A. and Lakshminarayana, B. "Three-Dimensional Analysis and Measurement of the Flow in a Three Blade Rocket Pump Inducer"; NASA CR-2290, 1973.
3. Giesing, J. P. "Extension of the Douglas-Newmann Program & Problems of Lifting, Infinite Cascades," Douglas Aircraft Division LB-31653, 2 July 1964.
4. Lakshminarayana, B. and White, M. "Airfoil in a Contracting or Diverging Stream", Journal of Aircraft V9 No. 5, May 1972, p. 354-360.
5. Yamaoka, H., Lakshminarayana B. and Anand A. "Investigation and Analysis of Flow Phenomena in Axial Flow Inducers", Progress Report to NASA, The Pennsylvania State University, July 1971.
6. Wislicenus, G. F. "Fluid Mechanics of Turbomachinery", Dover, Vol. II, p. 646-683.
7. Schwarz, W. H., and Frieke, C. A., "Deviations from the Cosine Law for Yawed Cylindrical Anemometer Sensors", Journal of Applied Mechanics, Paper No. 68-WA/APM-16, December 1968.
8. Hinze, J. O., "Turbulence, An Introduction to its Mechanism and Theory", McGraw Hill, New York, 1959.

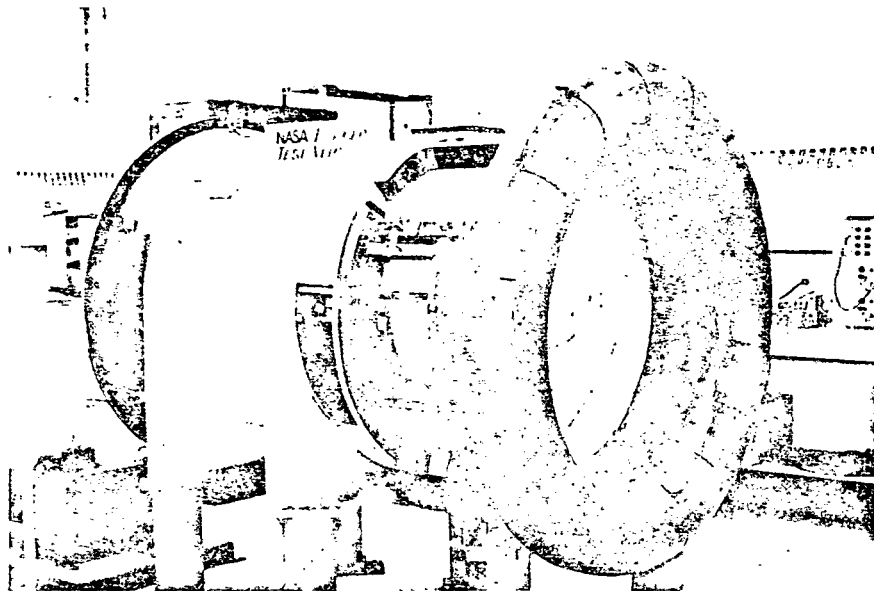


FIGURE 1a: INDUCER TEST FACILITY

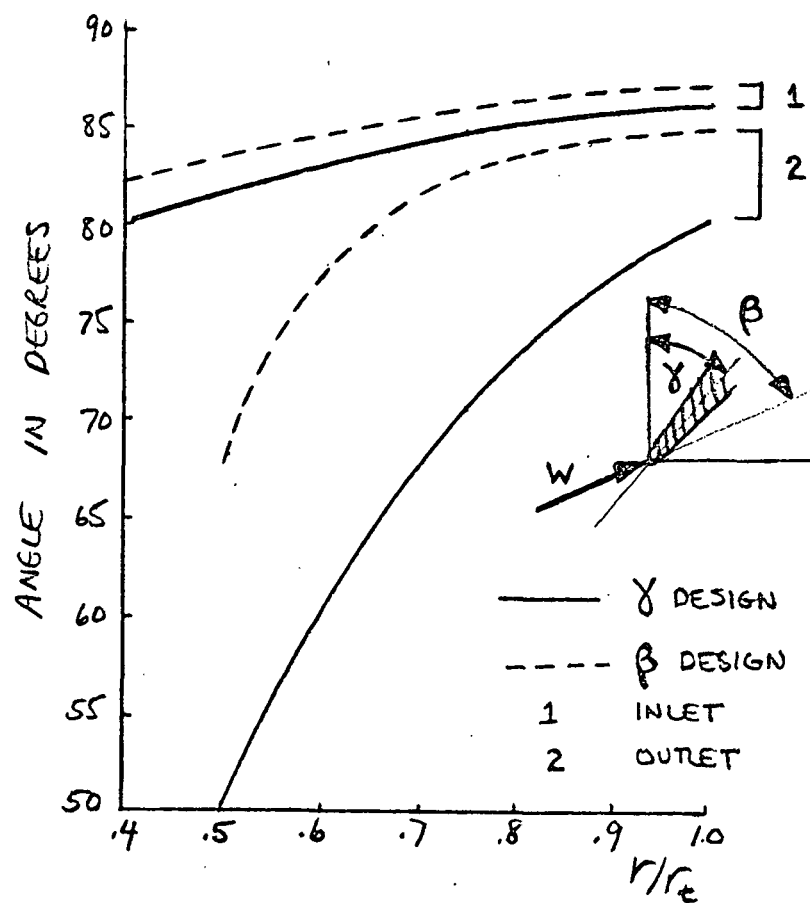


FIGURE 1b: INDUCER INLET AND OUTLET ANGLE



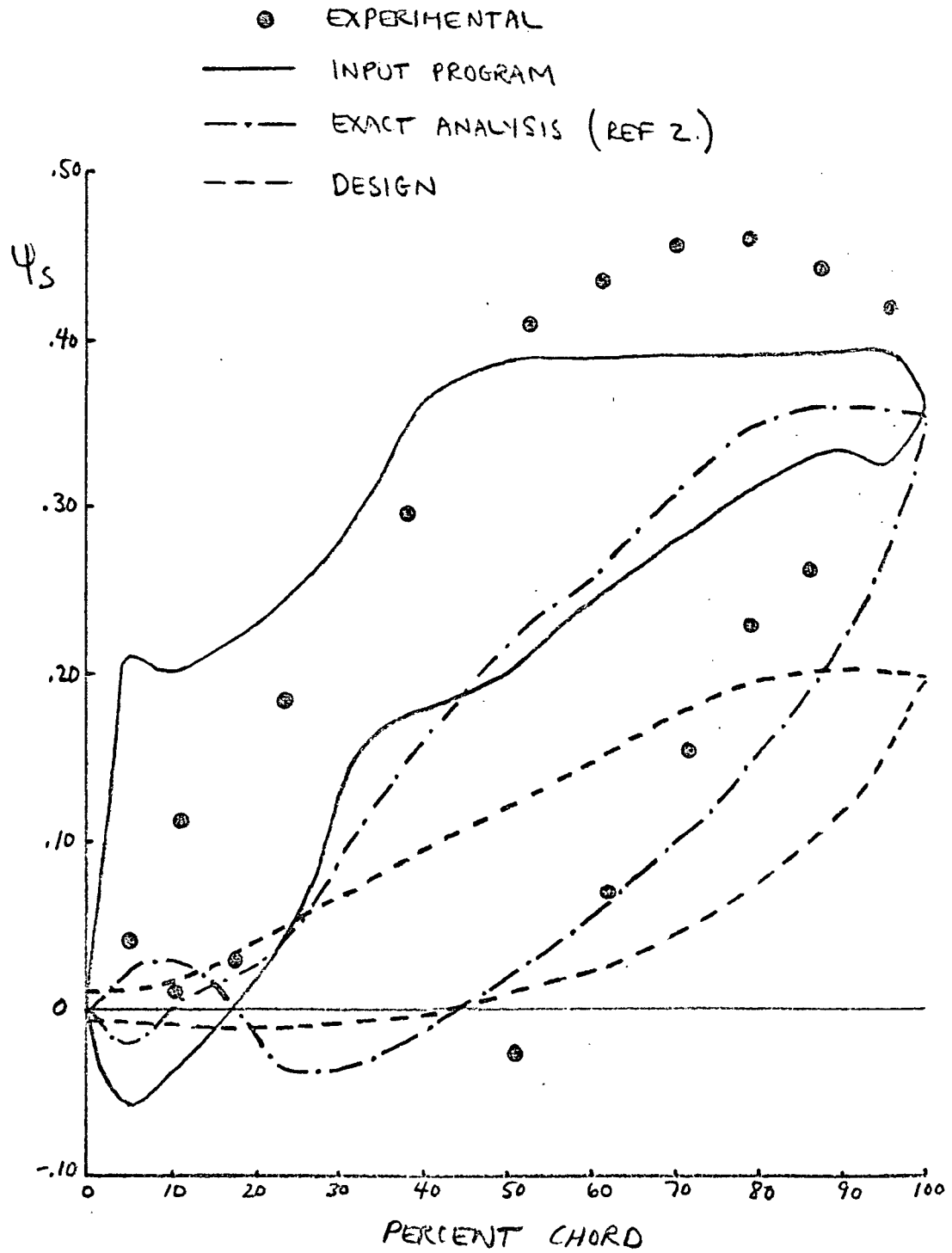


FIGURE 2a:  $\Psi_s$  DISTRIBUTION AT TIP

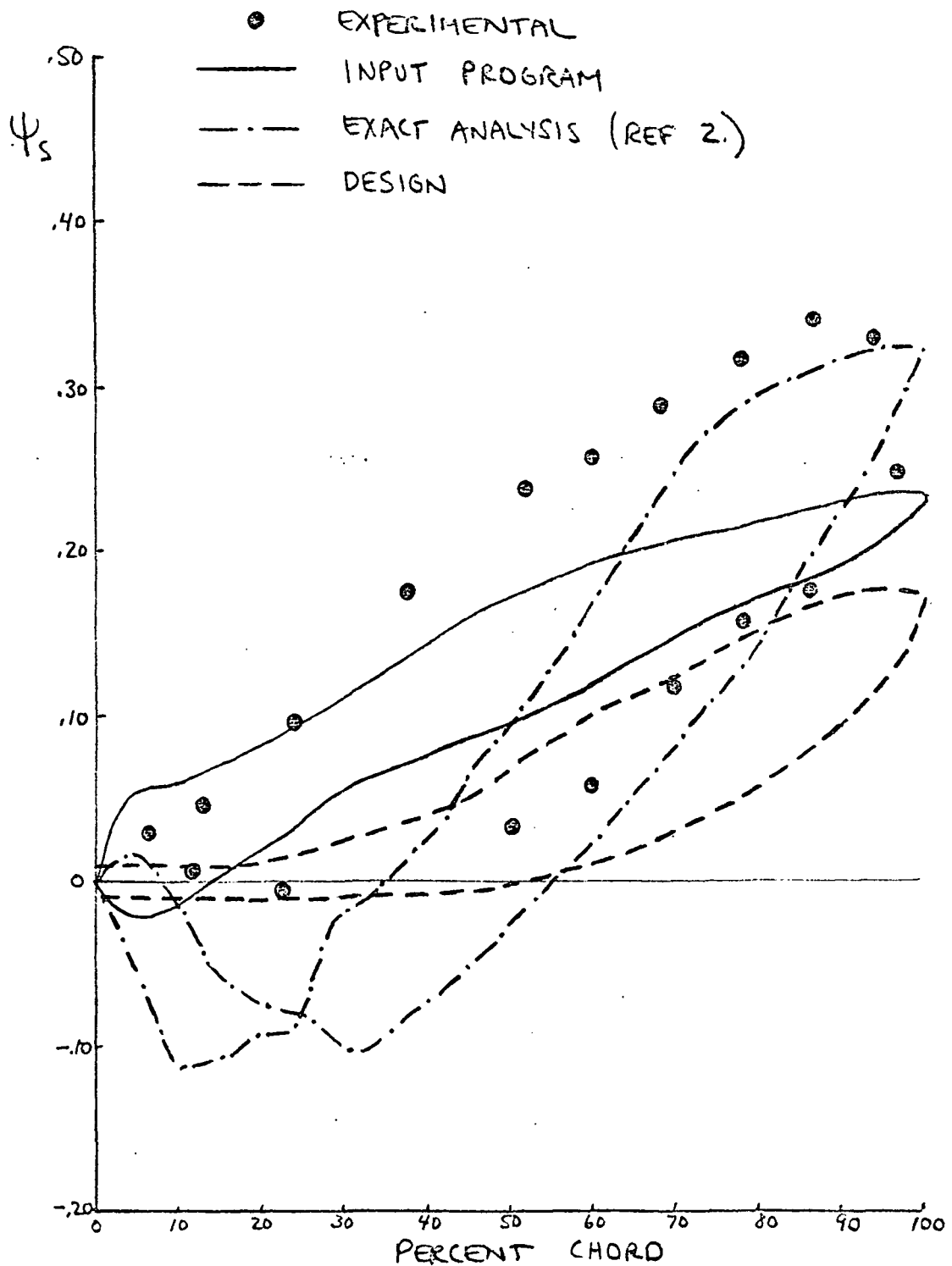


FIGURE 2b:  $\Psi_s$  DISTRIBUTION AT MID-PASSAGE

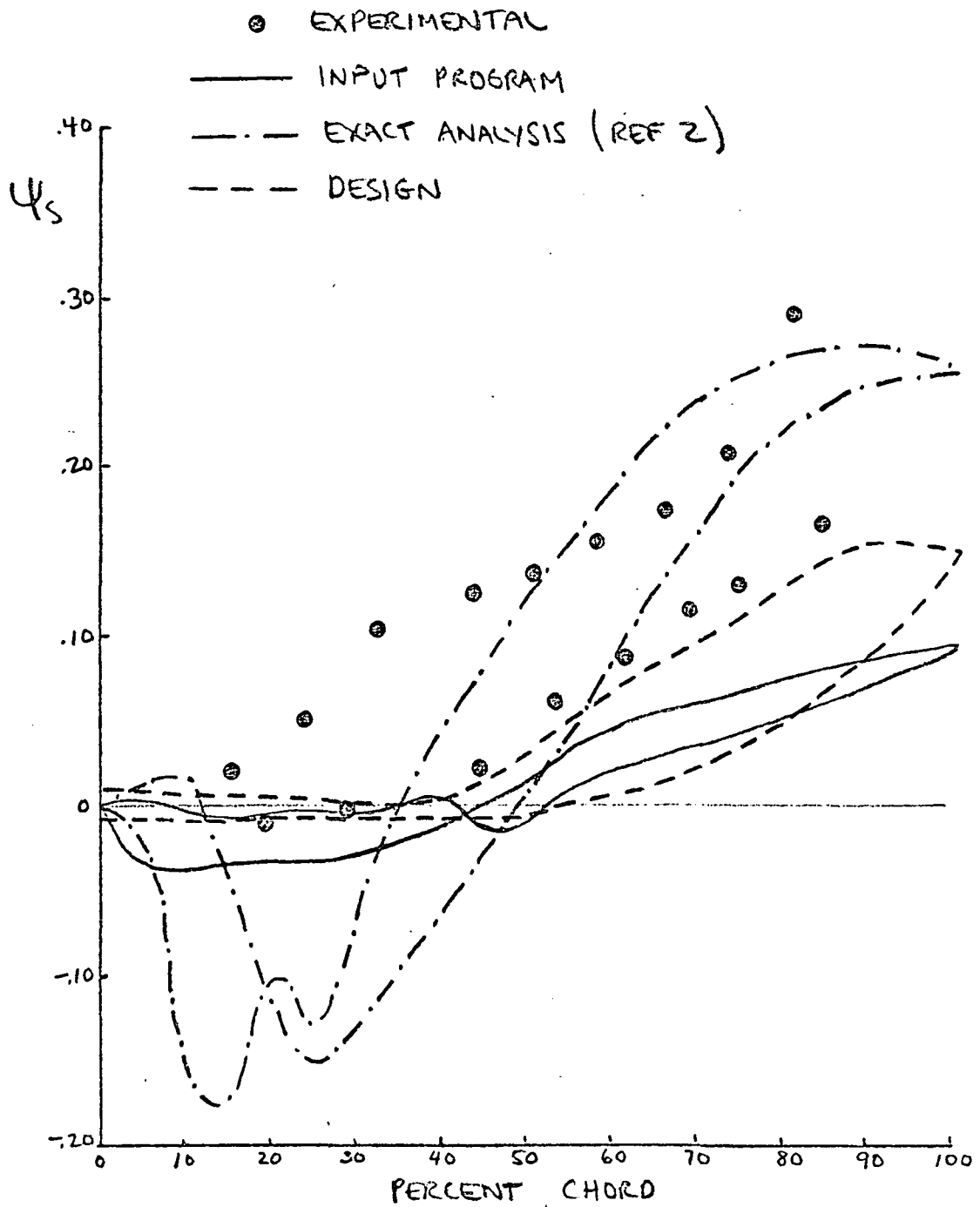


FIGURE 2c :  $\Psi_s$  DISTRIBUTION AT HUB

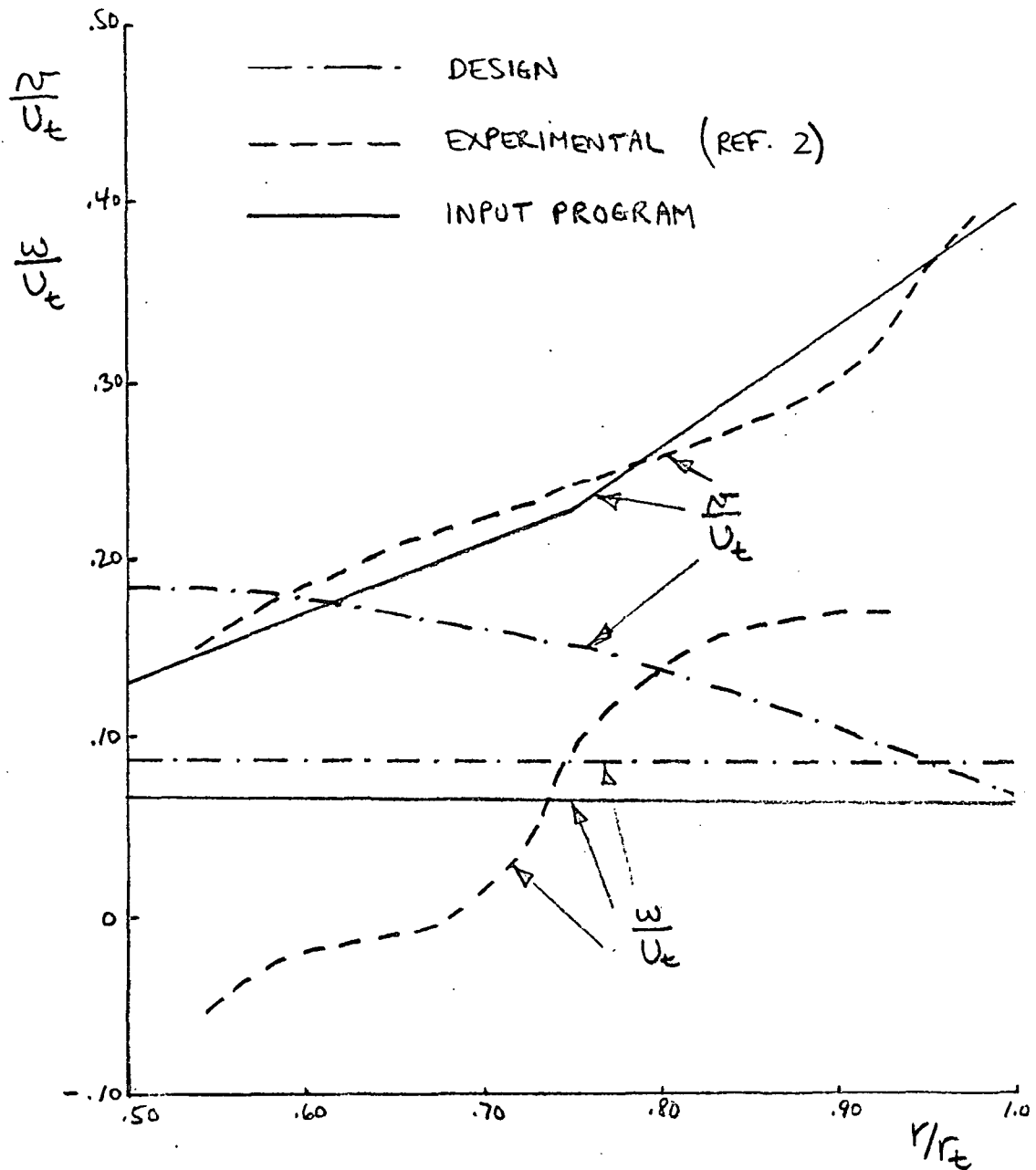


FIGURE 2d: COMPARISON OF RESULTS - STATION 5

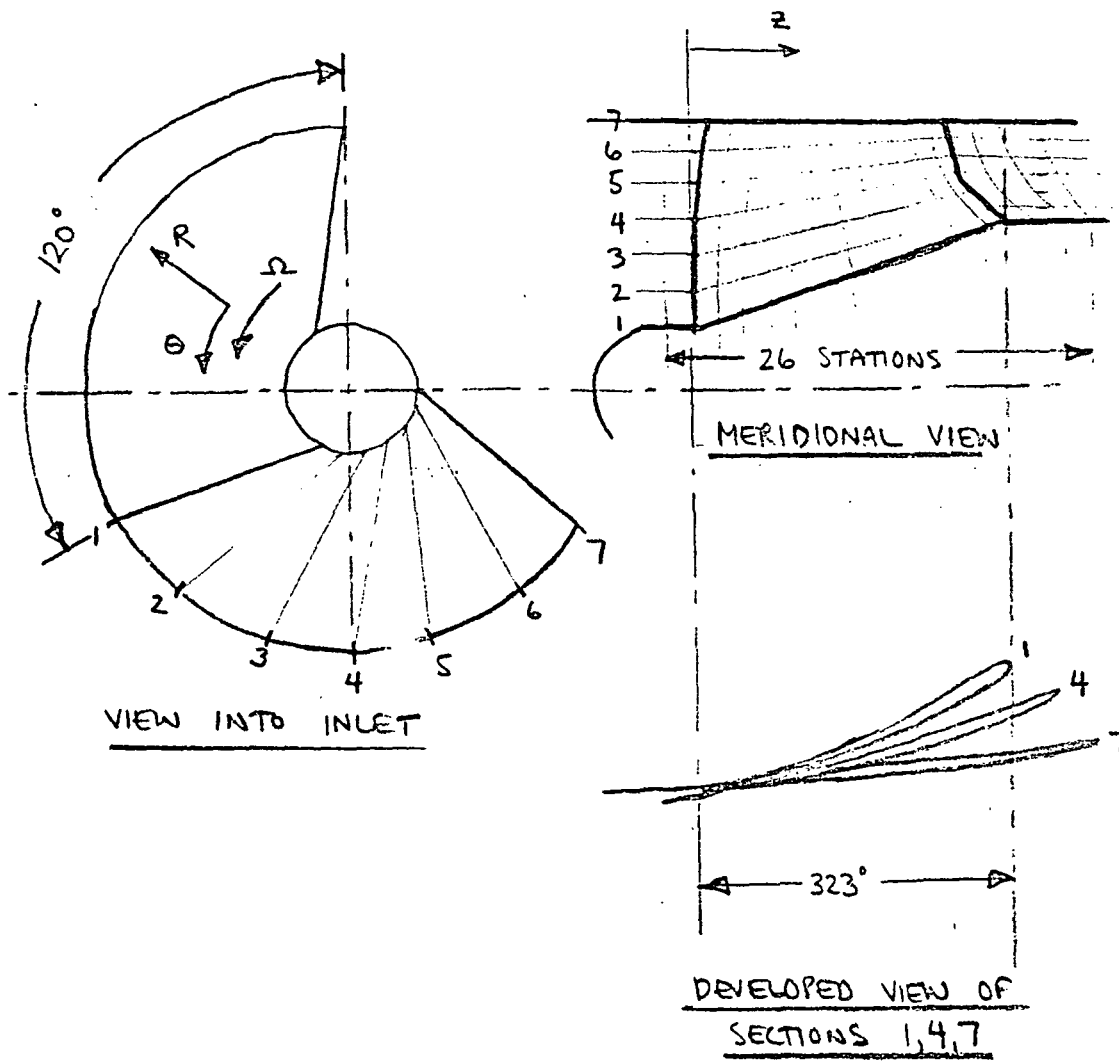


FIGURE 3 : INDUCER GEOMETRY FOR NUMERICAL ANALYSIS

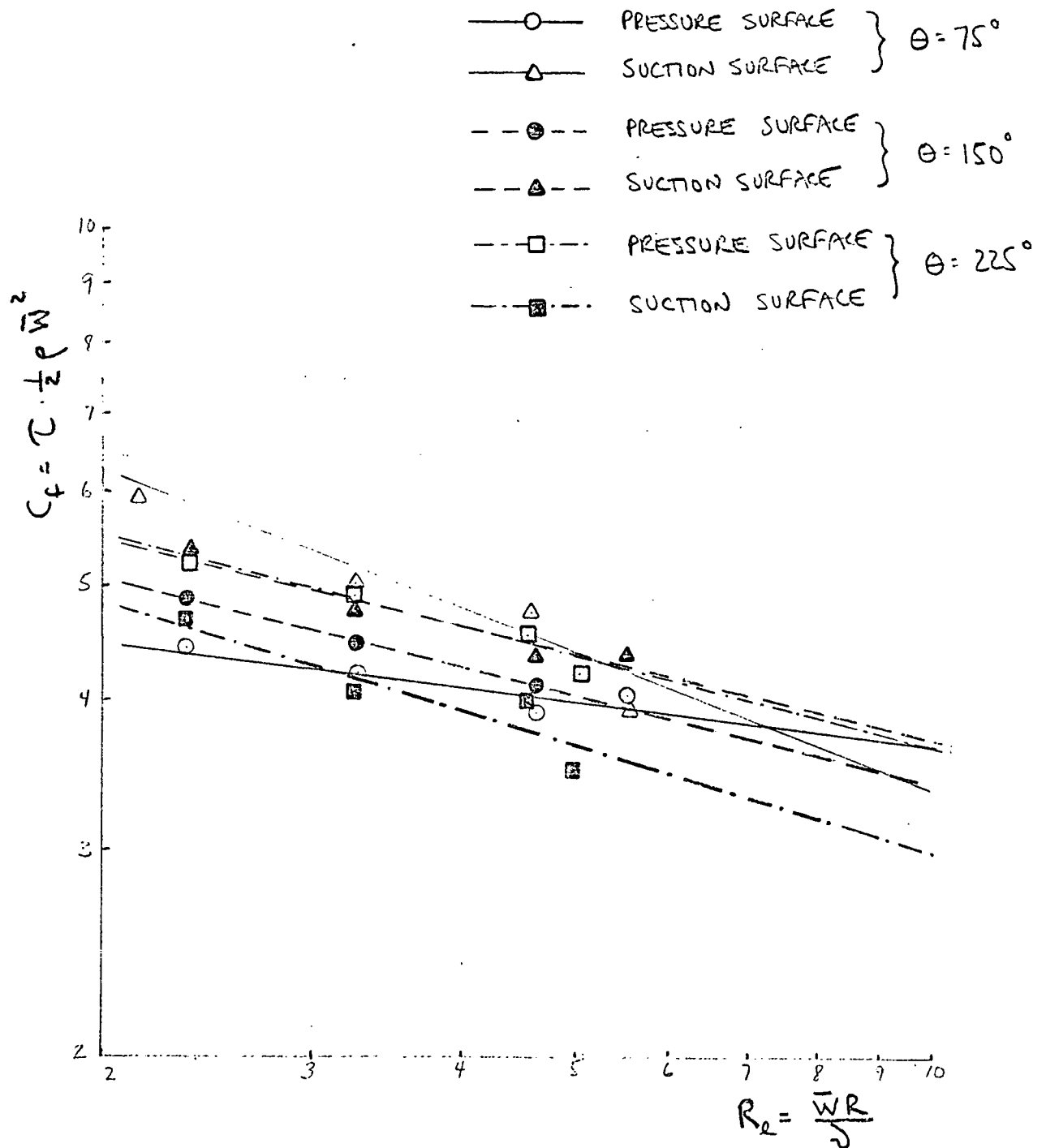


FIGURE 4: SKIN FRICTION COEFFICIENT VS. REYNOLDS NUMBER

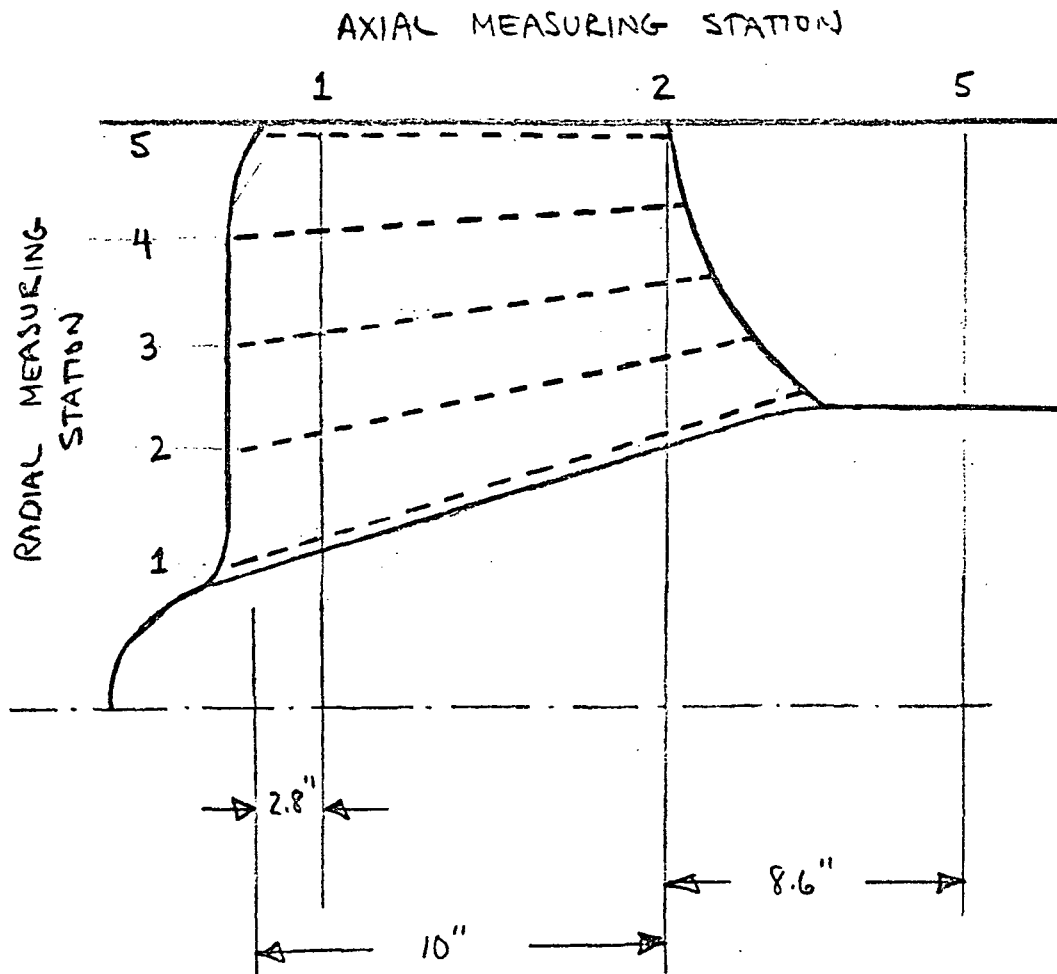


FIGURE 5 : LOCATION OF FLOW MEASURING STATIONS

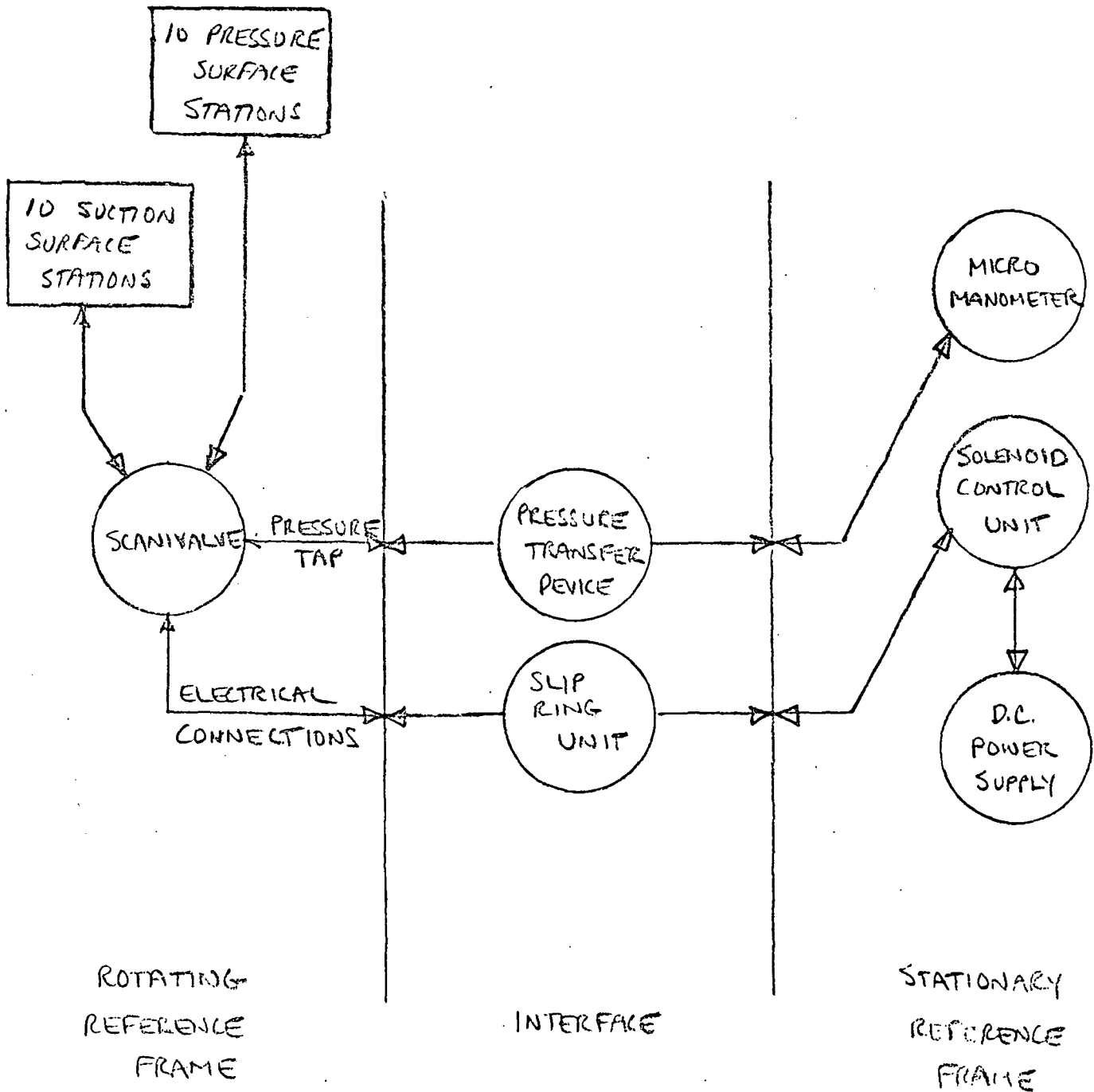


FIG. 6: SCHEMATIC DIAGRAM OF BLADE STATIC PRESSURE TEST SETUP



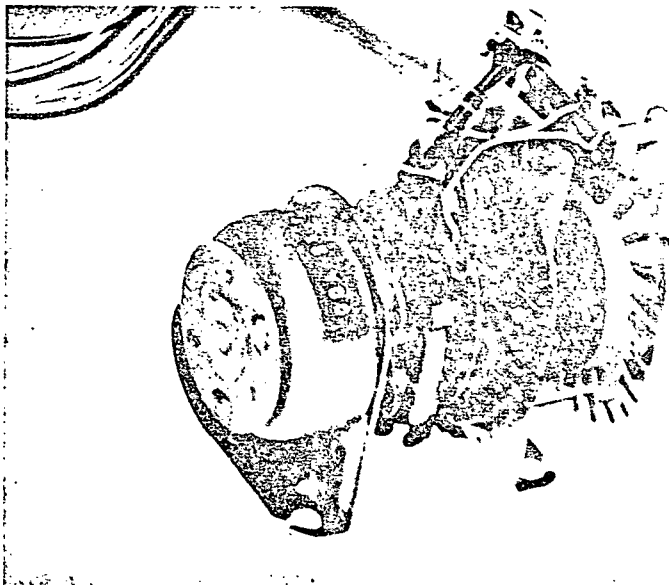


FIGURE 7a: SCANIVALVE

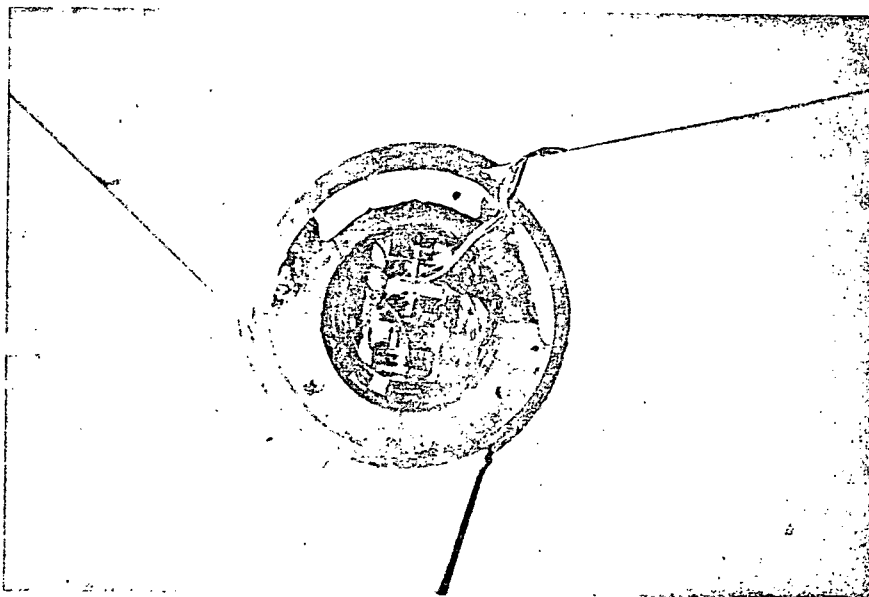


FIGURE 7b: SCANIVALVE MOUNTED IN HUB

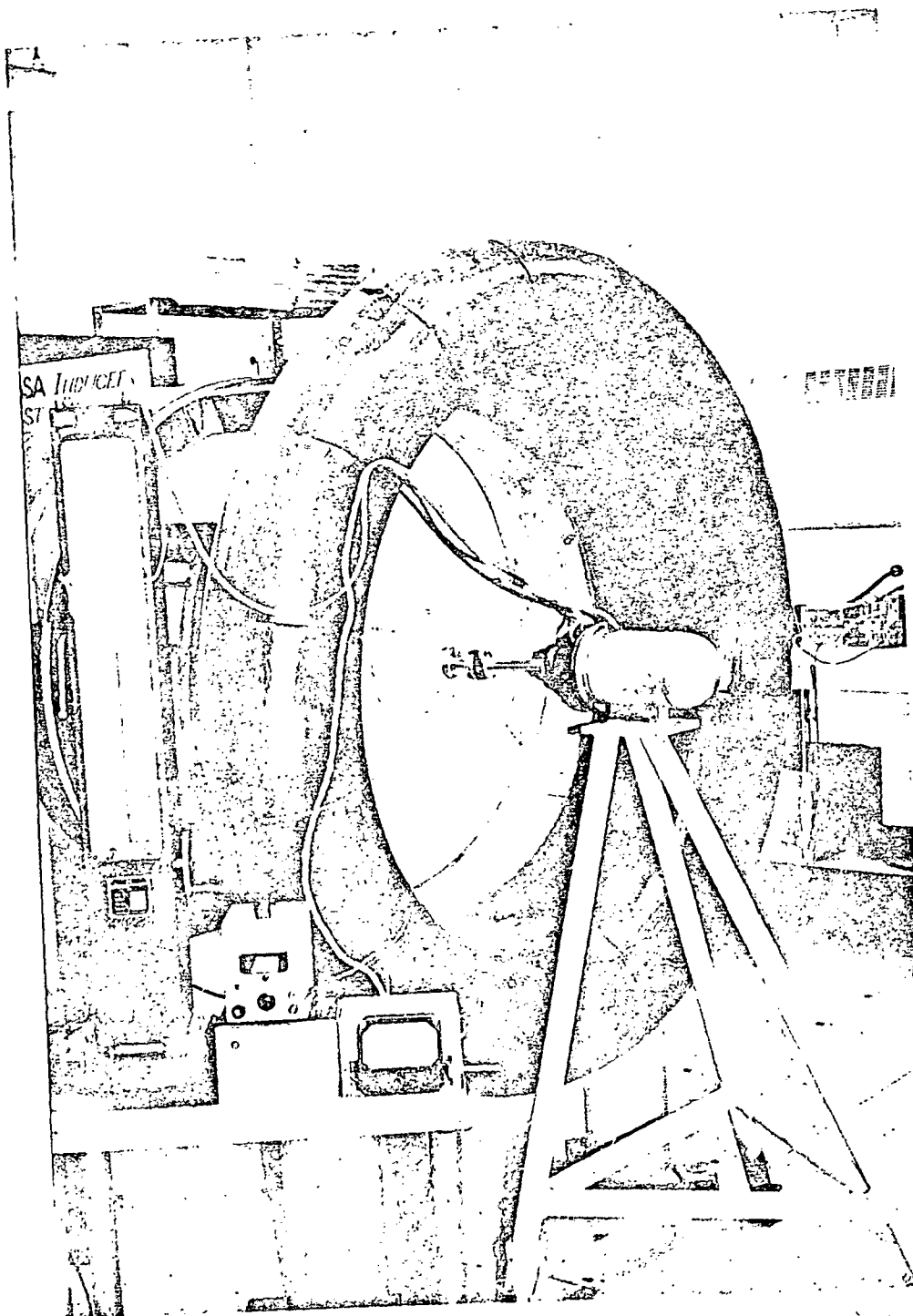


FIGURE 7C : BLADE STATIC PRESSURE TEST SETUP

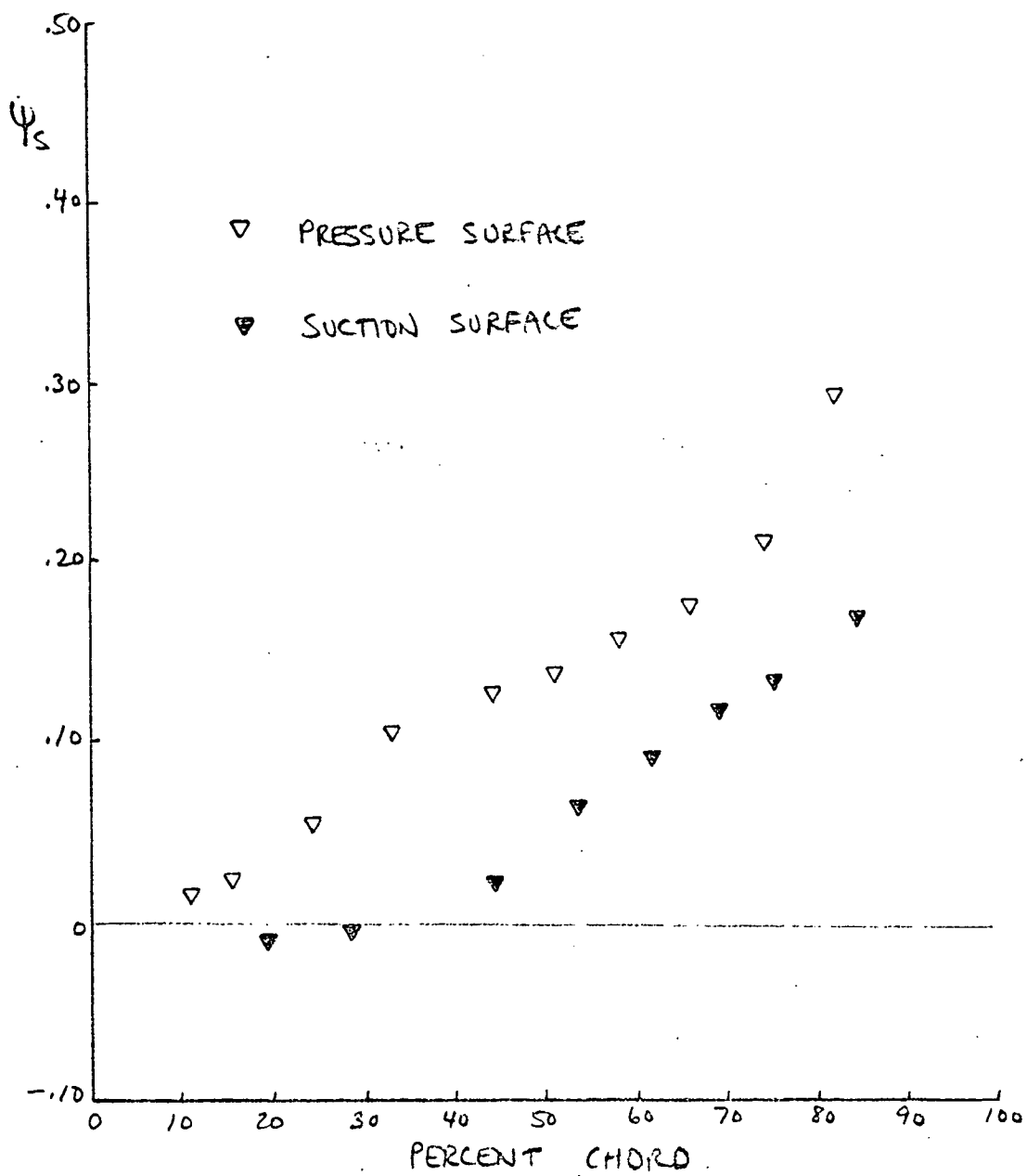


FIGURE 8a:  $\Psi_s$  DISTRIBUTION - RADIAL STATION 1

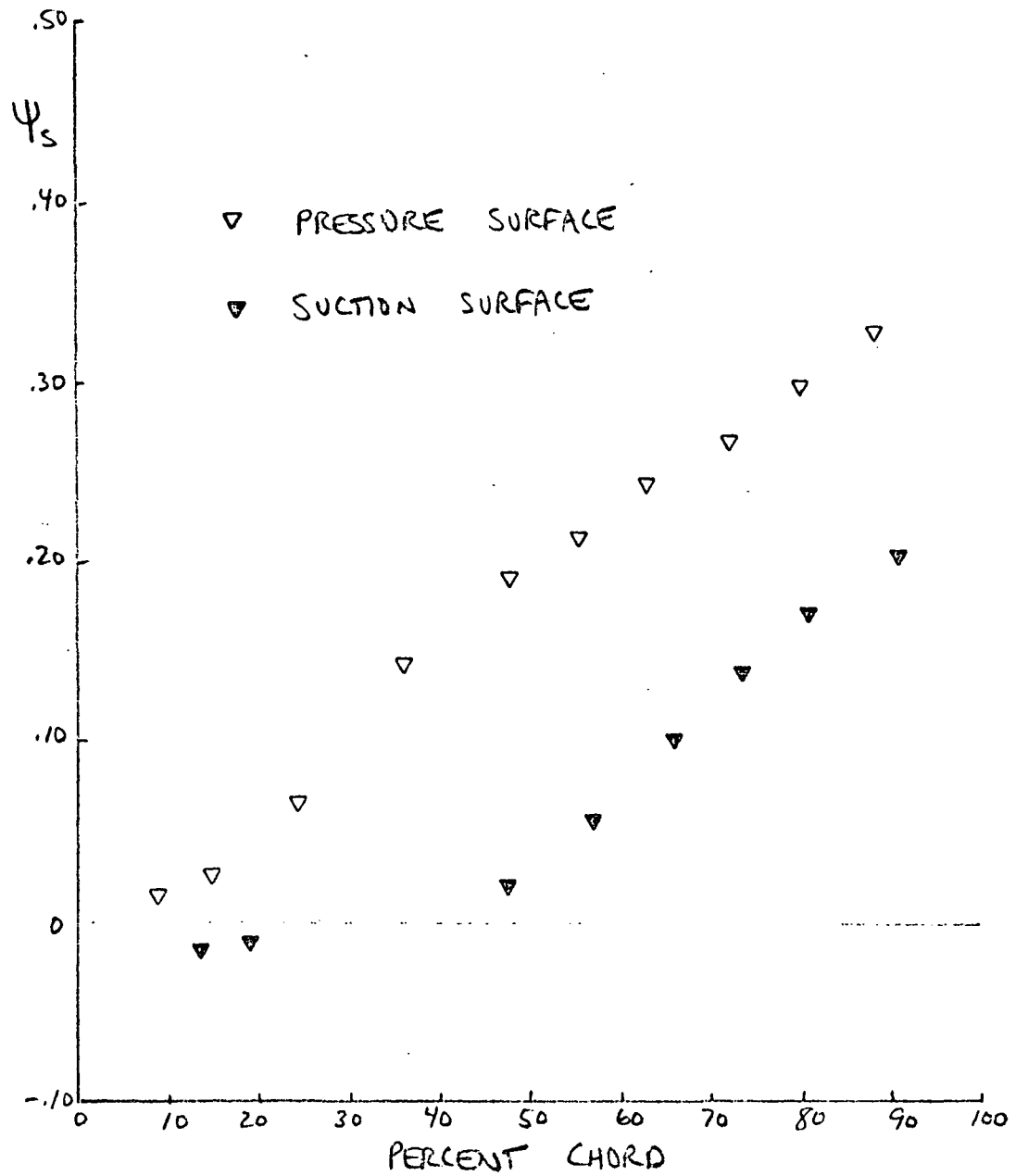


FIGURE 8b:  $\Psi_s$  DISTRIBUTION - RADIAL STATION 2

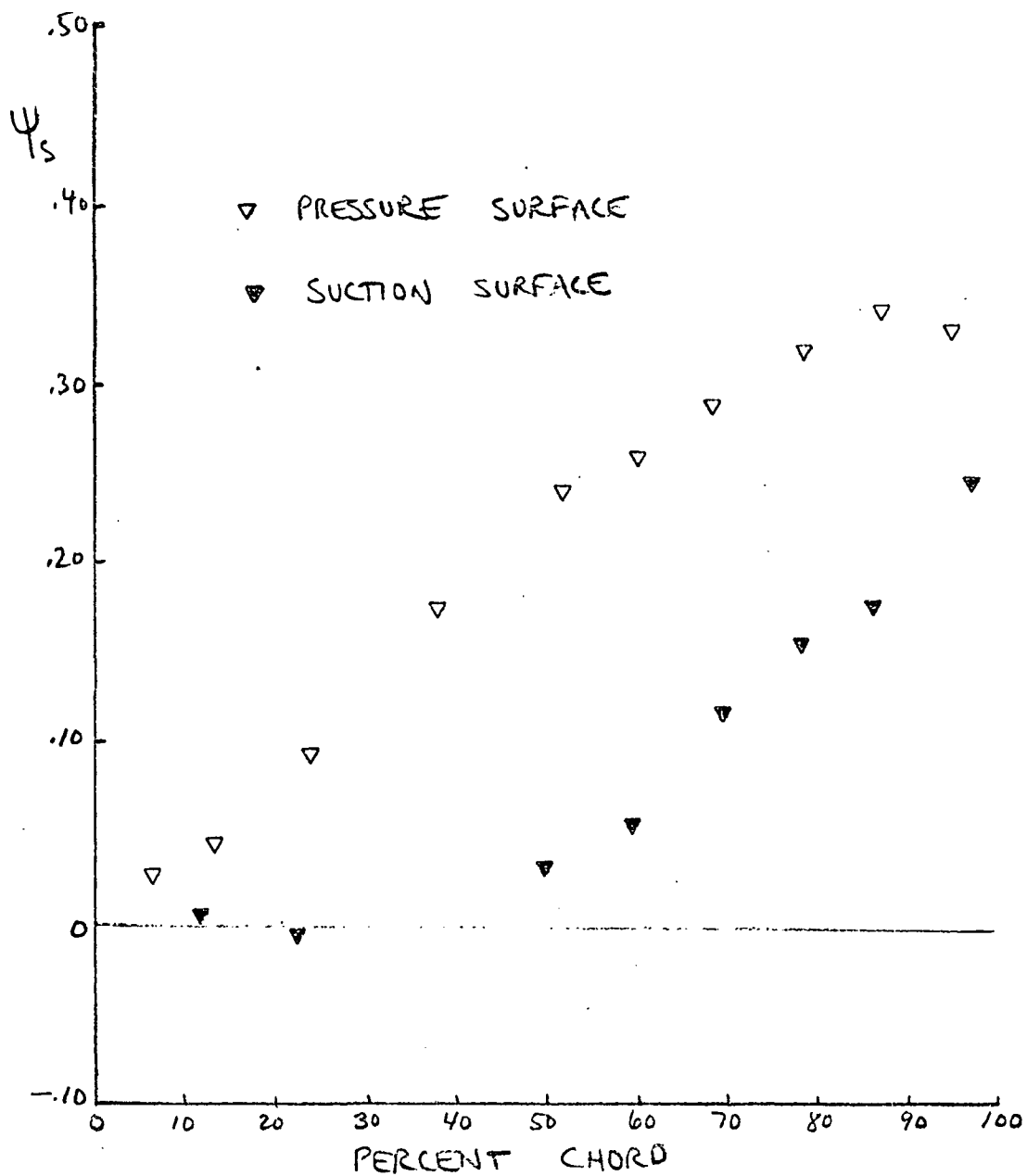


FIGURE 8c:  $\Psi_s$  DISTRIBUTION — RADIAL STATION 3

**"Page missing from available version"**

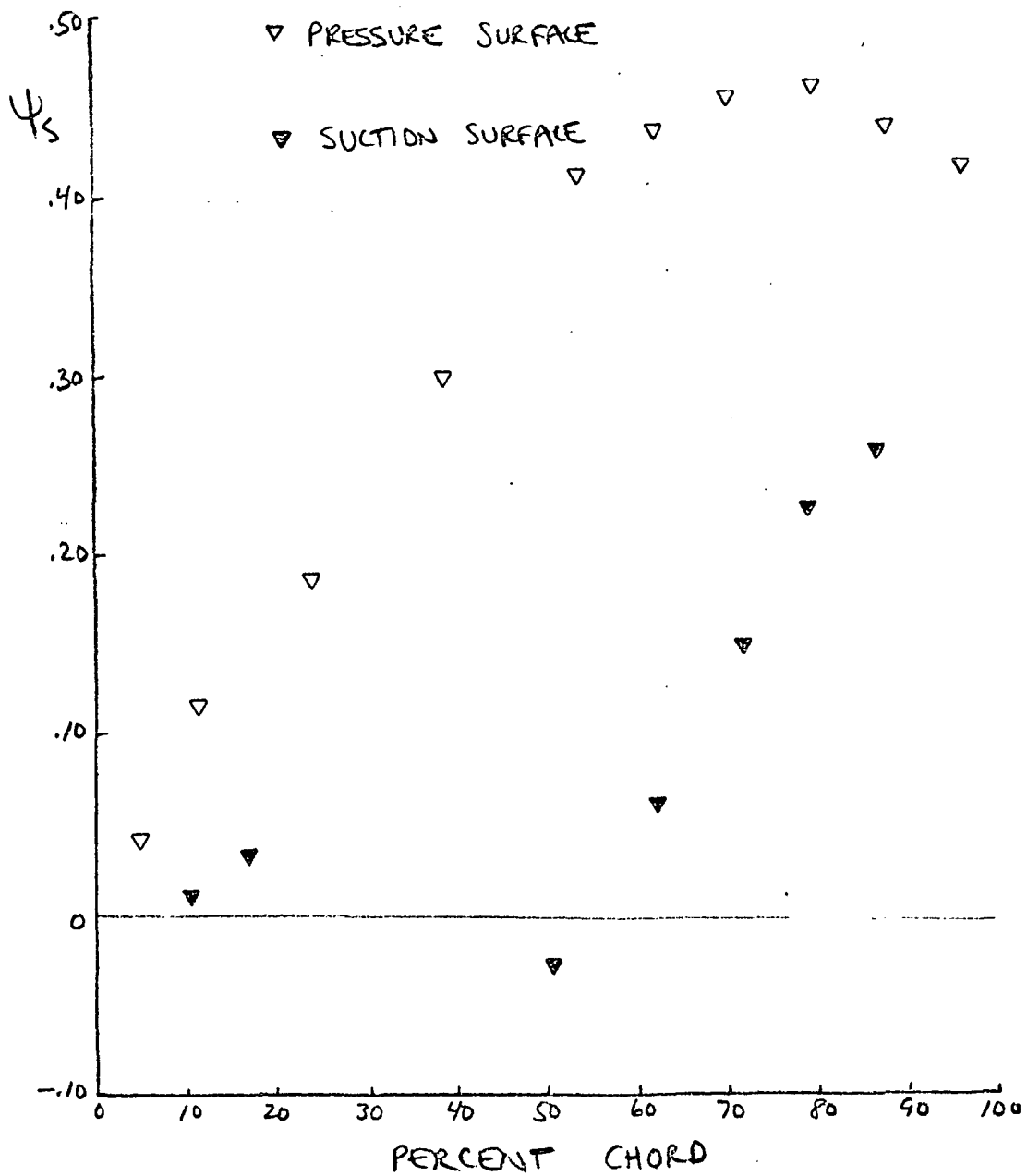


FIGURE 82:  $\Psi_s$  DISTRIBUTION - RADIAL STATION 5

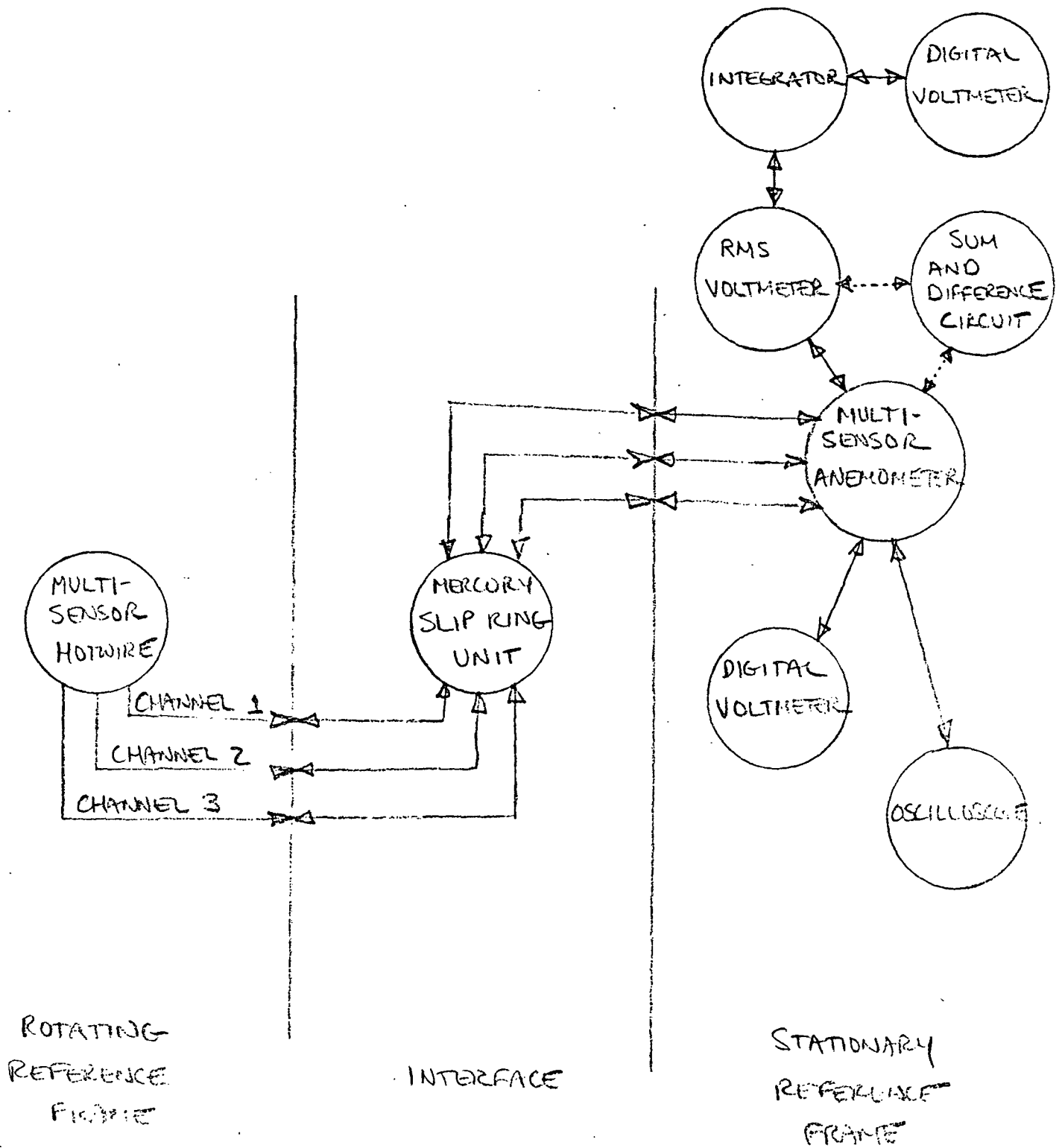


FIG. 9: SCHEMATIC DIAGRAM OF ROTATING HOTWIRE TEST SETUP



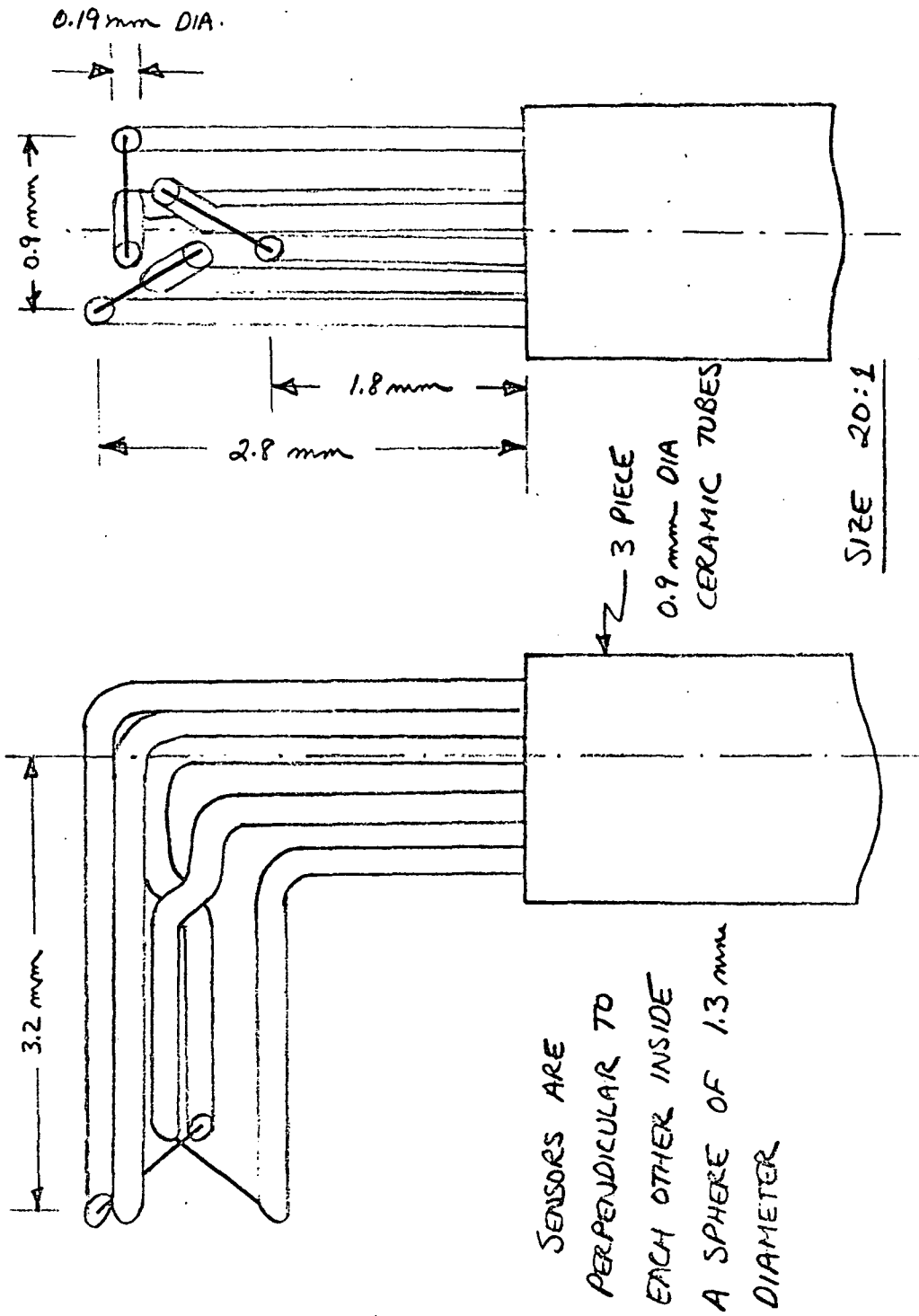


FIGURE 10: SUB-MINIATURE TRIAXIAL PROBE

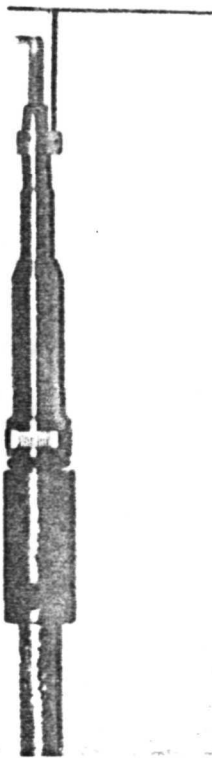


FIGURE 11a: TRIAXIAL  
PROBE AND SUPPORT

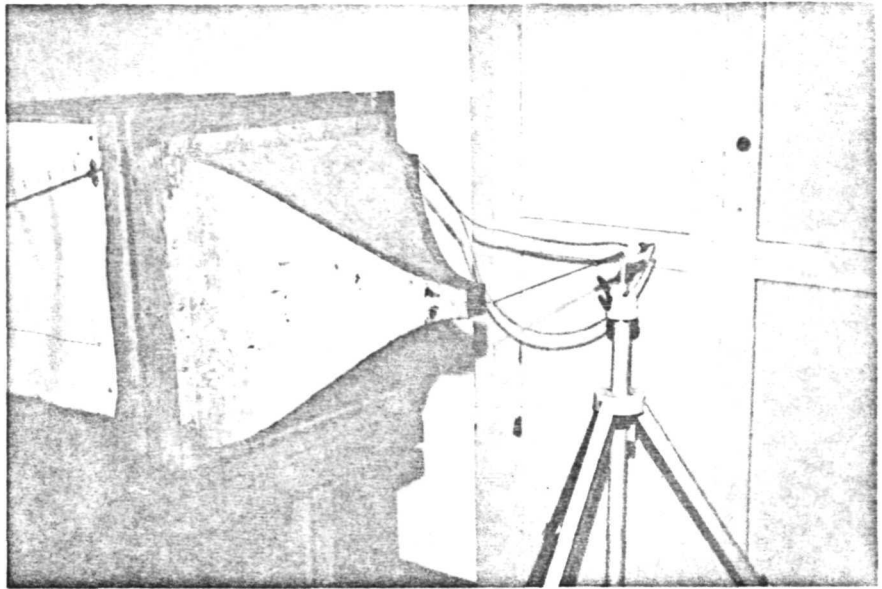


FIGURE 11b: CALIBRATION TUNNEL

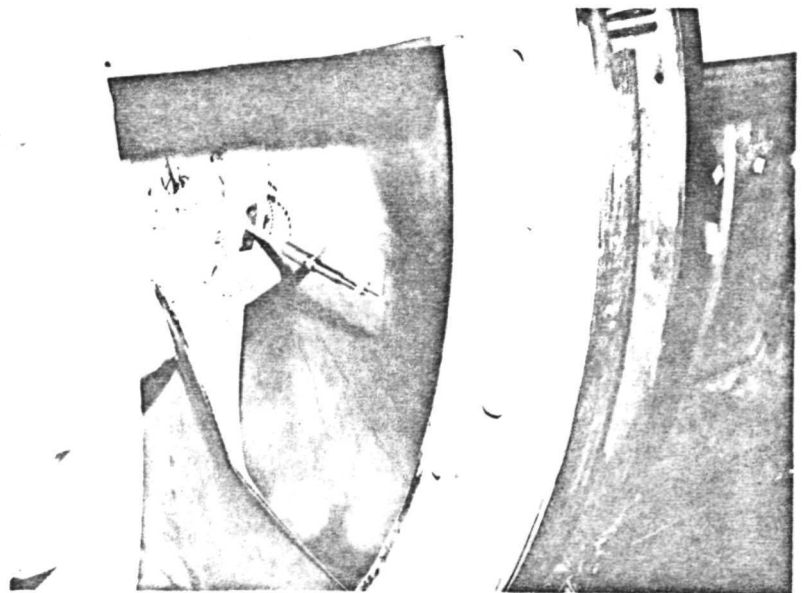


FIGURE 11c: TRIAXIAL PROBE MOUNTED  
IN INDUCER HUB

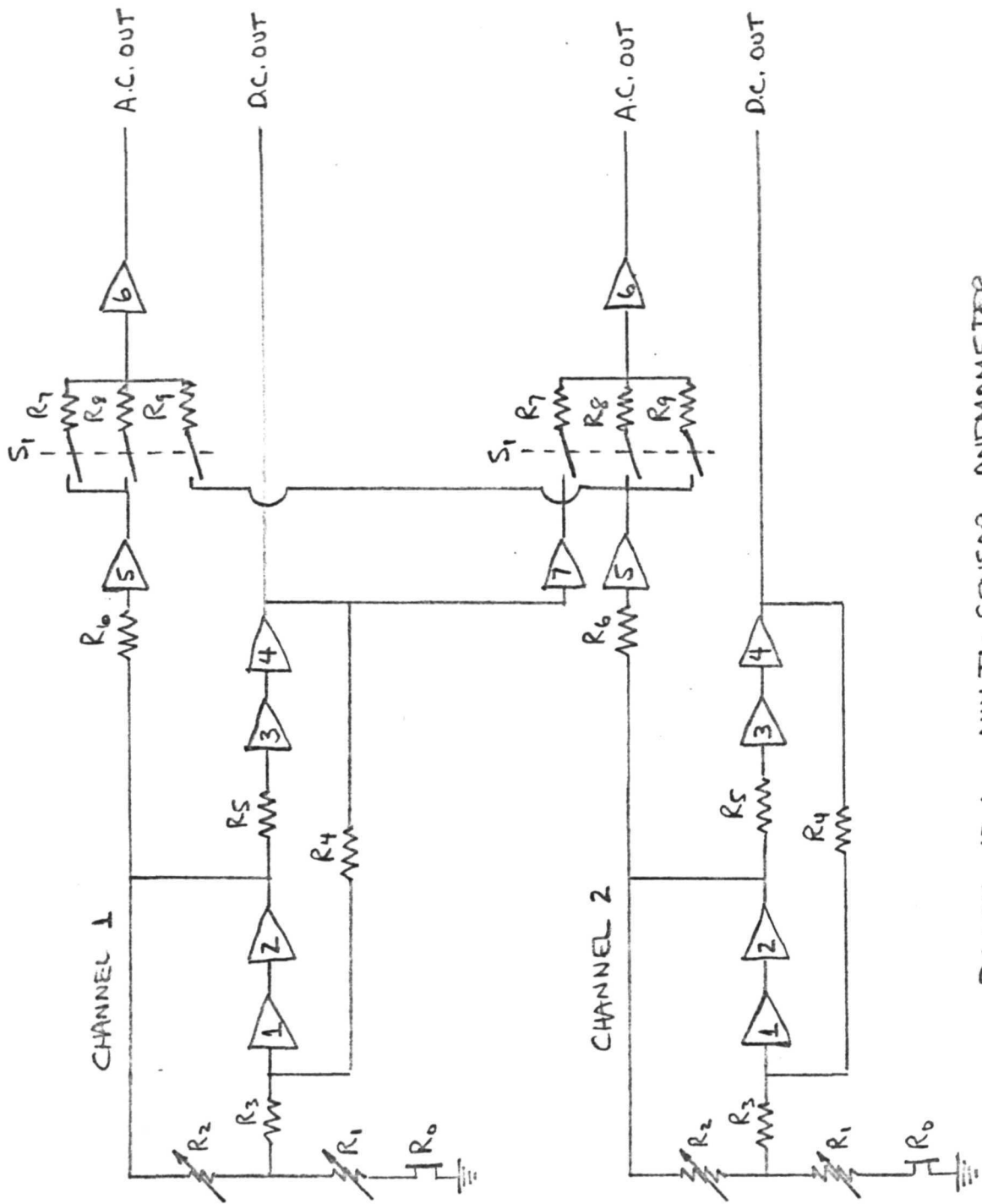


FIGURE 12: MULTI-SENSOR ANEMOMETER

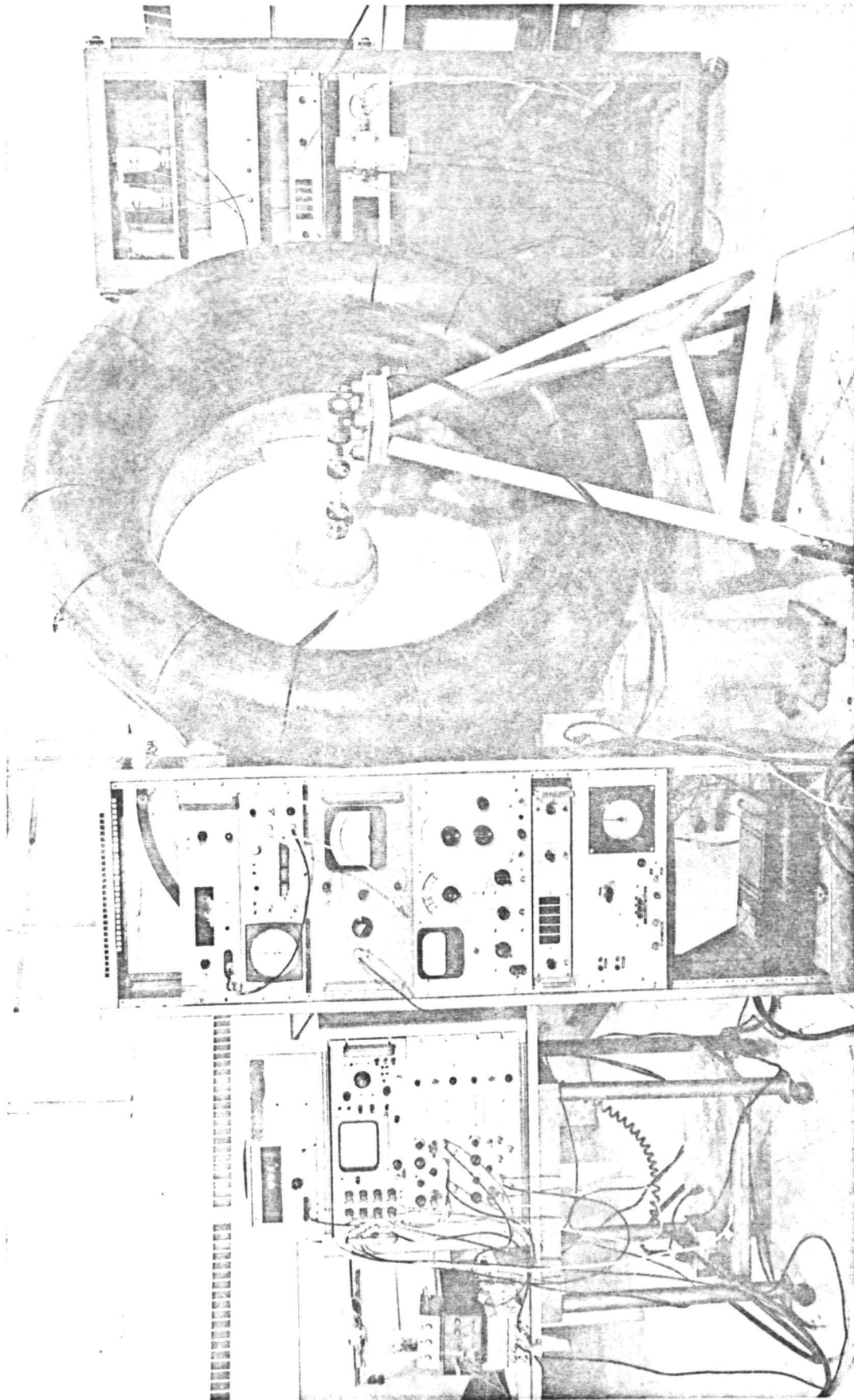


FIGURE 13: ROTATING HOTWIRE TEST SETUP

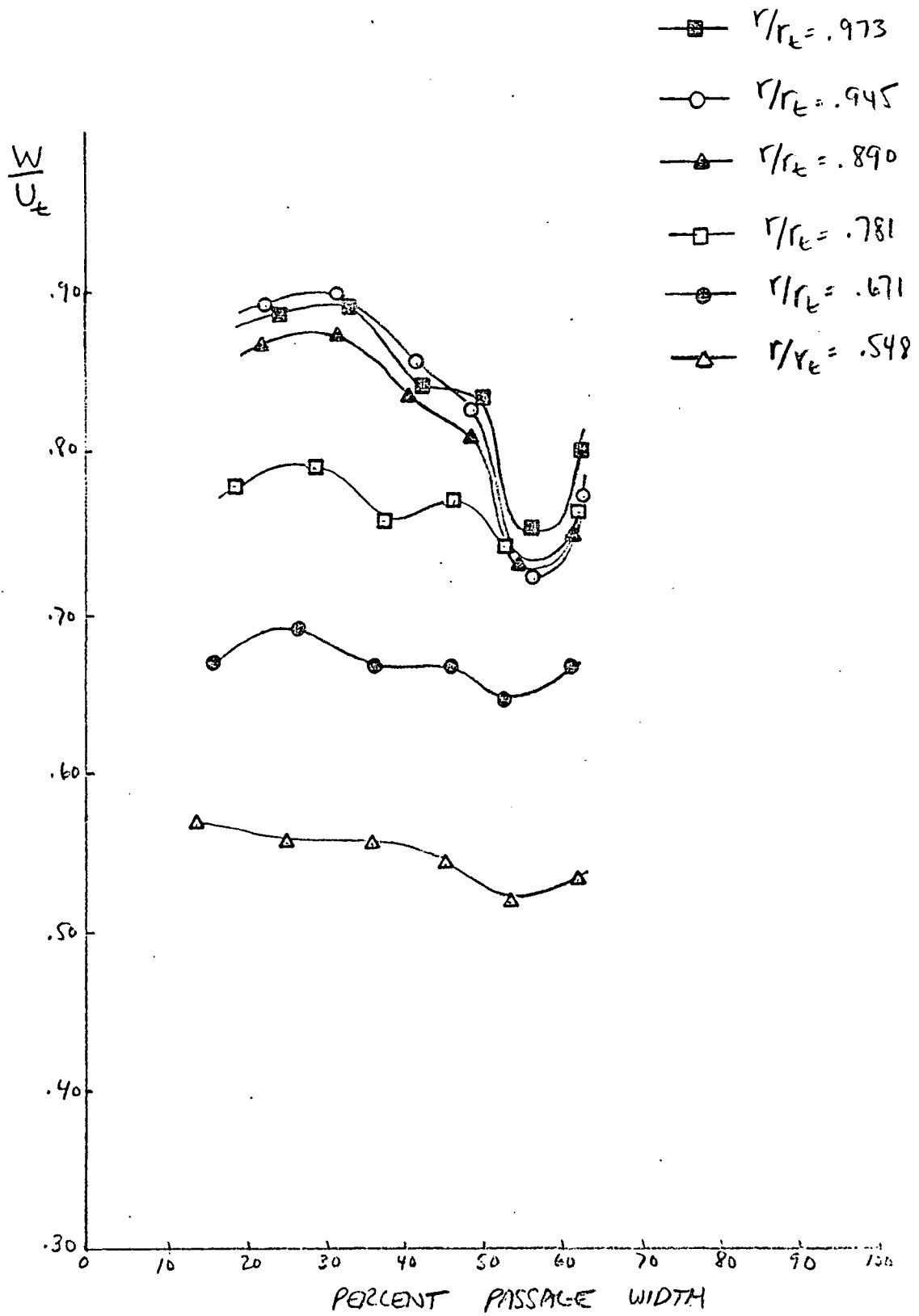


FIGURE 14a : TOTAL RELATIVE VELOCITY vs. PASSAGE WIDTH - STATION 1

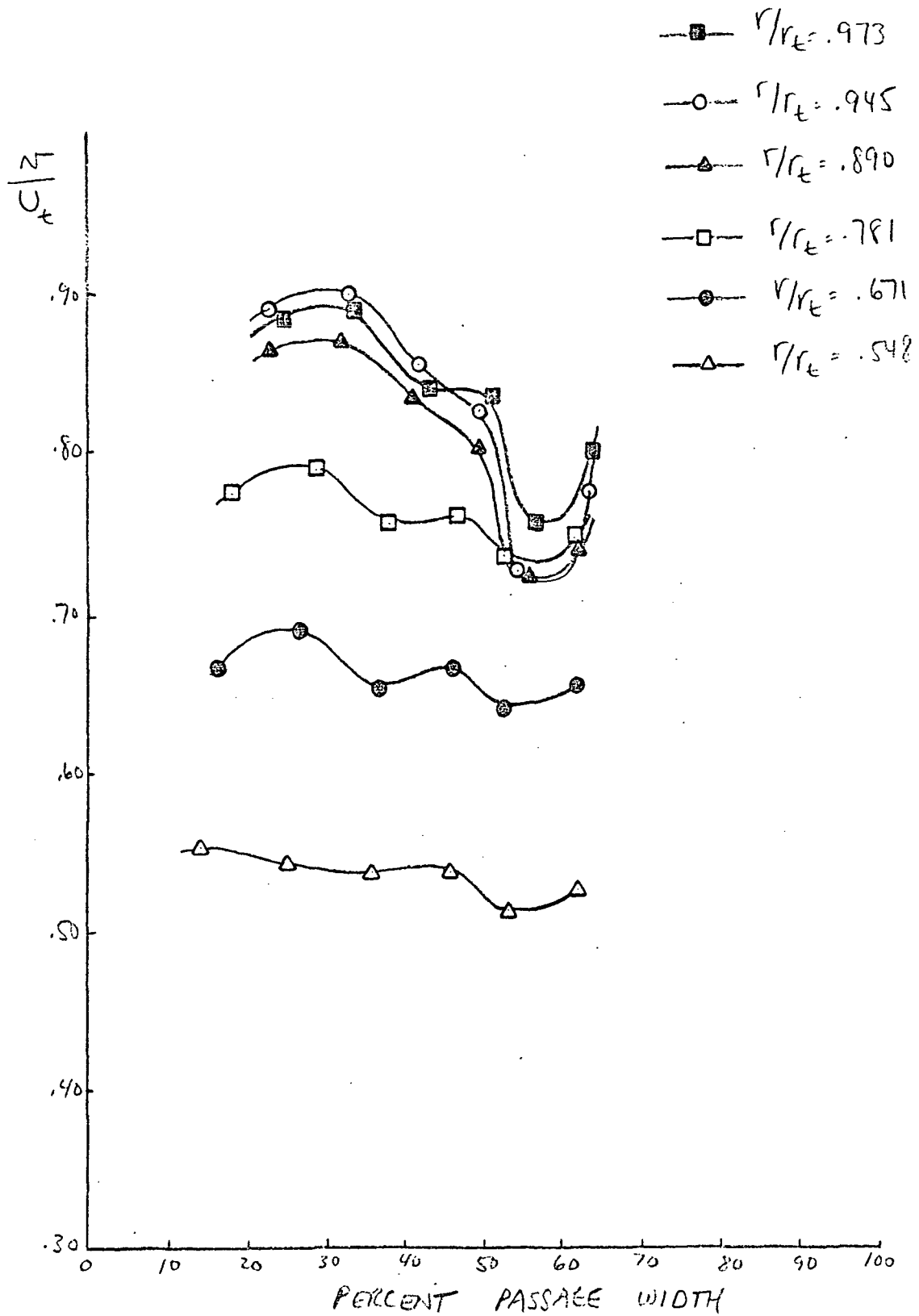


FIGURE 146 : RELATIVE TANGENTIAL VELOCITY VS. PASSAGE WIDTH - STATION 1

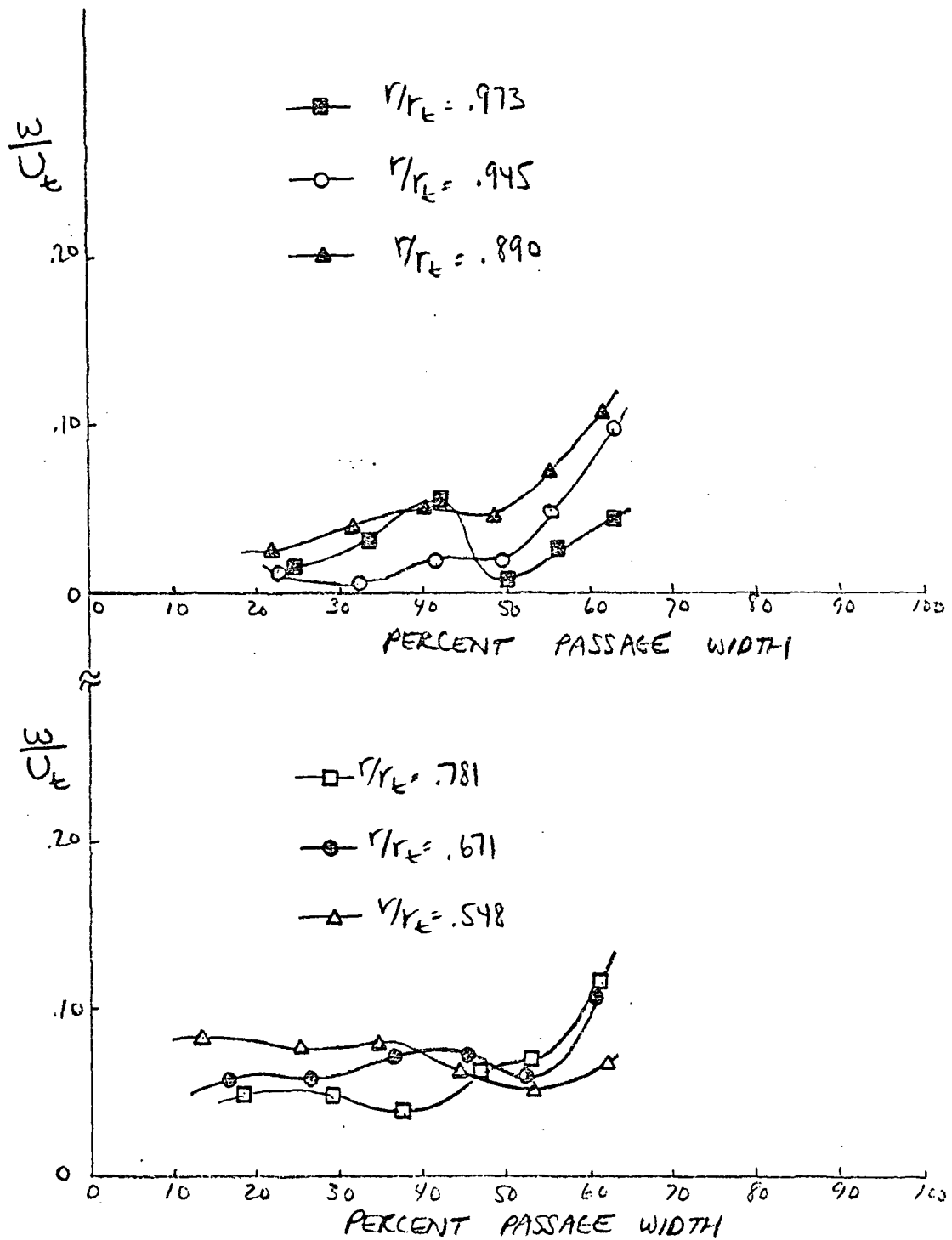


FIGURE 14C: RELATIVE AXIAL VELOCITY VS. PASSAGE WIDTH —  
STATION 1

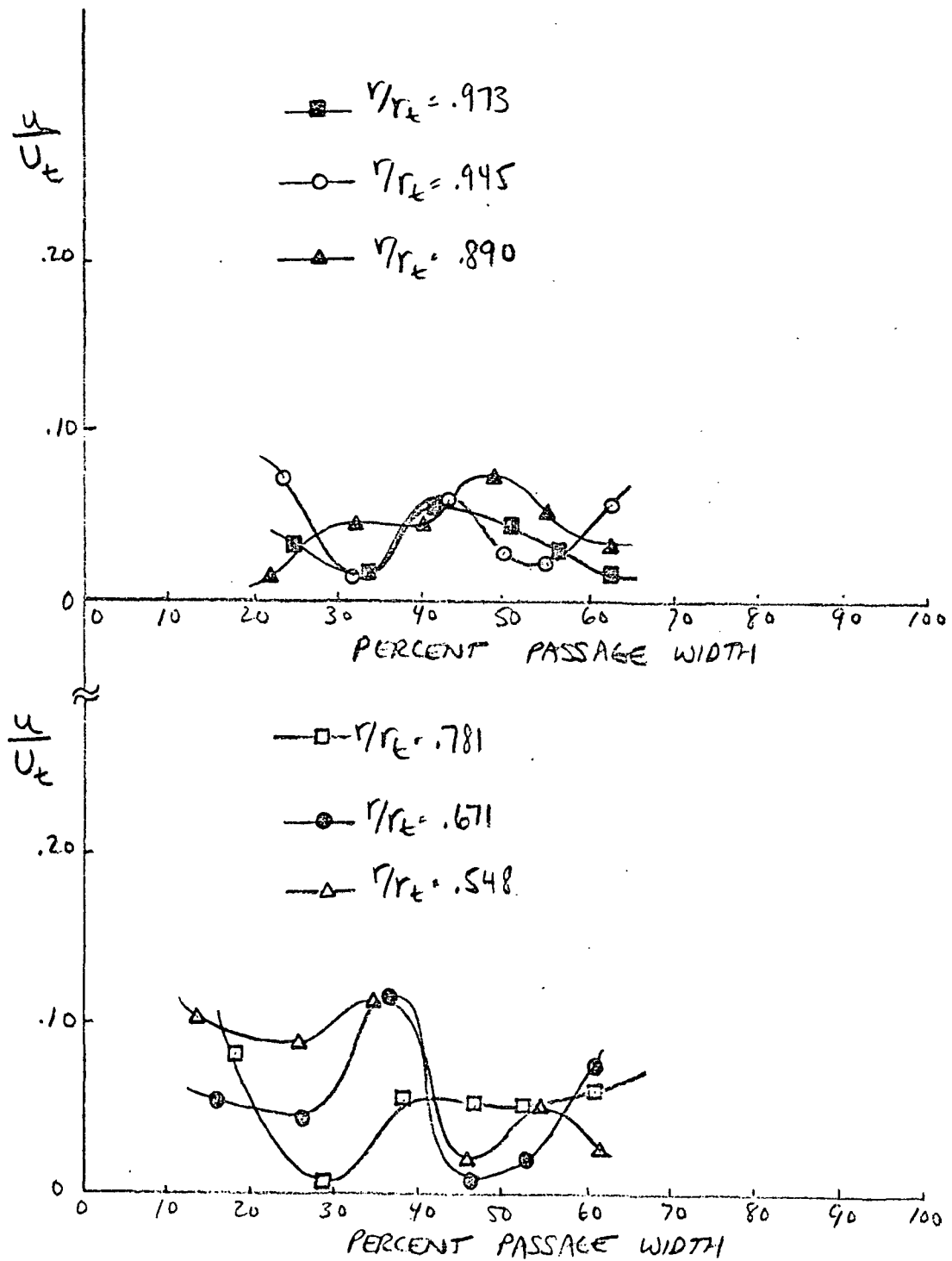


FIGURE 14d: RELATIVE RADIAL VELOCITY VS PASSAGE WIDTH -  
STATION 1



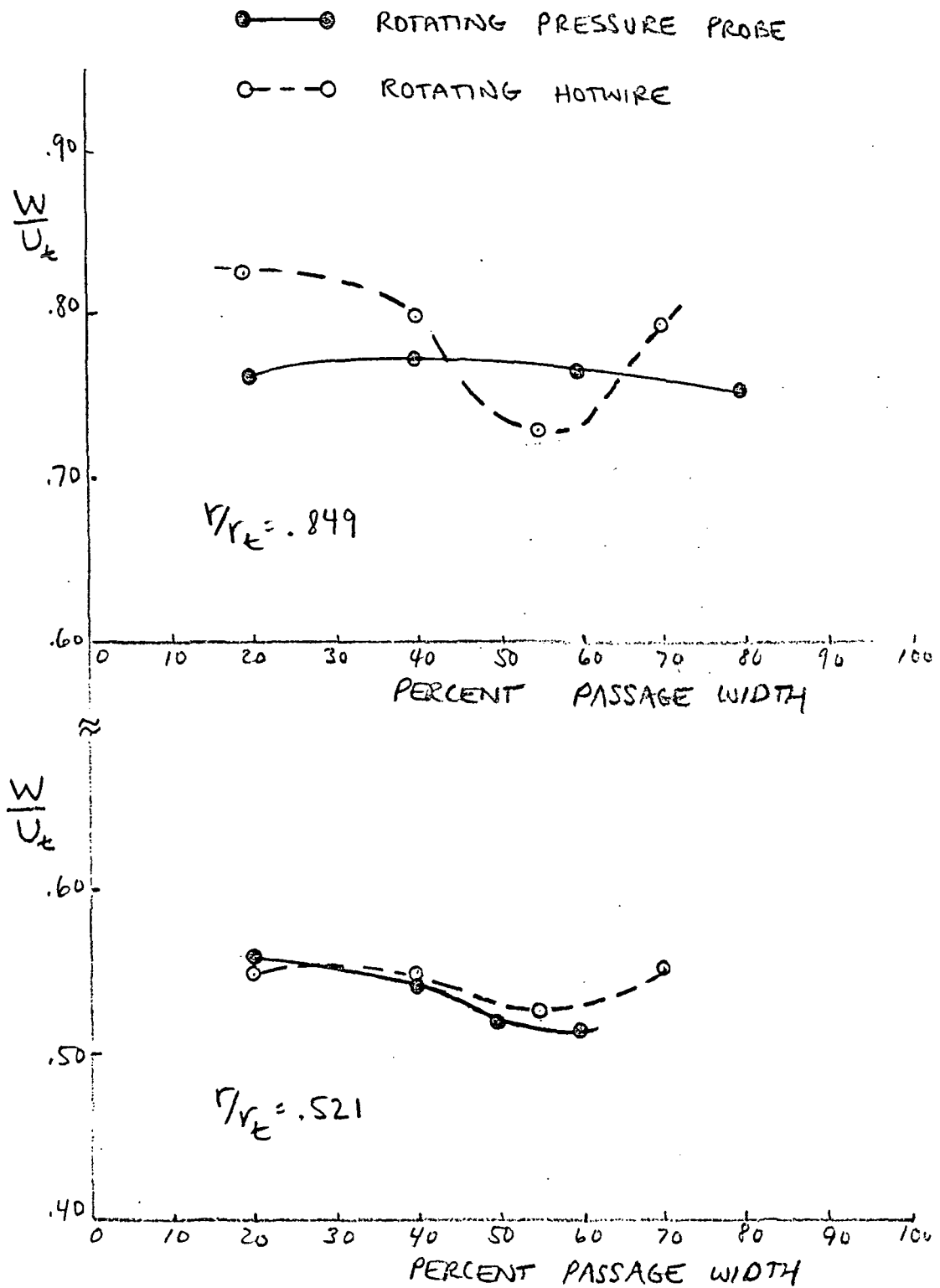


FIGURE 15: COMPARISON OF ROTATING HOTWIRE AND ROTATING PRESSURE PROBE MEASUREMENTS

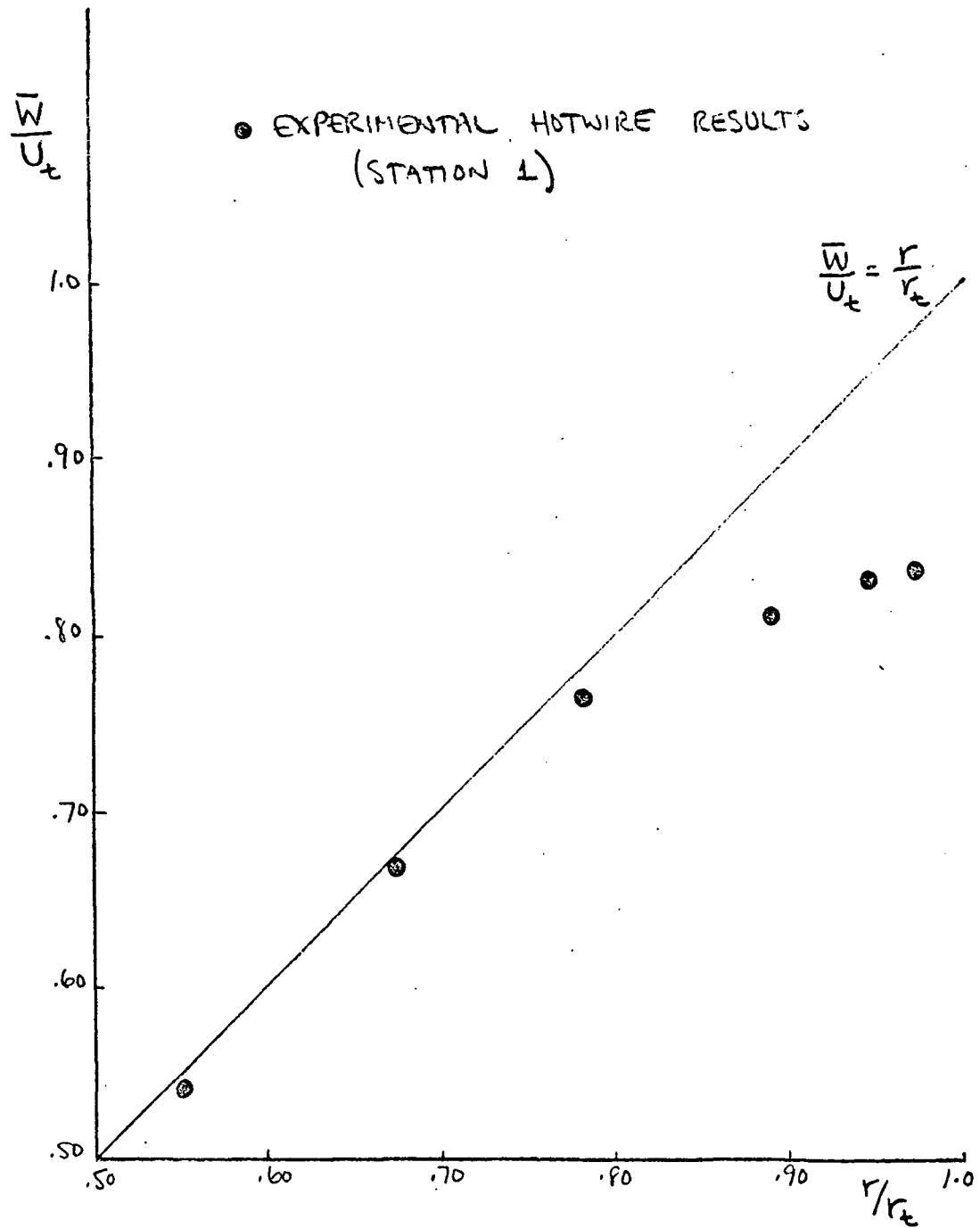


FIGURE 16: TOTAL RELATIVE VELOCITY VS.  $r/r_t$

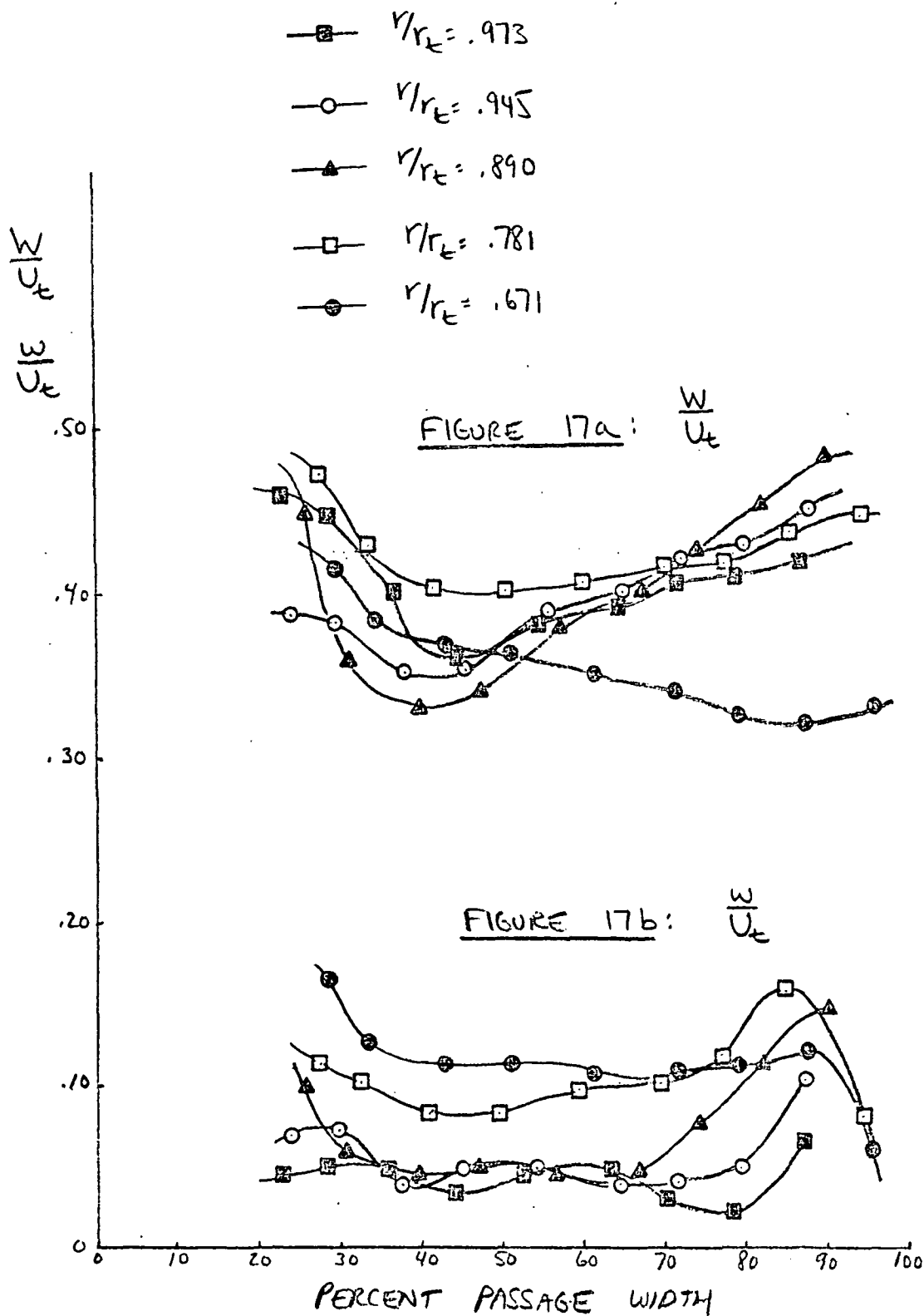


FIGURE 17 a-b : RELATIVE VELOCITY vs. PASSAGE WIDTH - STATION 2

- $r/r_t = .973$
- $r/r_t = .945$
- ▲—  $r/r_t = .890$
- $r/r_t = .781$
- $r/r_t = .671$

$\frac{N}{U_t}$   
 $\frac{u}{U_t}$

FIGURE 17c:  $\frac{N}{U_t}$

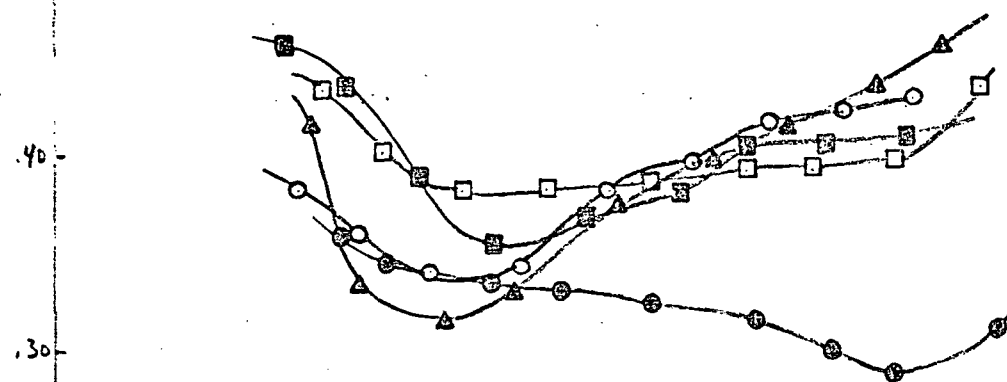


FIGURE 17d:  $\frac{u}{U_t}$

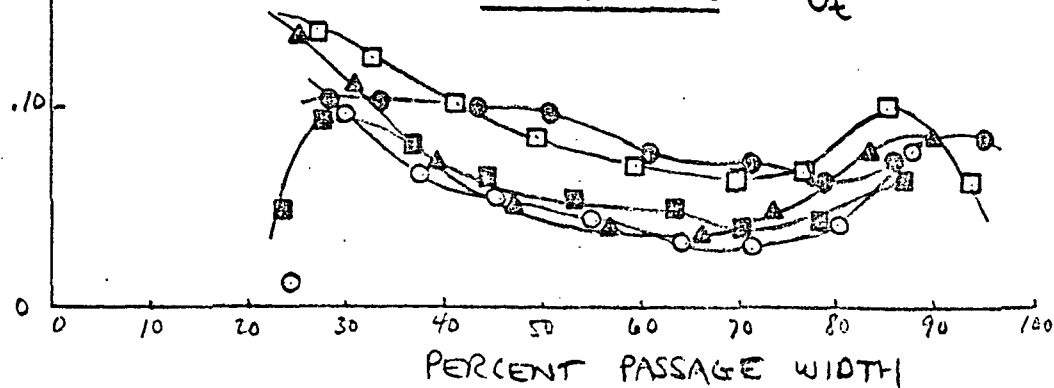
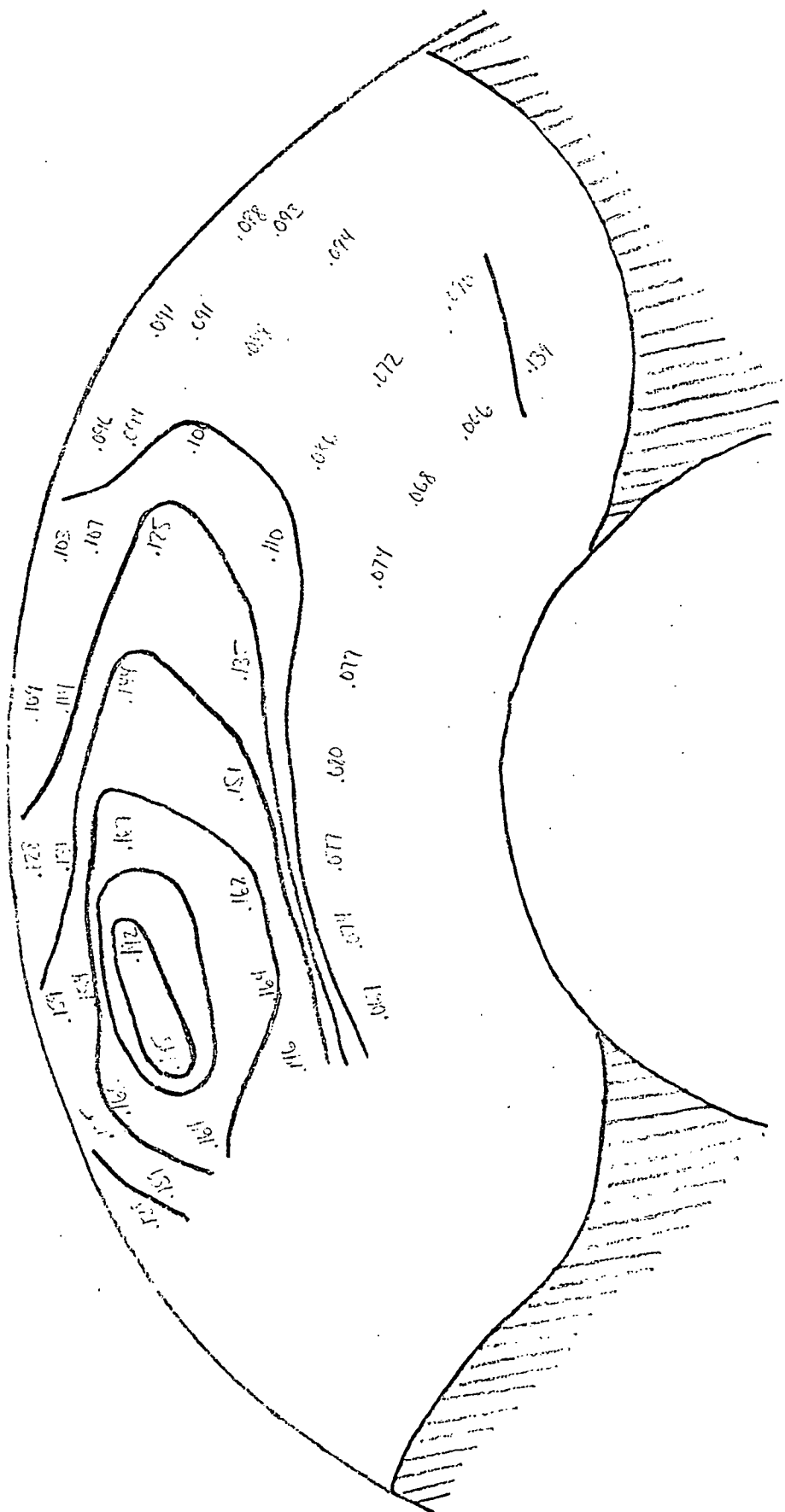
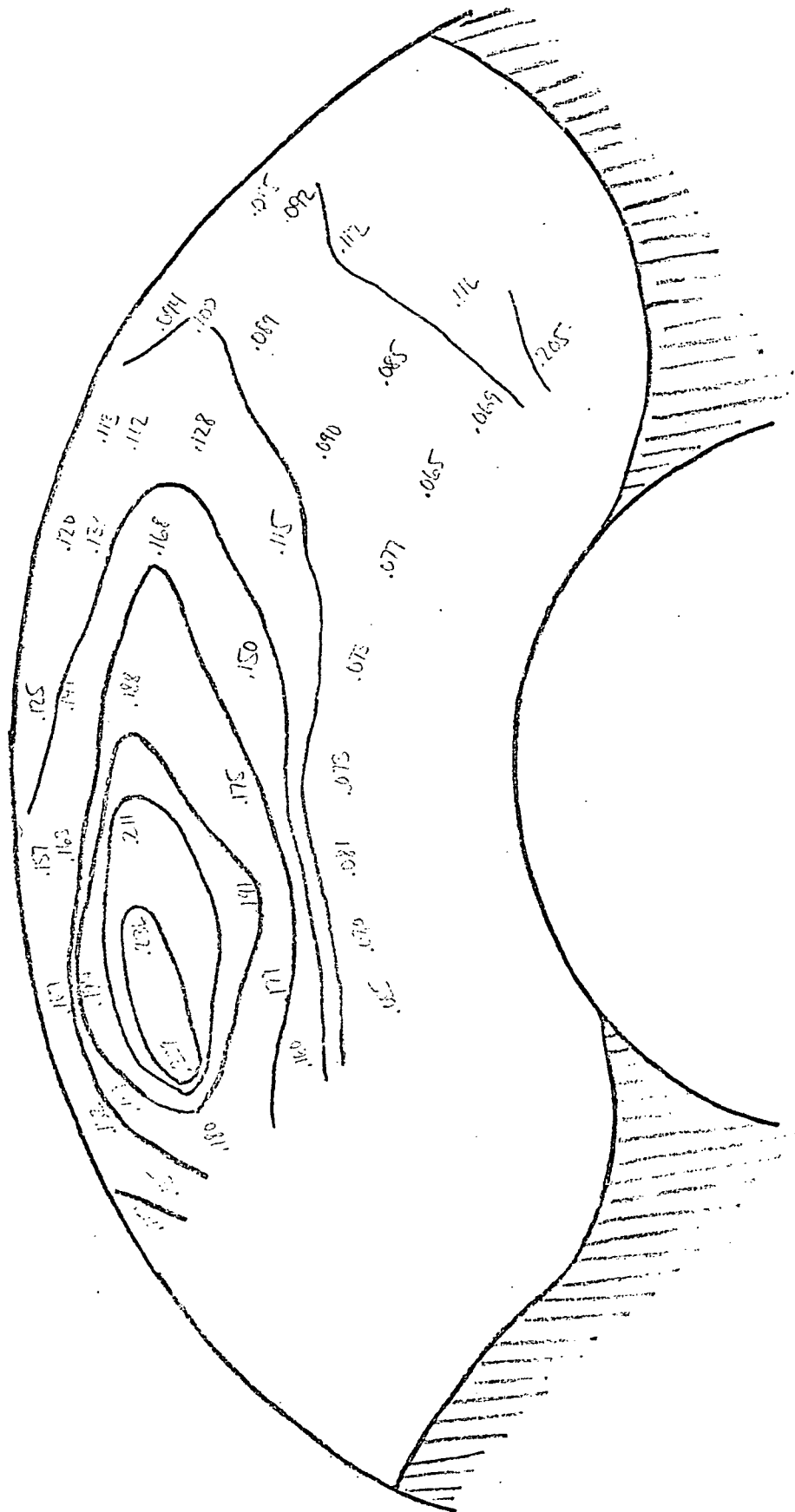


FIGURE 17 c-d: RELATIVE VELOCITY VS. PASSAGE WIDTH — STATION 2



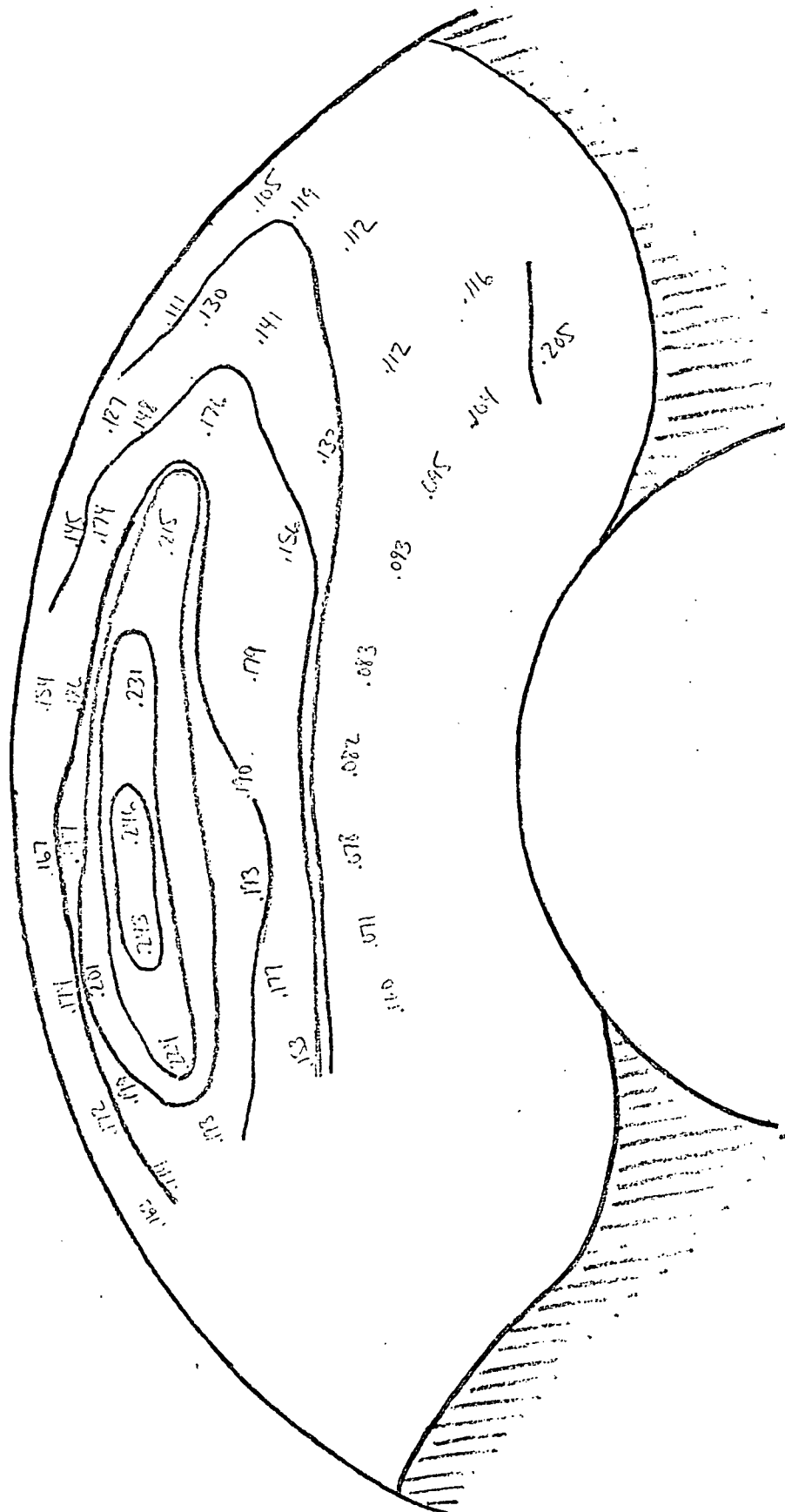
$$\frac{\sqrt{u'^2}}{W}$$

FIGURE 18 a: TANGENTIAL TURBULENCE INTENSITY ISOCONTOUR



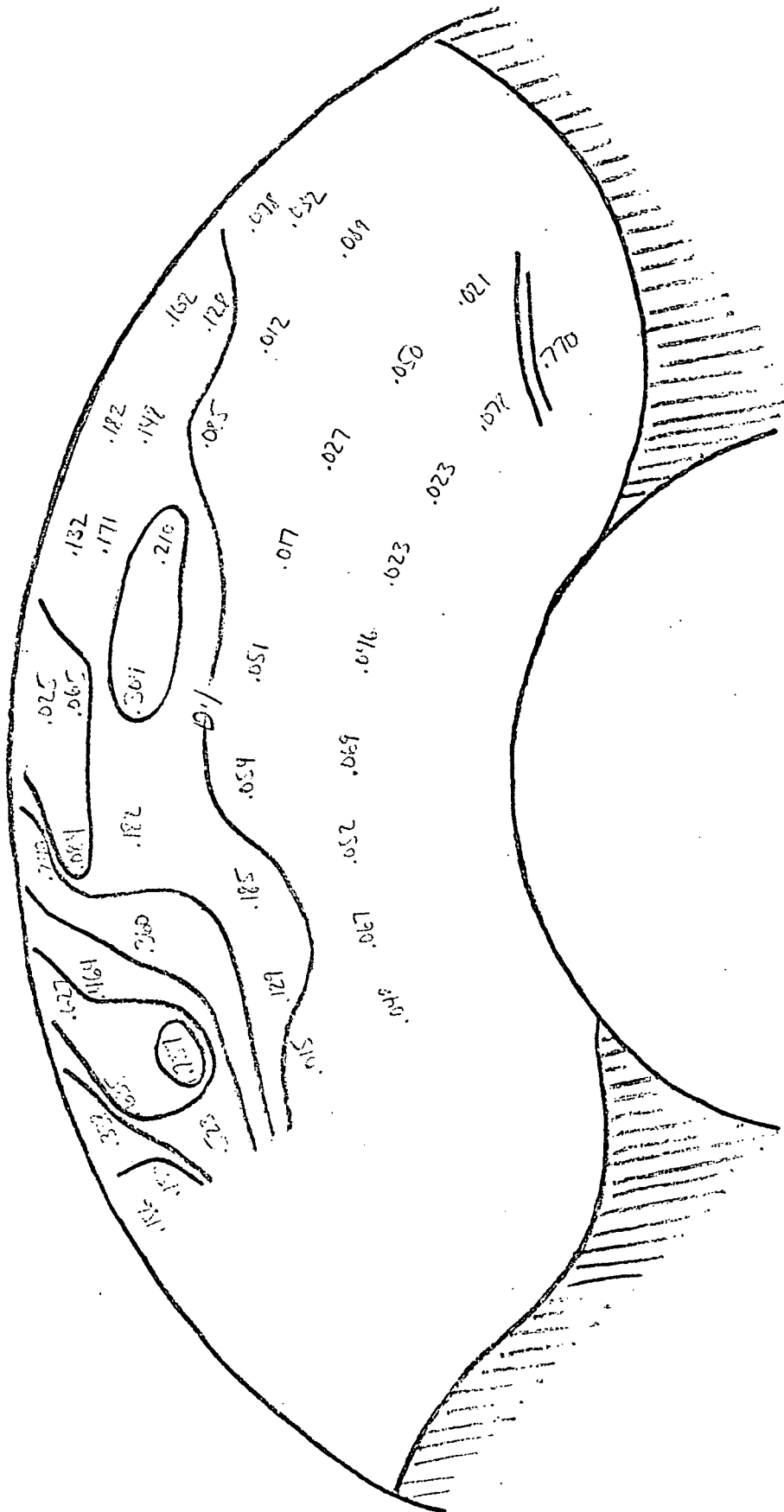
$$\frac{\sqrt{u'^2}}{W}$$

FIGURE 18 b: RADIAL TURBULENCE INTENSITY ISOCONTOUR



$$\frac{\sqrt{w'^2}}{W}$$

FIGURE 18 c: AXIAL TURBULENCE INTENSITY ISOCONTOUR



$$\left( \frac{\overline{u'w'}}{w^2} \right) \times 10^{-2}$$

$\overline{u'w'}$  ISOCONTOUR

FIGURE 19a:



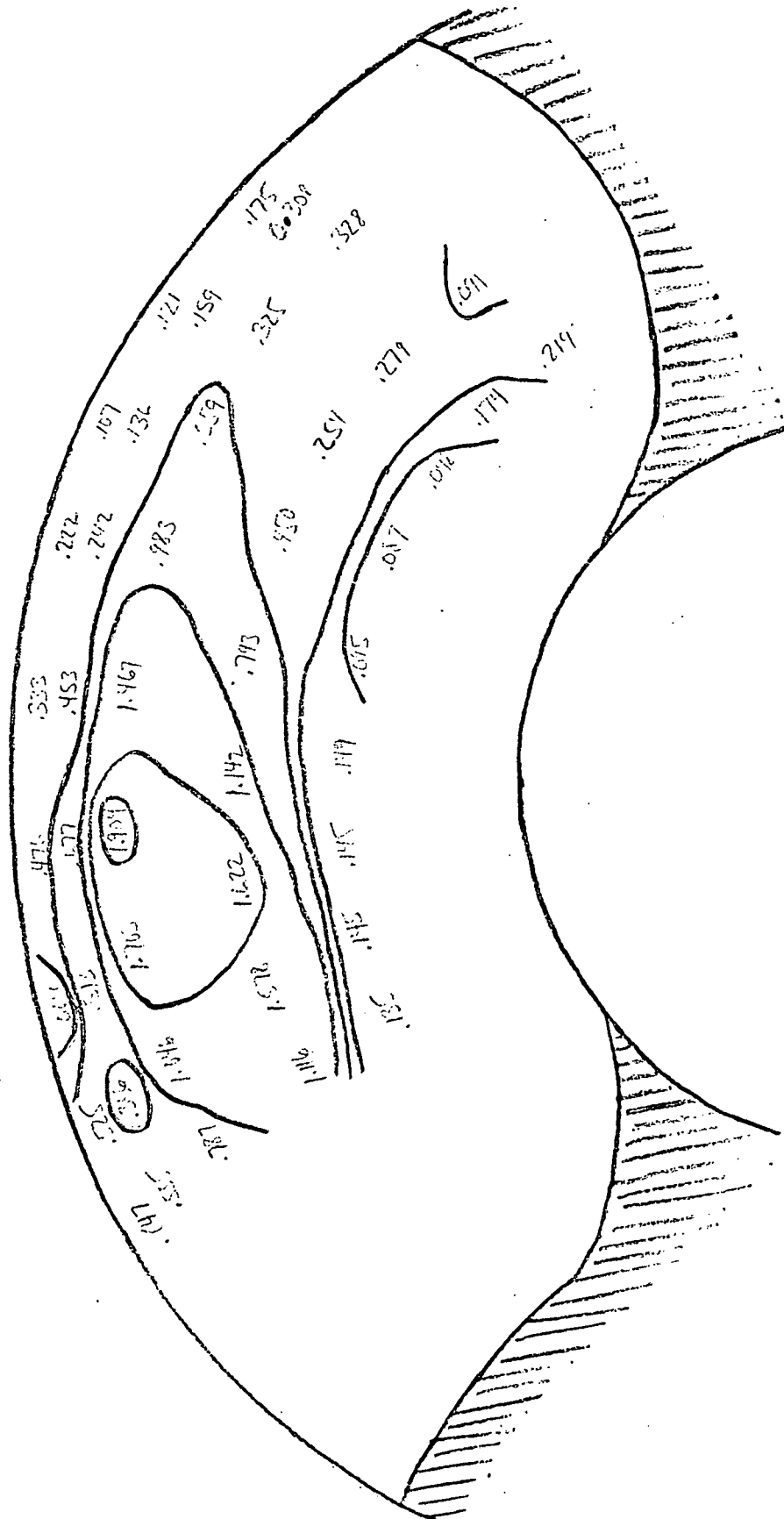
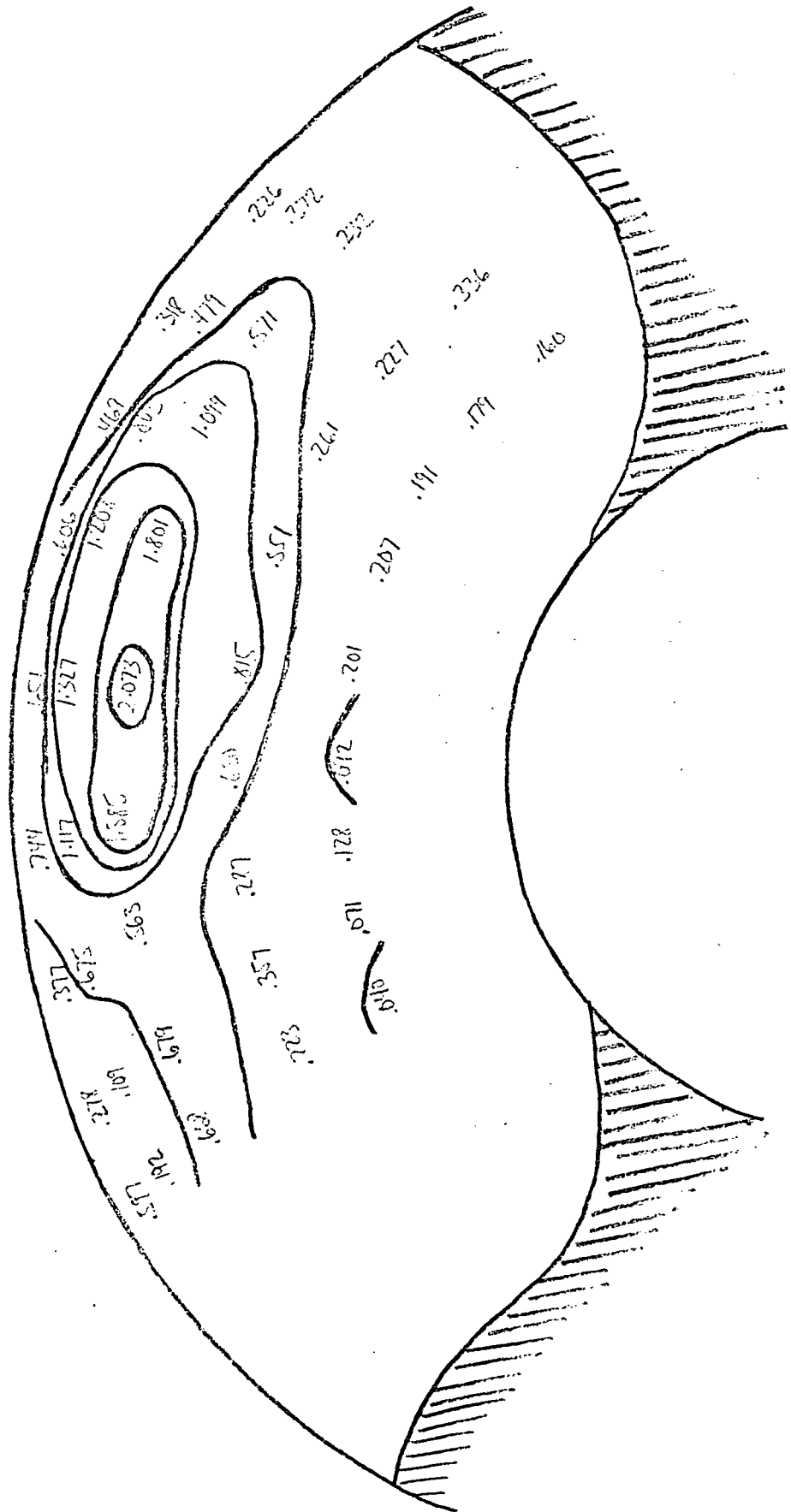


FIGURE 19b:  $n'w'$  ISOCONTOUR

$$\begin{pmatrix} 3 & 2 \\ 2 & 3 \end{pmatrix} \times 10^{-2}$$



$$\left( \frac{u'w'}{w^2} \right) \times 10^{-2}$$

ISOCONTOUR

$$\overline{u'w'}$$

FIGURE 19C:

## PRESSURE MEASUREMENT STATIONS

MEASUREMENT STATION	FLOW	PASSAGE	RADIAL	STATION	
	1 (HUB)	2	3 (MID)	4	5 (TE)
PRESSURE SURFACE					
1 (LE)	11.3	8.9	6.5	5.7	4.9
2	15.5	14.3	13.	12.	11.
3	24.	24.	24.	23.8	23.5
4	34.	36.	38.	38.	38.
5	44.	48.	52.	52.3	52.5
6	51.	55.5	60.	60.5	61.
7	58.	63.	68.	69.	70.
8	66.	72.	78.	78.5	79.
9	74.	80.	86.	86.5	87.
10 (TE)	82.	88.	94.	95.	96.
SUCTION SURFACE					
1 (LE)	15.	13.3	11.5	11.	10.4
2	19.5	18.9	18.2	17.6	17.
3	28.4	29.2	30.	30.	30.
4	45.	47.5	50.	50.5	51.
5	54.	57.	60.	61.	62.
6	62.	66.	70.	70.8	71.5
7	69.	73.5	78.	78.5	79.
8	75.	80.5	86.	86.	86.
9	81.	86.5	92.	92.3	92.5
10	85.	91.	97.	97.	97.

220

TABLE 2: RADIAL LOCATION ( $r/r_c$ ) OF BLADE  
 STATIC PRESSURE MEASUREMENT STATIONS

MEASUREMENT STATION	FLOW PASSAGE RADIAL STATION				
	1 (HUB)	2	3 (MID)	4	5 (TIP)
PRESSURE SURFACE					
1 (LE)	.291	.466	.644	.815	.985
2	.295	.466	.637	.808	.985
3	.322	.479	.654	.819	.985
4	.342	.500	.664	.823	.985
5	.356	.514	.671	.823	.985
6	.370	.521	.678	.829	.985
7	.390	.541	.689	.835	.985
8	.411	.555	.699	.842	.985
9	.438	.575	.719	.849	.985
10 (TE)	.473	.609	.726	.863	.985
SUCTION SURFACE					
1 (LE)	.288	.466	.640	.815	.985
2	.301	.479	.644	.823	.985
3	.322	.486	.658	.823	.985
4	.342	.500	.664	.823	.985
5	.356	.514	.671	.829	.985
6	.370	.527	.678	.835	.985
7	.390	.541	.685	.835	.985
8	.397	.548	.692	.835	.985
9	.425	.555	.699	.835	.980
10 (TE)	.435	.561	.692	.842	.983

$$r_c = 18.25''$$